Springer Earth System Sciences

Kate Horan

Falkland Islands (Islas Malvinas) in the Permo-Carboniferous

From Icehouse to Greenhouse

Springer

Springer Earth System Sciences

More information about this series at http://www.springer.com/series/10178

Kate Horan

Falkland Islands (Islas Malvinas) in the Permo-Carboniferous

From Icehouse to Greenhouse

Springer

Kate Horan
Department of Earth Sciences
University of Cambridge
Cambridge, Cambridgeshire
UK

and

Department of Earth Sciences
Durham University
South Road
Durham, County Durham
UK

ISSN 2197-9596 ISSN 2197-960X (electronic)
Springer Earth System Sciences
ISBN 978-3-319-08707-8 ISBN 978-3-319-08708-5 (eBook)
DOI 10.1007/978-3-319-08708-5

Library of Congress Control Number: 2014955063

Springer Cham Heidelberg New York Dordrecht London

Printed on acid-free paper

Springer International Publishing AG Switzerland is part of Springer Science+Business Media (www.springer.com)

Editorial Support to Author

Simon Crowhurst read Experimental Psychology at the University of Oxford and worked for more than 20 years with Nick Shackleton learning the principles of astronomical forcing of sediment sequences. He has many publications of which he is a co-author, and illustrated the Willis and McElwain book on the Evolution of Plants. He now works as the Senior Laboratory Technician at the University of Cambridge Earth Sciences department.

Contact: Mr. Simon Crowhurst, Senior Research Technician, Department of Earth Sciences, University of Cambridge, Downing Street, Cambridge, CB2 3EQ.
Email: sjc13@cam.ac.uk

Phil Stone is a Research Associate with the British Geological Survey in Edinburgh. Between 1998 and 2009 he acted as Geological Advisor to the Department of Mineral Resources, Falkland Islands Government, and was responsible for recovering from the Falkland Islands the borehole core that forms the basis of this study.

Contact: Dr. Phil Stone, British Geological Survey, Murchison House, West Mains Road, Edinburgh, EH9 3LA.
Email: psto@bgs.ac.uk

Preface

The opportunity to study palæoclimate has been an exciting, challenging and rewarding experience. As a Natural Sciences undergraduate student at the University of Cambridge, I developed a strong interest in Earth Sciences, in particular climate change, sedimentology and geomorphology. During my master's degree, I was lucky enough to take these interests further in a three-month research project. It is the results of this project which provided the impetus for writing this book.

Developing an understanding of Earth's climatic history has become all the more intriguing and necessary in order to appreciate current climate change in the context of longer timescales. Transitions from icehouse to greenhouse worlds and vice versa are the largest of the climatic switches known to occur on Earth and they are accompanied by extreme palæoenvironmental changes. This book documents one such change, the Late Carboniferous to Permian deglaciation of southern Gondwana, by drawing upon evidence from a Gondwana fragment that became the Falkland Islands (Islas Malvinas) microplate following the break-up of the supercontinent.

The sedimentology of the Hells Kitchen Member of the Port Sussex Formation in East Falkland comprises deposits that document the switch from icehouse to greenhouse conditions. These Falkland Islands strata correlate with glacigenic units in South Africa and South America, all of which were deposited during the widespread, Late Carboniferous to Early Permian glaciation of Gondwana. Sedimentary logging, X-ray fluoresence (XRF) scanning and reflectance scanning were carried out on solid rock cores which host these sediments. The data collected was used to support a facies evaluation and an investigation into the nature of the climate change. In addition, it presented a unique opportunity to explore the application of Milankovitch orbital cycles to sedimentary sequences at this time.

This book is published as part of the series of Springer Earth System Sciences. It serves as a case study because the Falkland Islands cores pinpoint evidence from just one locality nested within the Gondwanan supercontinent at the time of the icehouse to greenhouse transition. The research complements other accounts of Falkland Islands geology, the climate and palæotectonic reconstructions of the Gondwanan supercontinent and long-term climate change. It is hoped that it will be

a valuable resource to both scientists and students working across a range of disciplines within the Earth Sciences, but primarily its focus is geared towards those with research interests in the above areas.

Kate Horan

Acknowledgments

I am extremely grateful to my teachers, in particular Richard Tighe and Merrick Weems, who were responsible for sparking my initial interest in this subject area and inspiring me to go on to university to pursue my interests. Special thanks go to Simon Crowhurst for his strong support and enthusiasm throughout the project which, combined with his insightful contributions particularly into time series work, have been invaluable. The borehole cores on which this study was largely based were acquired between 2005 and 2007 by Falklands Gold and Mineral Ltd. Thanks go to Dr. Phil Stone for recovering these cores from the Falkland Islands and to the British Geological Survey for making them available for this study. Logistical support for shipping the borehole cores to the UK was provided by the British Antarctic Survey. Phil Stone also provided excellent scientific editorial guidance.

Additionally, I would like to thank Dr. Morag Hunter and Prof. David Hodell for their helpful discussions during the production of the project at Cambridge. Further thanks go out to James Rolfe who assisted with Total Organic Carbon measurements and to Dr. Claus-Dieter Hillenbrand, Vikki Peck and Claire Allen, from the British Antarctic Survey, who provided guidance on how to approach interpretations of glacial sediments. It has been a great pleasure to work with many different people all of whom have in some way provided me with some inspiration and made the project a lot of fun. Girton College, Cambridge, also kindly covered some of the project expenses.

Finally, I would like to thank my parents for their support during my studies.

Contents

Abbreviations

LPIA	Late Palæozoic Ice Age
TOC	Total Organic Carbon
IRD	Ice Rafted Debris
ETP	Synthetic Carboniferous orbital solution including eccentricity, tilt and precession
L*	Reflectance parameter: lightness
a*	Reflectance parameter: red/green ratio
b*	Reflectance parameter: blue/yellow ratio
XRF	X-ray fluorescence
Fe10	For elements measured at more than one energy band by the Avaatech XRF core scanner, the number represents the voltage in kV; here iron measured on the 10 kV run
pCO_2	Partial pressure of carbon dioxide
$\delta^{13}C_{org}$	Isotope ratio of $^{13}C/^{12}C$ in organic matter
$\delta^{13}C_a$	Isotope ratio of $^{13}C/^{12}C$ in atmospheric CO_2
PCA	Principal Component Analysis
SPSS	Statistical Package for the Social Sciences
BGS	British Geological Survey

Abstract

The Late Carboniferous to Early Permian ‘icehouse to greenhouse’ transition in the Falkland Islands was accompanied by cyclical waxing and waning of the Gondwanan, south polar ice sheet. The cyclical changes are manifested in the sedimentary deposits of the Fitzroy Tillite and Port Sussex formations. This study looks in detail at two sediment cores spanning these formations that were recovered from the Falkland Islands in 2008 following a mineral exploration programme. The lithologies and sedimentary fabrics appear to record a switch from deposition under a grounded ice sheet to glaciolacustrine or glaciomarine deposition punctuated by minor episodes of ice advance and retreat during a period of net ice sheet retreat. X-ray fluorescence and reflectance data have been used to quantify the change in terms of geochemical and geophysical properties respectively. Elements including zirconium, manganese, chromium, iron and titanium helped to constrain the cyclicity. Wavelet and spectral analyses, run to look for prominent periodicities in the data, were suggestive of orbitally forced oscillations within the transition. This permitted the development of a hypothetical time framework for the series spanning approximately 1.2 million years through age modelling. The integrated approach of this research, which combines sedimentological data with geochemistry, makes it a robust insight into this past climatic transition and may help to evaluate and inform predictions of future climate change.

Keywords Falkland Islands · Fitzroy Tillite Formation · Hells Kitchen Member · Permo-Carboniferous · Icehouse to greenhouse · Gondwana · Deglaciation

Chapter 1
Introduction

Abstract Investigating the dynamic behaviour of Earth's climate system remains a significant challenge. It is partly motivated by our limited knowledge of how the system will evolve in the future and the resilience of ice sheets to perturbations. Throughout geological history, the Earth has been subjected to extreme climatic transitions. These have taken place over various spatial and temporal scales ranging from localised decadal oscillations through to millennial- and multi-millennial-scale processes affecting the whole planet. The focus of this study lies within the latter kind, wherein the Earth flips between icehouse and greenhouse states. During the Permo-Carboniferous, when the Gondwanan supercontinent lay close to the South Pole, sedimentary deposits developed that documented one such transition. This chapter outlines the potential for study in material extracted from East Falkland during a mineral exploration programme in 2008. The geographical location of the Falkland Islands in the Permo-Carboniferous based upon Palæozoic reconstructions of Gondwana is discussed and the stratigraphic links between the Falklands deposits and other similar deposits from across the continent explored. Our understanding of how major climatic changes proceed, and the possible triggers behind them, could be significantly improved by studies of such deposits.

Keywords Permo-Carboniferous climate change · Icehouse to greenhouse · Gondwana · Falkland Islands · Ice sheets

1.1 Overview

The climatic conditions of the Late Palæozoic Earth oscillated between cold 'icehouse' states with persistent polar ice and warm 'greenhouse' states without polar ice (Fig. 1.1). With many questions about the long-term future of our climate,

Electronic Supplementary Material The online version of this Chapter (DOI 10.1007/978-3-319-08708-5_1) contains supplementary material, which is available to authorized users.

K. Horan, *Falkland Islands (Islas Malvinas) in the Permo-Carboniferous*,
Springer Earth System Sciences, DOI 10.1007/978-3-319-08708-5_1

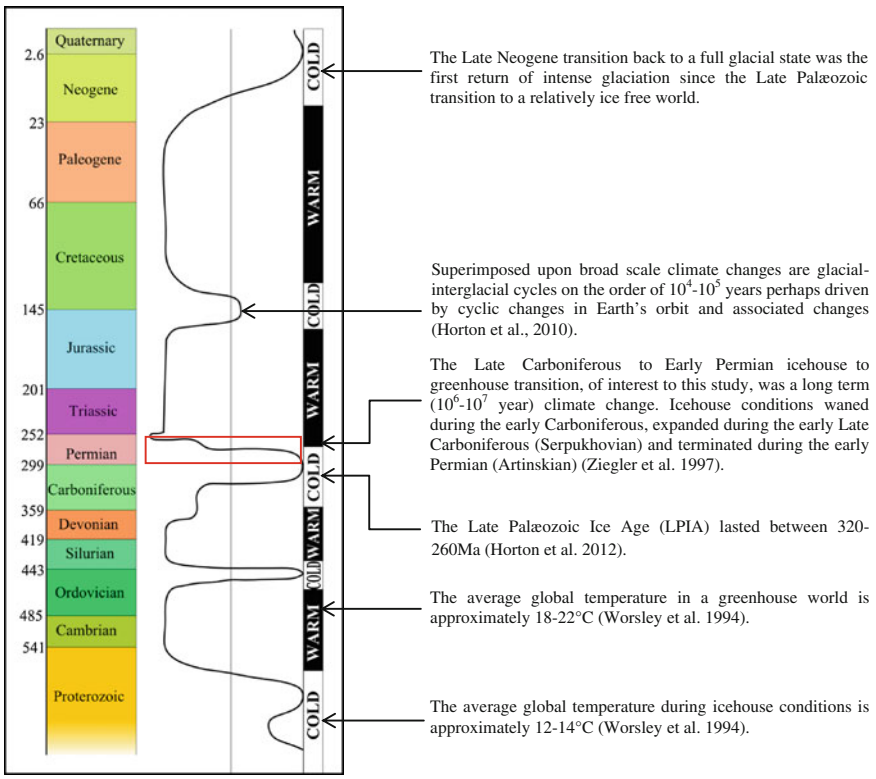

Fig. 1.1 Earth's long-term climate history modified from Scotese et al. (1999) to reflect the recent international chronostratigraphic chart (International Commission on Stratigraphy, August, 2012). *Numbers on the left hand side* of the figure refer to age in millions of years. Note that this figure does not account for the diachroneity of climate change across continents

it is increasingly important to improve understanding of how these major climatic changes proceed. The Late Carboniferous Ice Age provides the last complete record of a transition from icehouse to greenhouse conditions (Gastaldo et al. 1996) and forms the focus of this study.

Mineral exploration drilling in the Falkland Islands between 2005 and 2007 generated eight core sections located between Old House Rocks and Black Rock, East Falkland, that span the Permo-Carboniferous icehouse to greenhouse transition. Commercial interest in these cores declined in 2008 and permission was obtained from the exploration company, Falklands Gold and Minerals Ltd., for samples to be taken and returned to the UK for assimilation into the national core archive. This is maintained by the British Geological Survey (BGS) at their headquarters in Keyworth, Nottingham. The main objective of this book is to place sedimentological and geochemical data collected from these cores within a framework that explains the interactions between climate and glacier dynamics over

the segment of the Gondwanan continent from which the East Falkland Islands formed. The core sequences contain deposits belonging to the Fitzroy Tillite and Port Sussex formations. These are characterised by subglacial, massive diamictite passing upwards into glaciomarine/glaciolacustrine diamictites, mudstones and black shales; a record which provides an excellent opportunity to study ice sheet advance and retreat across the East Falklands margin.

The nature of the icehouse to greenhouse transition may be explored through addressing the following four questions.

1. Does the transition occur through gradual climatic drift to a warmer state or is it marked by oscillations, episodic or periodic, between the extremes before a tipping point is reached?
2. What are the links between the sedimentological and the physicochemical properties of the deposits?
3. Could the climate changes within the course of the transition have been orbitally forced? Improving our understanding of the climate system earlier in Earth's history may have relevance for our ability to gauge future climate change projections operating under similar climate dynamics.
4. How do the deposits in the Falkland Islands correlate with deposits in other localities that also span the transition? Synthesising the stratigraphic record from the Falkland Islands with records across Gondwana could help to constrain the waxing and waning of glacial intervals of the Late Palæozoic Ice Age (LPIA) and provide insights into the drivers of ice growth and deglaciation.

1.2 Geographical Context

Today, the Falkland Islands are an archipelago in the South Atlantic Ocean situated between 51° and 52° 30′S and 57° 30′ and 61° 30′W. They comprise two main islands, East and West Falkland, and several hundred smaller islands (Fig. 1.2).

In contrast, current Late Carboniferous reconstructions of the Gondwana supercontinent place the Falkland Islands at high latitudes off the east coast of South Africa and in a rotated position close to Port Elizabeth. These reconstructions (e.g. Adie 1952; Marshall 1994) are based on the continuity of structural trends from the Gondwanan orogeny (Curtis and Hyam 1998), outcrop patterns, palæo-ice flow directions, palæomagnetic reconstructions (Mitchell et al. 1986) and palæocurrent data (Hyam et al. 1997) and are supported by the distribution of Early Devonian marine faunas of the Malvinokaffric Province (Bradshaw 1998). Comparison of Permian facies, ichnology and palæocurrents in the Falkland Islands and the Dwyka, Ecca and Beaufort (part) groups in South Africa also support this (Trewin et al. 2002). Nevertheless, despite the compelling evidence for microplate rotation arising from comparisons of onshore geology, it should be noted that there is a contrary view held mainly by those working with offshore data generated by the hydrocarbon exploration programmes currently active around the Falklands.

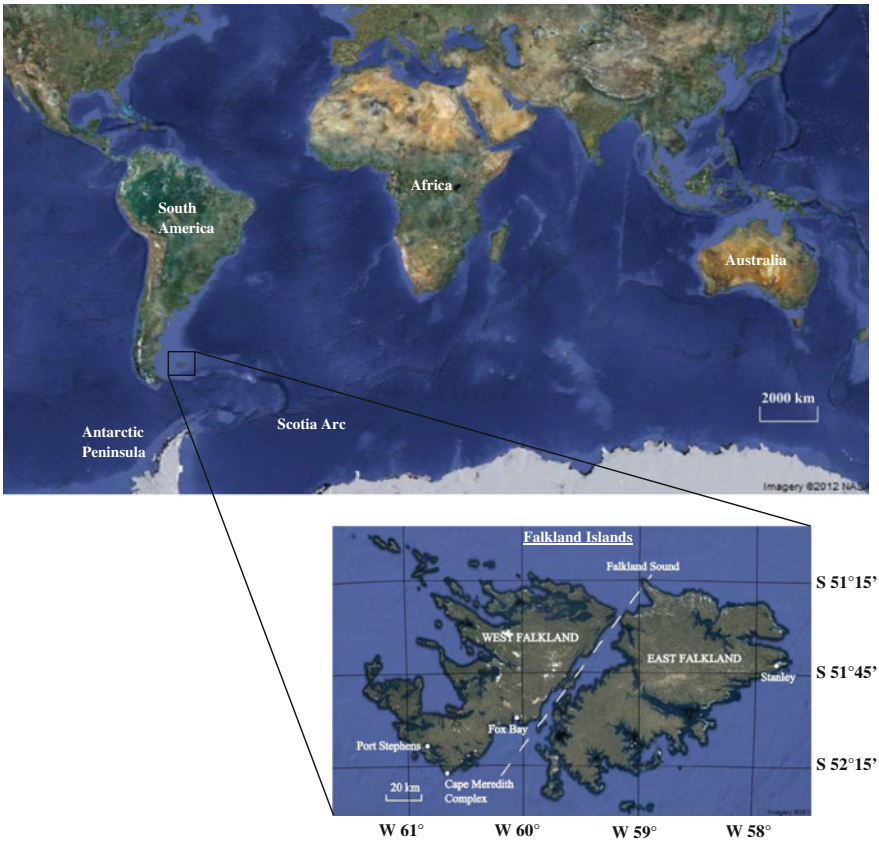

Fig. 1.2 Geographical location of the Falkland Islands with locations relevant to the LPIA in Gondwana labelled. *Inset* highlights study site. Images were taken and adapted from Google Earth

The offshore data provide no evidence in support of the rotational model. Indeed, they are more readily reconciled with a Gondwana break-up in which the Falklands remain a part of a fixed Falkland Plateau extending from the South American margin (e.g. Lawrence et al. 1999). This debate continues.

Gondwana migrated across the South Pole during the Late Palæozoic (Fig. 1.3), and as a result, glaciation began in western Gondwana (present-day South America) in the Famennian (Late Devonian) (Caputo et al. 2008) and ended in eastern Gondwana (eastern Australia) in the Capitanian (Middle Permian) (Fielding et al. 2008a). As a consequence, secular climate change associated with this latitudinal movement across zonal climatic belts was superimposed on the change from ice-house to greenhouse (Scotese et al. 1999).

Crowell and Frakes (1972), Crowell (1983) and Caputo and Crowell (1985) concluded that a centre of glaciation migrated across South America, South Africa and Antarctica from 350 to 240 Ma. Ice centres waxed and waned across the

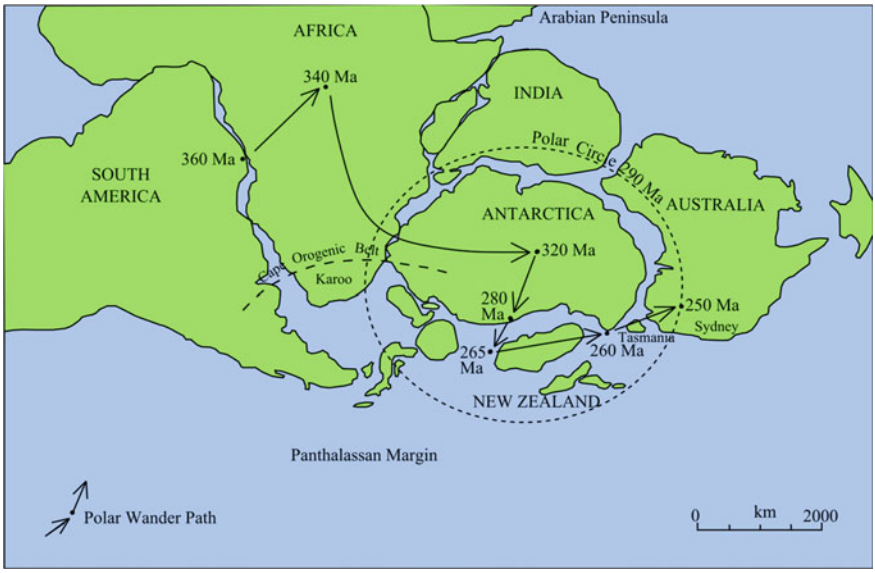

Fig. 1.3 Palæomagnetic studies demonstrate that movements of the continents resulted in a relative drift in the position of the South Pole; figure adapted from Henry et al. (2012), and Crowell and Frakes (1972)

different sites during this time interval. Glaciation likely ensued when broad continental areas reached near-polar positions, and expanses of open water were sufficiently near to provide evaporative moisture. A reconstruction of ice cover in the Late Carboniferous is provided in Fig. 1.4 and illustrates the likely ice flow patterns.

In most localities from the Gondwanan landmasses, glacigenic deposits are relatively thin and consist of a variety of rock types and/or striated surfaces interpreted to indicate terrestrial or grounded marine ice sheets (Matsch and Ojakangas 1992). When Gondwana began to break up ~200 Ma (Stone et al. 2012), the glacial deposits became dispersed across the continents. Table 1.1 collates information from various sources on the thickness and age of the corresponding glacial deposits across the present-day continents, and Fig. 1.5 synthesises this information in time. Difficulties in correlating thicknesses arise because glacial strata are often eroded; only those dumped during glacial retreat are typically preserved. The correlation carried out in the time domain involved hypotheses about the relative timing of events documented in the sedimentary record. Some inconsistencies between sources (shown in Table 1.1) mean some boundaries are approximate, highlighting the need for improved chronology. Oman, Pakistan and Yemen were in the Northern Hemisphere at this time, which explains their deviation from the trend of glacial strata becoming progressively younger in successive stratigraphical columns from left to right across Fig. 1.5. Australia underwent early

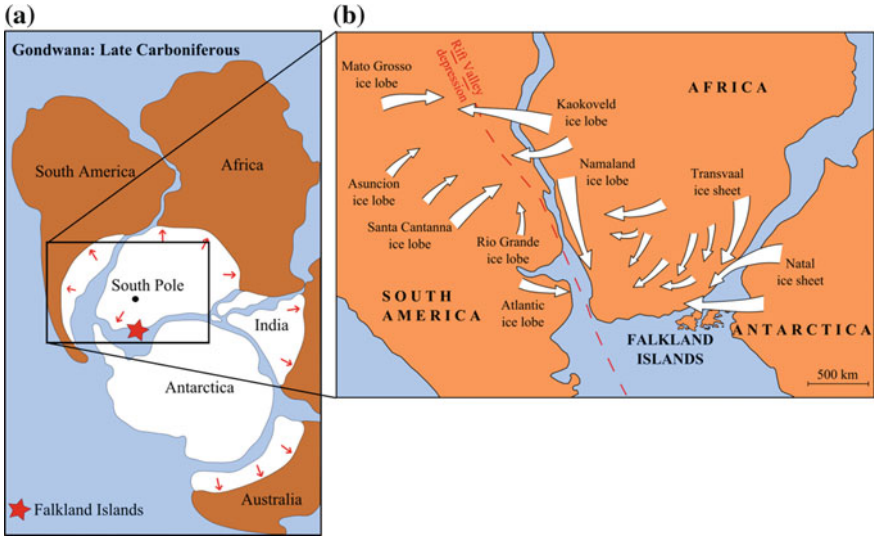

Fig. 1.4 **a** Reconstruction of ice extent across Gondwana with supporting evidence from various authors utilised (e.g. Scotese et al. 1999). The Falkland Islands lay off the southeast coast of South Africa at this time. **b** Ice flow patterns in the Late Palæozoic; adapted from Stollhofen et al. (2008). Work by Visser (1987, 1997) and Grill (1997) showed that not all of these ice centres were active at the same time

glaciations and later Permian glaciations as a result of its position relative to the South Pole (Fielding et al. 2008b, c). Therefore, it is also difficult to correlate Australia with glaciations in Antarctica, Africa, the Falklands and South America.

1.3 Geological Context

The geology of the Falkland Islands has three main divisions: the Proterozoic Cape Meredith Complex, the Silurian to Devonian West Falkland Group and the Carboniferous to Permian Lafonia Group (Aldiss and Edwards 1999). These are illustrated in Fig. 1.6. The Lower Lafonia Group, of interest to this study, is composed of three stratigraphic units, the Bluff Cove, Fitzroy Tillite and Port Sussex Formations (Fig. 1.7).

1.4 Structural and Tectonic History

The Falkland Islands are just one segment of the Permo-Triassic Gondwanan Fold Belt which was displaced during the fragmentation of Gondwana and opening of the South Atlantic Ocean ~300 Ma. As the ocean opened, the Falkland Islands

Table 1.1 A summary of the stratigraphic links across Gondwana at the Permo-Carboniferous

	Argentina	Paraná Basin, Brazil	South Africa	Falkland Islands	Antarctica (Ellsworth Mountains)	Yemen	Oman	Pakistan	Eastern Australia	Western Australia	Tasmania
Glacial strata	e.g. Sauce Grande Formation, Sierre de la Ventana. e.g. Hoyada Verde Formation: Hoyada Verde, Tres Saltos and El Retamo subunits.	Itararé Group	Dwyka Tillite Formation	Fitzroy Tillite Formation	Whiteout conglomerate	Khulan Formation	Al Khlata	Tobra Formation	Lithostratigraphic nomenclature for Eastern Australia's glacial deposits varies considerably among basins.	Lithostratigraphic nomenclature for Western Australia's glacial deposits varies considerably among basins and some basins have more than one formation e.g. three in the Canning Basin.	Wynard Formation
Transitional strata/ Postglacial strata	e.g. Piedra Azul Formation is the transitional strata, Bonete Formation is postglacial. e.g. Hoyada Verde Formation: Esquina Gris subunit.	Palermo Formation, Rio Bonito Formation	Prince Albert Shale is the transitional strata. Whitehill formation is post glacial. These formations form the Ecca Group.	Hells Kitchen Member is the transitional strata. Black Rock Member is post glacial.	Polarstar Formation	Akbarah Formation	Gharif Formation				Inglis Fomration
Age	Hoyada Verde, Tres Saltos and El Retamao subunits are Late Carboniferous. The Esquina Gris is Early Permian (Sakmarian).	The Itararé Group strata are thought to be Pennsylvannian (Moskovian) to Early Permian (Cisuralian or Asselian-Sakmarian): 17-23 m.y. (Rocha-Campos et al., 2008). Average U-Pb zircon dating suggested an age of 298.5±2.6Ma for tonstein layers from the Rio Bonito Formation which immediately overlies the Itararé Group in the Paraná Basin (Gradstein, 2004). Holz et al. (2008) state base of Itararé is Baskirian.	Dwkya Tillite: Late Carboniferous (Late Westphalian or Stephanian) to the Early Permian (Artinskian). Latest glaciogenic deposit is Artinskian-Kungurian (latest Early Permian) Prince Albert/Whitehill: Early Permian and Early or Late Permian. Base of the Prince Albert Formation has been dated absolutely as 288.0 ± 3.0 and 289.6 ± 3.8Ma.	Glacial episode ~290 Ma	Whiteout Conglomerate is Permo-Carboniferous. The Gondwana glaciation in Antarctica may have existed for as long as 47 m.y. (333-286 Ma) or for as short as 10 m.y. (296-286 Ma) (Veevers and Powell, 1987). Correlation of fossil pollen with western Australia suggests Asselian-Sakmarian (Lower Permian).	Palynological assemblages including indeterminate monosacate pollen suggest lower Kuhlan Formation and the Akbarah Formation are likely to be late Carboniferous.	Al Khlata Formation is Moscovian to Sakmarian (Martin et al., 2008) 15m.y. of glacial conditions in Oman have been inferred.	Late Carboniferous-Permian It has been correlated to the South Oman biozone making it Late Pennsylvanian in age.	The late Palæozoic ice age lasted for ~67Ma. The earliest evidence for glacial conditions is identified in Queensland and New South Wales at 326.5-325.5 Ma (Late Mississippian).		Glacigenic strata of the Wynyard Formation in Tasmania, Australia, were deposited in southeastern Gondwana during the latest Carboniferous-Early Permian: Gzhelian-Sakmarian (Henry et al., 2012).
Thickness	The Sauce Grande Formation reaches a thickness ~300m. In the study site of Henry et al. (2008) there were 175m of glacial deposits and 85m of post-glacial mudrocks.	Itararé subgroup: up to 1500m. Glacial marine succession: 1100-1400m.	Glacial marine succession: 1000m	The Fitzroy Tillite is ~600-900m, the Hells Kitchen Member is ~7m and the Black Rock Member is ~150-250m in East Falkland.	Diamictites can be 1000m thick. In the Darwin Glacier Region, the Tillite is 148m thick and is unconformably overlain by 1370m of fluvial-deltaic strata (Polarstar Formation).		Al Khlata Formation is up to ~800m.	The Carboniferous-Permian succession comprises ~610m of sedimentary rocks.	Very variable depending on basin.	Permian-Carboniferous sections deposited under glacial conditions >2000m.	
Comments	Glacigenic strata associated with the proto-Precordillera were deposited in the Calingasta-Uspallata and Río Blanco back-arc basins and the Paganzo foreland basin in west-central Argentina.	The late Palæozoic palæolatitude (40° to 50°S) for the Paraná basin suggests a temperate warm-based regime for the glaciers. At least nine major cycles of ice advance and retreat have been recognised in the Itararé subgroup.	Glacigenic deposits occur within the Karoo basin throughout southern Africa. Overlying beds include plant fossils such as *Glossopteris* (Upper Carboniferous and lowest Permian). In Southern Africa, palynological zones in the Karoo system suggest that the Dwka Tillite is transitional between Carboniferous and Permian; these microflora studies place the Dwyka Tillite younger than correlations based on the megaflora. It is possible that much of the tillite was deposited when the glaciers were finally waning, so contained fossils represent only later episodes. Debris eroded earlier from the floor beneath the centres would have been carried far away. The Prince Albert Formation comprises fluvially dominated delta complex deposits. Sensitive high resolution ion microprobe (SHRIMP) dates of juvenile zircons obtained from tuff beds indicate that the deglaciation cycles were 3.6-8.2 m.y. in duration.	Rare archaeocyathan limestone pebbles in the tillite provide evidence of the link with Antarctica (Stone, Thomson and Rushton, 2012). Palæoice flow directions in South Africa and Falkland Island tillites match following rotation of the Falklands (Visser, 1987).	Glacial-marine origin inferred for deposits in the Sentinel Range. Polarstar Formation has Permian *Glossopteris* flora. Generalised sedimentation rates based on the 1000m thick Whiteout in northern Sentinels would be 2-10cm/1000yrs. Antarctica provides the only likely source for the Dwyka erratics in South Africa and the Fitzroy erratics in the Falklands. However, recent discoveries in South America (in conglomerates and the Sauce Grande tillite) complicate the picture.	The association of the diamictite bearing Akbra Shale (Yemen) with the Endaga Arbi Tillite of Ethiopia implies that ice cover may have extended over present-day East Africa. McClure (1980: In Martin et al., 2008) suggested that ice extended into Oman from the NW Indian plate.	Lower parts of the Al Khlata Formation have equivalent palynology to that in the Kuhlan and Akbarah Formation in Yemen. Facies distribution indicates ice moving north and northeast into Oman and Saudi Arabia, giving a trend of glacial to nonglacial sedimentation from south to north. Locally evidence exists for ice transport both from the southwest and northeast and includes the possibility of local ice centres active at various times (Martin, et al., 2008).	The Tobra Formation in Zaluch Nala lacks the deglaciation sequence present in other nearby basins such as those in South Arabia and Western Australia	The acme of the LPIA in terms of areal extent, ice volume and longevity occurred during the early Permian. The glacial conditions deteriorated through the Middle Permian and ended by the Late Permian. The ice age was recorded as a series of discrete glacial episodes. These patterns are independent of the changing nature of depositional environments and underlying tectonic forcing.	The majority of glacial deposits are dated from palynological and microfaunal assemblages. The most widespread extend from the Gzhelian (Late Carboniferous) to early Sakmarian (Early Permian). In the Perth Basin. Glacial deposits are from the Kangurian (late Early Permian) in the Perth and Southern Carnavon Basins.	The Wynyard Formation of Tasmania, Australia, provides the youngest evidence of grounded ice during the Late Carboniferous to Early Permian.
Key References	Alessandretti et al., 2013; Amos and Gamundi, 1981; Henry et al., 2008	Holz et al., 2008; Rocha-Campos et al., 2008; Stephenson, 2008	Visser, 1987; Isbell et al, 2008a; Trewin et al., 2002	Crowell and Frakes, 1972; Veevers and Powell, 1987	Matsch and Ojakangas, 1992	Stephenson et al., 2011; Stephenson et al., 2012	Martin et al., 2008	Jan and Stephenson, 2011	Fielding et al., 2008b	Mory et al., 2008	Henry et al., 2012

Missing information and inconsistencies reflect gaps in current understanding and a need, in particular, for improved chronology

UPPER CARBONIFEROUS
LOWER PERMIAN
UPPER PERMIAN
Kasimovian
Gzhelian
Asselian
Sakmarian
Artinskian
Kungurian
Roadian
Wordian
Capitanian
ARGENTINA
Sauce Grande Formation
Piedra Azul Formation
Bonete Formation
BRAZIL
Tubarao Group
Itarare Subgroup
Guata Subgroup
Passa Dois Group
SOUTH AFRICA
Dwyka Tillite Formation
Prince Albert Shale
Whitehill Formation
FALKLAND ISLANDS
Fitzroy Tillite Formation
Hells Kitchen Member
Black Rock Member
ANTARCTICA
Whitecout Conglomerate
Polarstar Formation
OMAN
Al Khlata Formation
Lower Gharif Member
PAKISTAN
Tobra Formation
Dandot Formation/ Warcha Formation
YEMEN
Kuhlan Formation
Akbarah Formation
These E. Australian formations preserve evidence of four Permian glacial episodes
EASTERN AUSTRALIA e.g. Sydney Basin
Wasp Head Formation
Shoalhaven Group
WESTERN AUSTRALIA e.g. South Carnarvon Basin
Stockton Group
Westralia Sandstone
Ewington Coal Measures
TASMANIA
Wynard Formation
Inglis Formation
Alessandretti et al., 2013
Sephton, 2008; almost consistent with Rocha-Campos, 2008
Stephenson, 2008; almost consistent with Isbell, 2003
Fakas & Cowell, 1967; Alkas & Edwards, 1999
Maisch & Oyakangas, 1992
Stephenson, 2008; consistent with Martin et al., 2008
Jan & Stephenson, 2011
Stephenson et al., 2012
Henry et al., 2008
Mory et al., 2008
Henry et al., 2012

◀**Fig. 1.5** Synthesis of existing stratigraphic records from Australia, Antarctica, South Africa and South America suggests that major climate events were diachronous across Gondwana. Dominantly, Carboniferous glaciation in South America was gradually succeeded by dominantly Permian glaciation in Antarctica and Australia

microplate was rotated clockwise by 120° and then translated 300 km south (Marshall 1994). Palæomagnetic poles from Jurassic dolerite dykes on West Falkland show significant rotation (~100°) occurred before the Cretaceous opening of the South Atlantic, which caused a further ~55° rotation (Rabinowitz and Brecque 1979). From the asymmetry of the aeromagnetic anomalies associated with individual dykes, Stone et al. (2009) suggested that rotation occurred between the intrusion of the Early Jurassic dykes at about 180–190 Ma and the emplacement of a second swarm of Early Cretaceous dykes that were intruded between about 121

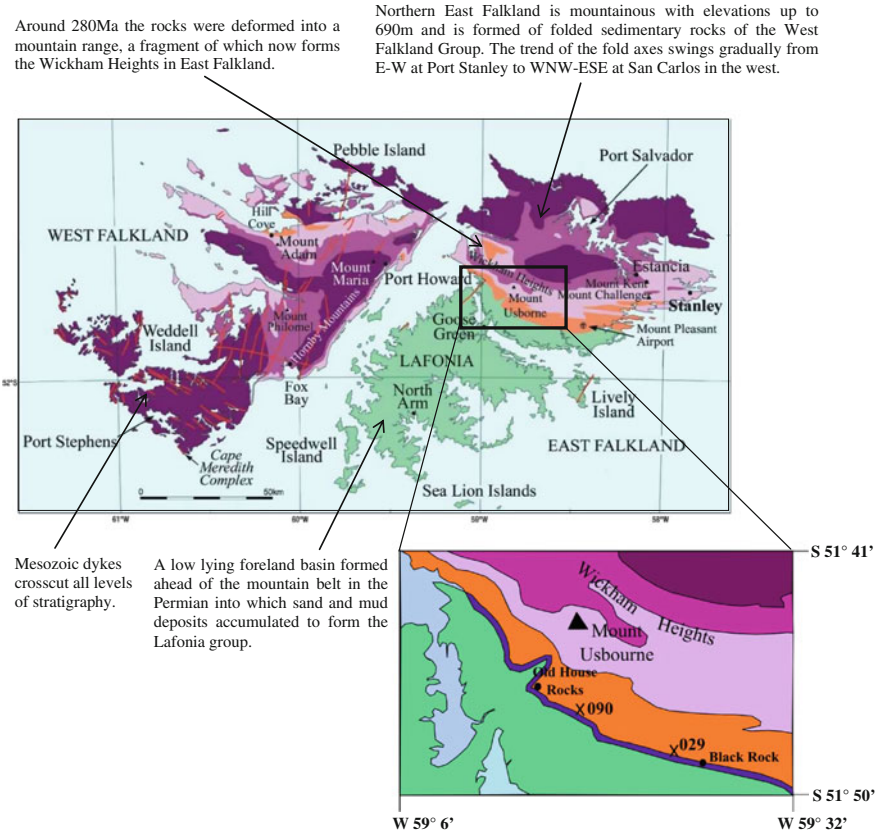

Fig. 1.6 Geology of the Falkland Islands; modified from Stone and Aldiss (2001). *Inset* shows location of core sites: borehole DD029 [377975 4260500] and DD090 [374470 4261720]. A guide to lithologies is provided in the stratigraphic column (Fig. 1.7)

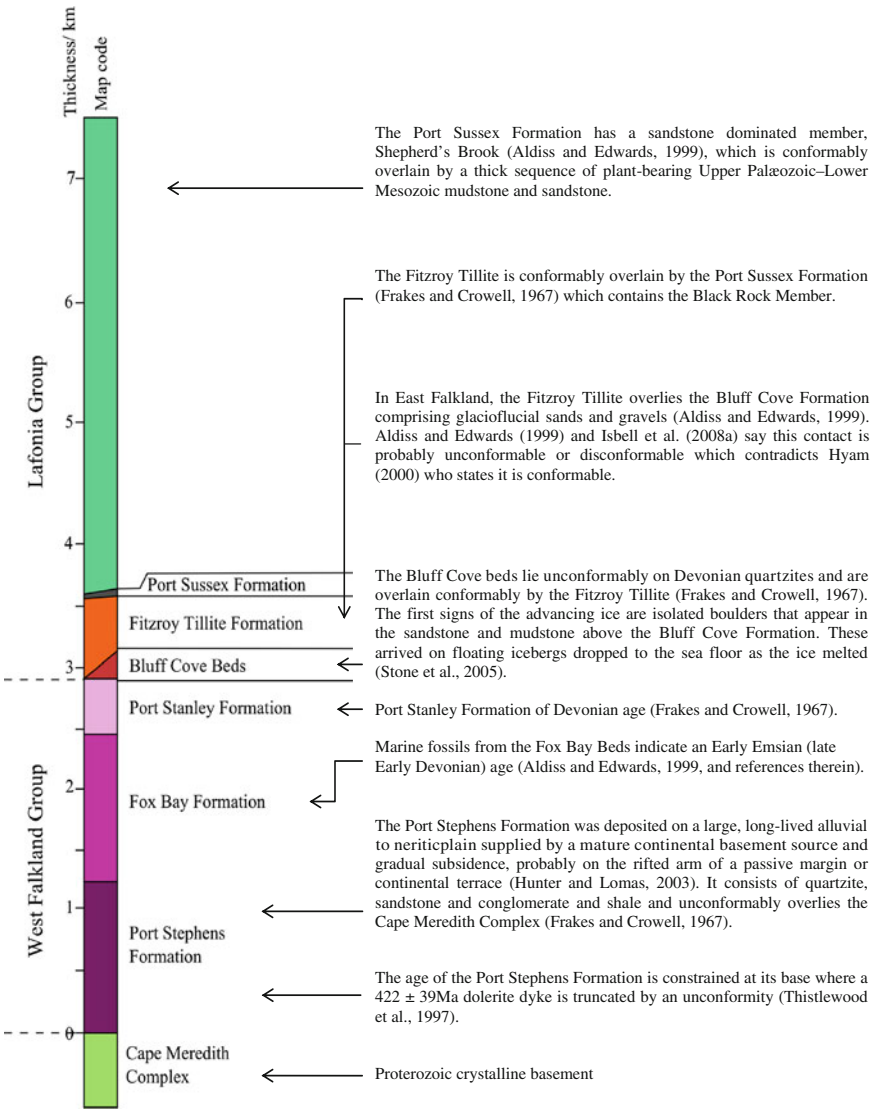

Fig. 1.7 Generalised stratigraphic column illustrating the three broad stratigraphic zones and the three lithologies found in these Late Carboniferous–Early Permian cores (the Fitzoy Tillite, the Hells Kitchen Member and the Black Rock Member)

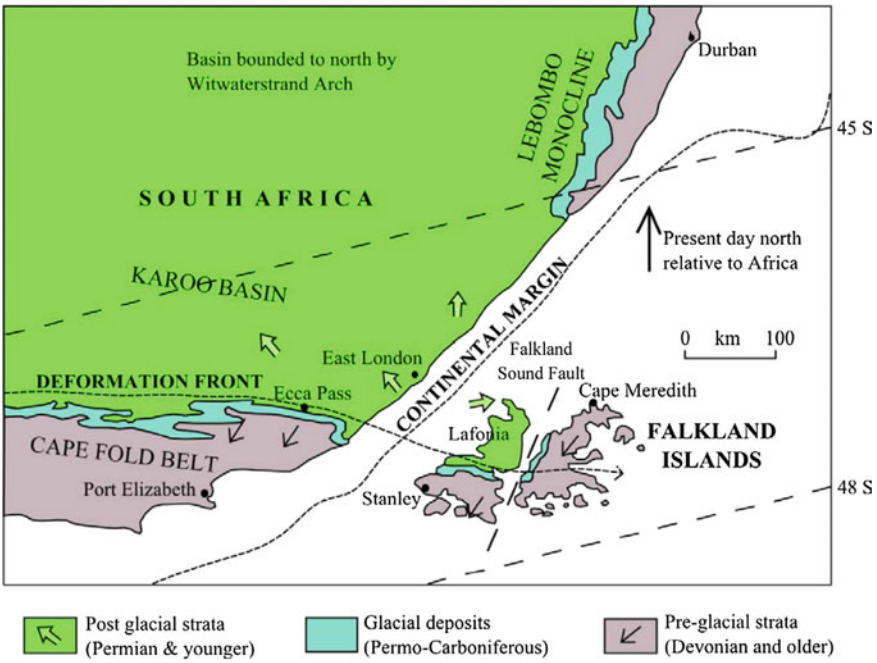

Fig. 1.8 Summary of the deposits and structural deformation in the Falkland Islands ~180 Ma, modified from Trewin et al. (2002). *Arrows* indicate mean palæocurrent vectors. The Falklands microplate is rotated through almost 180° and placed off the east coast of South Africa in proximity to East Antarctica and the Ellsworth Mountains microplate. The Falkland Sound Fault marks a significant deformation edge to the Cape Fold Belt. Tectonism along the convergent margin of Gondwana resulted in the Karoo Basin of South Africa evolving into a foreland basin (during Dwyka Group accumulation) bounded by the southern (Cape fold belt) and northern (Cargonian Highlands) uplands. In the Falkland Islands, the Fitzroy Tillite Formation is the equivalent of the Dwyka Group, while the upper part of the Lafonia Group equates to the Karoo foreland basin deposits

and 135 Ma (Richards et al. 2013). Geophysical models offshore find undisturbed Jurassic–Tertiary beds which support an Early Jurassic age for rotation (Hyam et al. 2000). This reconstruction is consistent with structural, geometric, seismic, palæocurrent and palæomagnetic constraints which also suggest the Falkland plateau arrived at its present geometry ~130 Ma. Based on the palæomagnetic data of Taylor and Shaw (1989), rotation must have taken place during or after the emplacement of the mafic dykes (190 Ma) and before or during the development of the sedimentary basins; this rules out rotation during the main phase of Gondwanan folding 278–230 Ma (Curtis and Hyam 1998). When the islands are restored to their prerotation position, palæo-ice flow directions from the tillites appear east to west, matching those in South Africa (Frakes and Crowell 1967) (Fig. 1.8). The final breakout and associated movements of these and other Gondwana fragments was rapid and correlated with a major magmatic pulse related to a mantle plume beneath Africa and Antarctica at 130 Ma (Curtis and Hyam 1998).

References

Adie RJ (1952) The position of the Falkland Islands in a reconstruction of Gondwanaland. Geol Mag 89:401–410

Aldiss DT, Edwards EJ (1999) The geology of the Falkland Islands. British Geological Survey technical report: WC/99/10

Allessandretti L, Philip RP, Chemale F Jr, Brückmann MP, Zvirtes G, Matté V, Ramos VA (2013) Provenance, volcanic record, and tectonic setting of the Palæozoic Ventania Fold Belt and the Claromecó Foreland Basin: implications on sedimentation and volcanism along the southwestern Gondwana margin. J S Am Earth Sci 47:12–31

Amos AJ, Gamundi OL (1981) Late Palæozoic sauce grande formation of eastern Argentina. In: Hambrey MJ, Harland WB (eds) Earth's pre-pleistocene glacial record. Cambridge University Press, Cambridge, pp 872–877 (April 2011)

Bradshaw MA (1998) Early Devonian bivalve faunas and their relationship to the palæogeography of Gondwana. J Afr Earth Sc 27:36–37

Caputo MV, Crowell JC (1985) Migration of glacial centres across Gondwana during the Palæozoic Era. Geol Soc Am Bull 96:1020–1036

Caputo MV, de Melo JHG, Streel M, Isbell JL (2008) Late Devonian and early Carboniferous glacial records of South America. Geol Soc Am Spec Pap 441:161–173

Crowell JC (1983) Ice ages recorded on Gondwanan continents. 18th Alex L Du Toit memorial lecture. Geol Soc South Africa Trans 86:237–262

Crowell JC, Frakes LA (1972) Late Palæozoic glaciation: Part V, Karroo Basin, South Africa. Geol Soc Am Bull 83:2887–2912

Curtis ML, Hyam DM (1998) Late Palæozoic to Mesozoic structural evolution of the Falkland Islands: a displaced segment of the Cape Fold Belt. J Geol Soc 155:115–129

Fielding CR, Frank TD, Isbell JL (2008a) The late Palæozoic ice age—A review of current understanding and synthesis of global climate patterns. Geol Soc Am Spec Pap 441:343–354

Fielding CR, Frank TD, Birgenheier LP, Rygel MC, Jones AT, Robert J (2008b) Stratigraphic record and facies associations of the Late Palæozoic Ice Age in eastern Australia (New South Wales and Queensland). Geol Soc Am Spec Pap 441:41–57

Fielding CR, Frank TD, Birgenheier LP, Rygel MC, Jones AT, Roberts J (2008c) Stratigraphic imprint of the Late Palæozoic Ice Age in eastern Australia: a record of alternating glacial and nonglacial climate regime. J Geol Soc London 165:129–140

Frakes LA, Crowell JC (1967) Facies and Palæogeography of Late Palæozoic Diamictite, Falkland Islands. Geol Soc Am Bull 78:37–58

Gastaldo RA, DiMichele WA, Pfefferkorn HW (1996) Out of the icehouse into the greenhouse: a late Palæozoic analogue for modern global vegetational change. GSA Today 10:1–7

Gradstein FM, Ogg JG, Smith AG (2004) A geological time scale. Cambridge University Press, Cambridge

Grill H (1997) The Permo-Carboniferous glacial to marine Karoo record in southern Namibia: Sedimentary facies and sequence stratigraphy. Beringeria, 19:1–98

Henry LC, Isbell JL, Limarino CO (2008) Carboniferous glacigenic deposits of the proto-Precordillera of west central Argentina. Geol Soc Am Spec Pap 441:131–142

Henry LC, Isbell JL, Fielding CR, Domack EW, Frank TD, Fraiser ML (2012) Proglacial deposition and deformation in the Upper Carboniferous to Lower Permian Wynard Formation, Tasmania: a process analysis. Palæogeogr Palæoclimatol Palæoecol 315–316:142–157

Holz M, Souza PA, Iannuzzi R (2008) Sequence stratigraphy and biostratigraphy of the Late Carboniferous to Early Permian glacial succession (Itararé Subgroup) at the eastern-southeastern margin of the Paraná Basin, Brazil. Geol Soc Am Spec Pap 441:115–129

Horton DE, Poulsen CJ, Pollard D (2010) Influence of high-latitude vegetation feedbacks on late Palæozoic glacial cycles. Nat Geosci 3:572–577

Horton DE, Poulsen CJ, Montanez IP, DiMichele WA (2012) Eccentricity-paced late Palæozoic climate change. Palæogeogr Palæoclimatol Palæoecol 331–332:150–161

Hunter M, Lomas SA (2003) Reconstructing the Siluro-Devonian coastline of Gondwana: insights from the sedimentology of the Port Stephens Formation, Falkland Islands. J Geol Soc London 160:459–476

Hyam DM, Marshall JEA, Sanderson DJ (1997) Carboniferous diamictite dykes in the Falkland Islands. J Afr Earth Sc 25:505–517

Hyam DM, Marshall JEA, Bull JM, Sanderson DJ (2000) The structural boundary between East and West Falkland: new evidence for movement history and lateral extent. Mar Pet Geol 17:13–26

Isbell JL, Lenaker PA, Askin RA, Miller MF, Babcock LE (2003) Reevaluation of the timing and extent of late Palæozoic glaciation in Gondwana: role of the Transantarctic Mountains. Geology 31:977–980

Jan IU, Stephenson MH (2011) Palynology and correlation of the Upper Pennsylvannian Tobra Formation from Zaluch Nala, Salt Range, Pakistan. Palynology 35:212–225

Lawrence SR, Johnson M, Tubb SR, Marshallsea SJ (1999) Tectono-stratigraphic evolution of the North Falkland region. In: Cameron NR, Bate RH, Clure VS (eds) The oil and gas habitats of the South Atlantic. Geol Soc London Spec Publ 153:409–424

Marshall JEA (1994) The Falkland Islands: a key element in Gondwana palæogeography. Tectonics 13:499–514

Martin JR, Redfern J, Aitken JF (2008) A regional overview of the late Palæozoic glaciation in Oman. Geol Soc Am Spec Pap 441:175–186

Matsch CL, Ojakangas RW (1992) Stratigraphy and sedimentology of the Whiteout Conglomerate: an upper Palæozoic glaciogenic unit, Ellsworth Mountains, West Antarctica. In: Webers GF, Craddock C, Splettstoesser JF (1992) Geology and palæontology of the Ellsworth Mountains, West Antarctica, vol 170. Geological Society of America, Memoir, pp 37–62

Mitchell C, Taylor GK, Cox KG, Shaw J (1986) Are the Falkland Islands a rotated microplate? Nat London 319:131–134

Mory AJ, Redfern J, Martin JR (2008) A review of Permian-Carboniferous glacial deposits in Western Australia. Geol Soc Am Spec Pap 441:29–40

Rabinowitz PD, LaBrecque (1979) The Mesozoic South Atlantic Ocean and evolution of its continental margins. J Geophys Res 84:5973–6002

Richards PC, Stone P, Kimbell GS, McIntosh WC, Phillips ER (2013) Mesozoic magmatism in the Falkland Islands (South Atlantic) and their offshore sedimentary basins. J Pet Geol 36:61–74

Rocha-Campos AC, dos Santos PR, Canuto JR (2008) Late Palæozoic glacial deposits of Brazil: Paraná Basin. Geol Soc Am Spec Pap 441:97–114

Scotese CR, Boucot AJ, McKerrow WS (1999) Gondwanan palæogeography and palæoclimatology. J Afr Earth Sc 28:99–114

Stephenson MH (2008) A review of the palynostratigraphy of Gondwana Late Carboniferous to Early Permian glacigene successions. Geol Soc Am Spec Pap 441:317–330

Stephenson MH, Kader Al-Mashaikie SA (2011) Stratigraphic note: update on the palynology of the Akbarah and Kuhlan formations, northwest Yemen. GeoArabia 16:17–24

Stephenson MH, Jan IU, Kader Al-Mashaikie SA (2012) Palynology and correlation of Carboniferous-Permian glacigene rocks in Oman, Yemen and Pakistan. Gondwana Research. http://dx.doi.org/10.1016/j.gr.2012.06.005. Accessed 10 Oct 2012

Stollhofen H, Werner M, Stanistreet IG, Armstong RA (2008) Single-zircon U-Pb dating of Carboniferous-Permian tuffs, Namibia, and the intercontinental deglaciation cycle framework. Geol Soc Am Spec Pap 441:83–96

Stone P, Aldiss DT (2001) The Falkland Islands. Stone runs—Rock in the landscape British Geological Survey for Department of Mineral Resources, Falkland Islands Government. Keyworth, Nottingham

Stone P, Aldiss DT, Edwards EJ (2005) Rocks and fossils of the Falkland Islands. British Geological Survey for Department of Mineral Resources, Falkland Islands Government

Stone P, Kimbell GS, Richards PC (2009) Rotation of the Falklands microplate reassessed after recognition of discrete Jurassic and Cretaceous dyke swarms. Pet Geosci 15:279–287

Stone P, Thomson MRA, Rushton AWA (2012) An Early Cambrian archaeocyath-trilobite fauna in limestone erratics from the Upper Carboniferous Fitzroy Tillite Formation, Falkland Islands. Earth Environ Sci Trans R Soc Edinb 102:201–225

Taylor GK, Shaw J (1989) The Falkland Islands: new palæomagnetic data and their origin as a displaced terrane from southern Africa. Geophys Monogr 50:59–72

Thistlewood L, Leat PT, Millar IL (1997) Basement geology and Palæozoic-Mesozoic mafic dykes from the Cape Meredith complex, Falkland Islands: a record of repeated intracontinental extension. Geol Mag 134:355–367

Trewin NH, Macdonald DIM, Thomas CGC (2002) Stratigraphy and sedimentology of the Permian of the Falkland Islands: lithostratigraphic and palæoenvironmental links with South Africa. J Geol Soc London 159:5–19

Veevers JJ, Powell CM (1987) Late Palæozoic glacial episodes in Gondwanaland reflected in transgressive depositional sequences in Euramerica. Geol Soc Am Bull 98:475–487

Visser JNJ (1987) The palæogeography of part of southwestern Gondwana during the Permo-Carboniferous glaciation. Palæogeogr Palæoclimatol Palæoecol 61:205–219

Visser JNJ (1997) Deglaciation sequences in the Permo-Carboniferous Karoo and Kalahari basins of southern Africa: a tool in the analysis of cyclic glaciomarine basin fills. Sedimentology 44:507–521

Worsley TR, Moore TL, Fraticelli CM, Scotese CR (1994) Phanerozoic CO_2 levels and global temperatures inferred from changing palæogeography. Geol Soc Am Spec Pap 288:57–73

Ziegler AM, Hulver ML, Rowley DB (1997) Permian world topography and climate. In: Martini IP (ed) Late glacial and postglacial environmental changes: quaternary, Carboniferous-Permian and Proterozoic. Oxford University Press, Oxford, pp 111–146

Chapter 2
Materials and Methodology

Abstract Two borehole cores extracted between Old House Rocks and Black Rock, East Falkland, were studied using a combination of detailed sedimentary logging and geochemical analyses. The former involved grain and clast studies while the latter included X-ray fluorescence (XRF) and reflectance scanning using an Avaatech XRF core scanner. Logging data collected incorporated details on grain composition, size, shape, sorting, orientation, colour, sedimentary structures and fossils as well as a detailed account of variations in clast characteristics. A full scan of the original hand-drawn log is presented in the data postscript at the end of this book, and a digital version may be found online as a SPRINGER EXTRA. The high-resolution log was generated at a scale comparable to the X-ray fluorescence and reflectance data collected by the core scanner to encourage subsequent, more detailed climatic interpretations. The core scanner measured variations in element concentrations downcore and three reflectance parameters: lightness, red:green ratio and yellow:blue ratio. Total Organic Carbon (TOC) measurements on loose fragments throughout core DD090 were also taken. Cyclicity observed in the XRF and reflectance data was compared alongside Milankovitch orbital cycles through age modelling, thereby helping to constrain the time frame spanned by the deposits.

Keywords Sedimentary logging · XRF · Reflectance · Clast content · Total Organic Carbon · Age modelling

2.1 Overview

Detailed sedimentary logging was combined with high-resolution X-ray fluorescence (XRF) and reflectance scanning of two borehole cores, DD029 and DD090, to allow precise stratigraphic correlations and detailed sedimentary and climatic reconstructions. The cores used in this study, DD090 and DD029, have incomplete recovery in the diamictite sections ($\sim$10–20 %) but were selected because they captured the contact between the Fitzroy Tillite and the Hells Kitchen Member and because they appeared to have the most stratigraphically complete sequence through the Hells Kitchen Member, which is crucial to understanding the climatic transition. Table 2.1 summarises the sections of cores DD029 and DD090 that were available and used in this study.

K. Horan, *Falkland Islands (Islas Malvinas) in the Permo-Carboniferous*,
Springer Earth System Sciences, DOI 10.1007/978-3-319-08708-5_2

Table 2.1 Measured thicknesses of the three main units in cores DD029 and DD090 and the parts involved in this study

Core	Total core length (m)	FT available (m)	FT studied (m)	HK available (m)	HK studied (m)	BRMa available (m)	BRMa studied (m)	BRMb available (m)	BRMb studied (m)
DD029	227	222.8–181.3	181.3–190	181.3–176.4	181.3–176.4	176.4–170	176.4–170	0	0
DD090	395	395–392	395–392	392–383.5	392–383.5	383.5–375	383.5–375	153.8–161.8	155.8–156.7, 157.9–158.7

Fitzroy Tillite (*FT*), Hells Kitchen Member (*HK*) and Black Rock Member (*BRMa* and *BRMb*). Subdivision of core here is that of Stone (BGS report 2011)

Note Thicknesses indicated are not equivalent to stratigraphic thicknesses

2.2 Logging

A 2:1 stratigraphic log was produced by recording millimetre-scale changes in lithology along the length of both cores. Log depths were corrected for the drilling angle and the dip of the beds (Fig. 2.1). Scanned images of the original logs and a digital version are presented in the appendix.

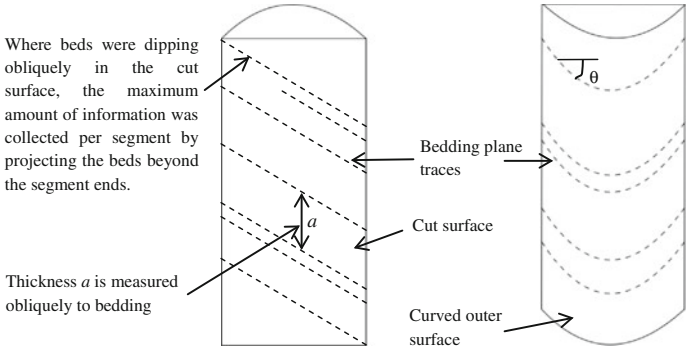

Fig. 2.1 Technique for measuring bed thickness

Box 2.1 Conversion of Apparent Thickness (*a*) to True Stratigraphic Thickness (*t*)
The true thickness of a bed (*t*) is the perpendicular distance between adjacent bedding planes. However, because the beds were dipping and the drilling angle was oblique to bedding, the measured value '*a*' was multiplied by the cosine of the maximum angle the beds made with the horizontal (θ), measured on the curved surface, to find '*t*': $t = a \cos \theta$.

2.3 Reflectance Scanning

Reflectance scanning was carried out using the Avaatech core scanner in the sedimentary laboratory, University of Cambridge. Preparation of core samples included sanding the upper cut surfaces of the segments to remove the original ink labels and milling lines. Sanding by hand proved the most effective method since pieces were commonly fractured or brittle and had to be handled with care. Prior to scanning, the light in the scanner was allowed to warm up for around 30 min and a blind was drawn to avoid alteration to image brightness.

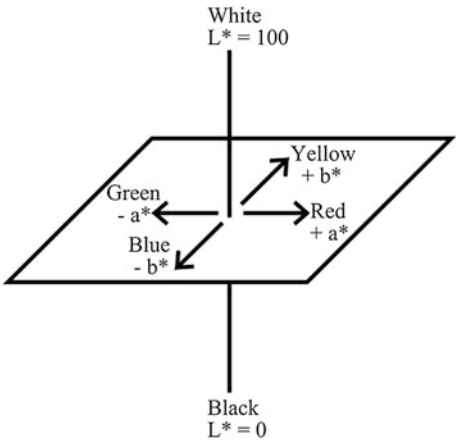

Fig. 2.2 CIE L*a*b* colour scale defined by the Commission international de l'Éclairage, HunterLab manual (2008); figure is modified from this manual. L* characterises lightness scaled from 0 (*black*) to 100 (*white*). The parameters a* and b* are chromaticity coordinates that define the colour: a* ranges from −60 (*green*) to +60 (*red*) and b* from −60 (*blue*) to +60 (*yellow*)

The cores were then illuminated by high-intensity light with a broad spectrum across all wavelengths to allow photographs and reflectance data to be collected. Scans were run at lens aperture '8+' against standard colour charts. This process is non-destructive and fairly rapid. Long reflectance measurement bands were then drawn on the images generated, over the same central section of the core where XRF data were also collected to ensure effective comparison later. Colour reflectance values were summarised using the L*, a* and b* parameters (Fig. 2.2). This ratio scheme was used because raw colour is dominated by brightness and so gives less independent information.

The reflectance scanning results have been assimilated onto a depth scale comparable to the log and clast data (Box 2.2) and are shown in the appendix.

Box 2.2: Generation of Depth Scale for Reflectance and XRF Data
Original depth labels on the segments were approximate and marked according to drilling depths rather than true stratigraphic thicknesses. They had been extrapolated from drillers' markings which amounted to a figure for the top and bottom of each core box (each box would hold about 5–6 m) and an insert, where present or legible, every 1–1.5 m marked with the depth figure. When producing a depth scale, the positioning of these labels was initially not corrected for using the dip of the beds because their positions were clearly vague and this adjustment would only have increased implied overlap. Some indication of the position of the labels within a segment was measured though and the depth correction to reach the segment top applied.

Complications also arose because the XRF and reflectance data were collected along the cut surface rather than perpendicular to bedding. Therefore, to make these data sets comparable with the log and clast data, depth control points were inserted into the XRF and reflectance scales for the two cores at the beginning and end of each segment and the depths in-between linearly interpolated. The full procedure is outlined in Appendix A.1.

2.4 XRF Scanning

A continuous record of elemental data was collected non-destructively at the split core surface using the Avaatech X-ray core scanner. Before running samples through the scanner, the X-ray tube was allowed a warm-up time of 30 s and four standards were run twice at the 10 kV energy band; the 10 kV band is the most sensitive measure to fluctuations in counts. The removal of the ink labels during sanding also prevented biases to the signal. The labels were found to cause considerable alteration to the chemistry on trial XRF runs. Non-continuous segments were positioned with sufficiently wide gaps such that the detector could skip between them and avoid damage to its Ultralene window. The level of the core segments was checked using a mini-spirit level, and they were secured where necessary using foam to prevent them being caught by the moving window.

The X-ray source progressively irradiated the cross-core and downcore directions causing fluorescent energy, characteristic of atoms of specific elements, to be emitted. The chemical composition of the sediment was measured as element intensities in total counts. Heavier elements require more energetic photons in order to fluoresce, so both cores were run on three different energy levels (10, 30 and 50 kV) to activate different sets of elements and provide reliable element intensities (Fig. 2.3). A computer registered the energy of every photon, allowing for the creation of a spectrum. A spectrum interpretation software package, WinAxilBatch, was then used to interpret spectra quantitatively by assigning distributions of photons (counts) at different wavelengths to elements. Each metre segment was run over 24 h collecting two replicates at an interval of 1:25, a step size of 2.5 mm, a downcore slit size of 2.5 mm and a slit size across core of 12 mm; a level of resolution comparable to the logs. The data were then normalised to aluminium (Box 2.3). Standards were run to check the consistency of results and machine behaviour. The complete XRF data sets from both cores are presented in the appendix on the same depth scale transformation as the reflectance data.

Box 2.3: Normalisation
In variable settings, such as lakes (the arguable depositional setting here; see Chap. 4), the strength of the XRF-scanning method lies in an analysis of the relative variations of the different elements compared to a major conservative element to obtain an environmentally relevant signal (Löwermark et al. 2011). Without such normalisation, biological or diagenetic processes can influence elemental counts and interpretations would be at risk of becoming a mirror of organic matter (or carbonate) variations (Löwermark et al. 2011). Even with an absolute calibration, changes in flux rate of particular elements and dilution effects are extremely difficult to separate. While normalisation does not compensate for the effects of sediment composition, it does help to compensate for some effects of surface irregularity (Weltje and Tjallingi 2008). Therefore, the relative signal strength was used as an indication of compositional change and interpreted in terms of climatological and sedimentological change. Normalisation also enables presentation of data from elements with very different XRF count rates. Log ratios accommodate the non-linearity of the relationship between relative intensities and concentrations. Table 2.2 evaluates possible elements which may be used for normalisation and the rationale behind the choice of aluminium.

Table 2.2 Reasoning behind the choice of aluminium for normalisation summarised from Löwermark et al. (2011)

Element	Comment on suitability
Fe or Mn	Unsuitable because of their redox sensitive nature
Na, K, Sr or Mg	Easily dissolved and weathered out so unsuitable
Ti	Ti is an important component in many minerals, is abundant and not very active biologically. However, Ti is enriched in heavy minerals and in aeolian dust and is therefore used as a proxy for high current regimes or enhanced wind activity. Also, Ti content is highly influenced by the composition of the original protolith
Al	Normalisation to Al helps reduce problems associated with surface irregularities, which tend to decrease counts of most elements. Al is abundant and little affected by diagenetic and biological processes such as redox reactions. As it is a major structural component in the sand, silt and clay that enters basins, normalisation of the other elements against Al allows the changes in proportion of the individual elements in the lithogenic component of the sediment relative to each other over time to be indicated in terms of aeolian, terrestrial and biogenic inputs

2.5 Clast Data

Details on clast composition, size, frequency, sorting, roundness, sphericity and orientation were collected from core DD090 in order to better understand sediment source area and ice sheet flow patterns and processes. Frequency was recorded as a

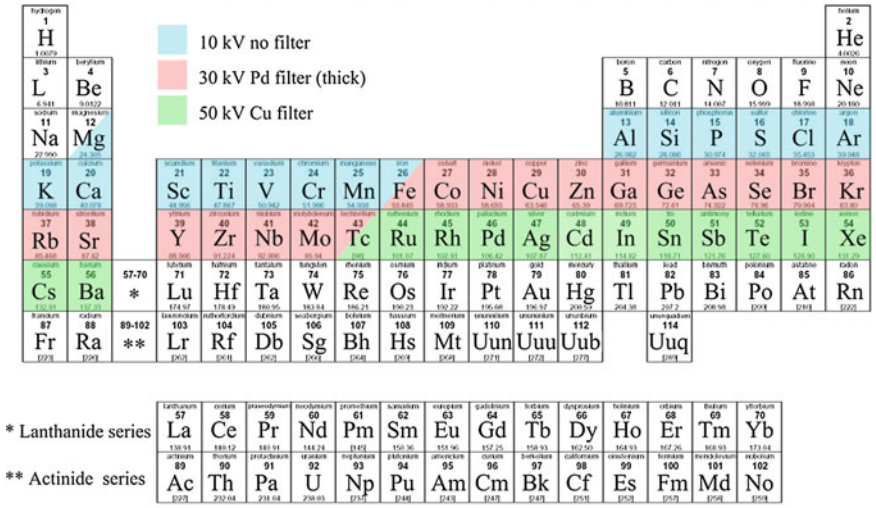

Fig. 2.3 The range of elements that are activated for the different instrument settings (information from Xelerate Documentation, University of Delft, Bloemsma (2012)) are highlighted on the periodic table. Elements between ^{13}Al and ^{92}Ur could be detected and included in the deconvolution

percentage while sorting, sphericity, roundness and orientation were ranked on scales 0–2, 0–10, 0–10 and 0–10, respectively; where the higher number in each case corresponds to a higher degree of the variable in question. The comparator charts used are provided in Fig. 2.4. Plotted data from the clast analysis are presented in the appendix.

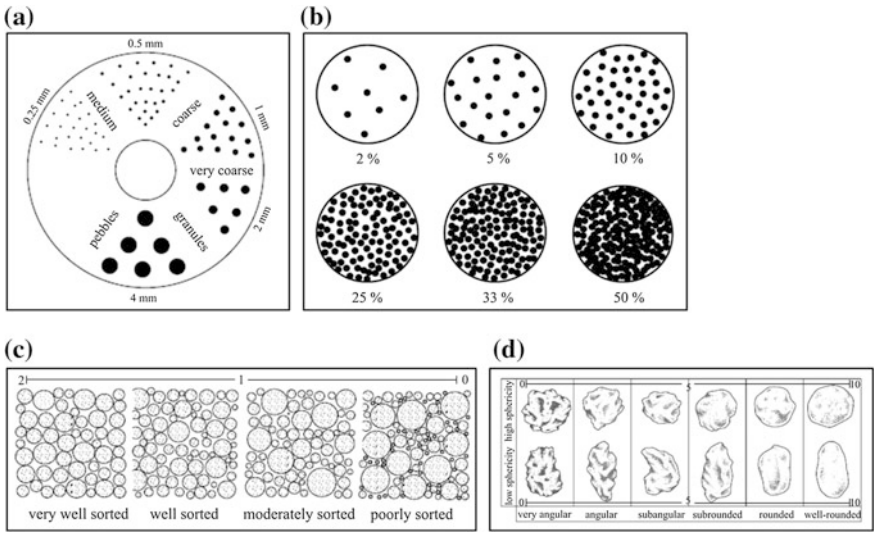

Fig. 2.4 Comparator charts used for estimating clast **a** size, **b** abundance, **c** shape (including *roundness and sphericity*) **d** sorting. Figure compiles and modifies relevant diagrams from Tucker (2003)

2.6 Total Organic Carbon

Nine loose fragments from core DD090 were collected for Total Organic Carbon (TOC) measurements: one from the diamictite, five from the Hells Kitchen Member and three from the Black Rock Member. The samples were ground to a powder before being placed in an oven at 60 °C to remove any moisture. They were weighed after 4 and 8 h to ensure constant weight. Once their mass stopped declining, they were added to separate beakers containing ~15 ml 1 M HCl to remove inorganic carbon present as carbonate. TOC content was then determined by dry combustion. This procedure collected information on ^{13}C isotopes also. The mass of the samples before and after drying and bathing in acid is shown in Table 6.1.

2.7 Development of an Age Model

The XRF and reflectance data were used to construct a relative age model, and the existing absolute dates from other localities across Gondwana informed judgements of when the transition took place in the Falklands. Spectral analyses and wavelet analyses were used to look for prominent periodicities in the depth domain and from these observations, a tentative relative age model was developed and further wavelet analyses undertaken (see Chap. 4). Although absolute timescales become increasingly imprecise with increasing age (Arthur and Garrison 1986), it was hoped that biostratigraphy in the form of micropalæontology might play a supporting role in constraining the time frame over which the icehouse to greenhouse transition took place. However, studies of similar Falkland Island material by Mike Stephenson of the British Geological Survey (personal communication) suggest a lack of suitable spores/fauna in the cores for absolute dating.

References

Arthur MA, Garrison RE (1986) Cyclicity in the Milankovitch band through geological time: an introduction. Palæoceanography 1:369–372

Bloemsma M (2012) Xelerate Documentation. Delft University. http://mennobloemsma.nl/project_description.php. Accessed 3 Jan 2013

HunterLab (2008) Insight on Color Hunter L, a, b Color Scale. http://www.hunterlab.se/wp-content/uploads/2012/11/Hunter-L-a-b.pdf. Accessed 12 Oct 2012

Löwermark L, Chen H-F, Yang T-N, Kylander M, Yu E-F, Hsu Y-W, Lee T-Q, Song S-R, Jarvis S (2011) Normalizing XRF-scanner data: a cautionary note on the interpretation of high resolution records from organic-rich lakes. J Asian Earth Sci 40:1250–1256

Tucker ME (2003) Sedimentary rocks in the field, 3rd edn. Wiley, West Sussex

Weltje GJ, Tjallingii R (2008) Calibration of XRF core scanners for quantitative geochemical logging of sediment cores: theory and application. Earth Planet Sci Lett 274:423–438

Chapter 3
Analysis of Results

Abstract Understanding the environment of deposition in detail is crucial to appreciating the global context and significance of Permo-Carboniferous climate change. This chapter looks in detail at the nature of the Falkland Islands sedimentary deposits logged over the icehouse to greenhouse transition. A discussion of the underlying mechanisms driving the observed variations in sedimentology is presented. In outline, a massive diamictite deposited subglacially and with a variety of clast types, gives way to an interlaminated unit of diamictite and mudstone followed by a mudstone-dominated unit. The interlaminated zone forms the focus of this chapter since it is this stratigraphic section which tracks the icehouse to greenhouse transition. In the more stratigraphically complete core, DD090, four broad lithological zones are identified within this section. These are thought to represent two major episodes of advance and retreat of an ice sheet. This signal is overprinted by higher frequency oscillations depicted in millimetre-scale laminations and sedimentary structures. Dominantly subglacial deposition was replaced by a fluctuating ice-proximal to ice-distal environment before the onset of ice free open water conditions persisted. The sedimentary log is compared with the XRF and reflectance scans and correlations drawn where possible.

Keywords Diamictite · Mudstone · Dropstones · Ice · Aqueous deposition · Facies · Elemental variations

3.1 Sedimentology and Structure

3.1.1 Fitzroy Tillite Formation

Core DD029: corrected depths 190–183.1 m
Core DD090: corrected depths 395.1–392.4 m

The Fitzroy Tillite is a glaciogenic diamictite widespread across the Gondwanan fragments. It records the glacial episode that the Falkland Islands region of the supercontinent experienced around 290 Ma (Stone et al. 2005). In both cores

K. Horan, *Falkland Islands (Islas Malvinas) in the Permo-Carboniferous*,
Springer Earth System Sciences, DOI 10.1007/978-3-319-08708-5_3

DD029 and DD090, the tillite is massive and unstratified with a relatively clast poor (~25 %) silty matrix displaying no evidence of bioturbation or microfossils (Plate 3.1). The pale grey colour of the matrix reflects its low total organic carbon content of 0.18 % and the high proportion of quartz (see XRF plots of Si/Al log ratios in Sect. 6.3). The poorly sorted matrix of sand and mud supports angular to rounded clasts of a wide range of lithologies including, on average, 50 % mudstone intraclasts, 2.5 % chert, 12.5 % sandstone, 2.5 % calcite and 7.5 % granite (Plate 3.1d). The average diameter of the clasts is 4 mm, maximum 35 mm, and using visual estimates, average clast sphericity is 6.5 and average roundness is 3. The long axes of the clasts are randomly orientated, and their subangular nature suggests little transport prior to incorporation into ice. Gneiss and granite clasts may have been plucked or abraded from the Pre-Cambrian Cape Meredith Complex and quartzites, sandstones and mudstones from the West Falkland Group. Others, such as clay fragments, for example at 393.3 m (core DD090), are probably intraformationally derived. Rare limestone clasts with an Early Cambrian archaeocyath–trilobite fauna were most likely sourced from the Transantarctic Mountains. This indicates that the Late Carboniferous ice sheet flowed from the contemporary polar region to at least ~60S before becoming waterlain (Stone and Thomson 2005; Stone et al. 2012).

Glaciotectonic structures are common in the tillite. Planar shearing is indicated by the shear lines running across beds and wrapped around clasts (Plate 3.1b), the dispersion tails of clay pinching out from clasts and the deformed soft sediment intraclasts. Whispy mudstone laminae and lenses in core DD029 often appear sheared, and well-defined clay rims surrounding some of the clasts probably formed by rotational processes in the deforming bed environment (Mckay et al. 2012). Fractures, brecciated bands, glossy surfaces, refracted cleavage, veins and slaty cleavage also reflect shearing and possibly ice sheet overriding and are found within the diamictite section.

Massive diamictites such as this may develop in subglacial, glaciomarine and/or open marine environments as a result of mass flow deposition (Anderson et al. 1980) or from homogenisation of glaciomarine sediment by iceberg scouring (Dowdeswell et al. 1994). Although waterlain till can form massive beds, any water movement causes reworking and sorting, so some stratification would be expected (Aldiss and Edwards 1999). The Fitzroy Tillite has no clear evidence for water sorting, suggesting there was limited subglacial meltwater and deposition occurred beneath grounded ice. Tentative minor intercalations of mudstone in core DD029 were later identified as joints lying subparallel to bedding, possibly similar to those described in outcrop by Aldiss and Edwards (1999). There is poor colour differentiation between them and the diamictite matrix. In addition, randomly orientated clasts, in particular bullet-shaped clasts (Plate 3.1c), are more indicative of lodgement till than waterlain deposits. Further, fissility of till, as found in core DD090, can indicate a subglacial origin (van der Meer et al. 2003) as do the shear structures in the top of beds (Plate 3.1b). The distal provenance of the clast compositions in the tillite might reflect large-scale grounded ice sheet expansion rather than local mass flows. Frakes and Crowell (1967) used evidence from palæocurrents, the orientation of linear sand bodies, the eastwards decrease in mean and maximum

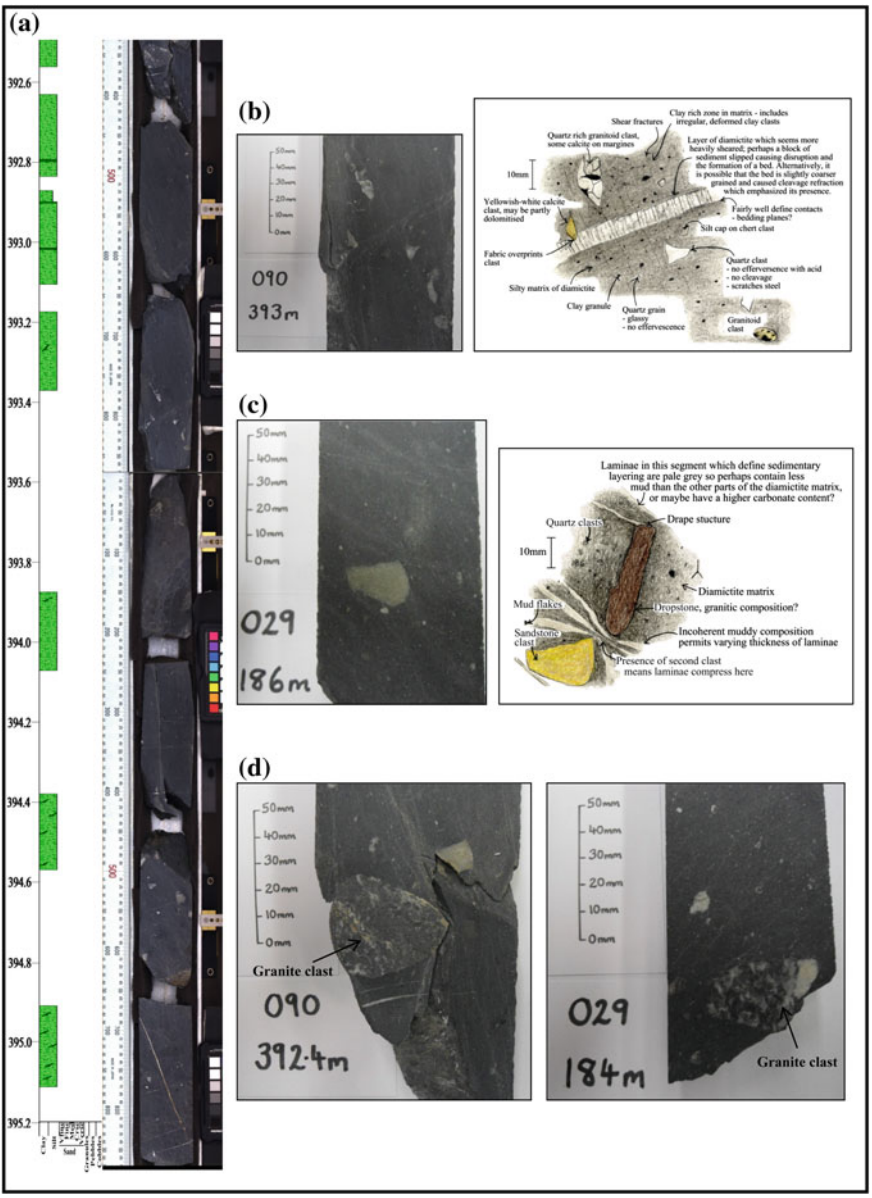

Plate 3.1 Fitzroy Tillite (sketches are taken from original lithological log). **a** Representative section of Fitzroy Tillite with photograph (core DD090). Scale refers to depth in metres marked on core. A full lithological key to the digital log extract shown here is provided alongside the complete lithological log in Sect. 6.1. **b** Bed interpreted to have formed through shearing by the overriding glacier; there is no change in lithology across contacts. Later vertical shear lines perhaps associated with tectonic deformation (Gondwanan orogeny) were then refracted through this bed. **c** Bullet shaped clast characteristic of lodgement till deforms sedimentary fabric around sandstone clast. **d** Large granitoid clasts in the Fitzroy Tillite. Other clasts visible include quartz, calcite, limestone and chert as well as clay intraclasts and granules

clast size, clast fabrics, rare ripple marks and primary current lineations to deduce an overall west-to-east transport direction across the Falkland Islands in their current rotated position. This is consistent with ice flow in the Eastern Cape (Fig. 1.4).

3.1.2 Hells Kitchen Member (Port Sussex Formation)

Core DD029: corrected depths 183.1–173.6 m
Core DD090: corrected depths 392.4–381.2 m

The massive diamictite is overlain by stratified muds and coarse beds belonging to the Hells Kitchen Member (Plate 3.2). This member is a transitional succession, comprising thinly interbedded diamictite, siltstone, claystone and rare wacke, that represents a temporary and fluctuating glacial regression. The interplay among depositional processes, including release of glacial debris from ice, gravity flows, iceberg calving and reworking by currents, makes the sedimentary facies complex. Depending on the thermal conditions of the ice and water, undermelting may also have been important, releasing debris close to the buoyancy line, or sea water may have frozen on resulting in sediment transport to the ice-shelf margin (Matsch and Ojakangas 1992). The following discussion focusses on the more stratigraphically complete core (DD090) which consists of four broad lithological zones in the Hells Kitchen Member.

1. The first part of the transition in core DD090, depths 392.4–391.2 m, is dominated by silt and clay beds but pebble laminae are interspersed. The presence of stratification and sorting could indicate current activity in the depositional

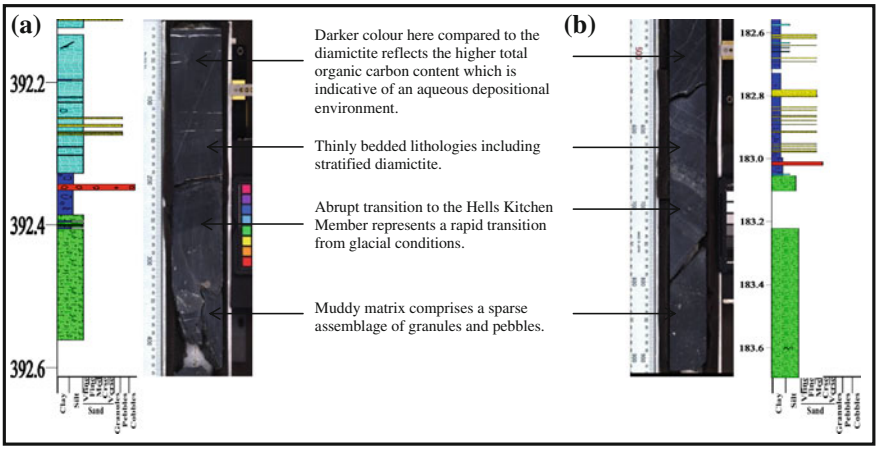

Plate 3.2 Lithological changes at the Fitzroy Tillite to Hells Kitchen Transition. **a** Fitzroy Tillite to Hells Kitchen Member transition at ~392.4 m in core DD090. **b** Fitzroy Tillite to Hells Kitchen Member transition at ~183.1 m in core DD029

environment (Matsch and Ojakangas 1992). Finer material may reflect hemipelagic suspension settling of fines (Passchier et al. 2011) derived from winnowed waterlain diamictites and a shift away from subglacial conditions to an environment more distal to the grounding line. Linear, sorted clast layers (Plate 3.3a) suggest aqueous sedimentation (Michalchuk et al. 2009) and perhaps some transportation away from the grounding line. Alternatively, the clasts may be fall out from large icebergs (Fig. 3.1). Abundant dropstones reflect icebergs or a floating ice-shelf transporting larger clasts to the site. Pebble beds increase in thickness towards the top of this silty zone. Clasts are often erratics composed of reworked diamictite matrix.

2. Between depths 391.2–389.5 m in core DD090, a zone characterised by a higher frequency of coarse beds, there are a series of fining upwards sequences. An ice-proximal environment can be a highly energetic zone depending on the stability of the ice margin. The fining up sequences may have formed by hyperconcentrated density flows or turbidity currents which are common in proximal proglacial environments where slopes are unstable (Powell and Dormack 2002). Alternatively, meltwater outflows at the retreating grounding line may be responsible. The gravelly and sandy laminae and occasional pods which follow have sharp upper and lower contacts, are millimetre to several centimetres thick and typically massive, and are interspersed with mudstone containing intraclasts and dropstones. Such coarse unstratified beds of diamictite may be interpreted as meltout through a narrow water column either directly from the basal debris layer of an ice shelf or from material transported in meltwater plumes (McKay et al. 2009). Their lack of internal structures and sharp contacts with dropstone bearing mudrocks and rhythmites is suggestive of deposits of rainout and debris flows (Henry et al. 2012).

   Stratified diamictite beds have aligned clasts of similar size interspersed with wavy mud laminae (Plate 3.3a). Again, this could reflect meltout of basal debris associated with lift off and development of a floating ice shelf (McKay et al. 2012). The presence of intraclasts and the compositional similarities to the underlying massive diamictites might support this. However, this process would provide a wide variety of clast sizes, whereas clasts in the bedded diamictite are restricted to granules and small pebbles. Sediment gravity flows, suspension settling of clay and silt from underflows and overflows, subaqueous debris flows and turbidity currents common in ice-proximal settings (McKay et al. 2009) are thus expected to have played some role in sorting the material too. Lithification and variation in porosity and permeability may also have assisted in the formation of layering (Frakes and Crowell 1967).

   Deformation in the diamictite beds is likely to be caused by a combination of glacial push, ice loading, compaction, debris flows and soft sediment deformation (Fig. 3.2). Deformation structures such as flames reflect water escape and loading by denser material, ice or dropstones into underlying water-saturated sediment (Plate 3.3 and 3.4). Some mudstone layers exhibit convolute bedding,

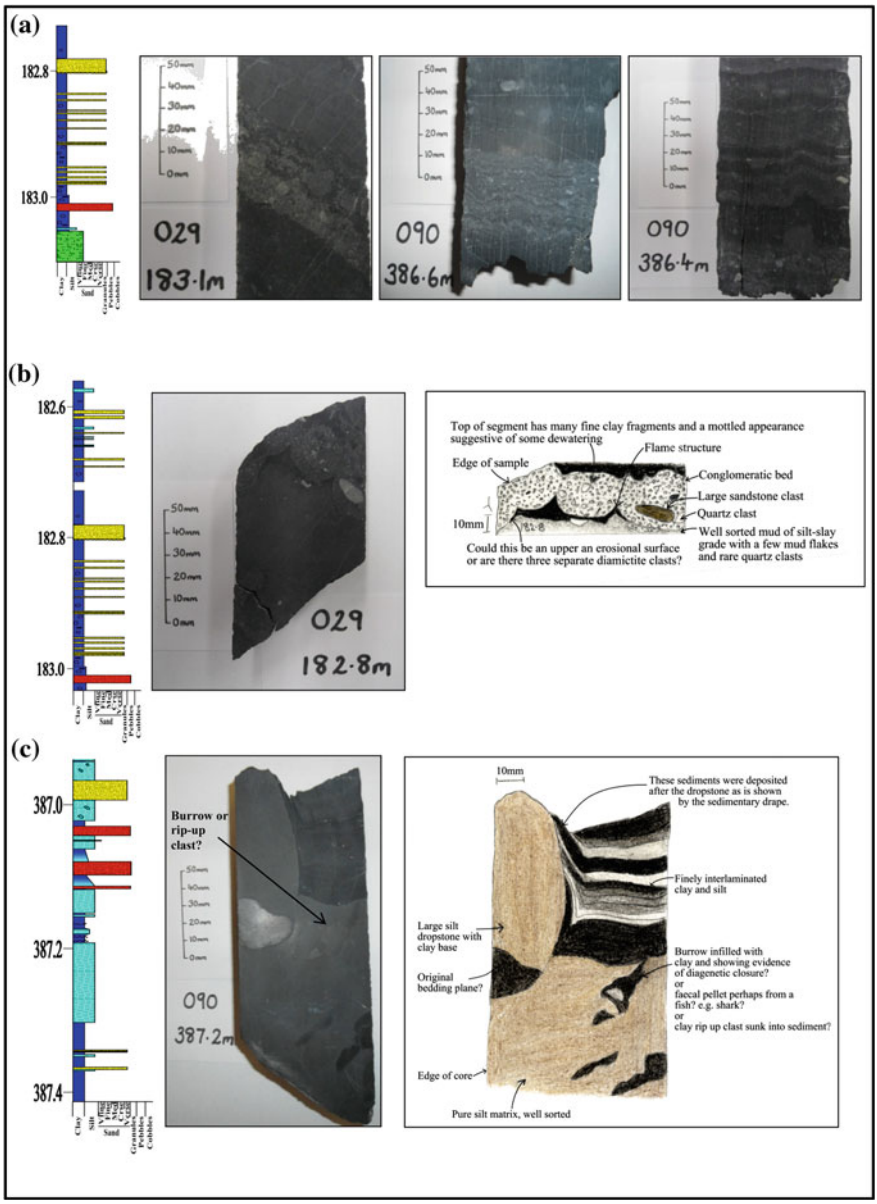

Plate 3.3 Styles of sedimentary deposition and soft sediment structures. **a** Stratified diamictite bed with wavy mud laminae and scattered dropstones are envisaged accumulating at the margin of a wasting glacier without significant alluvial or outwash reworking. Mud probably originated from suspension settling of hemipelagic material or from meltwater plumes during intervals when iceberg delivery was suppressed by the development of shorefast ice. Wavy individual layers 1 mm to 1 cm thick are deformed around clasts scattered within the sequence; they are examples of drape structures. **b** Flame structures either associated with loading by a diamictite layer which developed fissures on its upper surface by later dewatering, or alternatively this layer may comprise reworked clasts from the underlying till. **c** Example of large dropstone associated with sedimentary drape and tentative burrow structure.

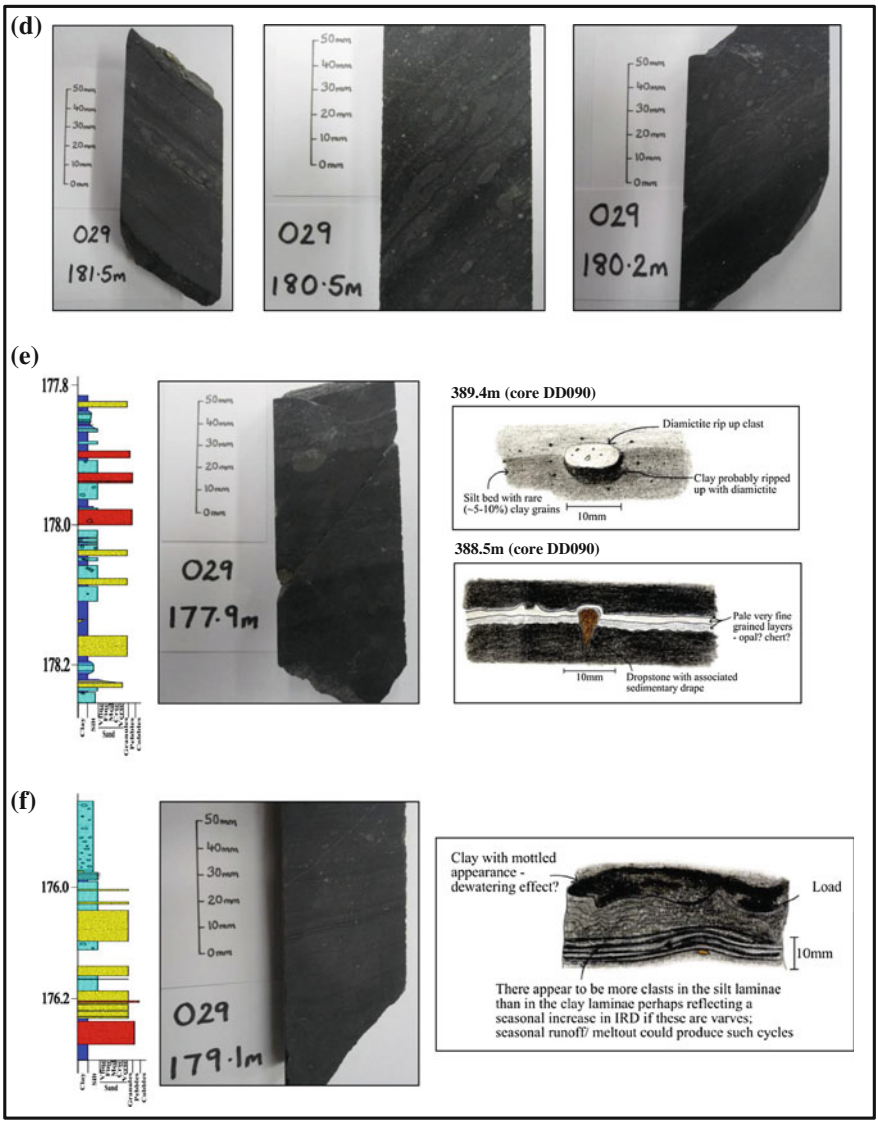

Plate 3.3 **d** Examples of reworked silt and diamictite clasts, sometimes they have lensoid shapes probably due to compression prior to lithification. **e** Examples of sedimentary fabrics associated with clasts. *Left* Dropstone with sedimentary drape, shown with corresponding log section. *Top right* Sketch of diamictite rip-up clast. *Bottom right* Sketch of dropstone piercing stratification. **f** Rhythmic thinly laminated varve-like deposits consisting of distinct silt-clay couplets with sharp contacts. The coarse component is likely deposited from overflow and interflow plumes generated during the ablation season whilst the fine component records gradual settling of the finest material during winter when there is little or no incoming water to the lake/marine environment (Benn and Evans 2010). Perhaps the term varve should be used with some caution though as it cannot be demonstrated for certain that they represent seasonal depositional cycles

slumping and warped contacts and mix with underlying stratified diamictite; commonly, they have not retained an even thickness during compaction and cementation, reflecting their incompetency.

Clasts in this part of the Hells Kitchen Member are angular to rounded, poorly sorted and lithologically variable although overall they seem to have a more local provenance than those found in the massive diamictite, for example, there is a reduction in granite and an increase in siltstone. Till pellets may be products of ablation, while rip-up clasts were scraped or lifted off the tillite by basal ice. Large clasts that pierce stratification or appear to have deformed sediment on impact were probably ice-rafted debris (IRD). Evidence for floating ice discounts the possibility of a fluvial origin for these deposits. Similarly, clumps of small pebbles and granules in the stratified diamictite were probably frozen aggregates of coarse sediment, held together by interstitial ice that fell from icebergs (Gilbert 1990). The lack of fossils and bioturbation and dispersed clasts probably indicate limited sub-ice-shelf oceanic circulation with high sedimentation rates (McKay et al. 2009) and low light penetration close to the grounding line.

3. A second zone of interlaminated clay and silt in core DD090 occurs between depths 389.5–387.1 m and is broadly similar to the first. However, its base is marked by abundant dark grey to black well-rounded granules which may be volcanic lapilli (see XRF analysis) followed by a chert nodule (Plate 3.5d). Volcanic detritus has previously been found within the Fitzroy Tillite and was suggested to have been derived from a magmatic arc associated with subduction on the Pacific margin of Gondwana (Cole 1992). As the grounding line retreated upstream relative to the drill site, mudstones appear to have been deposited

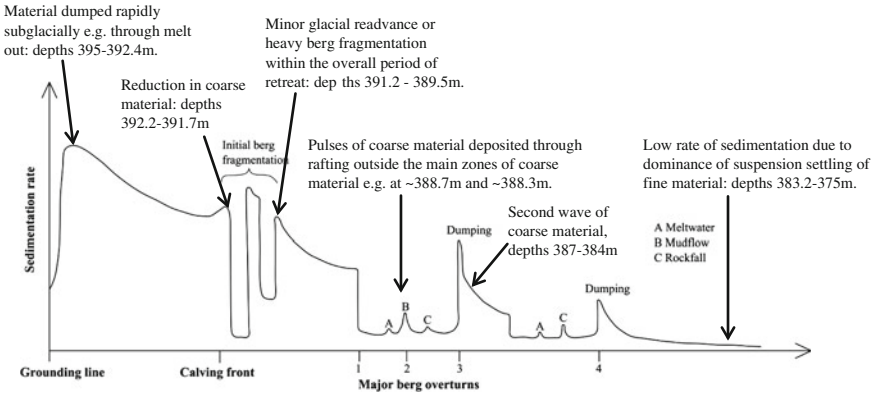

Fig. 3.1 An example of how debris may be released from drifting and melting icebergs showing the effects of calving, fragmentation and overturn (redrawn from Drewry 1986). Material may be dropped as the ice melts, perhaps as frozen aggregates or be released from crevasse fills through overturn. Where possible the core DD090 deposits are linked to this analogy

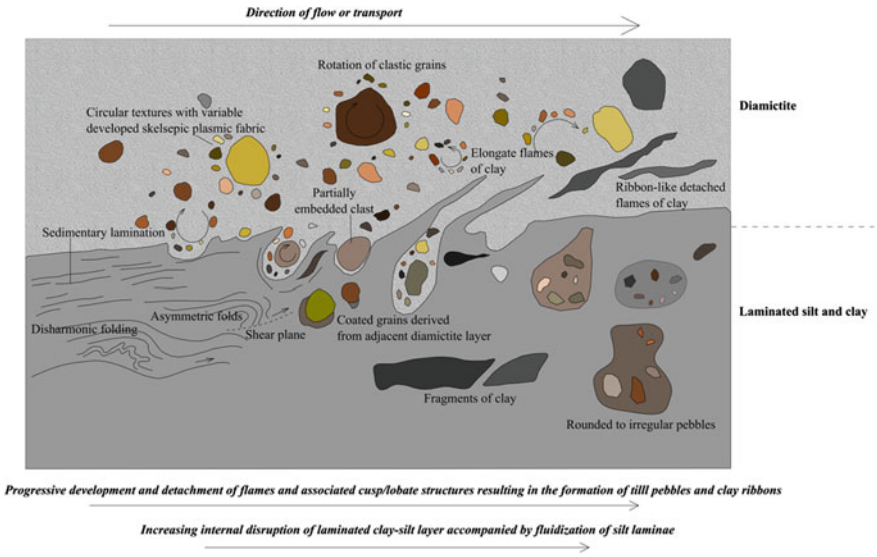

Fig. 3.2 Schematic diagram of microstructures that can develop at the base of a debris flow diamictite (adapted from Phillips 2006: In Benn and Evans 2010)

beneath a floating ice sheet with less basal debris. Thick mudstones with sparse diamictites and sandstones also hint at an increased input of meltwater from nearby terrestrial sources during glacial minima and deposition by suspension settling from such plumes. Perhaps there were some sporadic debris flows: pelagic mud alternating with silt may be rhythmites originating from underflows or turbidity currents (Cole 1991). Around 388.7 m, thin coarse beds reappear. Coarse beds make up ~30 % of this zone and increase in thickness towards the top. It is possible that the spacing of these beds is a reflection of high-frequency orbital cycles such as precession (see Chap. 4).

4. Between depths 387.1–385.6 m in core DD090, coarse beds ~20 mm thick become abundant and some of them fine upwards. The sediments are composed of varying mixtures of terrigenous deposits in the form of IRD and hemipelagic components. The increase in pebbles could signify the final breakout of marginal ice (Michalchuk et al. 2009). Clay and silt pebbles dominate, and roundness values ~6 suggest some reworking took place. A clast count indicates cyclical changes in lithologies, average clast diameters, sphericity and roundness possibly reflecting waxing and waning of the glaciers and changes in clast provenance. Individual beds up to 4 cm thick grading from diamictite or wacke to mudstone may have been produced by bottom currents and represent interludes of more energetic water circulation accompanying the periodic retreat of the ice shelf in the generally quiet realm of aqueous sedimentation. Normally graded beds and rapid stratigraphic changes could also occur as a result of fluctuating discharge.

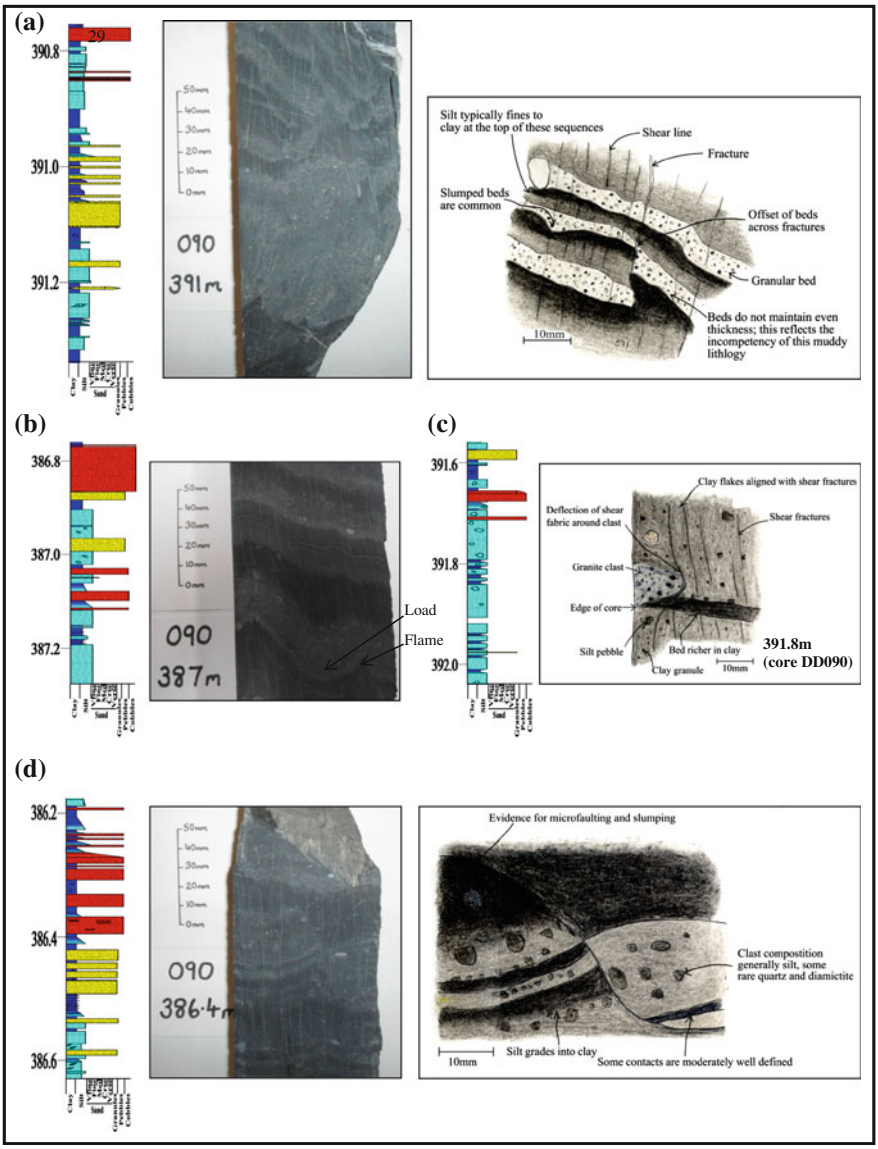

Plate 3.4 Deformation in the Hells Kitchen Member. **a** Small fault blocks may have formed from ice push or as material slid downslope. **b** Slumping and folding in stratified diamictite with associated loads and flames may be linked with ice-marginal deformation. Folding likely occurred due to frictional differences along the basal surface of the bed as it moved across the substrate. **c** Example of shear fabric wrapping around a clast. Since these deposits are not thought to be subglacial the shearing may be linked with later tectonic deformation such as the Gondwanan orogeny. **d** Second example of microfaulting with ~2 cm offset. It is from a zone of coarse beds (387.1–385.6 m) so the faulting maybe linked with the more energetic subaqueous conditions during increased glacier and iceberg cover

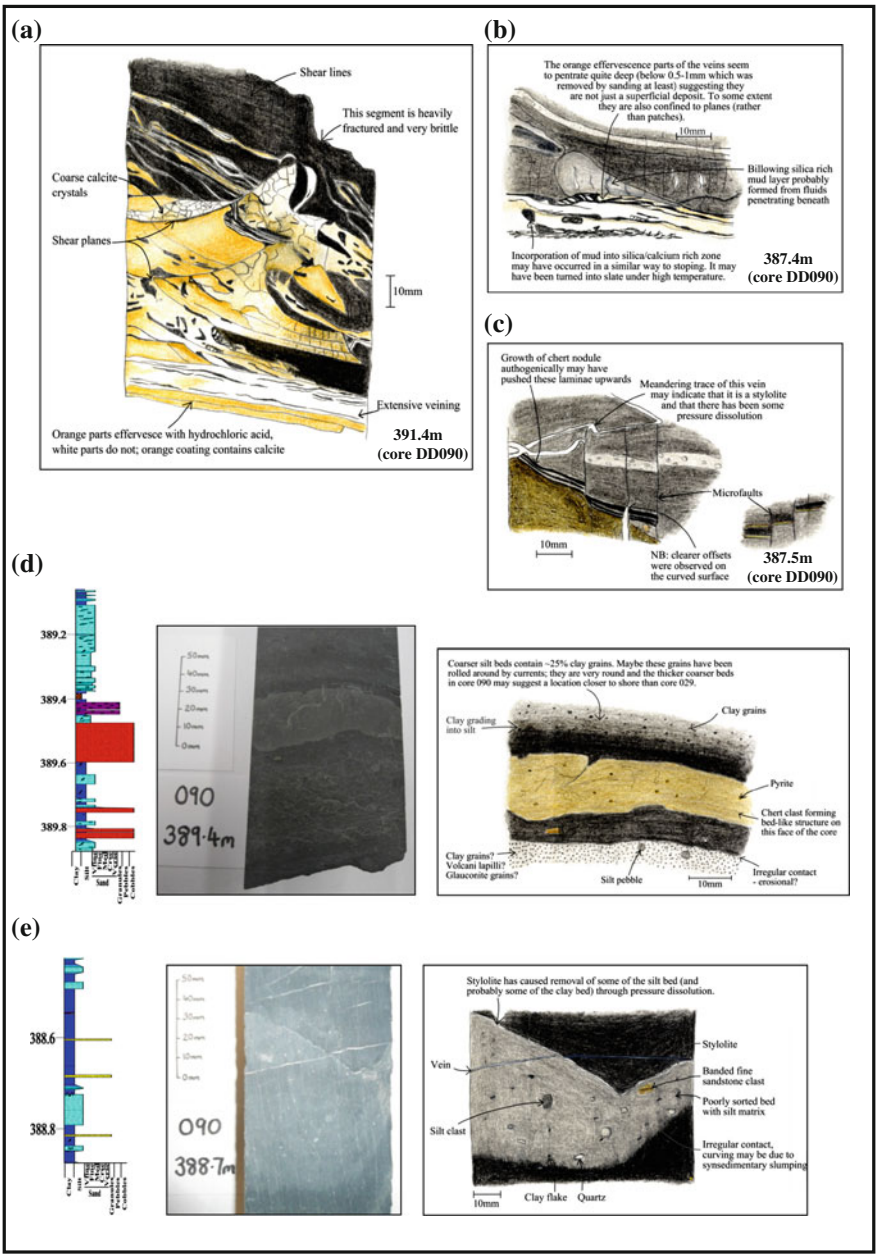

Plate 3.5 Diagenesis and volcanics. **a** Extensive calcite veining penetrates clay bed. Orange colouration in parts is probably due to iron staining. **b** Pale 'plume' probably caused by the introduction of silica-rich fluid in association with veining. **c** Chert nodule associated with microfaulting. **d** *Dark black* grains thought to be volcanic lapilli on account of their elemental composition (rich in heavy mineral elements and low in potassium). Up sequence there is a chert nodule; curved core surface indicated that it is not laterally continuous. **e** Pressure dissolution along silt-clay contact associated with stylolite. Some fine white calcite veins are also visible

In the youngest part of this zone, there are abundant black clasts less than 1 mm long. Their irregular shapes suggest they are deformed clay clasts rather than volcanogenic clasts. They are often elongated in the direction of shearing and may be interpreted as fragments of frozen sediment not fully lithified prior to deformation. Deformed lenses of clay and silt are also found. The mottled appearance of some of the silt may be due to bioturbation, dewatering or seismic activity disrupting the laminae. The frequency and thickness of pebbly beds decreases towards the top of the Hells Kitchen Member.

3.1.3 Black Rock Member (Port Sussex Formation)

Core DD090: corrected depths 381.2–374.8 m
Core DD029: corrected depths 173.6–170 m

The transition from the Hells Kitchen Member into the post-glacial mudstone of the Black Rock Member is gradational. In this analysis, the Black Rock Member was distinguished from the Hells Kitchen Member by the absence of coarse laminae. The Black Rock Member is instead composed of black/dark grey, laminated, thinly bedded or massive mudstones over which dispersed ice-rafted clasts become scarcer, more scattered and smaller up sequence (Plate 3.6). Beds appeared dark and carbonaceous when seen on cut and polished surfaces, but TOC values of ~3 % suggest the dark coloration is due to dark minerals (perhaps containing iron or manganese) rather than organic material. Occasionally, beds are pyritic or cherty. Between depths 381.2–374.8 m in core DD090, there is high silt content. It is greenish with abundant clay lenses and laminae (Plate 3.6c). Core DD029 has comparable greenish silt with clay lenses beginning around 171 m. Bioturbation is rare.

To characterise fully these post-glacial deposits, two sections were also taken from further up sequence in core DD090; corrected depths 158.88–157.67 m and 156.75–155.71 m. Here, the Black Rock Member consists of clay and authigenic pyrite sometimes in bands (Fig. 3.3). Some white acicular grains may be glendonites, calcite pseudomorphs after ikaite.

The low clast content in the Black Rock Member suggests deposition by suspension settling and occasional iceberg rainout in a quiet, distal proglacial setting with little dissolved oxygen and soft-sediment deformation. The increase in clay probably reveals a deepening water body and a decrease in energy. The greenish-black organic-rich laminated sediments, if bentonitic, may reflect the onset of open water conditions. Silt laminations in clay likely reflect increased meltwater outflow. The presence of localised currents is indicated by the small channel structure in core DD090, and these may have been generated by wind shear, upwellings, ice melting or sediment gravity flows.

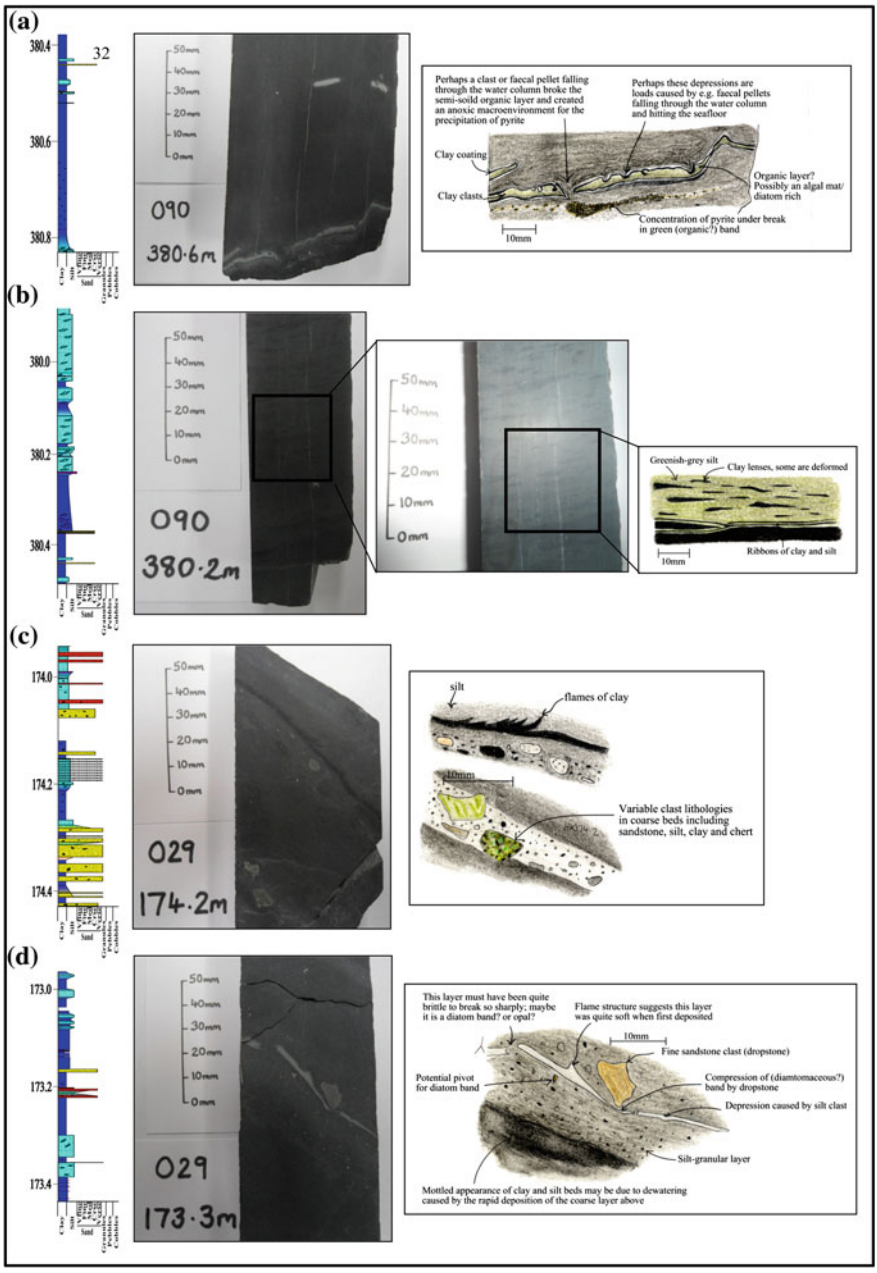

Plate 3.6 Sedimentary features of the Black Rock Member. **a** Fragmentary organic layer with load structures or borings and a small concentration of pyrite indicating an anoxic microenvironment. **b** Green silt (bentonitic?) with abundant clay lenses. **c** Mudstone bed with cusp-shaped flame structures formed due to deposition of coarse sandstone up sequence. **d** Dropstone deforming pale (opal?) band which has a possible flame structure

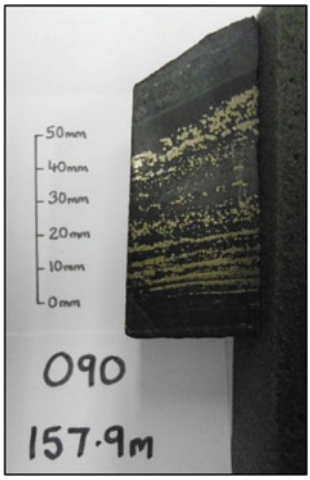

Fig. 3.3 Post-glacial anoxic black mudstone with abundant framboidal authigenic pyrite grains arranged in bands

3.2 Reflectance Data

Colour reflectance served as a proxy for lithological variability through the cores. In the diamictite, the moderately high L* (lightness) values, ~55, reflect the medium-grey colour of the silty quartz-rich matrix. Coarse beds are typically pale because they are rich in silica, while hemipelagic deposits are usually dark and 'red'. L* and a* (red/green) therefore provide fairly reliable indicators of whether sediment was deposited during ice advance or retreat and were used in wavelet analyses (see Chap. 4). Cyclicity in reflectance parameters parallels the lithologies logged. Extreme excursions in lightness were caused by calcite veins (Plate 3.5a). In the outlier sections of the Black Rock Member, the b* (yellow/blue) and L* decline, while the a* rises because this clay is geologically very dark and red. The sharp downward deflection at 377 m in core DD090 is due to the concentration of light coloured pyrite.

3.3 XRF Data

The variations in elemental ratios show trends through time related to sedimentary processes. This means they contain clues about environmental shifts and climatic changes comparable with the physical properties of the sediment logged. In the tillite, elemental ratios are fairly stable reflecting the fairly homogenous matrix composition. A few peaks in certain elements can however be tied with clast mineralogy or veins, for example, the peak in all elements around 393 m in core DD090 and the corresponding granite clast. Based on the sedimentological analysis,

the Fitzroy Tillite to Hells Kitchen Member transition seems to reflect retreat of an ice shelf and the establishment of aqueous deposition distal to an oscillating ice margin. The first major shift in the elemental concentrations in the XRF record occurs at this boundary (Fig. 3.4). There is an increase in the amplitude of the signal in all records and log ratios of the elements silicon, manganese, chromium and zirconium, and iron decrease; zirconium by a factor ~ 3.

The XRF profiles pick out subtle changes in source area and help to identify glacier advance and retreat. The elements zirconium, titanium and chromium are associated with heavy minerals (zircon, rutile/ilmenite, spinel, respectively), and their variation may reflect changes in sediment provenance. There is a positive correlation between the terrigenous elements, silicon, iron, manganese, chromium and zirconium, and the physical properties documented by the L* and b* parameters. There are, however, some deviations from the broad elemental correlations. For example, at 391.4 m, there is a rise in zirconium (with potassium), while some element ratios fall. Perhaps this reflects the high granite clast content of the coarse beds here which are rich in potassium feldspar and detrital zircon grains from weathered granitic sources.

The ln(Si/Al) ratio (where ln is the natural logarithm) was used as a proxy for sand:mud ratio because sand (SiO_2) is rich in silica, while clays are typically richer in aluminium. This approximation appeared reasonable since trends in ln(Si/Al) closely matched grain size trends documented in the logs. In addition, potassium is found mostly in clay minerals such as illite (McKay et al. 2012) so may be used to

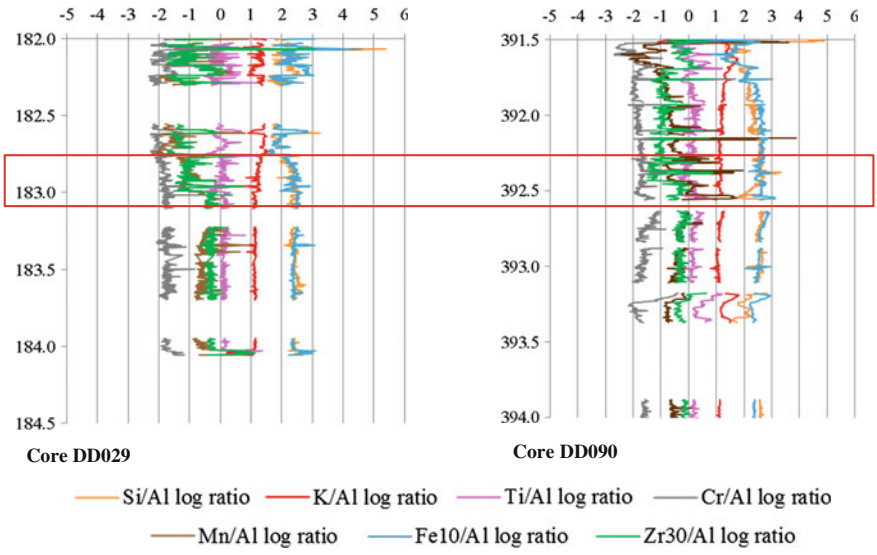

Fig. 3.4 Elemental ratios at the transition to Hells Kitchen Member. Transition occurs within the outlined zone. Depth scales are in metres

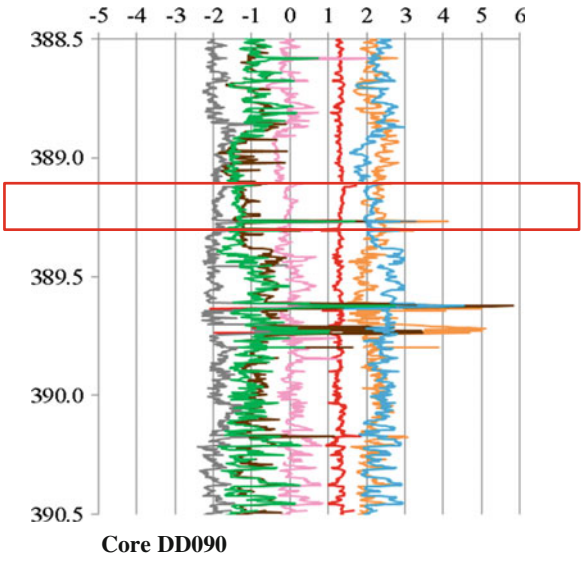

Fig. 3.5 XRF section highlighting the peak in heavy mineral elements at the volcanic lapilli in core DD090. Refer to key in Fig. 3.2

estimate clay content. Ln(K/Al) is lowest in the diamictite beds where potassium-poor clasts and abundant quartz are found, and higher in the muddy intervals. Ln(K/Al) is generally inversely correlated with the heavy mineral elements and correlates positively with the a* parameter. Two sharp peaks in all elements but potassium around 389.4 m in core DD090 correspond to the beds with dark black granules which are thus more likely to be volcanic lapilli than clay (Fig. 3.5).

Ln(Ti/Al) is often used as a measure of provenance or energy change (e.g. Spofforth et al. 2008). Overall, this ratio shows a decrease to more negative values from the diamictite to the mudstone, reflecting the gradual decrease in energy up sequence. An elevated ln(Ti/Al) ratio, for example at 391.5 m (DD090), could be interpreted as arising from a decrease in aeolian dust input, since the absolute counts in titanium and iron show a temporary decrease indicating a drop in the input of these elements. Minerals such as quartz and those rich in aluminium remain in the sediment, while more mobile minerals are rapidly weathered and transported away. The increase in Ln(Ti/Al) could therefore be interpreted to be a consequence of periods of increased precipitation causing increased chemical weathering, enhanced flushing of organic matter into the water and possibly also higher water levels which causes dysoxic conditions at the sediment surface and hence enhanced organic matter preservation (Löwermark et al. 2011).

There are two places where there is a clear negative correlation between iron and silicon in core DD090 ($\sim$382.6 and 383.3 m), and both coincide with the presence of pyrite. Thus, the iron here has an authigenic rather than a terrestrial origin, supported also by the peak in manganese, a redox element, in these beds.

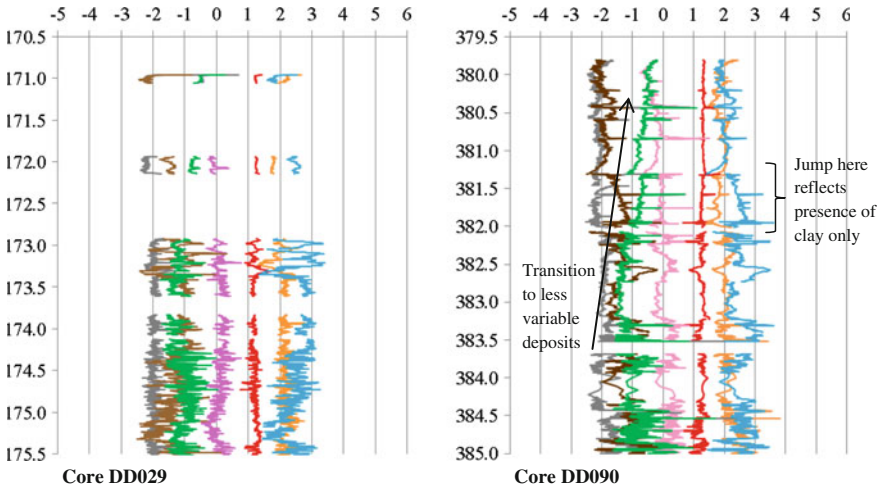

Fig. 3.6 Elemental ratios across the Hells Kitchen Member to Black Rock Member transition. The transition begins at ~383 m in DD090 and 174.3 m in core DD029. Refer to key provided in Fig. 3.4

Manganese correlates almost precisely with iron in both cores except for around 387.7, 387.5 and 392.2 m. The difference at 387.7 m can be explained by diagenetic veining, and around 387.5 m, there is a zone of dewatering which may be linked with oxygenation of the bottom waters and hence an increase in the production of manganese oxides. Similarly, in core DD090, 392.2 m marks the start of the Hells Kitchen Member, and this transition to subaqueous rather than subglacial conditions may be linked with a rise in oxygen and hence a more pronounced peak in manganese oxide formation than iron compounds.

The gradational lithological shift between the Hells Kitchen Member and the Black Rock Member is captured well by the XRF data of core DD090 (Fig. 3.6). Throughout the cores, there is a gradual upwards increase in the potassium content from 1 to 1.3 on the natural log scale, reflecting the increasing proportion of clay. This is supported by the grain size measurements. Sharp peaks in iron are typically related to concentrations of pyrite. Potassium is inversely correlated with iron because the proportion of clay declines in the layers where authigenic pyrite precipitates. Pyrite was probably formed in situ, as elevated ln(Fe/Al) ratios are indicative of scavenging of iron from the water column. Presence of pyrite also indicates a relatively constant replenishment of iron and sulphur to the water. Reducing conditions at the base of the water column and within the sediments can lead to alteration of much of the iron and manganese oxyhydroxides within the sediments via redox cycling (Dean 1993).

3.4 Total Organic Carbon

As far as it was possible to determine, TOC values reached a maximum of 0.34 % in the Hells Kitchen Member. This probably reflects the cold sub-ice-shelf conditions which are unfavourable to life. Changes in $\delta^{13}C_{org}$ (isotope ratio of $^{13}C/^{12}C$ in organic matter) in marine and lacustrine settings often relate to changes in productivity and/or changes in water and continental organic matter burial that drive or act together with changes in pCO_2 and $\delta^{13}C_a$ (isotope ratio of $^{13}C/^{12}C$ in atmospheric CO_2) (Birgenheier et al. 2010). The general positive shift in $\delta^{13}C_{org}$ could suggest a drop in pCO_2 and/or an increase in $\delta^{13}C_a$ and warming. The negative $\delta^{13}C$ values in the green, possibly bentonitic, silt at ~382.2 m might indicate de-oxygenation of the sediments since an injection of ash can increase local productivity (Frogner et al. 2001). Increased proximity to openwater zones of primary productivity would have caused the increase in TOC. Previous analysis of the organic carbon and kerogen in the Black Rock Member found TOC contents up to 40 % (mean 15.5 %) that were dominated by amorphous organic matter (Marshall 1994). The lower values found in the Black Rock Member in core DD090, ~3 %, suggest either lower organic productivity, more aerobic conditions or a dominance of terrigenous input.

References

Aldiss DT, Edwards EJ (1999) The geology of the Falkland Islands. British Geological Survey Technical Report: WC/99/10

Anderson JB, Kurz DD, Dormack EW (1980) Glacial and glacial marine sediments of the Antarctic continental shelf. J Geol 88:399–414

Benn DJ, Evans DJA (2010) Glaciers and glaciation, 2nd edn. Hodder Education, Oxford

Birgenheier LP, Frank TD, Fielding CR, Rygel MC (2010) Coupled carbon isotopic and sedimentological records from the Permian system of eastern Australia reveal the response of atmospheric carbon dioxide to glacial growth and decay during the late Palæozoic Ice Age. Palæogeography, Palæoclimatology, Palæoecology 286(3–4):178–193

Cole DI (1991) Depositional environment of the group in the Boshof-Hertzogville region, Orange Free State. S Afr J Geol 94:272–287

Cole DI (1992) Evolution and development of the Karoo Basin. In: De Wit MJ, Ransome IGD (eds) Inversion tectonics of the Cape Fold Belt, Karoo and Cretaceous Basins of southern Africa. Balkema, Rotterdam, pp 87–99

Dean WE (1993) Geochemistry of surface sediments of Minnesota Lakes. Geol Soc Am Spec Pap 276:115–133

Dowdeswell JA, Whittington RJ, Marienfeld P (1994) The origin of massive diamicton facies by iceberg rafting and scouring, Scoresby Sund, East Greenland. Sedimentology 41:21–35

Drewry DJ (1986) Glacial geologic processes. Edward Arnold, London

Frakes LA, Crowell JC (1967) Facies and Palæogeography of Late Palæozoic Diamictite, Falkland Islands. Geol Soc Am Bull 78:37–58

Frogner P, Gislason SR, Oakarsson N (2001) Fertilizing potential of volcanic ash in ocean surface water. Geology 29:487–490

Gilbert R (1990) Rafting in glacimarine environments. In: Dowdeswell, JA, Scourse JD (eds) Glacimarine environments: processes and sediments, vol 53. Geological Society of America (Special Publication), New York, pp 105–120

Henry LC, Isbell JL, Fielding CR, Domack EW, Frank TD, Fraiser ML (2012) Proglacial deposition and deformation in the Upper Carboniferous to Lower Permian Wynard Formation: a process analysis. Palæogeogr Palæoclimatol Palæoecol 315(316):142–157

Löwermark L, Chen H-F, Yang T-N, Kylander M, Yu E-F, Hsu Y-W, Lee T-Q, Song S-R, Jarvis S (2011) Normalizing-scanner data: a cautionary note on the interpretation of high resolution records from organic-rich lakes. J Asian Earth Sci 40:1250–1256

Marshall JEA (1994) The Falkland Islands: a key element in palæogeography. Tectonics 13:499–514

Matsch CL, Ojakangas RW (1992) Stratigraphy and sedimentology of the Whiteout Conglomerate: an upper Palæozoic glaciogenic unit, Ellsworth Mountains, West Antarctica. In: Webers GF, Craddock C, Splettstoesser JF (1992) Geology and Palæontology of the Ellsworth Mountains, West Antarctica, vol 170. Geological Society of America, Memoir, New York, pp 37–62

McKay R, Browne G, Carter L, Cowan E, Dunbar G, Krissek L, Naish T, Powell R, Reed J, Talarico F, Wilch T (2009) The stratigraphic signature of the late Cenozoic Antarctic Ice-sheets in the Ross Embayment. Geol Soc Am Bull 121:1537–1561

McKay R, Naish T, Powell R, Barrett P, Scherer R, Talarico F, Kyle P, Monien D, Kuhn G, Jackolski C, Williams T (2012) Pleistocene variability of Antarctic Ice-sheet extent in the Ross Embayment. Quatern Sci Rev 34:93–112

Michalchuk BR, Anderson JB, Wellner JS, Manley WM, Majewski W, Bohaty S (2009) Holocene climate and glacial history of the northeastern Antarctic Peninsula: the marine sedimentary record from a long SHALDRIL core. Quatern Sci Rev 28:2049–3065

Passchier S, Browne B, Fielding CR, Krissek LA, Panter K, Pekar SF, ANDRILL-SMS Science Team (2011) Early and Middle Miocene Antarctic glacial history from the sedimentary facies in the AND-2A drill hole, Ross Sea. Geol Soc Am Bull 123:2352–2365

Phillips ER (2006) Micromorphology of a debris flow deposit: evidence of basal shearing, hydrofracturing, liquefaction and rotational deformation during emplacement. Quat Sci Rev 25:720–738

Powell RD, Dormack EW (2002) Modern glacimarine environments. In: Menzies J (ed) Modern and past glacial environments. Butterworth-Heinemann Ltd., Oxford, pp 361–389

Spofforth DJA, Pälike H, Green D (2008) Palæogene record of elemental concentrations in sediments from the Arctic Ocean obtained by analyses. Palæoceanography 23:1–13

Stone P, Thomson MRA (2005) Archaeocyanthan limestone blocks of likely Antarctic origin in Gondwanan tillite from the Falkand Islands. Geol Soc London Spec Publ 246:347–357

Stone P, Aldiss DT, Edwards EJ (2005) Rocks and fossils of the Falkland Islands. Department of Mineral Resources, Falkland Islands Government

Stone P, Thomson MRA, Rushton AWA (2012) An Early Cambrian archaeocyath-trilobite fauna in limestone erratics from the Upper Carboniferous, Falkland Islands. Earth Environ Sci Trans R Soc Edinb 102:201–225

van der Meer JJM, Menzies J, Rose J (2003) Subglacial till: the deforming glacier bed. Quatern Sci Rev 22:1659–1685

Chapter 4
Discussion

Abstract The depositional framework outlined for the Falkland Islands deposits in the previous chapter is investigated in the context of the Gondwanan supercontinent. The focus in this chapter switches from trying to recognise the immediate physical processes responsible for the sedimentological variations, to seeking an explanation for the underlying mechanisms responsible for initiating the dynamic environmental setting. The sedimentology, combined with a review of the existing literature, points most convincingly towards the idea that Gondwana was host to a large subglacial lake. Milankovitch orbital forcing is explored as an explanation for the cyclical nature of the deposits. Firstly, the XRF and reflectance data were subjected in the depth domain to spectral analysis through which prominent periodicities (in depth) could be identified. Then, by considering the data alongside a synthetic Carboniferous orbital solution, an age model and a time constraint for deposition were developed. Orbital cycles appear to be expressed in this stratigraphic record at 100 and 400 kyr periodicities, implying the transition took approximately 1.2 myr. Within the course of the transition, glaciological processes (including the build-up of an unstable ice sheet regime following the intense and prolonged icehouse state) may also have assisted in driving the oscillations. Taking into consideration the phases of glaciation documented across other landmasses that were also once part of Gondwana, together with the expected diachroneity of climate change across the continent, the transition in the Falkland Islands is constrained to the Sakmarian Stage of the Early Permian. Possible causes of deglaciation are also briefly explored in this chapter.

Keywords Lacustrine · Orbital forcing · Age modelling · 400 kyr · Sakmarian · Principal Component Analysis · Wavelet analysis

K. Horan, *Falkland Islands (Islas Malvinas) in the Permo-Carboniferous*,
Springer Earth System Sciences, DOI 10.1007/978-3-319-08708-5_4

4.1 Understanding the Environments of Deposition: Facies Evaluation

4.1.1 Overview

The sedimentological and geochemical results support the idea of dynamic and fluctuating glacial and non-glacial conditions in a high latitude, ice-proximal environment within the overall Permo-Carboniferous icehouse to greenhouse transition. The facies interpretation for the sedimentary sequences and structures observed is summarised in Table 4.1.

Two cycles of glacial advance and retreat are recorded clearly by coarse bed frequency and thickness in core DD090. The scarcity of erosional contacts reflects the fact that the deposits preferentially record glacial retreat. Core DD029 shows a less clear environmental signal with coarse beds distributed throughout the transition; the early silt dominated zone found in core DD090 is less well distinguished in core DD029. A possible explanation for this trend is that the more easterly location of core site DD029 remained under grounded ice for longer. However, wavelet and spectral analyses suggest there are the same number of orbital cycles documented in the both cores and principal component analysis (PCA) suggests that climate is the main cause of variance in the sediments rather than sedimentological processes such as turbidites (see Sect. 4.4). Further, core DD029 has similar sedimentary features to several different parts of core DD090; for example, turbiditic sequences near the start and a zone rich in deformed clay clasts further up sequence. The volcanic lapilli in core DD090 are not found in core DD029 probably because the later core is less complete but possibly because of a local shielding effect from the dust. Overall, it seems most likely that the differences between the cores arise from the less complete nature of core DD029.

In summary, the sedimentology of both cores reveals the evolution of a palæoenvironment in which a subglacial diamictite interpreted to have formed by in situ wasting of debris-laden ice became overlain by a marine/lacustrine ice-shelf succession comprising deposits originating from subaqueous mudflow deposits, mobilised till and outwash material. The climate transition is interpreted to have taken place though climatic oscillations rather than occurring gradually. A fluctuating grounding line or periodic anchoring and detachment of a large ice shelf on a submarine topographic high are envisaged, similar to the interpretation of Matsch and Ojakangas (1992) for the Meyer Hills deposits, Antarctica.

4.1.2 Core Comparison: Autocorrelation Test

A 21-point least squares smoothing was applied to the a* reflectance parameter data sets linearly resampled at 0.0001 Ma and an autocorrelation was run (Fig. 4.1). A 21 points smoothing was used because this is the widest smoothing permitted in a

Table 4.1 Sedimentological interpretation summary

Facies association	Lithologies	Sedimentology	Depositional environment, characteristic sedimentary processes	Glacial regime and grounding line proximity
Fitzroy Tillite Formation	Glaciogenic diamictite	Poorly sorted terrigenous clastic sedimentary rock with a wide range of grain sizes, polymict composition	Meltout and shearing of continental subglacial lodgement till	Subglacial, non-aqueous environment
Hells Kitchen Member, Port Sussex Formation	Interbedded mudrock and conglomerate–dimictite	Alternating well-sorted laminae and beds of fine and coarse-grained lithologies with isolated dispersed gravel and some soft sediment deformation	Seasonal or other periodic influx of mixed sediment from ice melt into a lake or marine environment or suspension fallout from cyclic meltwater pulses. Hydroplastic deformation occurs through slumping and dewatering. Some of the coarse material may be destabilized glacigenic debris that accumulated proglacially on a basin ramp and moved downslope by mass flow processes	Fluctuating ice-proximal to ice-distal environment as floating ice-shelf expands and retreats
	Rhythmites	Rhythmically interstratified claystones and siltstones with dispersed gravel, dropstones, deformed bedding and microfaults	Influx of sediment into the lake or shallow sea environment under strongly seasonal (varved) or other periodic discharge, gravel indicates ice-rafted debris	
	Mudrocks with outsized dispersed clasts	Laminated mudstone with dropstones and soft-sediment deformation such as loading	Water-saturated sediments and the remobilisation of sediment suggest rapid deposition such as meltwater plumes (Henry et al. 2012). The fine sand and mud were likely deposited by meltwater plumes and waning turbidity currents in a sea or lake floor setting with coarse debris dropped or dumped from	

(continued)

Table 4.1 (continued)

Facies association	Lithologies	Sedimentology	Depositional environment, characteristic sedimentary processes	Glacial regime and grounding line proximity
			floating ice (ice-rafted debris). Sand aggregates may record fall of frozen sand masses through the water column	
	Coarse ash tuff	Granules in mudstone, no grain size grading	Subaqueous pyroclastic fallout from distal source	
Black Rock Member, Port Sussex Formation	Anoxic black mudstones	Lamination, dropstone-free, rare borings	Suspension settling, rare signs of bioturbation	Glacial retreat and development of sediment starved open water conditions

This sedimentological analysis characterises and interprets changes in depositional processes and environments documented in the logs over the icehouse to greenhouse transition. Relevant references are cited in the text as appropriate to the discussion of this summary

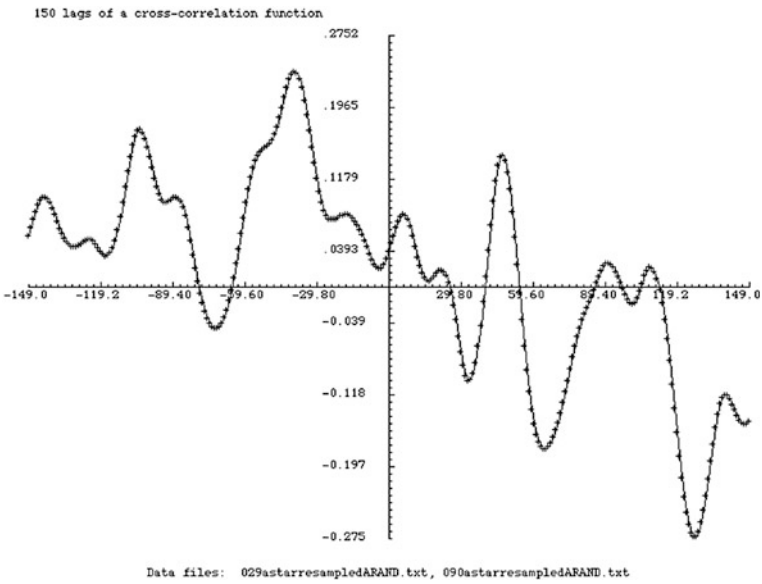

Fig. 4.1 Measure of the correlation between the two cores based on the a* reflectance parameter

single step on the analyseries programme used. The purpose of this exercise was to find how closely the sediments of the two cores were correlated and if there was an offset in time that would improve the stratigraphic correlations. Smoothing the data sets improved the correlation between them by a factor of two (see preliminary autocorrelation in the appendix) but it is still low (coefficient $\sim$0.24). The positive peak at $\sim$40 kyr could suggest that a 40 kyr offset of one of the cores would improve the correlation the most. However, it is likely that the autocorrelation was affected by finer-scale sedimentary changes (e.g. on the obliquity and precession scales) and the age modelling thus far does not attempt to match cycles at these scales (see Sect. 4.4.3). Finer-scale age modelling would improve the correlation between the two sites, although increasing the risk of artificial enhancement of the match.

4.2 Lacustrine Versus Marine Environment

The depositional environment in East Falkland during the Permo-Carboniferous has previously been suggested to have been marine. Frakes and Crowell (1967) claimed that the presence of poorly sorted turbidites, the lack of laminated layers and the great thicknesses of associated diamictite supported this interpretation. Stone et al.

(2005) also suggested a terrestrial to glaciomarine facies transition occurred across the Falklands microplate based on fieldwork studies of the Fitzroy Tillite. Interstadial phases in the Dwyka Group have also been characterised as brackish–marine conditions according to the stratigraphic distribution and abundance of marine fossils, ichnofauna and geochemical salinity proxies (Bangert et al. 2000; Scheffler et al. 2003).

However, on the basis of these Falkland Island cores, there is no clear evidence that the deposits are marine. Instead, the finely laminated varve-like layers lend themselves better to an interpretation involving a lacustrine environment. Further, there is no hummocky or swaley cross-stratification which might be expected in a wave-dominated environment and there is no palæontological evidence for marine conditions; the borings and tentative burrows noted do not verify either environment. In support of a lacustrine hypothesis, Simões et al. (2012) described non-marine bivalves and identified leaf fossils belonging to *Glossopteris* sp. cf. *G. communis*, in the Middle Permian strata of the Falkland Islands. It therefore seems logical to infer that the preceding strata found in the cores were also deposited on land. Further support for the lacustrine hypothesis comes from Trewin et al. (2002) who noted trace fossils in the Brenton Loch Formation belonging to Late Palæozoic typically freshwater lacustrine ichnofacies. These compared well with Late Carboniferous forms from lake deposits in Argentina (Buatois and Mangano 1993, 1995; Acenolaza and Buatois 1993). Simões et al. (2012) also note that morphologically similar bivalves are found in Permian freshwater deposits of Tanzania, South Africa and the Ohio Range Antarctica, all of which formed part of the same Gondwanan sedimentary province. In addition, *Botyrococcus* spp., a fresh to brackish water algae, was found to occur in the Kuhlan Formation in Yemen (Stephenson and Kader Al-Mashaikie 2011). The absence of marine macrofauna in Yemen, coupled with the presence of palynological assemblages dominated by continental spores and fauna, therefore favours a glaciolacustrine rather than a marine depositional setting here also (Osterloff et al. 2004). In South Africa, Visser (1987) found no marine forms in the Eastern Cape Province. In situ *Glossopteris* foliage found in Permian strata of the Ellsworth Mountains, West Antarctica (Taylor and Taylor 1992), would also support a lacustrine environment with the terrestrial lithologies immediately overlying the transitional strata.

Figure 4.2 summarises how a lacustrine environment might have developed and led to the formation of the deposits observed. The location of the lake in the Late Palæozoic tectonic configuration is marked tentatively in Fig. 4.3. In the reconstruction of Veevers et al. (1994) a shallow sea lay to the west of South Africa and an arm of the sea extended east into the Karoo about as far as Ecca Pass area, an embayment formed during glacio-eustatic transgression; this might explain the marine–brackish fossils in the Dwyka Group.

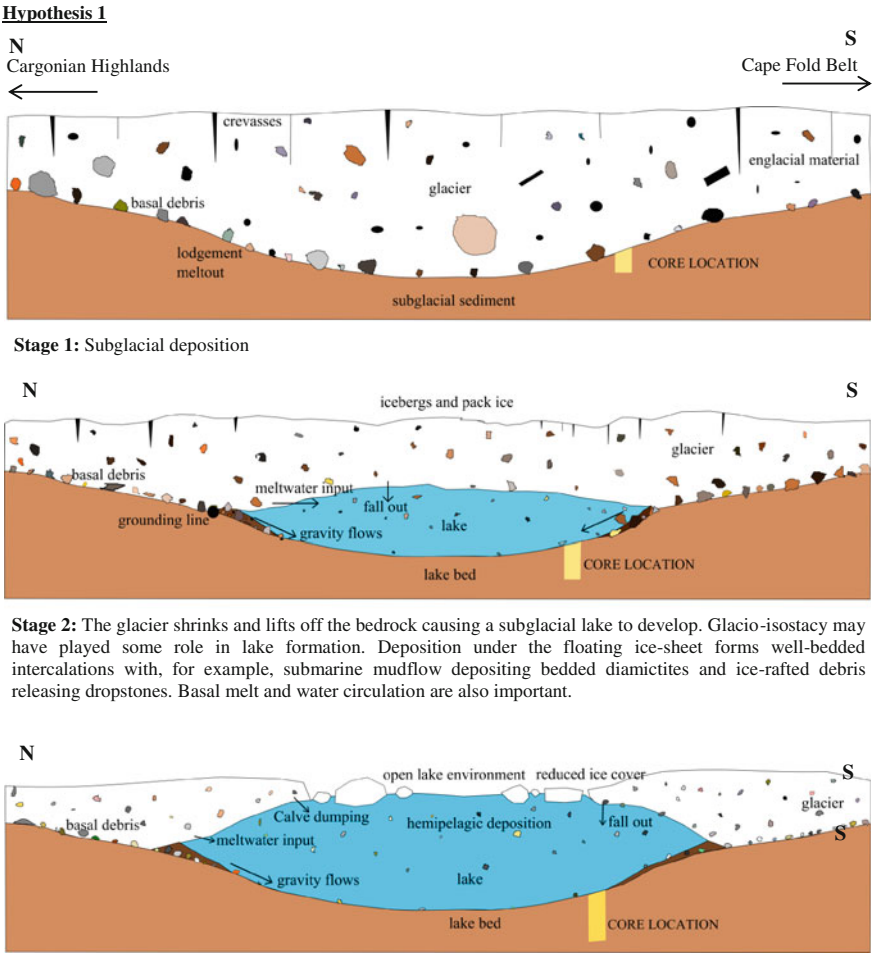

Fig. 4.2 Deposition of core sequence in a subglacial lacustrine environment. An analogue for this facies interpretation might be Lake Agassiz, which developed during the Wisconsin Glacial in North America. Diagrams are not to scale

Another potentially important aspect of the Fitzroy Tillite cores is the evidence therein for soft-sediment deformation. This can be indicative of a supraglacial lake environment due to the continuous meltout of underlying ice and ice walls (Benn

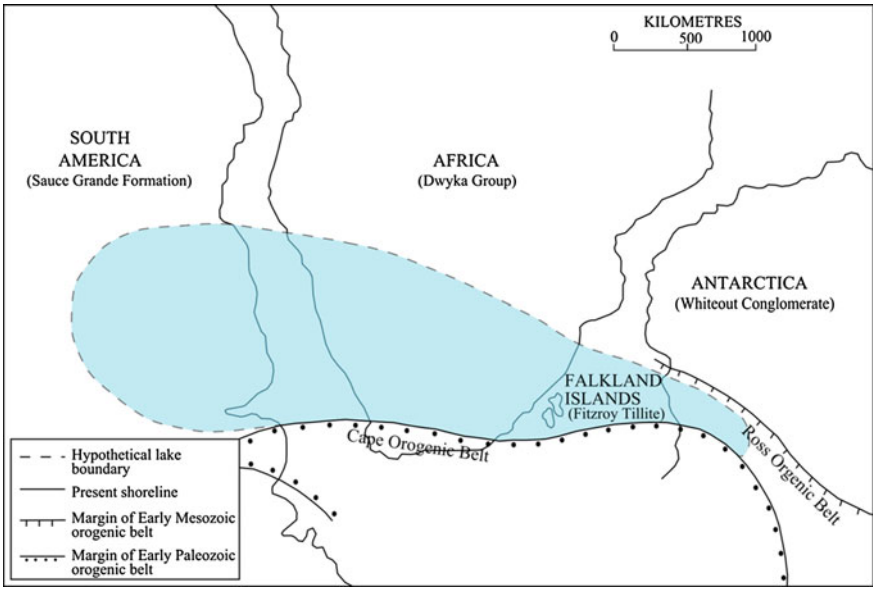

Fig. 4.3 Large subglacial lake envisaged is shown here bounded to the south by the Cape Orogenic Belt. Outline of continents after Crowell and Frakes (1972)

and Evans 2010). However, this second hypothesis (Fig. 4.4) can be rejected on the basis of abundant dropstones in the Hells Kitchen Member. A third hypothesis is a marine environment (Fig. 4.5).

4.3 Phases of Glacial Activity

Many reconstructions of the LPIA (e.g. Veevers and Powell 1987) invoke a single long-lived ice sheet, $\sim 150 \times 10^6$ km^3 (Fig. 1.5). More recent research into the direct, ice proximal record of glaciation (e.g. Isbell et al. 2003) instead suggests it was less spatially extensive and occurred in shorter discrete intervals (during the Mississipian, Pennsylvanian and Early Permian). Although most reviews of the LPIA suggest it collapsed during the Late Early Permian, the eastern Australian record shows persistence of glacial conditions for a further 20 myr (Birgenheier et al. 2010). Figure 4.6 summarises how understanding of the LPIA developed. Figure 4.7 explores the evidence across the various fragments of Gondwana that supports the most recent account, which is detailed in box 4 of Fig. 4.6.

Hypothesis 2

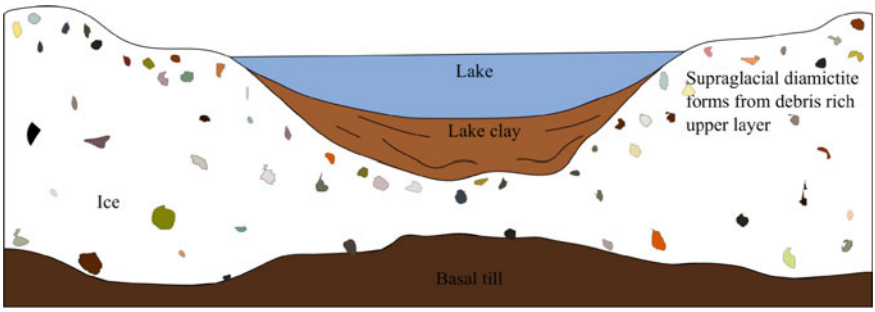

Equivalent Stage 2 on figure 4.2: During glacier wastage, large volumes of meltwater become dammed between the ice margin and local topography. This results in the development of supraglacial lakes into which stratified sediments and mass flow diamictites can accumulate (Eyles et al.1987; Schomacker and Kjær 2008).

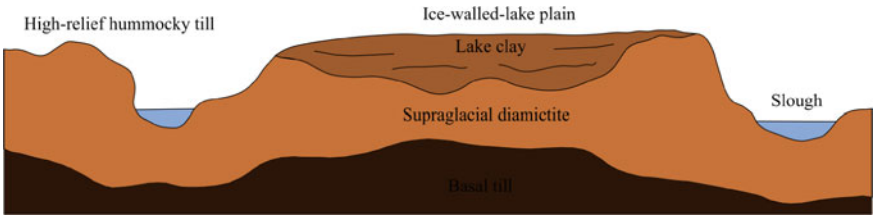

Equivalent stage 3 on figure 4.2: Sedimentary sequences and structures observed in a supraglacial lake comprise thick units of inter-stratified sorted sediments and diamictite. The dominant grain size varies with distance from the sediment influx point so upward-fining sequences from stratified diamictite to rhythmites reflect increasingly distal sedimentation as ice recedes from the basin. Ablation of the ice results in various degrees of disturbance of the sediment pile either post or syndepositionally.

Fig. 4.4 Alternative lake interpretation for stages 2 and 3. The thick lake infill shows the lake plain was probably stable, so glacier melting was probably slow (adapted from Benn and Evans 2010)

4.4 Understanding the Cause of the Facies Changes

4.4.1 Overview

The evolving configuration of continents about the South Pole has been suggested to be the first order cause of the LPIA (e.g. Blakey 2008). However, although the South Pole lay over Gondwana from the Late Proterozoic until the Early Triassic, Gondwana did not have extensive glacial events throughout the Palæozoic so other factors must have been at play. Veevers and Powell (1987) argued that uplift in South America and Australia and the closing of the Palæo-Tethys-Rheic Ocean were important. Eyles (1993) suggested atmospheric CO_2, temperatures of the global continents, long-term Milankovitch controls, volcanism and tectonic supercycles might have been significant too. The general circulation model of Horton et al. (2012) suggests atmospheric pCO_2 concentration exerted the primary control on

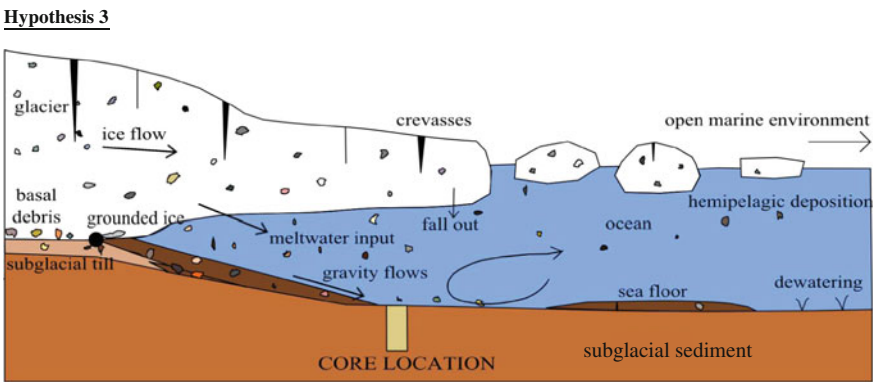

Fig. 4.5 Deposition in an ice-proximal marine environment under a floating ice sheet, equivalent to stages 2–3 in Fig. 4.3. This interpretation fits with that of Frakes and Crowell (1967) for East Falkland. The basin requires a moderately steep gradient to accommodate the Hells Kitchen Member sequence; in Sect. 4.4.3, this is calculated to span ~1.2 Ma. Perhaps strong discharges of freshwater from melting of the ice masses in this coastal setting could explain freshwater fauna found by other researchers e.g. Trewin et al. (2002)

high-latitude Late Palæozoic continental ice sheets. The model indicates that within 840 ppm < pCO_2 < 420 ppm, high-latitude glaciers waxed and waned (by up to 33 m in sea-level equivalent) in response to orbital insolation fluctuations. However, it does not consider continental landmass distributions. When eccentricity is high, precessionally driven changes are amplified and seasonal variability is increased but when eccentricity is low, precessional changes are damped, seasonal variability remains relatively constant and high-latitude continental ice sheet stability is promoted. Significant ice sheet volume increases occurred during anomalously cold Southern Hemisphere summer orbits (high eccentricity, low obliquity and Southern Hemisphere summer solstice at aphelian) whereas ice sheet volume decreases coincided with anomalously warm Southern Hemisphere summer orbits (high eccentricity, low obliquity and southern hemisphere summer solstice at perihelion).

4.4.2 A Role for Orbital Forcing? Milankovitch Theory and its Application in the Carboniferous

To understand the climatic history of the Earth, it is important to understand accurately its orbital evolution. Milankovitch cycles with current periodicities ~23 kyr (precession), ~41 kyr (obliquity), ~100 (eccentricity) and ~400 kyr (eccentricity) are the orbital parameters that modulate ice age climate (Hays et al. 1976; Schwarzacher 1993; Ruddiman 2003). Eccentricity modulates the amplitude of the precessional cyclicity and leads to summer temperature maxima and minima

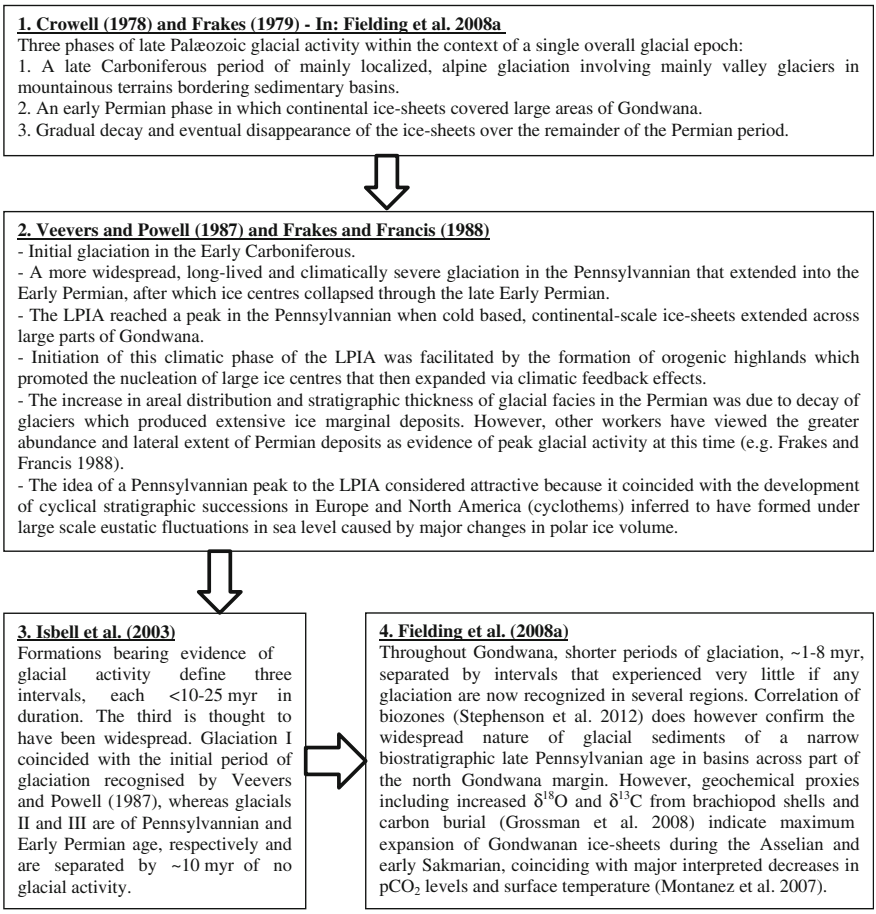

Fig. 4.6 Flow diagram summarising how understanding on the LPIA developed based on information supplied in Fielding et al. (2008a), Veevers and Powell (1987), Frakes and Francis (1988), Isbell et al. (2003), Grossman et al. 2008, Stephenson et al. (2012) and Montanez et al. (2007)

in the high latitudes. Uncertainties in the orbital calculations mean that the precise orbital solution for the Earth may be limited to 35–50 Ma (Laskar 1999). The 400 and 100 kyr eccentricity periods are the product of interplanetary gravitational forces so have probably remained stable through at least the last 600 myr (Walker and Zahnle 1986). By contrast, the 41-kyr obliquity and 23-kyr precession cycles depend partly on the precession of the equinoxes. Approximation of orbital palæoperiods indicates that obliquity period was ~35 kyr in the Carboniferous (Levrard and Laskar 2003).

Energy balance models have indicated that supercontinents are very sensitive to Milankovitch fluctuations (Crowley et al. 1993) and Milankovitch cyclicity has previously been identified in Permo-Carboniferous sediments. Periodic variations in

Earth's orbit and consequent variations in the amount and pattern of solar insolation received at the surface influence climate and sedimentary deposits. For example, 5–10 m thick Carboniferous cyclothems have been related to orbitally driven glacioeustatic changes associated with waxing and waning of Gondwanan ice sheets in the Southern Hemisphere at eccentricity frequencies 100 and 400 kyr (Heckel 1986; Wright 1992). Permo-Carboniferous rhythmites from the Paraná Basin, southeastern Brazil (Franco et al. 2012) and several formations in eastern Australia, such as the Lower Permian Pebbly Beach Formation also have strong indications of Milankovitch components.

This section explores the possibility that the cyclical processes encoded in the sediments of East Falkland may be understood in terms of Milankovitch cyclicity. This seems plausible because the log, clast, XRF and reflectance records from the Hells Kitchen Member show some cyclicity on the scale of metres. If Milankovitch forcing is able to provide a physical framework for explaining the output signal of the climate system at this time, this will also help constrain the duration of the record and clarify the geophysical and climatological mechanisms involved. The results of this investigation are presented below.

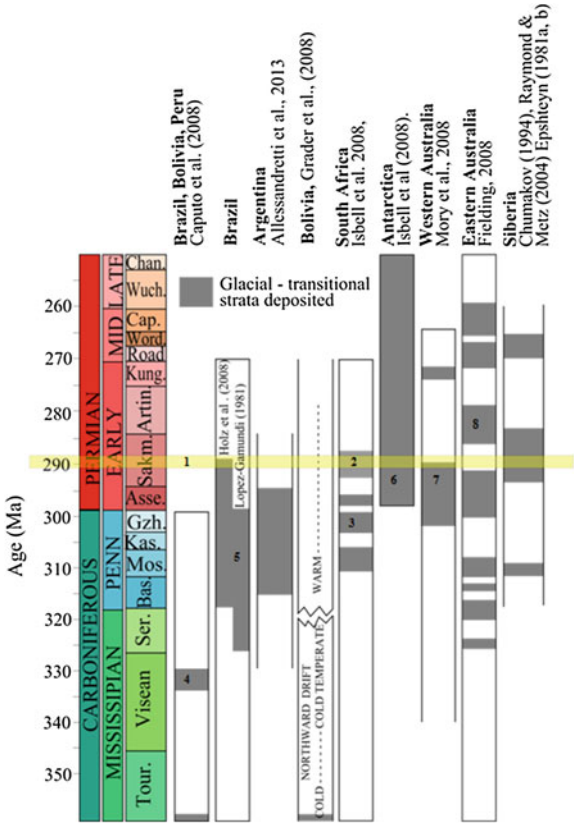

◀**Fig. 4.7** Summary of the series of short glaciation events, ~1–8 myr in duration, in the LPIA, adapted from Fielding et al. (2008a). Fielding et al. present evidence for eight discrete glacial intervals in the Permo-Carboniferous based on Eastern Australian strata (Grossman et al. 2008). Stratigraphic records suggest that the LPIA began with short-lived localised glacial events in South America during the Late Tournasian and the Visean. These events were followed at the start of the Serpukhovian by ice expansion into other areas of Gondwana. At the start of the Bashkirian, ice expanded further across South America and Australia and at the start of the Moscovian, into southern Africa. This accounts for the diachroneity of glacial episodes. A large expansion of ice occurred at the Pennsylvanian–Permian boundary and glaciation became bipolar (Fielding et al. 2008a). However, the exact timing of waxing and waning of ice centres during each glacial episode will have been influenced by basin dynamics, topographic barriers, glaciation styles and other local factors. Abbreviations used in this figure: *Penn* Pennsylvanian, *Ser.* Serpukhovian, *Bas.* Bashkirian, *Mos.* Moscovian, *Kas.* Kasimovian, Gzhelian, *Asse.* Asselian, *Sakm.* Sakmarian, *Artin.* Artinskian, *Kung.* Kungurian, *Road.* Roadian, *Word.* Wordian, *Cap.* Capitanian and *Wuch.* Wuchiapingian, *Chan.* Changhsingian. *1* The *yellow band* denotes the region within which the cores of this study lie. There were no further glaciations in the Falklands as shown by the very fine clay that continues above the Hells Kitchen Member, noted on sample collection at BGS. The limestone clasts from Antarctica also suggest that the record in these cores coincided with the occurrence of ice in Antarctica although the clasts could have come from recycling of earlier glacial deposits. *2* Lower Permian Dwyka Group of South Africa has been divided into four upward deglaciation sequences, each up to 350 m thick and of 5–7 myr duration and each capped by glaciolacustrine or glaciomarine deposits. The longer duration of the Dwyka cycles compared to the Pleistocene (~1.8 myr) could suggest a tectono-eustatic cause, or they may represent composite records of multiple glacial cycles. *3* There may be as many as four deglaciation sequences in the Falkland Islands but more evidence is required to validate this. Sedimentary dykes filled with diamictite in West Falkland are one of the oldest records of Gondwanan glaciation (Hyam et al. 1997). Two dykes dated using palynomorphs were found to be of Late Visean to Sakmarian age, which is older than the Fitzroy Tillite (Permian). The assemblage is also different and older than the Dwyka in South Africa but the similar and internally consistent nature of the dyke spore assemblages suggests they were not reworked from strata eroded before the main onset of glacial sedimentation. Comparable microfloras are described from the Carboniferous of Australia. *4* Three glacial episodes are identified in the Upper Devonian and Mississippian strata in South America. The earliest evidence for glaciation is a short-lived event at the end of the Famennian (Upper Devonian) in Brazil, Peru and Bolivia (Caputo et al. 2008). The second episode is of late middle to early late Tournaisian age and the third of Visean age. Western Gondwana underwent a steady drift from mid-latitudes (~50S) in the Early Carboniferous to lower latitudes (<40S) by Late Carboniferous time, and glacial deposition had ended in Bolivia by the early Pennsylvanian (Morrowan). *5* In Brazil, late Palæozoic glacial deposits are preserved in the Parana Basin showing multiple glacial intervals over the period from the base of the Serpukhovian to the top of the Gzhelian, an interval of ~27 myr. Holz et al. (2008) define three major glacial cycles. *6* The occurrence of multiple diamictites within the Antarctic succession led to the suggestion that four to six major glacial-interglacial cycles occurred during the Lower Permian, with possibly as many as 13 minor advances and retreats of the ice front across the Transantarctic Mountains. In Antarctica, late Palæozoic glaciogenic strata occur throughout the Transantarctic, Ellsworth and Pensacola Mountains and in the Shackleton and Heimefrontfjelles (Isbell et al. 2008b). The glacial record in the Transantarctic Mountains of Antarctica is restricted to the Lower Permian; the base of the Asselian to lower Sakmarian (Isbell et al. 2003). A correlation of fossil spores and pollen with Australian palynomorph zones suggests that the Antarctic glacigenic strata are restricted to the Lower Permian. *7* In Eastern Australia, eight discrete glacial intervals, 1–8 myr in duration, have been recognised (Fielding et al. 2008b) spanning c. 327–260 Ma (Asselian through Capitanian time). The timing and duration is consistent with interpreted minima in atmospheric pCO_2 and surface temperature inferred from mineralogical proxies (Montanez et al. 2007), with turnovers in palæobotanical assemblages from Euramerica (e.g. Gastaldo et al. 1996), and to an extent with interpreted sea-level trends (Rygel et al. 2008). *8* Multiphase glaciation in Western Australia from the Gzhelian to the mid-Sakmarian and a shorter discrete glaciation straddling the Artinskian-Kungurian boundary. All Palæozoic basins in Western Australia contain extensive Permo-Carboniferous deposits

4.4.3 Development of an Age Model

Data on an overlapping depth scale were used in preliminary spectral analyses to look for any prominent periodicities in depth (see Appendix A.2). On the basis of peaks plausibly corresponding to eccentricity periods (Fig. 4.9), it seemed reasonable to place age control points at least at the beginning and end of the sequences. To do this, the a* reflectance data were plotted alongside a synthetic 'Carboniferous ETP', representing the patterns of orbital variation that could be encountered in an orbital geometry with a more rapid ~35 kyr obliquity cycle (Fig. 4.8). The actual orbital variations for the Carboniferous cannot be calculated because of uncertainties in the orbital solution before about 50 Ma. However, the synthetic 'Carboniferous ETP' is intended to provide an impression of how the combination of cyclicities in the Carboniferous might appear in a climate record that, like the Late Pleistocene, might have a strong 100 kyr component, but in this case with a higher frequency obliquity component. Aspects such as details of the amplitude modulation of the 100 kyr component are likely to be incorrect. If appropriate, this transformation transfers the records from the depth domain to the time domain enabling the rate of the climatic transition to be hypothesised. Interpreting the large-scale cycles as 400 kyr cycles means that the implied accumulation rates fall between 5.6 and 13.5 m/Ma. This appears a reasonable estimate (Algeo and Wilkinson 1998) given that these old sediments must have undergone a considerable degree of compaction since the Carboniferous–Permian time (e.g. Arthur and Garrison 1986).

Two additional control points were inserted into the core DD029 record using Analyseries software in the places where maxima in the a* data coincided with a minima in insolation, to attempt to correct for some of the depth distortion. Stretching and squeezing of the record were considered justified because sedimentation rates would not have been linear throughout the cores. They would have

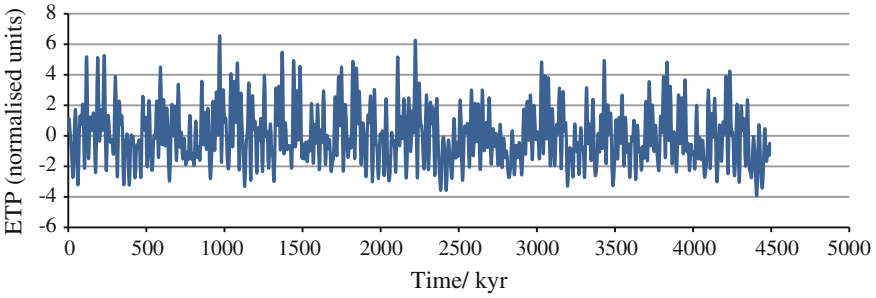

Fig. 4.8 Synthetic Carboniferous orbital solution including eccentricity, obliquity and precession (*ETP*). The obliquity (only) was shortened to a 35 kyr central periodicity, then resampled at 1 kyr intervals, and the Southern Hemisphere precession cycle was used (the precession cycle is out of phase between the two hemispheres). ETP (eccentricity, tilt and precession) cycles were chosen to create the forcing signal because the effect of the eccentricity cycle, the main cycle of interest, is under represented in insolation forcing

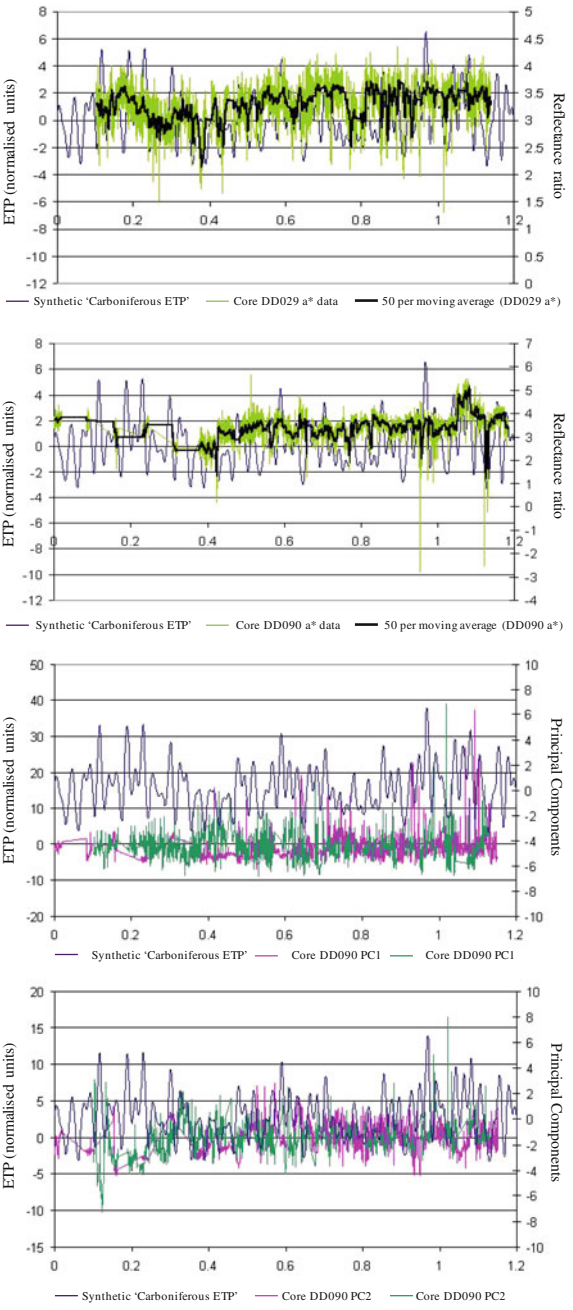

Fig. 4.9 Alignment of a* reflectance data and PC1 and PC2 against the synthetic 'Carboniferous ETP' to show how the age model was developed. The *x*-axis represents time in millions of years

Table 4.2 Table showing the accumulation rates implied by the age model in the two cores based on the insertion of two age control points in core DD090 and four in core DD029

	Depth range (m)	Accumulation rate (m/Ma)
Core DD029	173.00–175.59	9.4
	175.59–179.75	5.6
	179.75–183.56	9.5
Core DD090	374.85–395.1	13.5

varied depending on the original debris content of the icebergs as well as on the size, melting rates and flux of the icebergs. Higher rates of accumulation are generally associated with proximity to the grounding line (Matsch and Ojakangas 1992). The accumulation rates used are given in Table 4.2.

This exercise attempted to understand the short duration cyclicity that operated over the transition (refer to Fig. 1.1) with reasonable success. If the 400 kyr Milankovitch cycles were correctly identified, this astronomical tuning should be a fairly robust means of age-depth determination since there are no major erosional hiatuses in these cores; although there may be non-depositional episodes. However, it is still important to be cautious since factors independent of orbital modulation that affect cycle thickness and sedimentation rate could be important (Algeo and Wilkinson 1998). The Milankovitch-cycle paced changes in climate suggested do not account for all the sedimentological variability. Some variability arises from autocyclic depositional processes, periods of non-deposition, the changing morphology of the ice sheet/shelf and underlying tectonic processes such as mountain building during the Gondwanan orogenic phase. Stochastic deposits such as turbidites are the most likely cause of error here. The varves which capture the interannual climate variability could help constrain the age model further if it can be proven that they are seasonal lacustrine deposits rather than tidal cycles (see Chap. 5). Perhaps complexities inherent to orbital parameters such as the harmonics of Milankovitch cycles or differences related to regional climate were important also.

4.4.4 Principal Component Analyses

PCA is a simple, non-parametric method for reducing complex high-dimensional data sets to more manageable, lower dimensional linearly uncorrelated forms without losing too much information. The technique can help filter out noise and reveal underlying simplified structures in terms of the main causes of variance. A PCA was run using 'SPSS' software. Silver and tin were excluded from the multi-element XRF data sets prior to this analysis because they are present in the detector. Elements, such as iron, that were measured at more than one energy band were only considered once to avoid weighting the analysis. Further details on the PCA method are outlined in Box 4.1. The output correlation matrixes and factor tables with loadings are shown in Appendix A.3.

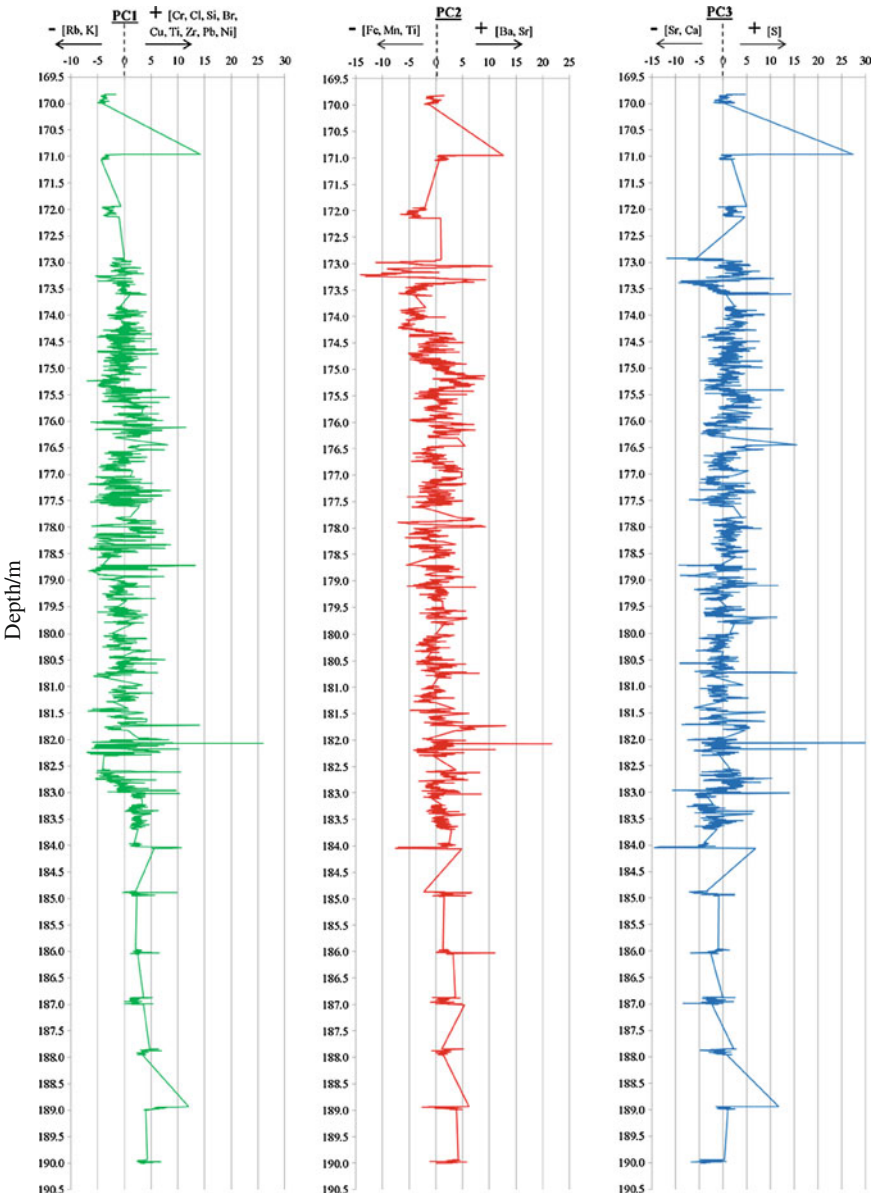

Fig. 4.10 Core DD029 PCA results

The results are presented in Figs. 4.10 and 4.11 together with annotations showing the elements loading positively or negatively on the components. PC1 seems to be responding to grain size since elements such as Rb and K, common to clays, peak in the fine-grained zones. Positive excursions correlate with most of the

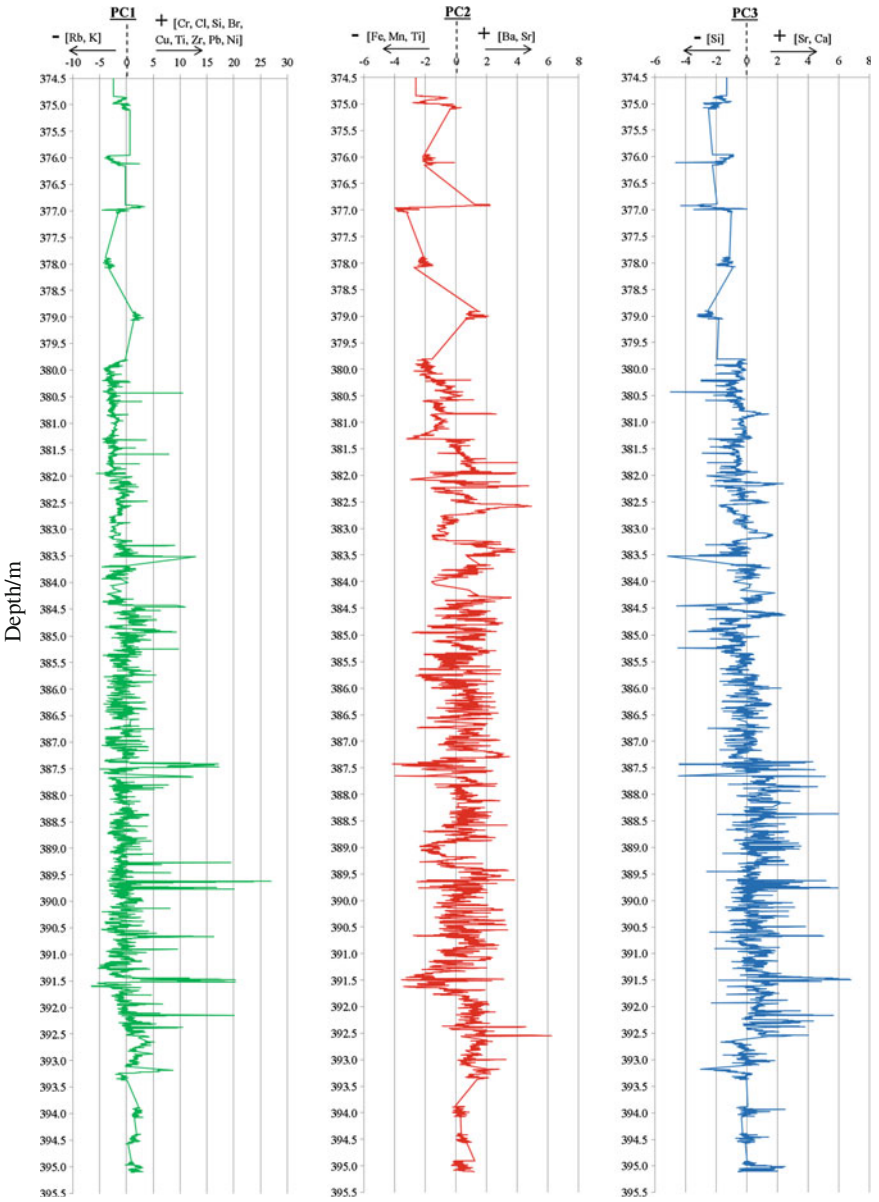

Fig. 4.11 Core DD090 PCA results

other elements found in higher abundance in the coarse beds. However, there are also sharp peaks associated with veins. PC2 seems to be related to redox processes with elements Fe, Mn and Ti loading negatively against Ba and Sr. PC3 shows positive loadings on Sr and Ca. These elements are linked since Sr may substitute

for Ca in dolomitisation, and so this principal component may characterise carbonate; it also shows sharp excursions at veins. PC4 and PC5 account for little of the variance and had noisy traces. They may be related to noise introduced through sanding during sample preparation or biases from clast compositions.

Box 4.1: Principal Component Analysis in More Detail
The projection of the original data vectors may be summarised into fewer directions and principal components, which span the subspace. The principal components are derived by finding the projections which maximise the variance. The first principal component is the direction in feature space along which projections have the largest variance and each succeeding component has the highest variance possible under the constraint that it is orthogonal to (i.e. uncorrelated with) the preceding components (Shlens 2009). Therefore, the second principal component is the direction orthogonal to the first component with most variance. Selecting orthogonal directions for principal components is the best solution to predict the original data. PCA assumes linearity which restricts the set of potential basis vectors.

The principal components of the XRF elemental data are the eigenvectors of the covariance matrix of the data. The eigenvalues (provided in the appendix) are proportional to the portion of the 'variance' (the sum of the squared distances of the points from their multi-dimensional mean) that is correlated with each eigenvector. Component scores are the transformed variable values corresponding to a particular data point, and loadings are the weight by which each standardised original variable should be multiplied to get the component score. Sometimes the components do measure real variables but sometimes they just reflect patterns of covariance which have many difference causes. The measurement of the variance along each principal component provides an opportunity to compare the relative importance of each dimension. The covariation matrix measures the degree of the linear relationship between two variables. A large positive value indicates positively correlated data, and a large negative value denotes negatively correlated data. An explanation was attempted for the first three principal components, any interpretation of other factors becomes increasingly speculative.

4.4.5 Wavelet Analyses

Palæoclimate signals vary in both amplitude and frequency over long periods of time. Wavelet analysis attempts to solve these problems by decomposing the data into time/frequency space simultaneously; thus, it can be applied to geological records that are proxies of palæoclimatic variations (Liu and Chao 1998). It provides information on the amplitude of any periodic signals within the series and how this amplitude varies with time (Box 4.2). Wavelet analyses were run using

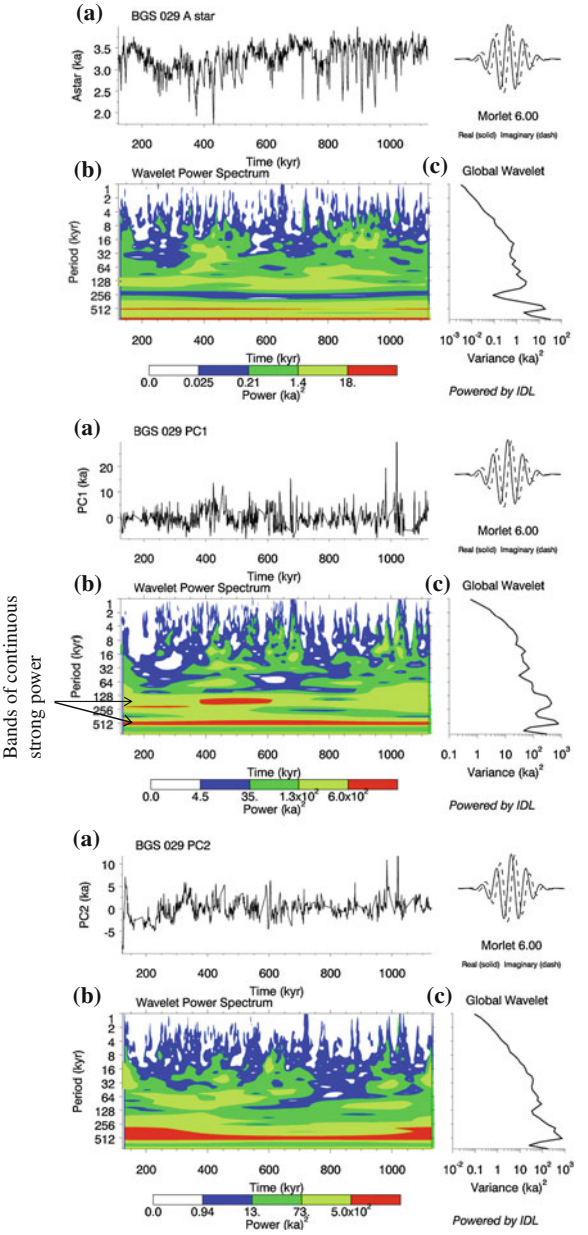

Fig. 4.12 Wavelet analyses on the a* parameter, PC1 and PC2 for core DD029. In each case, **a** is the timeseries, **b** is the wavelet power spectrum, using the Morlet wavelet. The *x*-axis is the wavelet location in time. The *y*-axis is the wavelet period in kyr and **c** is the spectral analysis showing the power of frequencies in the core

online software developed by Torrence and Compo initially on the a* and L* reflectance data (see Appendix A.2). Subsequently, on improved depth scales, they were applied to the PC1 and PC2 and a* data over depths 380.035–390.398 m ('0.384–1.1514 Ma') and 173–183.2 m ('0.1–1.14 Ma') for cores DD090 and DD029 respectively. The diamictite was inappropriate to use because it was a

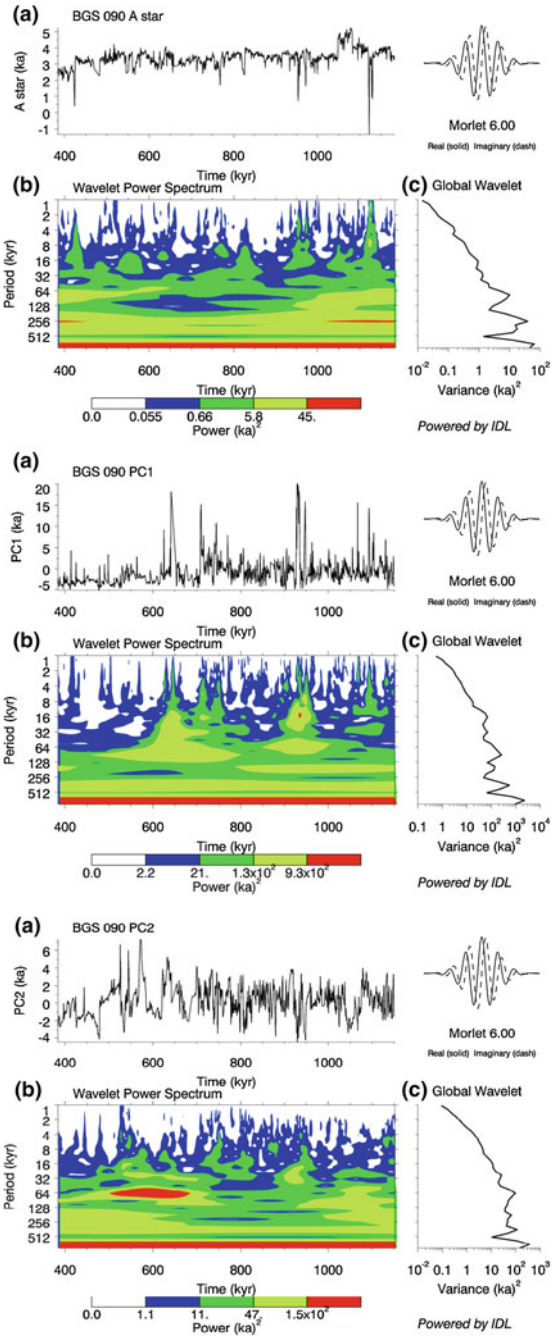

Fig. 4.13 Wavelet analyses on the a* parameter, PC1 and PC2 for core DD090. *Note* over the time interval used, there could not be more than two full 600 kyr cycles so the strong power at 600 kyr must be an edge effect. Edge effects degrade the reliability of the signal at the edge of the plot

sudden dump of material and was incomplete. Some of the Black Rock Member was also excluded due to its incomplete nature. The purpose here was to see how much of the observed climate variability could be accounted for by considering the period and amplitude modulations of the orbital forcing parameters. The results are shown in Figs. 4.12 and 4.13.

Box 4.2: Wavelet Analysis
Wavelet analysis works by using a variety of window sizes to build a picture of the changes in variance versus both time and window width. Frequency localisation is good at low frequencies, and time resolution is good at high frequencies. A wave packet of finite duration and with specific frequency can be used as the window function for the analysis of variance; this wavelet has the advantage of incorporating a wave of a certain period, as well as being finite in extent. The Morlet wave used here is a sine wave multiplied by a Gaussian envelope. By sliding this wavelet along the timeseries, it was possible to construct a new timeseries of the projection amplitude versus time. The scale of the wavelet was varied by changing its width; the size scaled up or down with the size of the window though its shape remained constant. The problem with this technique is that the box shape of the window introduces edge effects. The plots show the power (absolute value squared) of the wavelet transform. The $(\text{absolute value})^2$ gives information on the relative power in terms of periodicity at a certain time. The wavelet analysis also plots a power spectrum to describe the data in the frequency domain similar to the spectral analyses used in the preliminary investigation (Appendix A.2).

The results indicate that PC1 and PC2 have strong power in bands where 100 and 400 kyr periodicities would lie. Hence, the geochemical variation is compatible with an interpretation of climatic changes induced by Milankovitch forcing. The identification of cyclicity in these old records does not appear to have been hindered by diagenesis, such as compaction and cementation, which alter the original chemical and stratigraphic relationships across cycles. Further, although there is poor constraint on the absolute timescale for this sequence and limited determination of orbital variations older than 50 Ma adds further ambiguity, the results still provide a tenable timeframe over which this large climatic transition may have taken place (1.2 Ma). The age models are themselves deliberately simple and while they may be the best currently supported by the internal evidence of the cyclicities in the cores, this does not rule out the possibility of improvement or even major revision. For example, the section around '500–900 kyr' in core DD090 may be too compressed since the band of strong 100 and 400 kyr power deviates around this region. Perhaps the core DD029 record had the most striking power bands because it already had two extra control points in this central region.

In summary, this section emphasises the likely importance of external orbital forcing in controlling the phase, amplitude and frequency of the climate signal over

the course of the transition. The combined effect of the duration and intensity of insolation variations arising from orbital eccentricity in particular appears to be a key component. However, orbital forcing probably operated in conjunction with glaciological processes to drive the climate system. For example, the build-up of unstable ice sheet regimes, following an intense and prolonged glacial state, may have played a dynamic and pivotal role and led to self-sustained oscillations. Carbon cycle changes tied to abrupt millennial climate perturbations could have served secondary amplifying roles. Since both external and internal factors operate simultaneously, it becomes difficult to tease apart which are critical for driving the climate system, which serve as feedbacks and those which play little role. Some factors may also have had varying importance through time. The superposition of stochastic processes on the system increases the potential complexity and scope of the problem.

4.5 Demise of the Ice

Widespread collapse of ice sheets occurred in the Early Permian (mid-Sakmarian) with the onset of rising atmospheric CO_2 levels (López-Gamundí and Buatois 2010), though glaciation continued intermittently in Australia and Siberia throughout the Late Early and Middle Permian (Fig. 4.14) (Montanez et al. 2007). The transition to a relatively ice-free world, which was sustained until the Late Pleistocene, probably occurred once a CO_2 threshold had been reached and

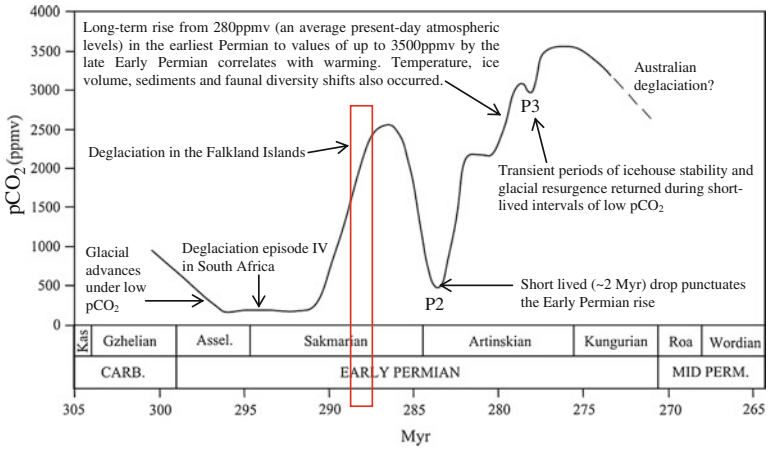

Fig. 4.14 pCO_2 history across the icehouse to greenhouse transition, adapted from Montanez et al. (2007). Stable isotope compositions of soil-formed minerals, fossil-plant matter and shallow water brachiopods were used to estimate pCO_2. The *red box* outlines the time over which the ~1.2 Ma deglaciation sequence in the Falklands accumulated. P2 and P3 refer to the Permian Australian glaciations 2 and 3

greenhouse stability precluded the reestablishment of glacial conditions. However, the diachroneity of glaciation across Gondwana means the demise of glaciation could not have been solely caused by global pCO_2. It is possible that the drift of the continents was the final trigger out of the icehouse state (Frank et al. 2008). Further, the glacier waxing and waning cycles observed in these cores took place when pCO_2 was high so another mechanism, probably orbital forcing, was at play throughout the transition. The upper part of deglaciation sequence 4 in the Karoo Basin coincides with the oldest event associated with the Cape orogeny (dated at 292 ± 5 Ma). Therefore, orogenesis may have triggered shelf subsidence and a rapid final collapse of the ice sheets in this part of Gondwana (Isbell et al. 2008a).

References

Acenolaza FG, Buatois LA (1993) Nonmarine perigondwanic trace fossils from the late Palæozoic of Argentina. Ichnos 2:183–201

Algeo T, Wilkinson BH (1998) Periodicity of mesoscale phanerozoic sedimentary cycles and the role of Milankovitch orbital modulation. J Geol 96:313–322

Arthur MA, Garrison RE (1986) Cyclicity in the Milankovitch band through geological time: an introduction. Palæoceanography 1:369–372

Bangert B, Stollhofen H, Greiger M, Lorenz V (2000) High resolution tephrostratigraphy, fossil record and age of Carboniferous-Permian glacio-marine mudstones within the Dwyka Group of southern Namibia. Commun Geol Surv Namibia 12:235–245

Benn DJ, Evans DJA (2010) Glaciers and glaciation (2nd edn). Hodder Education, Oxford

Birgenheier LP, Frank TD, Fielding CR, Rygel MC (2010) Coupled carbon isotopic and sedimentological records from the Permian system of eastern Australia reveal the response of atmospheric carbon dioxide to glacial growth and decay during the late Palæozoic Ice Age. Palæogeogr Palæoclimatol Palæoecol 286:178–193

Blakey RC (2008) Gondwana palæogeography from assembly to breakup—A 500 m.y. odyssey. Geol Soc Am Spec Pap 441:1–28

Buatois LA, Mangano MG (1993) Trace fossils from a Carboniferous turbiditic lake: implications for the recognition of additional nonmarine ichnofacies. Ichnos 2:237–258

Buatois LA, Mangano MG (1995) Sedimentary dynamics and evolutionary history of a Late Carboniferous Gondwanic lake in north-western Argentina. Sedimentology 42:415–436

Caputo MV, de Melo JHG, Streel M, Isbell JL (2008) Late Devonian and Early Carboniferous glacial records of South America. Geol Soc Am Spec Pap 441:161–173

Crowell JC, Frakes LA (1972) Late Palæozoic glaciation: Part V, Karroo Basin, South Africa. Geol Soc Am Bull 83:2887–2912

Crowley TJ, Yip KJJ, Baum SK (1993) Milankovitch cycles and Carboniferous climate. Geophys Res Lett 20:1175–1178

Eyles N (1993) Earth's glacial record and its tectonic setting. Earth-Sci Rev 35:1–248

Eyles N, Clark BM, Clague JJ (1987) Coarse-grained sediment-gravity flow facies in a large supraglacial lake. Sedimentology 34:193–216

Fielding CR, Frank TD, Isbell JL (2008a) The late Palæozoic ice age—A review of current understanding and synthesis of global climate patterns. Geol Soc Am Spec Pap 441:343–354

Fielding CR, Frank TD, Birgenheier LP, Rygel MC, Jones AT, Roberts J (2008b) Stratigraphic imprint of the Late Palæozoic Ice Age in eastern Australia: a record of alternating glacial and nonglacial climate regime. J Geol Soc London 165:129–140

Frakes LA, Crowell JC (1967) Facies and Palæogeography of Late Palæozoic Diamictite, Falkland Islands. Geol Soc Am Bull 78:37–58

Frakes LA, Francis JE (1988) A guide to Phanerozoic cold polar climates from high-latitude ice-rafting in the Cretaceous. Nat London 333:547–549

Franco DR, Hinnov LA, Ernesto M (2012) Millennial climate cycles in Permian-Carboniferous rhythmites: permanent feature throughout geologic time? Geol Soc Am 40:19–22

Frank TD, Birgenheier LP, Montanez IP, Fielding CR, Rygel MC (2008) Late Palæozoic climate dynamics revealed by comparison of ice-proximal stratigraphic and ice-distal isotopic records. Geol Soc Am Spec Pap 441:331–342

Gastaldo RA, DiMichele WA, Pfefferkorn HW (1996) Out of the icehouse into the greenhouse: a late Palæozoic analogue for modern global vegetational change. GSA Today 10:1–7

Grossman EL, Yancey TE, Jones TE, Bruckschen P, Chuvashov B, Mazzullo SJ, Mii H (2008) Glaciation, aridification, and carbon sequestration in the Permo-Carboniferous: the isotopic record from low latitudes. Palaeogeogr Palaeoclimatol Palaeoecol 268:222–233. http://www.sciencedirect.com/science/journal/00310182

Hays JD, Imbrie J, Shackleton NJ (1976) Variations in the Earth's orbit: pacemaker of the Ice Ages. Science 194:1121–1132

Heckel PH (1986) Sea-level curve for Pennsylvanian Eustatic Marine transgressive-regressive depositional cycles along midcontinent Outcrop Belt, North America. Geology 14:330–334

Henry LC, Isbell JL, Fielding CR, Domack EW, Frank TD, Fraiser ML (2012) Proglacial deposition and deformation in the Upper Carboniferous to Lower Permian Wynard Formation, Tasmania: a process analysis. Palæogeogr Palæoclimatol Palæoecol 315–316:142–157

Holz M, Souza PA, Iannuzzi R (2008) Sequence stratigraphy and biostratigraphy of the Late Carboniferous to Early Permian glacial succession (Itararé Subgroup) at the eastern-southeastern margin of the Paraná Basin, Brazil. Geol Soc Am Spec Pap 441:115–129

Horton DE, Poulsen CJ, Montañez IP, DiMichele WA (2012) Eccentricity-paced late Paleozoic climate change. Palaeogeography, Palaeoclimatology, Palaeoecology 331–332:150–161

Hyam DM, Marshall JEA, Sanderson DJ (1997) Carboniferous diamictite dykes in the Falkland Islands. J Afr Earth Sc 25:505–517

Isbell JL, Lenaker PA, Askin RA, Miller MF, Babcock LE (2003) Reevaluation of the timing and extent of late Palæozoic glaciation in Gondwana: role of the Transantarctic Mountains. Geology 31:977–980

Isbell JL, Cole DI, Douglas I, Catuneanu O (2008a) Carboniferous-Permian glaciation in the main Karoo Basin, South Africa: stratigraphy, depositional controls, and glacial dynamics. Geol Soc Am Spec Pap 441:71–82

Isbell JL, Koch ZJ, Szablewski GM, Lenakerm PA (2008b) Permian glacigenic deposits in the Transantarctic Mountains, Antarctica. Geol Soc Am Spec Pap 441:59–70

Laskar J (1999) The limits of Earth orbital calculations for geological time-scale use. R Soc London 357:1735–1759

Levrard B, Laskar J (2003) Climate friction and the Earth's obliquity. Geophys J Int 154:970–990

Liu H-S, Chao BF (1998) Wavelet spectral analysis of the Earth's orbital variations and Palæoclimatic cycles. Geodynamics Branch, NASA/GSFC, Code 921, pp 227–236

López-Gamundí OR, Buatois LA (2010) Introduction: Late Palæozoic glacial events and postglacial transgressions in Gondwana. Geol Soc Am Spec Pap 468:v–viii

Matsch CL, Ojakangas RW (1992) Stratigraphy and sedimentology of the Whiteout Conglomerate: an upper Palæozoic glaciogenic unit, Ellsworth Mountains, West Antarctica. In: Webers GF, Craddock C, Splettstoesser JF (1992) Geology and Palæontology of the Ellsworth Mountains, West Antarctica, vol 170. Geological Society of America, Memoir, pp 37–62

Montanez IP, Tabor NJ, Niemeier D, DiMichele WA, Frank TD, Fielding CR, Isbell JL, Birgenheier LP, Rygel MC (2007) CO_2-forced climate and vegetation instability during Late Palæozoic deglaciation. Science 315:87–91

Osterloff PL, Al-Harthy A, Penney R, Spaak P, Al-Zadjali F, Jones NS, Knox RWO'B, Stephenson MH, Oliver G, Al-Husseini MI (2004) Gharif and Khuff formations, subsurface Interior Oman. In: Al-Husseini M (ed) Carboniferous, Permian and Early Triassic Arabian stratigraphy, vol 3. GeoArabia Special Publication, pp 83–147

Ruddiman WF (2003) Orbital insolation, ice volume, and greenhouse gases. Quat Sci Rev 22:1597–1629
Rygel MC, Fielding CR, Frank TD, Birgenheier LP (2008) The magnitude of Late Palæozoic glacioeustatic fluctuations: a synthesis. J Sediment Res 78:500–511
Scheffler K, Hoernes S, Schwark L (2003) Global changes during Carboniferous-Permian glaciation of Gondwana: linking polar and equatorial climate evolution by geochemical proxies. Geology 31:605–608
Schomacker A, Kjær KH (2008) Quantification of dead-ice melting in ice-cored moraines at Brúarjokull, Iceland: a transitional state landform. J Quat Sci 21:85–93
Schwarzacher W (1993) Cyclostratigraphy and the Milankovitch theory. Elsevier, London
Shlens J (2009) A tutorial on principal component analysis. http://www.snl.salk.edu/∼shlens/pca.pdf. Accessed 23 Dec 2012
Simões MG, Quaglio F, Warren LV, Anelli LE, Stone P, Riccomini C, Grohmann CH, Chamani MAC (2012) Permian non-marine bivalves of the Falkland Islands and their palæoenvironmental significance. Alcheringa 36:543–554
Stephenson MH, Kader Al-Mashaikie SA (2011) Stratigraphic note: update on the palynology of the Akbarah and Kuhlan formations, northwest Yemen. GeoArabia 16:17–24
Stephenson MH, Jan IU, Kader Al-Mashaikie SA (2012) Palynology and correlation of Carboniferous-Permian glacigene rocks in Oman, Yemen and Pakistan. Gondwana Research. http://dx.doi.org/10.1016/j.gr.2012.06.005. Accessed 10 Oct 2012
Stone P, Aldiss DT, Edwards EJ (2005) Rocks and fossils of the Falkland Islands. British Geological Survey for Department of Mineral Resources, Falkland Islands Government
Taylor TN, Taylor EL (1992) Permian plants from the Ellsworth Mountains, West Antarctica. Geol Soc Am Mem 170:285–289
Torrence C, Compo GPA Practical Guide to Wavelet Analysis. http://paos.colorado.edu/research/wavelets.html. Accessed 21 Dec 2012
Trewin NH, Macdonald DIM, Thomas CGC (2002) Stratigraphy and sedimentology of the Permian of the Falkland Islands: lithostratigraphic and palæoenvironmental links with South Africa. J Geol Soc London 159:5–19
Veevers JJ, Powell CM (1987) Late Palæozoic glacial episodes in Gondwanaland reflected in transgressive depositional sequences in Euramerica. Geol Soc Am Bull 98:475–487
Veevers JJ, Cole DI, Cowan EJ (1994) Southern Africa: Karoo Basin and Cape fold belt. In: Veevers JJ, Powell CM (eds) Permian-Triassic Pangean Basins and Fold Belts along the Panthalassan Margin of Gondwanaland, vol 184. Geological Society of America Memoir, pp 223–279
Visser JNJ (1987) The palæogeography of part of southwestern Gondwana during the Permo-Carboniferous glaciation. Palæogeogr Palæoclimatol Palæoecol 61:205–219
Walker JCG, Zahnle KJ (1986) Lunar nodal tide and distance to the Moon during the Precambrian. Nat London 320:600–602
Wright VP (1992) Speculations on the controls on the cyclic peritidal carbonates: icehouse versus greenhouse eustatic controls. Sed Geol 76:1–5

Chapter 5
Conclusions Summarised and Research Opportunities Reviewed

Abstract The borehole core sections illustrating the Late Carboniferous to Early Permian glaciogenic succession in the Falkland Islands provide an insight into palæoenvironmental changes experienced in the Southern Hemisphere during an 'icehouse to greenhouse' transition. The critical data were acquired by detailed analyses of two core sections recovered from East Falkland that spanned the lithological transition zone. Within Gondwana, the Falkland Islands occupied relatively high latitudes at the time and the cores preserve glacial diamictite deposits from the Fitzroy Tillite Formation passing up into black mudstones from the Port Sussex Formation. The borehole cores provided a unique opportunity to investigate the relationship between ancient lacustrine depositional dynamics and climatic variations. The study used a combination of detailed sedimentary logging and high-resolution XRF and reflectance scans. It provides the first high-resolution data set from this part of the Gondwana supercontinent for the Carboniferous–Permian climatic transition. The XRF and reflectance scans enabled the identification of subtle changes in both sediment provenance and the prevailing environmental conditions.

Keywords Absolute dating · Accumulation rates · Climate transition

5.1 The Principal Conclusions

The geological material available for the study reported here afforded a rare opportunity to evaluate climate change relatively early in the Earth's Phanerozoic history, so providing a valuable complement to the many climatic studies that have concentrated on Quaternary changes. For this reason, data were collected at a very high resolution to generate results that ensured a comprehensive analysis. It is hoped that this research will improve understanding of the ancient geological record of climate change, while lending some insights into how major icehouse to greenhouse climatic transitions on Earth take place. The study illustrates how links

K. Horan, *Falkland Islands (Islas Malvinas) in the Permo-Carboniferous*,
Springer Earth System Sciences, DOI 10.1007/978-3-319-08708-5_5

between sedimentology and glacier processes may be tied to climate conditions and demonstrates the way in which Milankovitch orbital solutions may provide an explanation of the punctuated nature of such transitions. The Falkland Islands results may help to validate other projected Milankovitch estimates and calculations of the planet's orbital configuration and climatic responses in the distant past.

The following principal conclusions are stressed:

1. The depositional sequence preserves evidence of dynamic climate change with cyclic advance and retreat of a water-based ice sheet. There is broad shift in the style of sedimentation from terrigenous subglacial diamictite through interlaminated coarse and fine deposits to hemipelagic muds.
2. There is no clear evidence that the deposits are marine, and a lacustrine setting is preferred on the basis of palynology (e.g. Osterloff et al. 2004), a lack of marine fauna, presence of freshwater fauna such as bivalves in the Brenton Loch Formation (Simões et al. 2012), in situ Permian plant macrofossils (e.g. Taylor and Taylor 1992) and varve deposits (although it is appreciated that varves can sometimes form in marine settings).
3. Wavelet analyses of reflectance data and the first two principal components from XRF data reveal strongest power in zones where 100-kyr and 400-kyr Milankovitch periodicities might be expected to lie suggesting that changes in the eccentricity of Earth's orbit paced the accumulation and ablation of the ice sheets.
4. A tentative attempt at age modelling suggests that the transition spans $\sim$1.2 Ma. This is the interval over which glaciers appear to have waxed and waned in response to Milankovitch forcing. It is possible, however, that some cycles were destroyed by the erosive power of an advancing glacier and that this timeframe is an underestimate; this is thought to be unlikely as no unconformities were noted.
5. Sedimentological analysis suggests that the glacial cycles were part of an overall period of retreat, with the second wave of coarse beds appearing to be more distal in character than the first with, for example, deformed clay clasts.
6. Superimposed on these short cycles was a movement of the Falklands out of the high southern latitudes. It is hypothesised that this drift provided the climatic tipping point to permanent non-glacial conditions. Additionally, although changing patterns of thermohaline circulation and volcanic activity (for which there is evidence at this time in these cores) may also have had a role to play in the transition out of the icehouse world, the available data were insufficient to allow the consideration of those factors as a part of this study.
7. The borehole sections can be placed in the broader, regional context of coeval glacial records from other parts of Gondwana. Comparison and correlation of the Falkland Islands deposits with those elsewhere suggest that in the Falklands area, the transition took place during the Sakmarian stage of the Early Permian.

5.2 Potential Research Opportunities

The borehole cores that formed the basis of the work reported here are held by the British Geological Survey in the UK's National Geoscience Data Centre at Keyworth, Nottingham. The cores are therefore still available for further study, as are several additional core runs through the Falkland Islands glacigenic succession that were not utilised in this study. An inventory of the extant material is provided by Stone (2011) in a British Geological Survey Report that is available as a free download at www.nora.nerc.ac.uk/14415/.

The main opportunities for future research may lie within the following areas, all of which are acknowledged limitations of the reported study.

1. The lack of absolute dates on the cores and the approximations of the age modelling mean that uncertainties in the timing of events remain. Ideally, further constraints on core chronology are required, particularly for ages assigned to the base and top of the sequence; such data would help validate the relative age modelling. However, in general, the Pennsylvanian to Cisuralian, non-marine and cold marine sediments of the Gondwana continent have proved difficult to correlate both within the continent and with the standard stages. There is a lack of key zonal fossils, which are largely marine (Stephenson et al. 2012), while palynological correlation is made difficult by disparate stratigraphic and taxonomic methods and different standards of documentation across Gondwana (Stephenson 2008). It may be possible to date the volcanic lapilli in the Hells Kitchen Member if they are accompanied by volcanogenic zircons amenable to the U–Pb method.
2. The current age model is largely dependent upon the assumption of uniform accumulation rates throughout the sequence and consequently is subject to a depth distortion. Improvement to the age model may be possible by looking in more detail at sediment patterns such as the possible varves if it can be proven that they represent seasonal cycles. Also, turbidity currents in glacial lakes may last only a few minutes, but deposit several centimetres of sediment, whereas quiet-water settling of clays may only deposit a few millimetres or less over many months (Benn and Evans 2010), and an ideal age model would take this into account. A more thorough analysis of feedbacks in the system, such as albedo changes, would also be required to achieve a more robust understanding of the sedimentation changes.
3. Wavelet analyses could be run on the third and fourth principal components, and spectral analyses could be used to investigate the data further in the depth domain.
4. Further elemental analyses could be used. For example, barium or bromine only considered briefly could be investigated more thoroughly in an attempt to better characterise the organic content of the sediment. It might also be useful to look for any correlation between iron and phosphorus. A correlation between iron and phosphorus points to the formation of iron phosphates as a possible control on the amount of phosphorus available for primary producers making

phosphorus a limiting nutrient. Negative correlations between iron and organic carbon could be preceded by a breakdown in the correlation between iron and phosphorus rather than an in-phase relationship between the elements.

5. A more in-depth isotopic analysis using ^{18}O as well as ^{13}C on many samples through the cores may yield better insights into ice volume, organic productivity and whether a lacustrine or marine setting is most likely. However, this would be a destructive process and ^{18}O is almost certainly affected by diagenesis. In addition, since there were no clearly identifiable bioclasts, the oxygen and carbon isotope measurements would have to be carried out on bulk sediment, which is difficult to interpret.

References

Benn DJ, Evans DJA (2010) Glaciers and glaciation (2nd edn). Hodder Education, Oxford

Osterloff PL, Al-Harthy A, Penney R, Spaak P, Al-Zadjali F, Jones NS, Knox RWO'B, Stephenson MH, Oliver G, Al-Husseini MI (2004) Gharif and Khuff formations, subsurface Interior Oman. In: Al-Husseini M (ed) Carboniferous, Permian and Early Triassic Arabian stratigraphy, vol 3. GeoArabia Special Publication, pp 83–147

Simões MG, Quaglio F, Warren LV, Anelli LE, Stone P, Riccomini C, Grohmann CH, Chamani MAC (2012) Permian non-marine bivalves of the Falkland Islands and their palæoenvironmental significance. Alcheringa 36:543–554

Stephenson MH (2008) A review of the palynostratigraphy of Gondwana Late Carboniferous to Early Permian glacigene successions. Geol Soc Am Spec Pap 441:317–330

Stephenson MH, Jan IU, Kader Al-Mashaikie SA (2012) Palynology and correlation of Carboniferous–Permian glacigene rocks in Oman, Yemen and Pakistan. Gondwana Research. http://dx.doi.org/10.1016/j.gr.2012.06.005. Accessed 10 Oct 2012

Stone P (2011) Borehole core recovered from the late Carboniferous to early Permian Fitzroy Tillite and Port Sussex formations, Falkland Islands: geological background and sample details. British Geological Survey Open Report:11/028

Taylor TN, Taylor EL (1992) Permian plants from the Ellsworth Mountains, West Antarctica, vol 170. Geological Society of America Memoir, pp 285–289

Chapter 6
Data Postscript

Abstract The complete scan of the hand-drawn logs for cores DD029 and DD090 are presented in this chapter. Plots of reflectance data, and XRF data for the elements silicon, potassium, chromium, titanium, manganese, iron and zirconium are also shown for both cores. The XRF logs incorporate annotations tying the element fluctuations observed to sedimentological variations. Results from the clast analysis showing clast frequency, sorting, roundness, sphericity, size and composition are presented for core DD090, as is the raw data on total organic carbon. Details regarding the measurements made to generate the depth scales are provided alongside images of the polished cores. Please refer to the appendix for a summary of the preliminary age modelling work and the outputs generated from the principal component analysis.

Keywords Log · XRF scans · Reflectance scans · Clast composition · Total organic carbon · Preliminary spectral analyses · Principal Component Analysis output

Electronic Supplementary Material The online version of this Chapter (DOI 10.1007/978-3-319-08708-5_6) contains supplementary material, which is available to authorized users.

K. Horan, *Falkland Islands (Islas Malvinas) in the Permo-Carboniferous*,
Springer Earth System Sciences, DOI 10.1007/978-3-319-08708-5_6

6.1 Logging Data: Digital Version and Original Scans

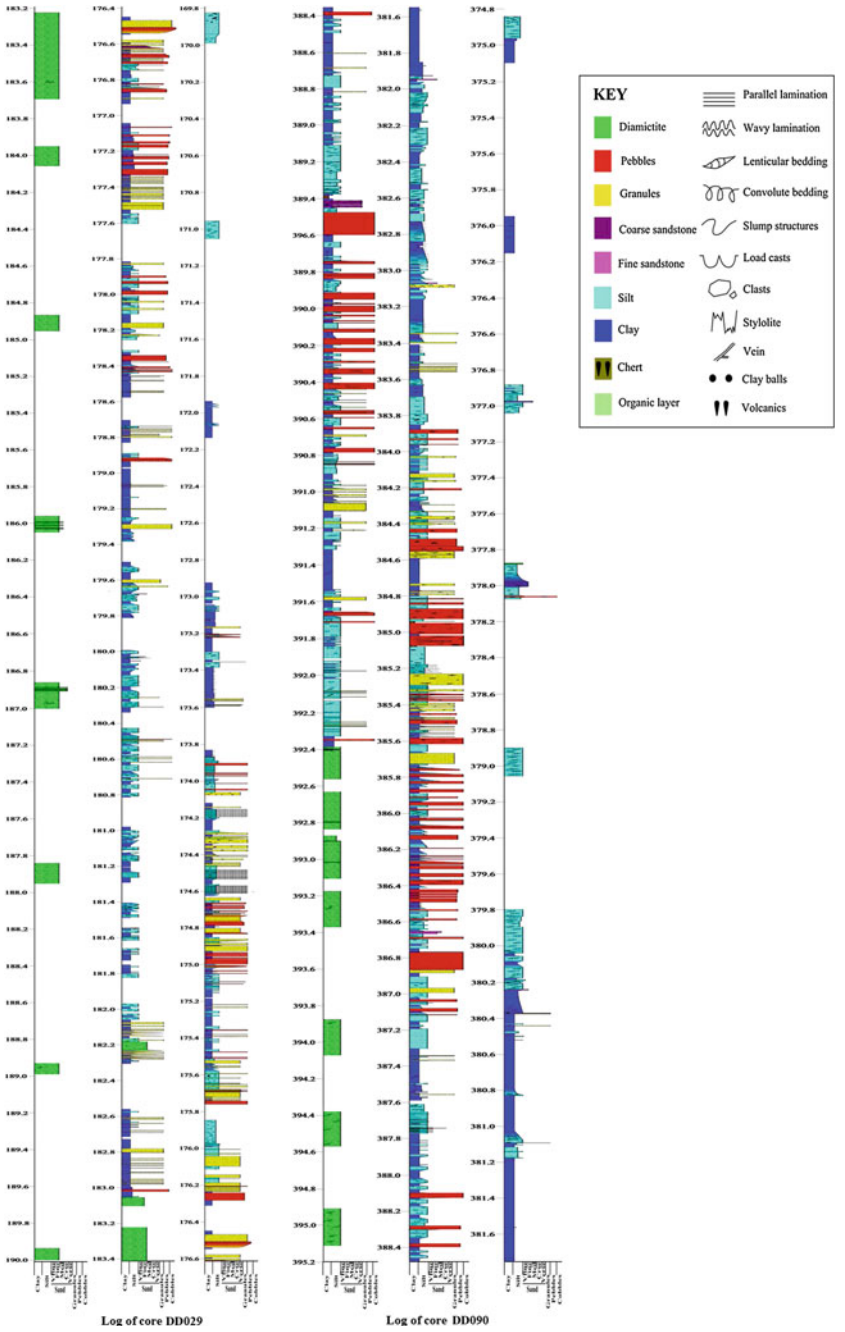

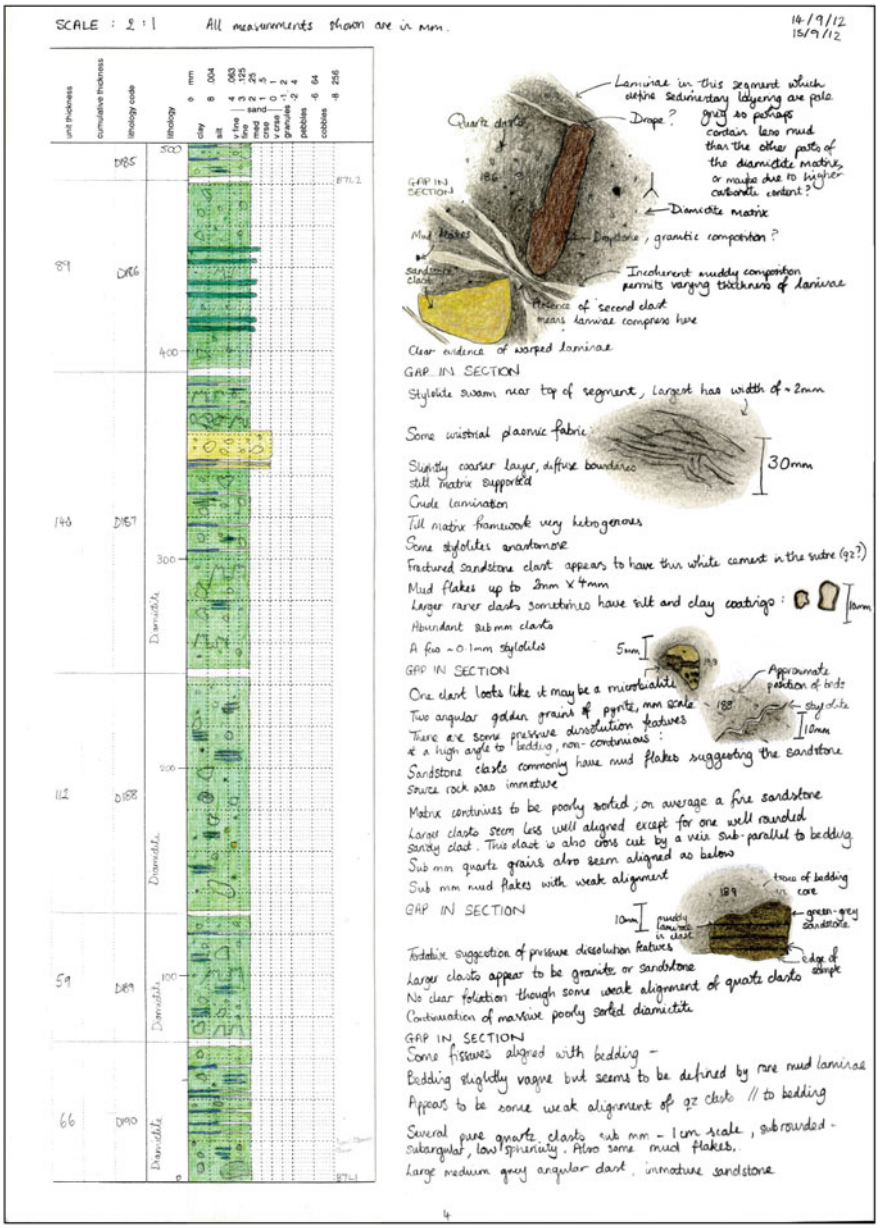
SCALE : 2 : 1
All measurements shown are in mm.
14/9/12
15/9/12
unit thickness
cumulative thickness
lithology code
lithology
clay
silt
v fine
fine
med
crse
v crse
granules
pebbles
cobbles
sand
DR85
DR86
DR87
DR88
DR89
DR90
Diamictite
500
400
300
200
100
0
871.2
871.1
89
148
112
59
66
Laminae in this segment which define sedimentary layering are pale grey as perhaps contain less mud than the other parts of the diamictite matrix, or maybe due to higher carbonate content?
Quartz clast
Drape?
GAP IN SECTION
Diamictite matrix
Mud flakes
Dolerite, granitic composition?
sandstone clast
Incoherent muddy composition permits varying thickness of laminae
Presence of second clast means laminae compress here
Clear evidence of warped laminae
GAP IN SECTION
Stylolite swarm near top of segment, largest has width of ~2mm
Some weak/local planar fabric
30mm
Slightly coarser layer, diffuse boundaries still matrix supported
Crude lamination
Till matrix framework very heterogeneous
Some stylolites anastomose
Fractured sandstone clast appears to have thin white cement in the fabric (qz?)
Mud flakes up to 2mm x 4mm
Larger rarer clasts sometimes have silt and clay coatings
1cm
Abundant sub mm clasts
A few ~0.1mm stylolites
5mm
GAP IN SECTION
One clast looks like it may be a microfossil
Approximate position of limb
stylolite
10mm
Two angular golden grains of pyrite, mm scale
There are some pressure dissolution features at a high angle to bedding, non-continuous
Sandstone clasts commonly have mud flakes suggesting the sandstone source rock was immature
Matrix continues to be poorly sorted, on average a fine sandstone
Larger clasts seem less well aligned except for one well rounded sandy clast. This clast is also cross cut by a vein sub-parallel to bedding
Sub mm quartz grains also seem aligned as below
Sub mm mud flakes with weak alignment
trace of bedding in core
10mm
muddy laminae in clast
green-grey sandstone
edge of sample
GAP IN SECTION
Tentative suggestion of pressure dissolution features
Larger clasts appear to be granite or sandstone
No clear foliation though some weak alignment of quartz clasts
Continuation of massive poorly sorted diamictite
GAP IN SECTION
Some fissures aligned with bedding -
Bedding slightly vague but seems to be defined by rare mud laminae
Appears to be some weak alignment of qz clasts // to bedding
Several pure quartz clasts sub mm - 1cm scale, subrounded - subangular, low sphericity. Also some mud flakes.
Large medium grey angular clast, immature sandstone
4

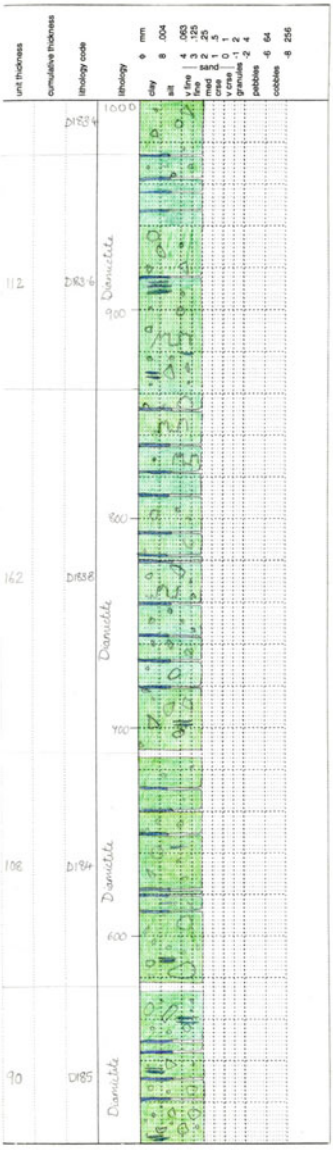

15/9/12
16/9/12

NOTE : Bedding does not have a consistent orientation in segments, it depends on which side of the core was collected! This may complicate XRF analysis also.

Most clasts seem to be subangular, include fsp, qz, sst, granite

Clasts of average - large size (~5mm) seem to have increased in abundance in this segment.

A few mud laminae can be picked out on curved surface, not clear on cut surface, probably lenses. Some globular mud lenses on cut surface

Clasts are sub-angular - sub-rounded

Broken surfaces are also mainly // to bedding

mud clasts are aligned // to bedding.

Stylolites in general have an orientation // to bedding

Estimate ~ 10% of matrix is mud clasts, 30% quartz clasts

Again, larger clasts tend to be composed of granite or sandstone.

Note: Care must be taken to ensure colour changes associated with differential sanding of cut surface are not mistaken for lithological changes.

The fragmentary nature of this segment emphasises how brittle parts of the diamictite are; vulnerable to breakage during sanding.

Several fractures developing near the top of this segment, perhaps associated with pressure dissolution? They form a branching network in places.

In addition to the clastic grains eg granite, sandstone, quartz, there seem to be 'till pebbles' composed of partially solidified diamictite.

A few examples where small clasts seem to have acted as a barrier to the propagating fractures as the stylolitic infill wraps around them

clast ← infilled fracture

2mm

Mud lenses only apparent on curved surface

weak alignment of mud and quartz grains

weak fractures infilled stylolites?

position of adjacent layers

189.8

Suggestion of a shear zone parallel to bedding

Diamictite matrix continues to be fairly structureless.

Silt and clay coatings also found on some clasts

Large (~20mm × 20mm) subrounded, poorly sorted greenish-grey Sandstone clast with mud cap. Silt cap

189.8

GAP IN SECTION

No clearly continuous mud laminae in this segment

Fractures ⊥ to bedding.

Coarse grained Sandstone clast

10mm

edge of segment

Larger clasts are mostly sub-rounded

Submm quartz grains and mudflakes have weak alignment

Ungraded and disorganised fabric as below

Muddy lenses are always parallel to bedding - probably conformable

Rod shaped clasts may be feldspathic, some are also mud

Continuation of matrix supported diamictite, poorly sorted, polymodal grain size

Large granitoid clast - see page 2

GAP IN SECTION

Foliated granite clast :

185

fairly well rounded

10mm

little alignment of clast with bedding; fits with less shearing base, suggested by fewer stylolites

Sub mm mud flakes aburdant

Poor alignment of large clasts

Clay coating to some clasts

10mm

Some muddy laminae and lenses

Rare stylolites sub-parallel to bedding, ~0.1mm (a much narrower than

Mixed clast lithology : sandstone, quartzite?, granite, carbonate? (very white clast near top of segment, could be quartz)

5

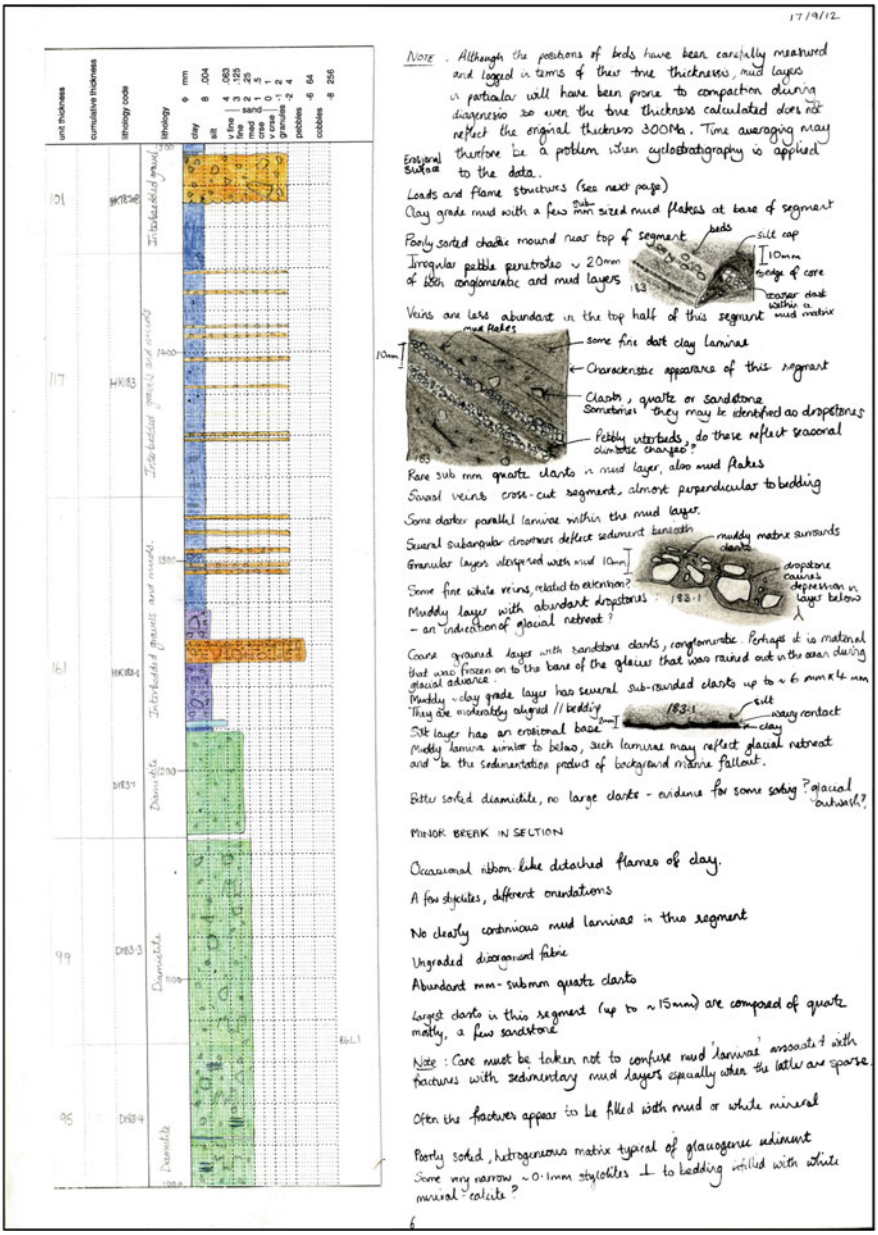
17/9/12
unit thickness
cumulative thickness
lithology code
lithology
clay
silt
v fine
fine
med
crse
v crse
granules
pebbles
cobbles
Interbedded gravel, sand and mud
Interbedded gravels and mud
Interbedded gravels and mud
Diamicton
Diamicton
Diamicton
101
117
161
99
95
HK1136
HK183
HK184
DH83-3
DH84
Note . Although the positions of beds have been carefully measured and logged in terms of their true thickness, mud layers in particular will have been prone to compaction during diagenesis so even the true thickness calculated does not reflect the original thickness 3000Ma. Time averaging may therefore be a problem when cyclostratigraphy is applied to the data.
Erosional Surface
Loads and flame structures (see next page)
Clay grade mud with a few sub-mm sized mud flakes at base of segment
Poorly sorted chaotic mound near top of segment
Irregular pebble penetrates ~ 20mm of otherwise conglomeratic and mud layers
beds
silt cap
10mm
wedge of core
coarser clast within a mud matrix
183
Veins are less abundant in the top half of this segment
mud flakes
10mm
some fine dark clay laminae
Characteristic appearance of this segment
Clasts, quartz or sandstone. Sometimes they may be identified as dropstones
Pebbly interbeds, do these reflect seasonal climatic changes?
183
Rare sub mm quartz clasts in mud layer, also mud flakes
Several veins cross-cut segment, almost perpendicular to bedding
Some darker parallel laminae within the mud layer.
Several subangular dropstones deflect sediment beneath
Granular layers dispersed with mud 10cm
Some fine white veins, related to extension?
Muddy layer with abundant dropstones - an indication of glacial retreat?
muddy matrix surrounds clasts
dropstone causes depression in layers below
183.1
Coarse grained layer with sandstone clasts, conglomeratic. Perhaps it is material that was frozen on to the base of the glacier that was rained out in the ocean during glacial advance.
Muddy - clay grade layer has several sub-rounded clasts up to ~ 6 mm x 4 mm
They are moderately aligned // bedding
Silt layer has an erosional base
Muddy laminae similar to below, such laminae may reflect glacial retreat and be the sedimentation product of background marine fallout.
silt
wavy contact
clay
183.1
Better sorted diamictite, no large clasts - evidence for some sorting? glacial outwash?
MINOR BREAK IN SECTION
Occasional ribbon like detached flames of clay.
A few stylolites, different orientations
No clearly continuous mud laminae in this segment
Ungraded disorganised fabric
Abundant mm - submm quartz clasts
Largest clasts in this segment (up to ~15mm) are composed of quartz mostly, a few sandstone
Note: Care must be taken not to confuse mud 'laminae' associated with fractures with sedimentary mud layers especially when the latter are sparse
Often the fractures appear to be filled with mud or white mineral
Poorly sorted, heterogeneous matrix typical of glaucogenic sediment
Some very narrow ~0.1mm stylolites ⊥ to bedding infilled with white mineral - calcite?
6

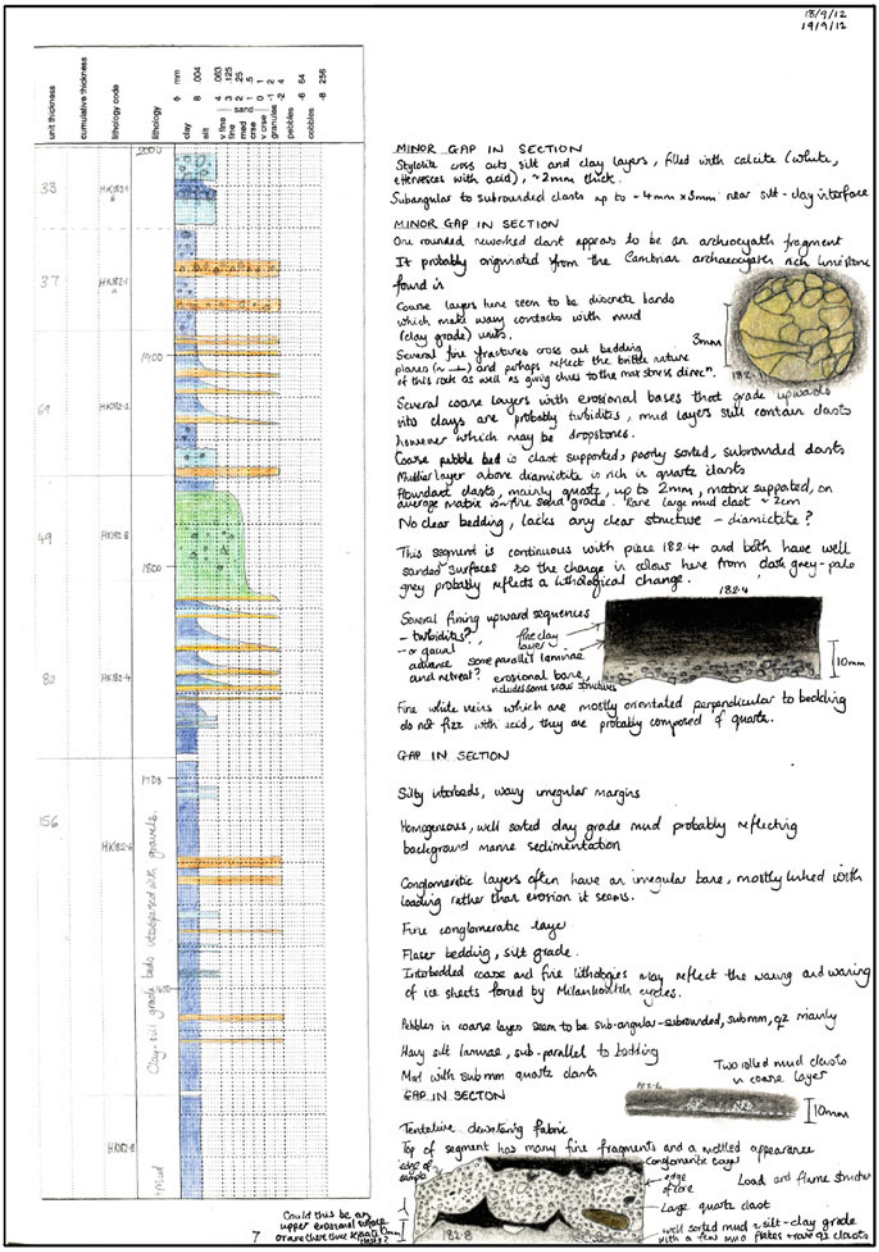
13/9/12
19/9/12
unit thickness
cumulative thickness
lithology code
lithology
clay
silt
sand
pebbles
cobbles
33
37
69
49
82
156
HK1B3.4
HK1B2.4
HK1B2.2
HK1B1.8
HK1B2.4
HK1B2.4
HK1B1.8
2000
1900
1800
1700
1600
Clay-rich grade beds interbedded with granules
Mud
MINOR GAP IN SECTION
Stylolite cross cuts silt and clay layers, filled with calcite (volute, effervesces with acid), ~2mm thick.
Subangular to subrounded clasts up to ~4mm x 3mm near silt - clay interface
MINOR GAP IN SECTION
One rounded reworked clast appears to be an archaeocyath fragment
It probably originated from the Cambrian archaeocyath rich limestone found in
Coarse layers have seen to be discrete bands which make wavy contacts with mud (clay grade) units.
Several fine fractures cross cut bedding planes (~ ⊥) and perhaps reflect the brittle nature of this rock as well as giving clues to the max stress direct".
3mm
182.4
Several coarse layers with erosional bases that grade upwards into clays are probably turbidites, mud layers still contain clasts however which may be dropstones.
Coarse pebble bed is clast supported, poorly sorted, subrounded clasts
Muddier layer above diamictite is rich in quartz clasts
Flowdated clasts, mainly quartz, up to 2mm, matrix supported, on average matrix is fine sand grade. Rare large mud clast ~ 2cm
No clear bedding, lacks any clear structure - diamictite?
This segment is continuous with piece 182.4 and both have well sorted surfaces so the change in colour here from dark grey - pale grey probably reflects a lithological change.
182.4
Several fining upward sequences - turbidites?, - or gravel advance and retreat?
fine clay layer
some parallel laminae
erosional base, included some wood fragments
10mm
Fine white veins which are mostly orientated perpendicular to bedding do not fizz with acid, they are probably composed of quartz.
GAP IN SECTION
Silty interbeds, wavy irregular margins
Homogeneous, well sorted clay grade mud probably reflecting background marine sedimentation
Conglomeritic layers often have an irregular base, mostly linked with loading rather than erosion it seems.
Fine conglomeratic layer
Flaser bedding, silt grade.
Interbedded coarse and fine lithologies may reflect the waxing and waning of ice sheets forced by Milankovitch cycles.
Pebbles in coarse layer seem to be sub-angular - subrounded, sub mm, qz mainly
Hazy silt laminae, sub-parallel to bedding
Mud with sub mm quartz clasts
Two rolled mud clasts in coarse layer
182.6
10mm
GAP IN SECTION
Tentative downlap fabric
Top of segment has many fine fragments and a mottled appearance
edge of clast
conglomeritic layer
edge of fibre
Load and flame structu
Large quartz clast
well sorted mud - silt - clay grade with a few mm flakes + raw qz clasts
182.8
Could this be an upper erosional surface
Coarse clast size 4mm
7

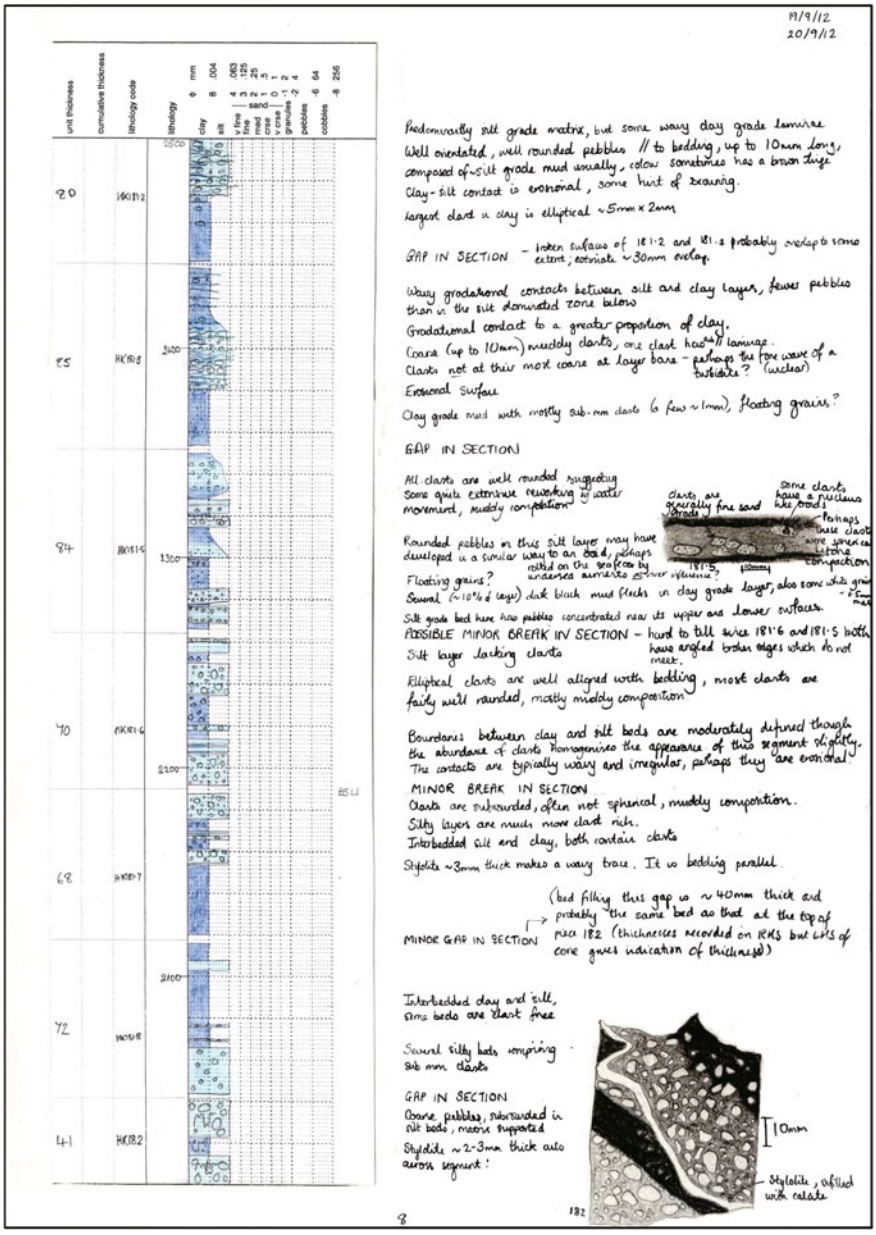
19/9/12
20/9/12
unit thickness
cumulative thickness
lithology code
lithology
clay
silt
sand
granules
pebbles
cobbles
80
85
84
70
68
72
41
Predominantly silt grade matrix, but some wavy clay grade laminae
Well orientated, well rounded pebbles // to bedding, up to 10mm long, composed of silt grade mud usually, colour sometimes has a brown tinge
Clay-silt contact is erosional, some hint of scouring.
largest clast a clay is elliptical ~5mm x 2mm
GAP IN SECTION - taken surfaces of 181.2 and 181.3 probably overlap to some extent, estimate ~30mm overlap.
Wavy gradational contacts between silt and clay layers, fewer pebbles than in the silt dominated zone below
Gradational contact to a greater proportion of clay.
Coarse (up to 10mm) muddy clasts, one clast has // laminae.
Clasts not at their most coarse at layer base - perhaps the fore wave of a turbidite? (unclear)
Erosional surface
Clay grade mud with mostly sub-mm clasts (a few ~1mm), floating grains?
GAP IN SECTION
All clasts are well rounded suggesting some quite extensive reworking of water movement, muddy composition
Some clasts have a nucleus like mud
Perhaps these clasts were generally softer in composition
Rounded pebbles on this silt layer may have developed in a similar way to on sand, perhaps rolled on the seafloor by unusually current or wave influence?
Floating grains?
Several (~10% of large) dark black mud flecks in clay grade layer, also some white grains
Silt grade bed here has pebbles concentrated near its upper and lower surfaces.
POSSIBLE MINOR BREAK IN SECTION - hard to tell since 181.6 and 181.5 both have angled broken edges which do not meet.
Silt layer lacking clasts
Elliptical clasts are well aligned with bedding, most clasts are fairly well rounded, mostly muddy composition
Boundaries between clay and silt beds are moderately defined though the abundance of clasts homogenises the appearance of this segment slightly. The contacts are typically wavy and irregular, perhaps they are erosional.
MINOR BREAK IN SECTION
Clasts are subrounded, often not spherical, muddy composition.
Silty layers are much more clast rich.
Interbedded silt and clay, both contain clasts
Stylolite ~3mm thick makes a wavy trace. It is bedding parallel.
MINOR GAP IN SECTION
(bed filling this gap is ~40mm thick and probably the same bed as that at the top of piece 182 (thicknesses recorded on RHS but bits of core gives indication of thickness))
Interbedded clay and silt, some beds are clast free
Several silty beds inspiring sub mm clasts
GAP IN SECTION
Coarse pebbles, subrounded in silt beds, matrix supported
Stylolite ~2-3mm thick cuts across segment
10mm
Stylolite, infilled with calcite
182
8

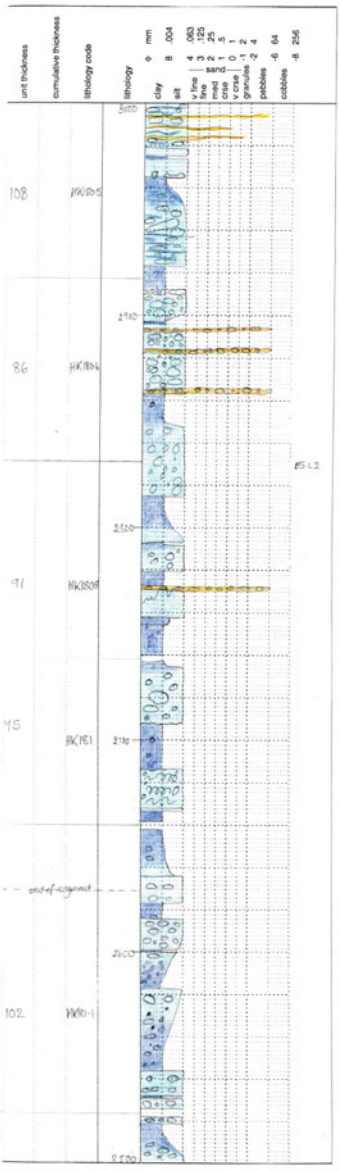

20/9/12
21/9/12

A mix of wavy clay, silt and coarse laminae with clasts of clay-medium sand grade throughout, clasts up to 25mm x 10mm.

Fine wavy clay layer

Dropstones compress clay at the top of this sequence

Gradual fining upwards sequence here → waning of glacial perhaps

Clasts often have elliptical shape especially the largest ones, all sub-well rounded, probably quite extensively reworked

Wavy trace of stylolite, sub parallel to bedding, filled with calcite

Sharp well defined clay layer – indicative of pure marine sedimentation?

Within the silt layer pebbles tend to concentrate in bands that have poorly defined boundaries

Clast content rises

Gradational contact between silt and clay

The clasts in the silt beds are well rounded. Some may be dropstones but it is possible that others are those picked up as the glacier advanced over previously deposited till following an episode of retreat. They were then subsequently deposited.

Some clasts in the silt look almost cherty

Pebble bed, >50% clasts

Stylolite cuts through silt and pebble layers

MINOR GAP IN SECTION

Some planes visible on rounded surface.

Most contacts seem to be erosional

A few subangular clasts 2mm – 20mm long in clay bed.

Silty layer seems to have syn-sedimentary slump features

Beds now dip in the opposite direction to piece 181-1 because the other half of the core has been provided.

MINOR GAP IN SECTION

Projection of top bed shown was beyond the thickness of segment 181-1

Clast composition, silt-clay, perhaps comes from the diamictite.

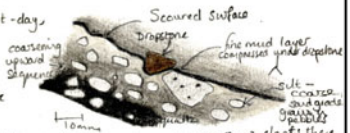

Further coarsening upwards sequences here

A few pure black clasts, most are medium grey ~3 qz clasts, these are subangular

Coarsening upwards sequence – indicative of ice sheet advance perhaps?

Fine mud layer not laterally continuous

Basal bed of this segment also silt with large pebbles up to 15mm x 15mm.

MINOR GAP IN SECTION beds seem to join up across gap and depth assignments suggests it is small)

No clear grading of pebbles in silty matrix layer, various sizes throughout

9

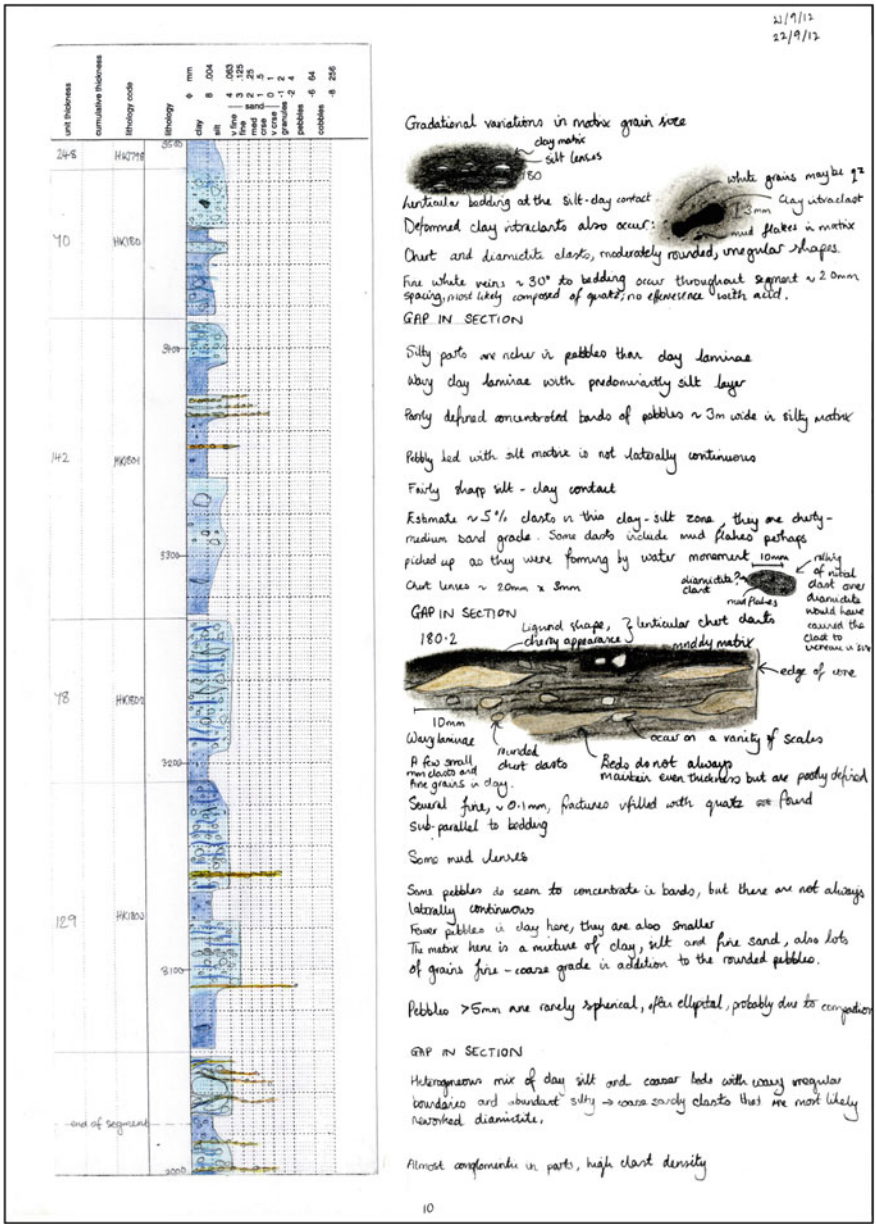
21/9/12
22/9/12
unit thickness
cumulative thickness
lithology code
lithology
clay
silt
v fine
fine
med
crse
v crse
granules
pebbles
cobbles
mm
sand
HK2718
HK1180
HK1801
HK1802
HK1803
end of segment
Gradational variations in matrix grain size
clay matrix
silt lenses
180
lenticular bedding at the silt-clay contact
Deformed clay intraclasts also occur:
white grains may be qz
clay intraclast
1.5mm
mud flakes in matrix
Chert and diamictite clasts, moderately rounded, irregular shapes.
Fine white veins ~ 30° to bedding occur throughout segment ~ 2.0mm spacing, most likely composed of quartz, no effervescence with acid.
GAP IN SECTION
Silty parts are richer in pebbles than clay laminae
Wavy clay laminae with predominantly silt layer
Poorly defined concentrated bands of pebbles ~ 3m wide in silty matrix
Pebbly bed with silt matrix is not laterally continuous
Fairly sharp silt - clay contact
Estimate ~5% clasts in this clay-silt zone, they are chiefly medium sand grade. Some clasts include mud flakes perhaps picked up as they were forming by water movement
10mm
diamictite? clast
mud flakes
wkg of initial clast over diamictite would have caused the clast to overturn in situ
Chert lenses ~ 20mm x 3mm
GAP IN SECTION
Ligand shape, ? lenticular chert clasts
180·2
chirty appearance
muddy matrix
edge of core
10mm
Wavy laminae
A few small mm clasts and fine grains in clay.
rounded chert clasts
occur on a variety of scales
Beds do not always maintain even thickness but are poorly defined
Several fine, ~0.1mm, fractures infilled with quartz are found sub-parallel to bedding
Some mud lenses
Some pebbles do seem to concentrate in bands, but these are not always laterally continuous
Fewer pebbles in clay here, they are also smaller
The matrix here is a mixture of clay, silt and fine sand, also lots of grains fine - coarse grade in addition to the rounded pebbles.
Pebbles >5mm are rarely spherical, often elliptical, probably due to compaction
GAP IN SECTION
Heterogeneous mix of clay silt and coarser beds with wavy irregular boundaries and abundant silty → coarse sandy clasts that are most likely reworked diamictite.
Almost conformable in parts, high clast density
10

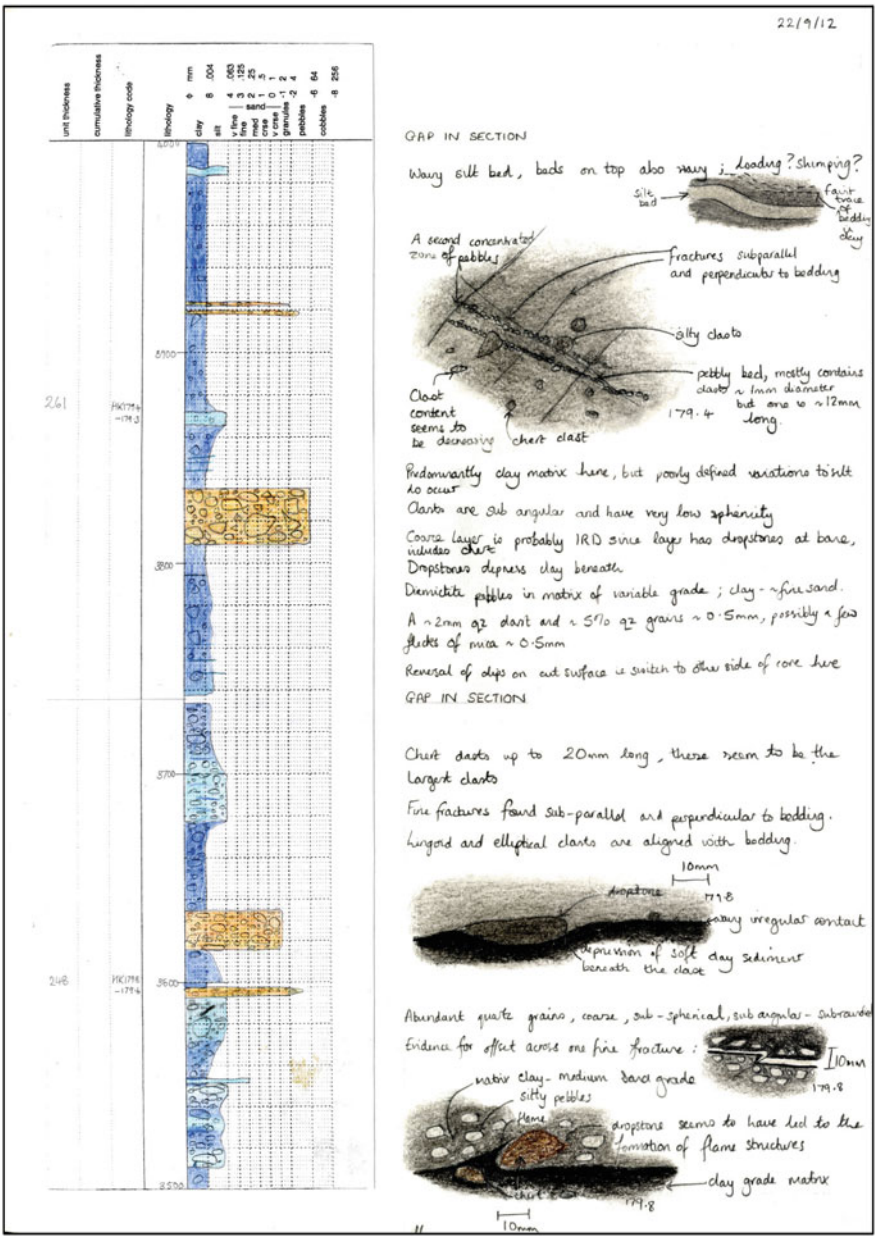
22/9/12
unit thickness
cumulative thickness
lithology code
lithology
clay
silt
sand
pebbles
cobbles
261
HKIT94
-179.3
248
HKIT94
-179.4
5700
5800
5900
6000
GAP IN SECTION
Wavy silt bed, beds on top also wavy ; loading ? shimping?
Silt bed
Fault trace of bedding
A second concentrated zone of pebbles
Fractures subparallel and perpendicular to bedding
Silty clasts
pebbly bed, mostly contains clasts ~ 1mm diameter but one to ~12mm long.
Clast content seems to be decreasing
chert clast
179.4
Predominantly clay matrix here, but poorly defined variations to silt to occur
Clasts are sub angular and have very low sphericity
Coarse layer is probably IRD since layer has dropstones at base, includes chert
Dropstones depress clay beneath
Dewicitic pebbles in matrix of variable grade ; clay - v fine sand.
A ~2mm qz clast and ~ 5% qz grains ~ 0·5mm, possibly a few flecks of mica ~ 0·5mm
Reversal of dips on cut surface is switch to other side of core here
GAP IN SECTION
Chert clasts up to 20mm long, these seem to be the largest clasts
Fine fractures found sub-parallel and perpendicular to bedding.
Elongated and elliptical clasts are aligned with bedding.
10mm
dropstone
179.8
wavy irregular contact
depression of soft clay sediment beneath the clast
Abundant quartz grains, coarse, sub-spherical, sub angular - subrounded
Evidence for offset across one fine fracture :
10mm
179.8
matrix clay - medium sand grade
silty pebbles
flame
dropstone seems to have led to the formation of flame structures
clay grade matrix
chert
179.8
10mm

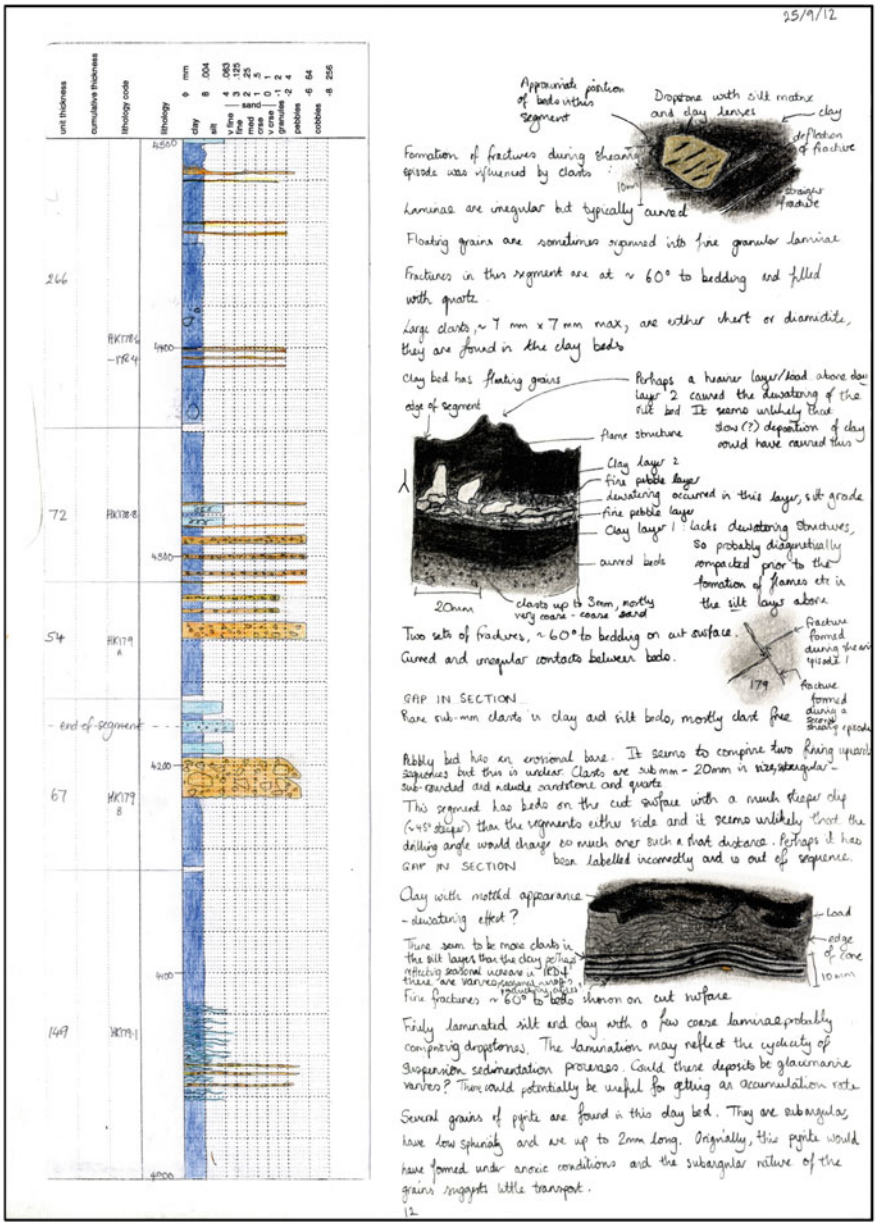
25/9/12
unit thickness
cumulative thickness
lithology code
lithology
clay
silt
sand
granules
pebbles
cobbles
4560
4400
4380
4200
4000
266
72
54
67
149
HK178
HK179
HK179 A
HK179 B
HK179.1
- end of segment
Apparent position of beds within segment
Dropstone with silt matrix and clay laminae
clay
deflation of fracture
straight fracture
10mm
Formation of fractures during shearing episode was influenced by clasts
Laminae are irregular but typically curved
Floating grains are sometimes organised into fine granular laminae
Fractures in this segment are at ~ 60° to bedding and filled with quartz
Large clasts, ~ 7 mm x 7 mm max, are either chert or diamictite, they are found in the clay beds
Clay bed has floating grains
edge of segment
Perhaps a heavier layer/load above dm layer 2 caused the dewatering of the silt bed. It seems unlikely that slow (?) deposition of clay could have caused this
Flame structure
Clay layer 2
Fine pebble layer
dewatering occurred in this layer, silt grade
Fine pebble layer
Clay layer 1
lacks dewatering structures, so probably diagenetically compacted prior to the formation of flames etc in the silt layer above
curved beds
20mm
clasts up to 3mm, mostly very coarse - coarse sand
Two sets of fractures, ~ 60° to bedding on cut surface.
Curved and irregular contacts between beds.
Fracture formed during shearing episode 1
179
fracture formed during a second shearing episode
GAP IN SECTION
Rare sub-mm clasts in clay and silt beds, mostly clast free
Pebbly bed has an erosional base. It seems to comprise two fining upward sequences but this is unclear. Clasts are sub mm - 20mm in size, subangular - sub-rounded and include sandstone and quartz
This segment has beds on the cut surface with a much steeper dip (~45° steeper) than the segments either side and it seems unlikely that the drilling angle would change so much over such a short distance. Perhaps it has been labelled incorrectly and is out of sequence.
GAP IN SECTION
Clay with mottled appearance - dewatering effect?
There seem to be more clasts in the silt layers than the clay perhaps reflecting seasonal increase in IRD? There are various coarsening upward packages
Load
edge of core
10 mm
Fine fractures ~ 60° to beds shown on cut surface
Finely laminated silt and clay with a few coarse laminae probably comprising dropstones. The lamination may reflect the cyclicity of suspension sedimentation processes. Could these deposits be glaciomarine varves? They could potentially be useful for getting an accumulation rate.
Several grains of pyrite are found in this clay bed. They are subangular, have low sphericity and are up to 2mm long. Originally, this pyrite would have formed under anoxic conditions and the subangular nature of the grains suggests little transport.
12

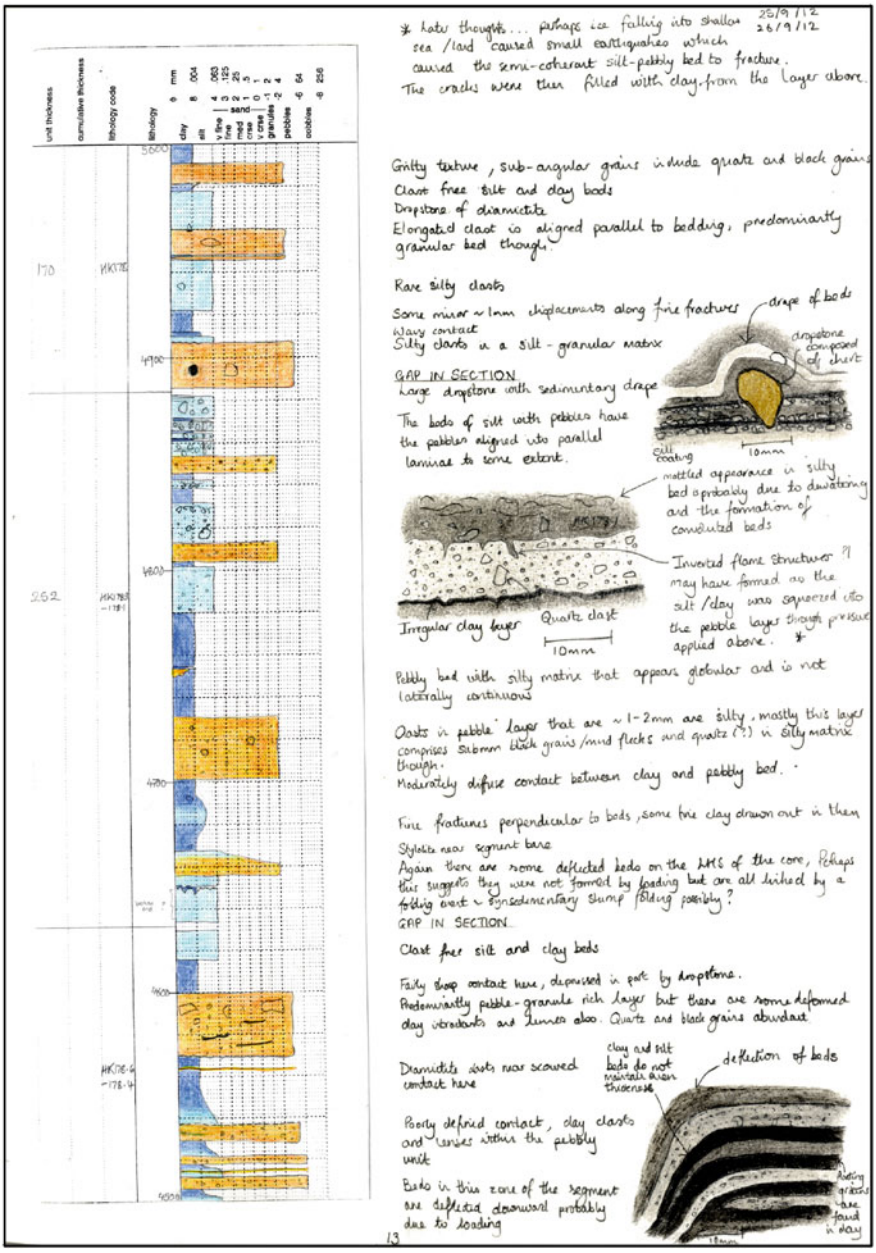

* later thoughts... perhaps ice falling into shallow sea / land caused small earthquakes which caused the semi-coherent silt-pebbly bed to fracture. The cracks were then filled with clay from the layer above.

25/9/12
26/9/12

Gritty texture, sub-angular grains include quartz and black grains
Clast free silt and clay beds
Dropstone of diamictite
Elongated clast is aligned parallel to bedding, predominantly granular bed though.

Rare silty clasts

Some minor ~1mm displacements along fine fractures

Wavy contact
Silty clasts in a silt - granular matrix

GAP IN SECTION
Large dropstone with sedimentary drape

The beds of silt with pebbles have the pebbles aligned into parallel laminae to some extent.

Pebbly bed with silty matrix that appears globular and is not laterally continuous

Clasts in pebble layer that are ~1-2mm are silty, mostly this layer comprises 5-8mm black grains / mud flecks and quartz (?) in silty matrix though.
Moderately diffuse contact between clay and pebbly bed.

Fine fractures perpendicular to beds, some fine clay drawn out in them

Stylolite near segment base
Again there are some deflected beds on the HHS of the core, Perhaps this suggests they were not formed by loading but are all linked by a folding event ± synsedimentary slump folding possibly?

GAP IN SECTION

Clast free silt and clay beds

Fairly sharp contact here, depressed in part by dropstone.
Predominantly pebble-granule rich layer but there are some deformed clay intraclasts and lenses also. Quartz and black grains abundant

Diamictite clasts near scoured contact here

Poorly defined contact, clay clasts and lenses within the pebbly unit

Beds in this zone of the segment are deflected downward probably due to loading

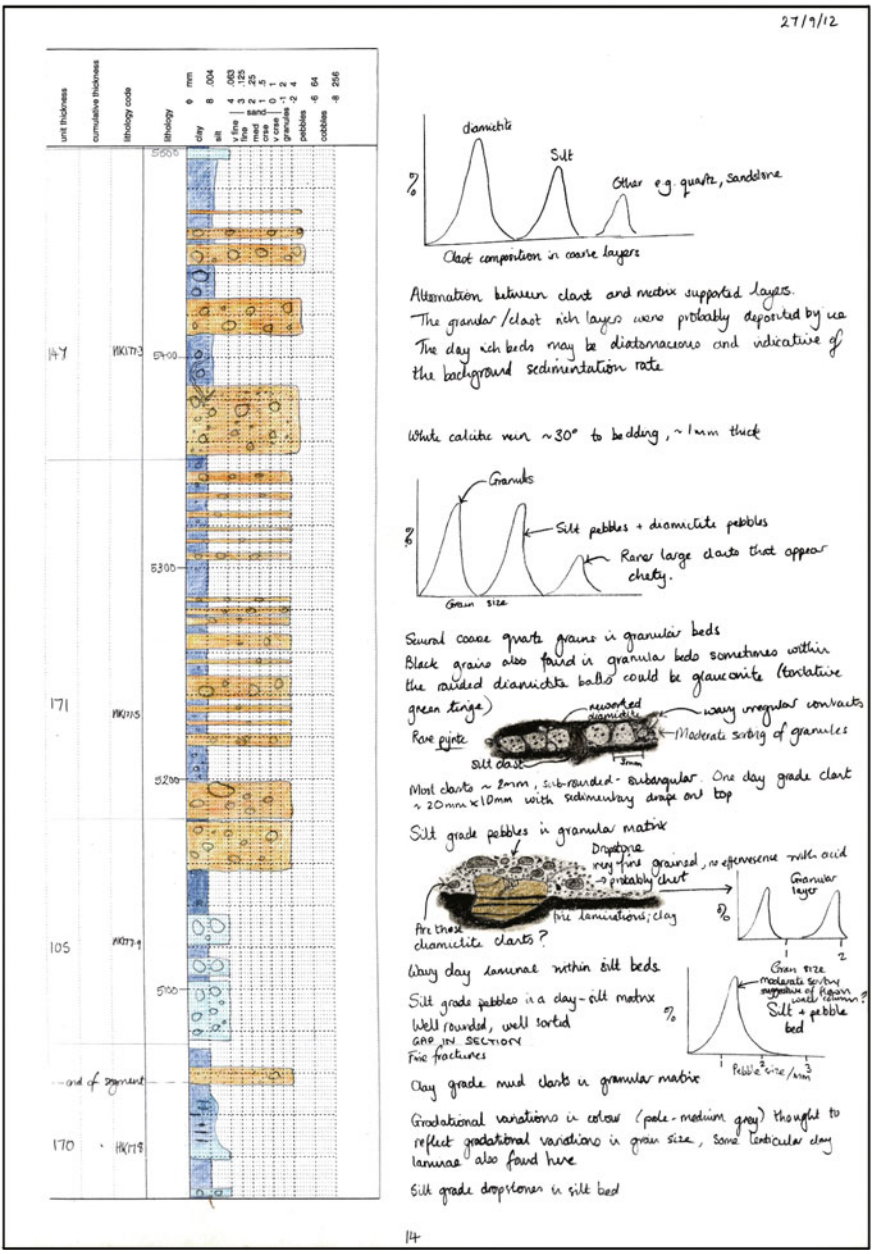
27/9/12
unit thickness
cumulative thickness
lithology code
lithology
clay
silt
sand
pebbles
cobbles
5600
5700
5800
5200
5100
147
171
105
170
end of segment
diamictite
Silt
Other e.g. quartz, sandstone
Clast composition in coarse layers
Alternation between clast and matrix supported layers.
The granular/clast rich layers were probably deposited by ice
The clay rich beds may be diatomaceous and indicative of the background sedimentation rate
White calcite vein ~30° to bedding, ~1mm thick
Granules
Silt pebbles + diamictite pebbles
Rare large clasts that appear chatty.
Grain size
Several coarse quartz grains in granular beds
Black grains also found in granular beds sometimes within the rafted diamictite balls could be glauconite (tentative green tinge)
Rare pyrite
reworked diamictite
wavy irregular contacts
Moderate sorting of granules
Silt clast
3mm
Most clasts ~2mm, sub-rounded - subangular. One clay grade clast ~20mm x 10mm with sedimentary drape on top
Silt grade pebbles in granular matrix
Dropstone
very fine grained, no effervescence with acid
→ probably chert
fine laminations; clay
Are these diamictite clasts?
Granular layer
Wavy clay laminae within silt beds
Silt grade pebbles in a clay-silt matrix
Well rounded, well sorted
GAP IN SECTION
Fine fractures
moderate sorting
Silt + pebble bed
Pebble size/mm
Clay grade mud clasts in granular matrix
Gradational variations in colour (pale-medium grey) thought to reflect gradational variations in grain size, some lenticular clay laminae also found here
Silt grade dropstones in silt bed
14

28/9/12

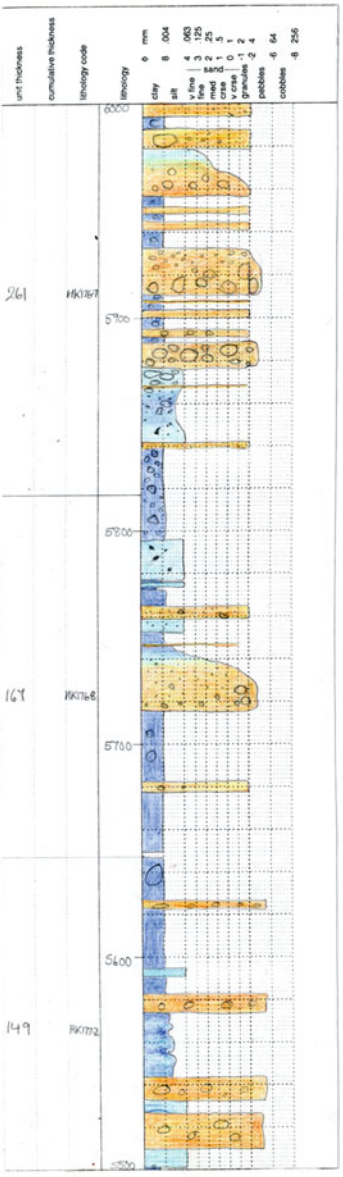

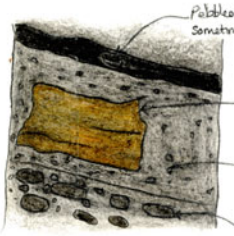

Pebbles in clay layers are often silty, sometimes they are reworked diamictite

Large chert clast in granular layer

Small white angular clasts slightly cloudy appearance - fsp?

Rounded silt grade pebbles in a clay/silt - granular matrix

Interbedded clay + granular layers some with silt-grade rounded pebbles also.

Granular layers have many more white flecks than those below maybe fsp grains → increase in ice flow over felsic source?

Clay flakes in this predominantly silt bed

Granular layer: ?

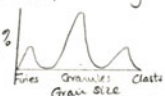

Dropstones are more angular than the pebbles within the layers and sometimes have chert / sandstone compositions.

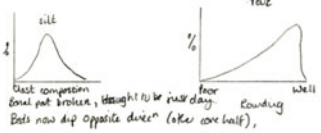

← Clay grade layer with ~1-2mm pebbles.

GAP IN SECTION

Large clay clast in clay layer

Some elongate silt pebbles were probably flattened by compaction

Clay almost clast free here, one ~1mm pebble

Most contacts are slightly wavy and gradational

Parallel silt and clay laminae, streaky appearance

One large ~15mm × 10mm clast, appears to be sandstone dropstone

Pebbles here just silt

A few mud flecks in the silt layer

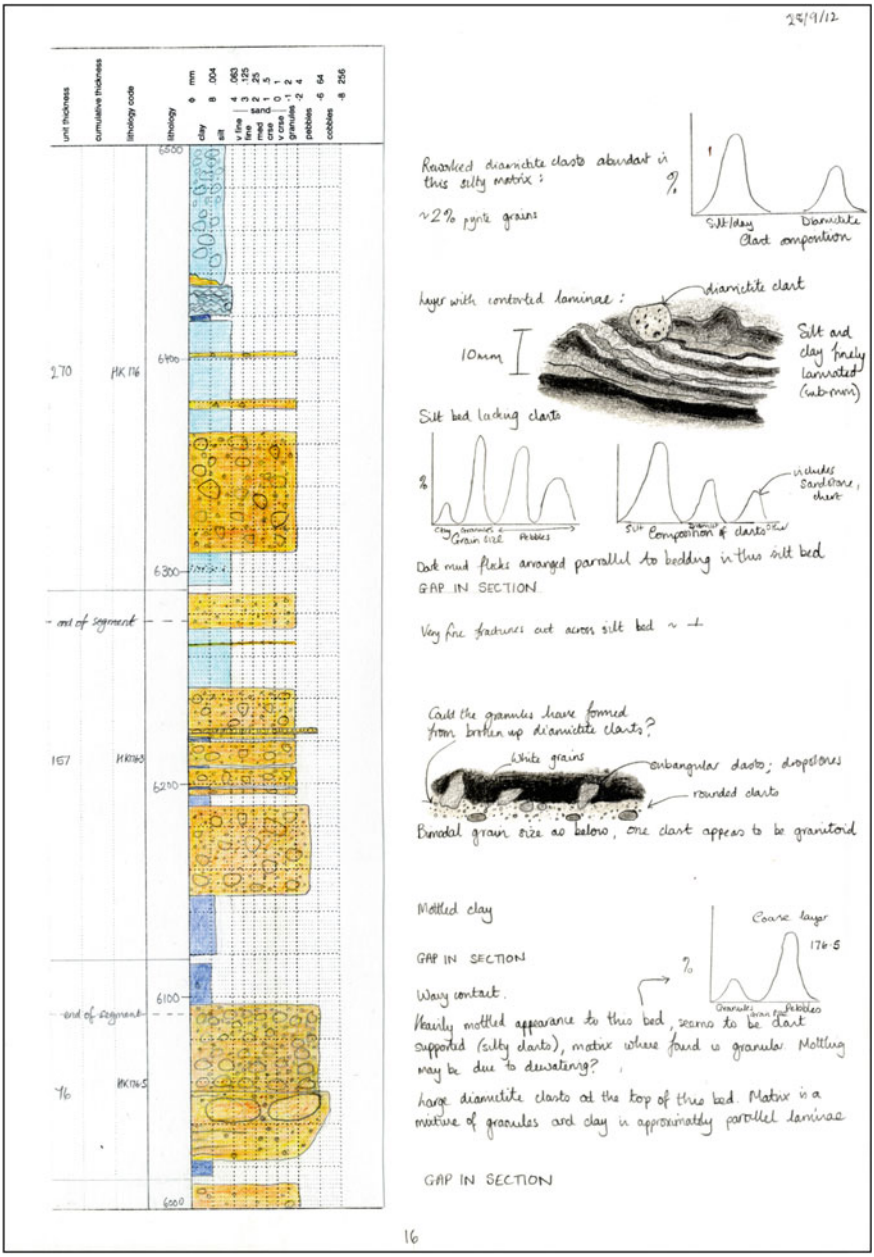
25/9/12
unit thickness
cumulative thickness
lithology code
lithology
clay
silt
sand
granules
pebbles
cobbles
6500
6400
6300
6200
6100
6000
2.70
HK 176
end of segment
1.67
HK 165
Y6
HK 164.5
Reworked diamictite clasts abundant in this silty matrix:
~2% pyrite grains
%
Silt/clay
Diamictite
Clast composition
Layer with contorted laminae:
diamictite clast
10mm
Silt and clay finely laminated (sub-mm)
Silt bed lacking clasts
%
clay
Grain size
pebbles
Composition & clasts
includes Sandstone clast
Dark mud flecks arranged parallel to bedding in this silt bed
GAP IN SECTION
Very fine fractures cut across silt bed ~ ⊥
Could the granules have formed from broken up diamictite clasts?
White grains
subangular clasts; dropstones
rounded clasts
Bimodal grain size as below, one clast appears to be granitoid
Mottled clay
GAP IN SECTION
Wavy contact
Coarse layer
176.5
%
Granules
Pebbles
Patchily mottled appearance to this bed, seems to be clast supported (silty clasts), matrix where found is granular. Mottling may be due to dewatering?
large diamictite clasts at the top of this bed. Matrix is a mixture of granules and clay in approximately parallel laminae
GAP IN SECTION
16

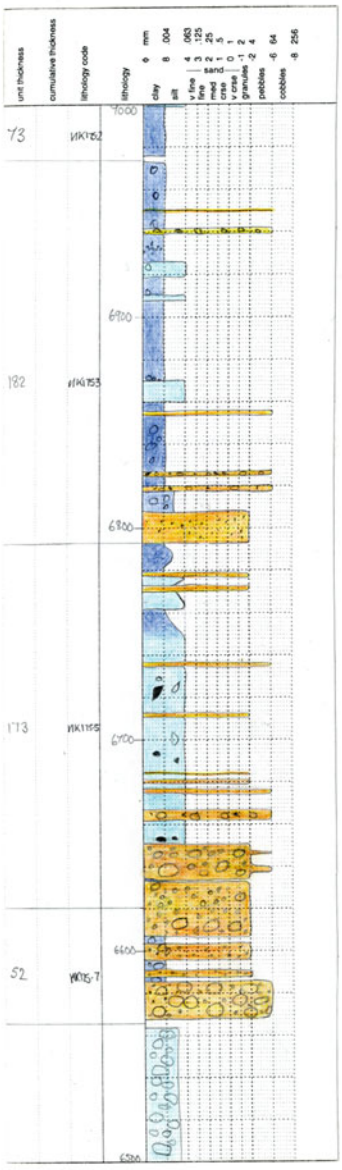

Note: The distinction between a clay bed with pebbles and a pebbly bed is made on the basis of matrix proportion. 29/9/12

GAP IN SECTION

Pronounced set of fine fractures at ~ 45° to beds on cut surface, filled with white mineral probably qz (no effervescence).

Some pebbly concentrations, all sub-mm scale

Rare silt clasts ~ 2mm probably dropstones in these alternating silt and clay beds

Contacts in this segment are all typically wavy and irregular

Pebbly bands may reflect the dumping of material frozen on to the base of ice bergs.

okay eg diamictite, sandstone, qz.

Granular layers comprise angular pyrite grains, rounded black clay(?) grains, quartz (10%), white fsp (<few %), ~3% clasts (sandstone, granite), ~40% silty matrix (< 50%)

Deformed clay clasts in silt beds:

Pyrite (~3%) increase in this unit (Black Rock member) is probably authogenic and indicative of deeper marine conditions where bottom waters have become anoxic.

Laminated chert clast is ~ 10mm x 10mm, all other clasts less.
~1-2% pyrite: angular, ~0.1mm, golden. Authogenic pyrite?
Quartz + white mineral (fsp) make up bulk of granules with rounded black grains of clay? also
Polymodal size of silty pebbles; on average ~ 1mm.
Granular matrix also hosts silty pebbles
Clay matrix in pebble layer but the silt grade pebbles are 'clast supported'

GAP IN SECTION

~ 50% matrix, 50% clasts.

17

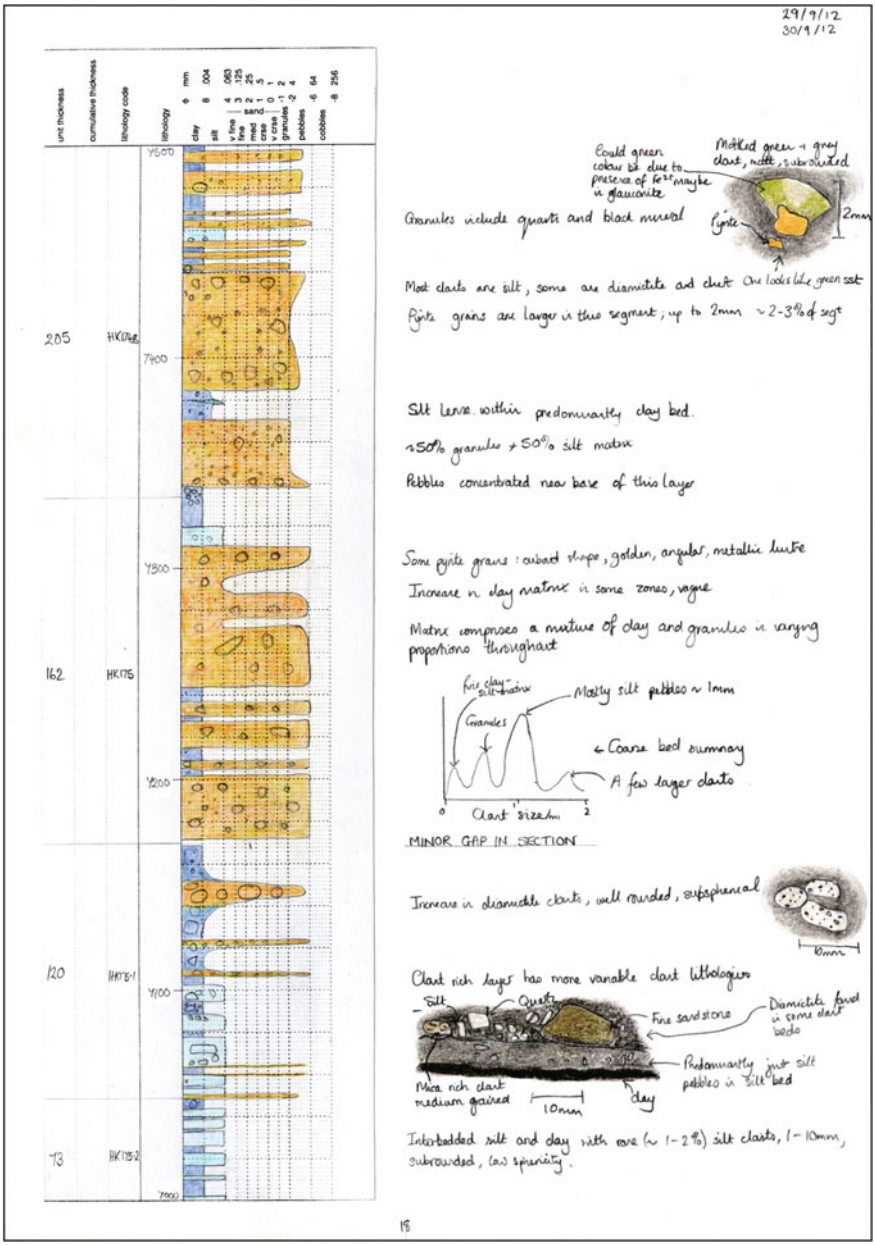
29/9/12
30/9/12
unit thickness
cumulative thickness
lithology code
lithology
clay
silt
sand
granules
pebbles
cobbles
205
HK176
162
HK175
120
HK175-1
43
HK175-2
Y600
Y700
Y800
Y900
Y000
Y100
Y200
Y000
Could green colour be due to preserve of Fe²⁺ maybe in glauconite
Mottled green + grey clast, matrix supported
Pyrite
2mm
Granules include quartz and black mineral
Most clasts are silt, some are diamictite and chert. One looks like green sst
Pyrite grains are larger in this segment; up to 2mm ~2-3% of sed
Silt lense within predominantly clay bed.
~50% granules + 50% silt matrix
Pebbles concentrated near base of this layer
Some pyrite grains: euhedral shape, golden, angular, metallic lustre
Increase in clay matrix in some zones, vague
Matrix comprises a mixture of clay and granules in varying proportions throughout
fine clay-silt matrix
Granules
Muddy silt pebbles ~ 1mm
← Coarse bed summary
A few larger clasts
0
Clast size/m
2
MINOR GAP IN SECTION
Increase in diamictite clasts, well rounded, subspherical
6mm
Clast rich layer has more variable clast lithologies
Silt
Quartz
Fine sandstone
Diamictite found in some clast beds
Predominantly just silt pebbles in silt bed
Mica rich clast medium grained
10mm
clay
Interbedded silt and clay with rare (~ 1-2%) silt clasts, 1-10mm, subrounded, (as) sphericity.
18

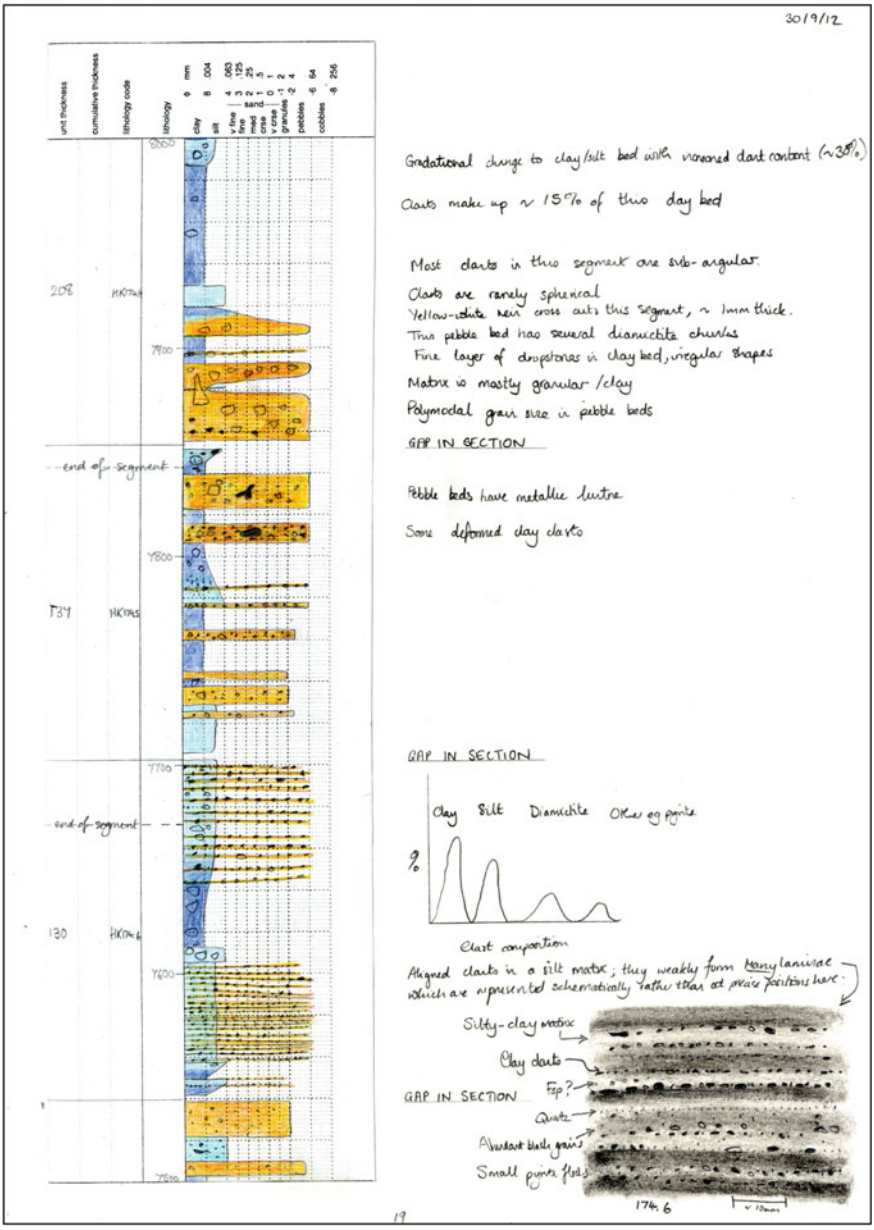
30/9/12
unit thickness
cumulative thickness
lithology code
lithology
φ mm
clay
silt
sand
v fine
fine
med
crse
v crse
granules
pebbles
cobbles
7800
7900
8000
8100
8200
208
HK7M4
end of segment
T37
HK7M3
130
HK7M4
Gradational change to clay/silt bed with increased clast content (~30%)
Clasts make up ~ 15% of this clay bed
Most clasts in this segment are sub-angular
Clasts are rarely spherical
Yellow-white resistant cross cuts this segment, ~ 1mm thick.
This pebble bed has several diamictite chunks
Fine layer of dropstones in clay bed, irregular shapes
Matrix is mostly granular / clay
Polymodal grain size in pebble beds
GAP IN SECTION
Pebble beds have metallic lustre
Some deformed clay clasts
GAP IN SECTION
Clay
Silt
Diamictite
OKm eg pyrite
%
Clast composition
Aligned clasts in a silt matrix; they weakly form many laminae which are represented schematically rather than at precise positions here:
Silty-clay matrix
Clay clasts
GAP IN SECTION
Fzp?
Quartz
Abundant black grains
Small pyrite flecks
174.6
~ 10mm
19

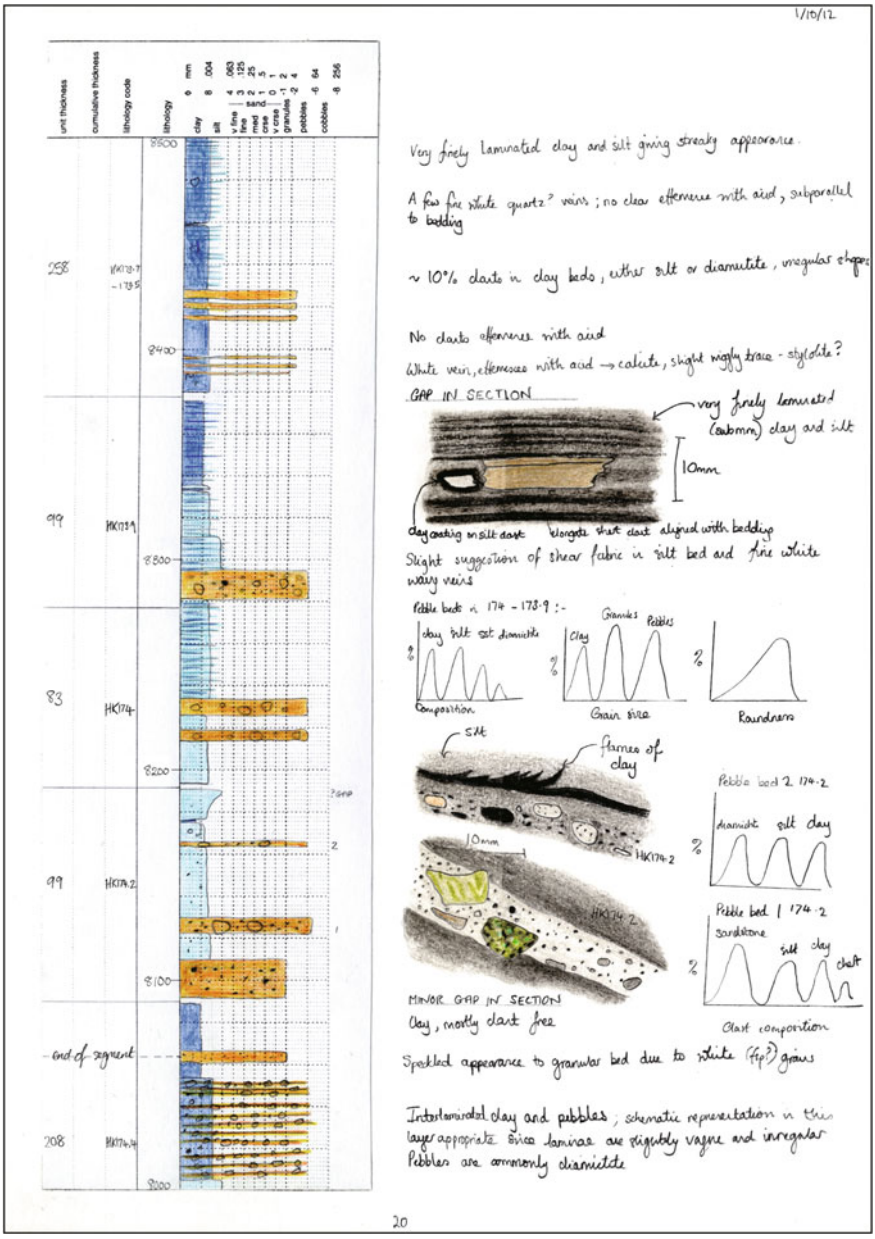
1/10/12
unit thickness
cumulative thickness
lithology code
lithology
clay
silt
sand
v fine
fine
med
crse
v crse
granules
pebbles
cobbles
mm
.004
.063
.125
.25
.5
1
2
4
64
256
8500
8400
8300
8200
8100
8000
258
99
83
99
208
HK173-7
-173.5
HK173-9
HK174
HK174-2
HK174-1
end of segment
Very finely laminated clay and silt giving streaky appearance
A few fine white quartz? veins; no clear effervesce with acid, subparallel to bedding
~ 10% clasts in clay beds, either silt or diamictite, irregular shapes
No clasts effervesce with acid
White veins, effervesce with acid → calcite, slight wiggly trace - stylolite?
GAP IN SECTION
very finely laminated (carbonate) clay and silt
10mm
clay coating on silt clast
elongate clast aligned with bedding
Slight suggestion of shear fabric in silt bed and fine white wavy veins
Pebble beds ~ 174 - 178·9 :-
clay silt sst diamictite
%
Composition
Granules
Pebbles
clay
%
Grain size
%
Roundness
silt
flames of clay
HK174-2
10mm
Pebble bed 2 174·2
diamict
silt
clay
%
HK174-2
Pebble bed 1 174·2
sandstone
silt
clay
chert
%
Clast composition
MINOR GAP IN SECTION
Clay, mostly clast free
Speckled appearance to granular bed due to white (ffp?) grains
Interlaminated clay and pebbles; schematic representation in thin layer appropriate since laminae are slightly vague and irregular
Pebbles are commonly diamictite
20

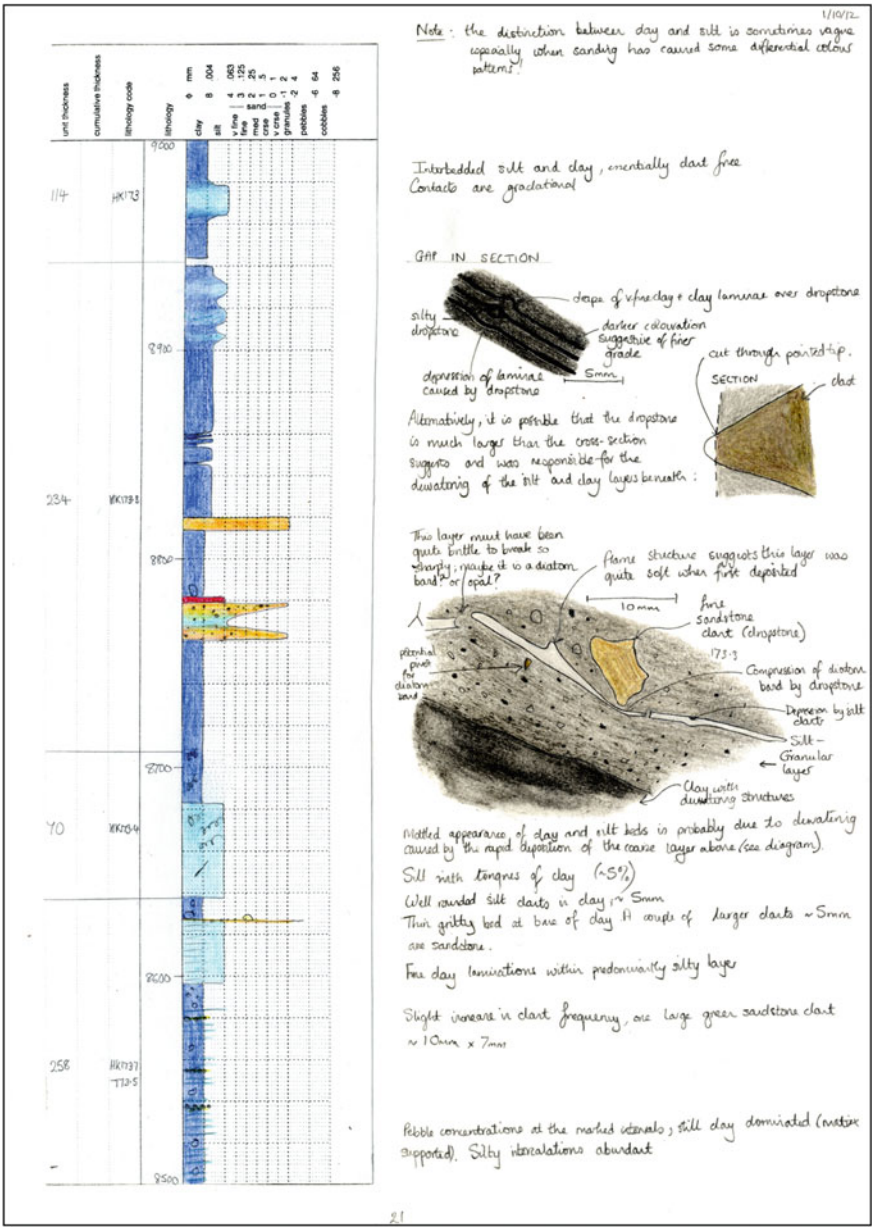
1/10/72
Note: the distinction between clay and silt is sometimes vague especially when sanding has caused some differential colour pattern.
Interbedded silt and clay, eventually clast free
Contacts are gradational
GAP IN SECTION
shape of v.fine clay + clay laminae over dropstone
silty dropstone
darker colouration suggestive of finer grade
5mm
depression of laminae caused by dropstone
Alternatively, it is possible that the dropstone is much larger than the cross-section suggests and was responsible for the dewatering of the silt and clay layers beneath:
cut through pointed tip.
SECTION
clast
This layer must have been quite brittle to break so sharply, maybe it is a diatom band? or opal?
flame structure suggests this layer was quite soft when first deposited
10mm
fine sandstone clast (dropstone)
173-3
Compression of diatom band by dropstone
Depression by silt clasts
Silt - Granular layer
Clay with dewatering structures
potential gaps for diatom band
lithology
clay
silt
v fine
fine
med
crse
v crse
granules
pebbles
cobbles
unit thickness
cumulative thickness
lithology code
9000
8900
8800
8700
8600
8500
114
234
40
258
HK173
HK173-3
HK174
HK173-7
TT2-5
Mottled appearance of clay and silt beds is probably due to dewatering caused by the rapid deposition of the coarse layer above (see diagram).
Silt with tongues of clay (~5%)
Well rounded silt clasts in clay, ~ 5mm
Thin gritty bed at base of clay with couple of larger clasts ~ 5mm are sandstone.
Few clay laminations within predominantly silty layer
Slight increase in clast frequency, one large green sandstone clast ~ 10mm x 7mm
Pebble concentrations at the marked intervals; silt clay dominated (matrix supported). Silty intercalations abundant
21

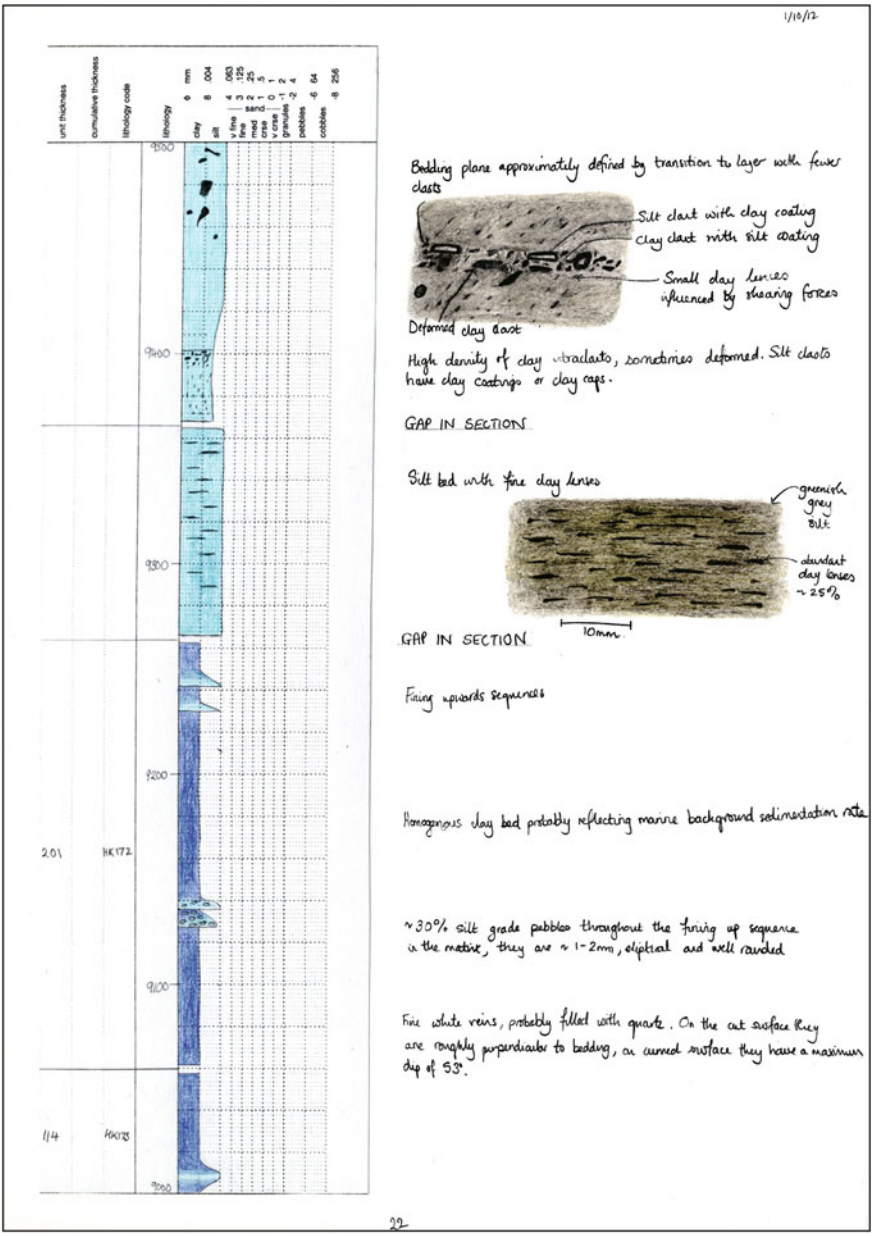
1/10/12
unit thickness
cumulative thickness
lithology code
lithology
clay
silt
sand
pebbles
cobbles
9350
9400
9300
9200
9100
9050
2.01
HK172
1.14
HK173
Bedding plane approximately defined by transition to layer with fewer clasts
Silt clast with clay coating
Clay clast with silt coating
Small clay lenses influenced by shearing forces
Deformed clay clast
High density of clay intraclasts, sometimes deformed. Silt clasts have clay coatings or clay caps.
GAP IN SECTION
Silt bed with fine clay lenses
greenish grey silt
abundant clay lenses ~25%
10mm
GAP IN SECTION
Fining upwards sequences
Homogenous clay bed probably reflecting marine background sedimentation rate
~30% silt grade pebbles throughout the fining up sequence in the matrix, they are ~1-2mm, elliptical and well rounded
Fine white veins, probably filled with quartz. On the cut surface they are roughly perpendicular to bedding, on curved surface they have a maximum dip of 53°.
22

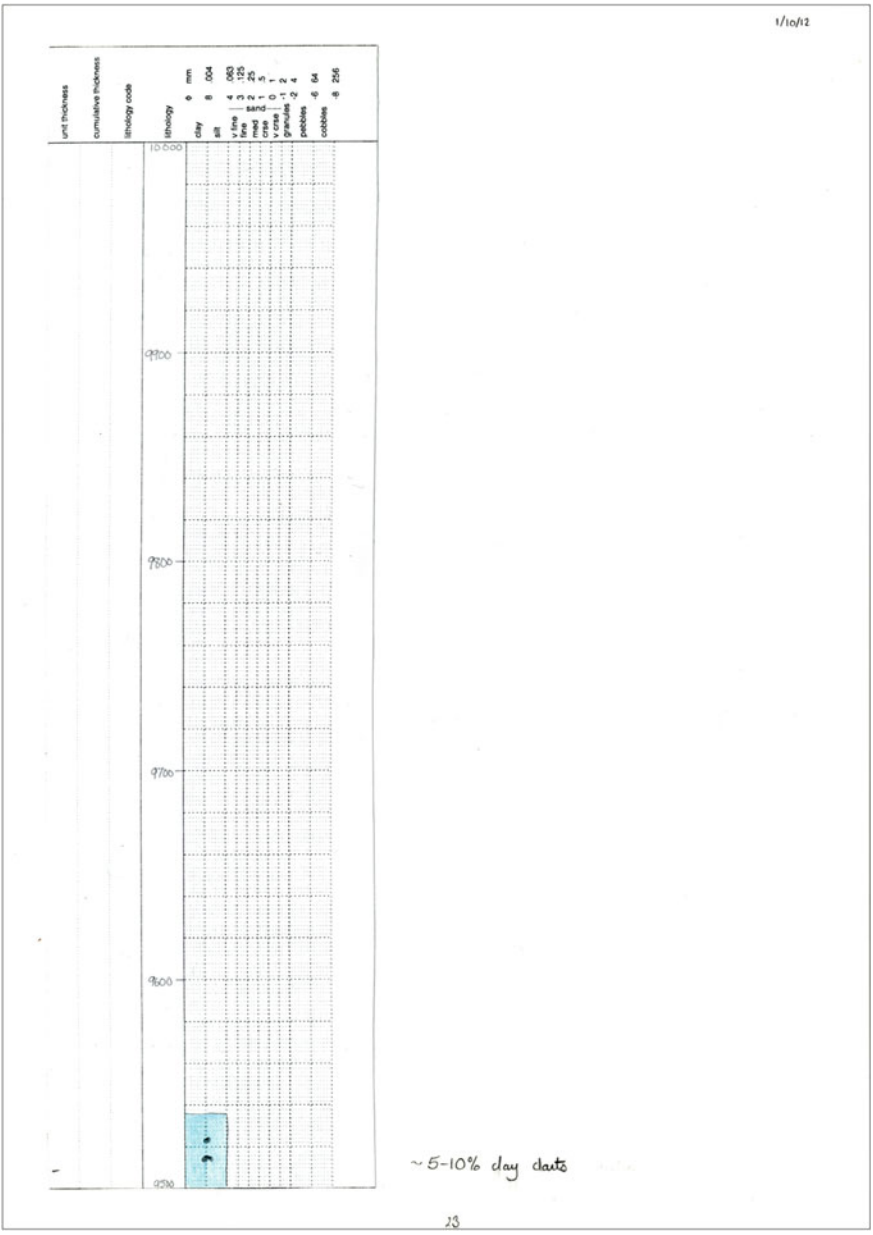
1/10/12
unit thickness
cumulative thickness
lithology code
lithology
φ mm
clay 8 .004
silt 4 .063
v fine 3 .125
fine 2 .25
med 1 .5
crse 0 1
v crse -1 2
granules -2 4
pebbles -6 64
cobbles -8 256
10,000
9900
9800
9700
9600
9530
~5-10% clay clasts
13

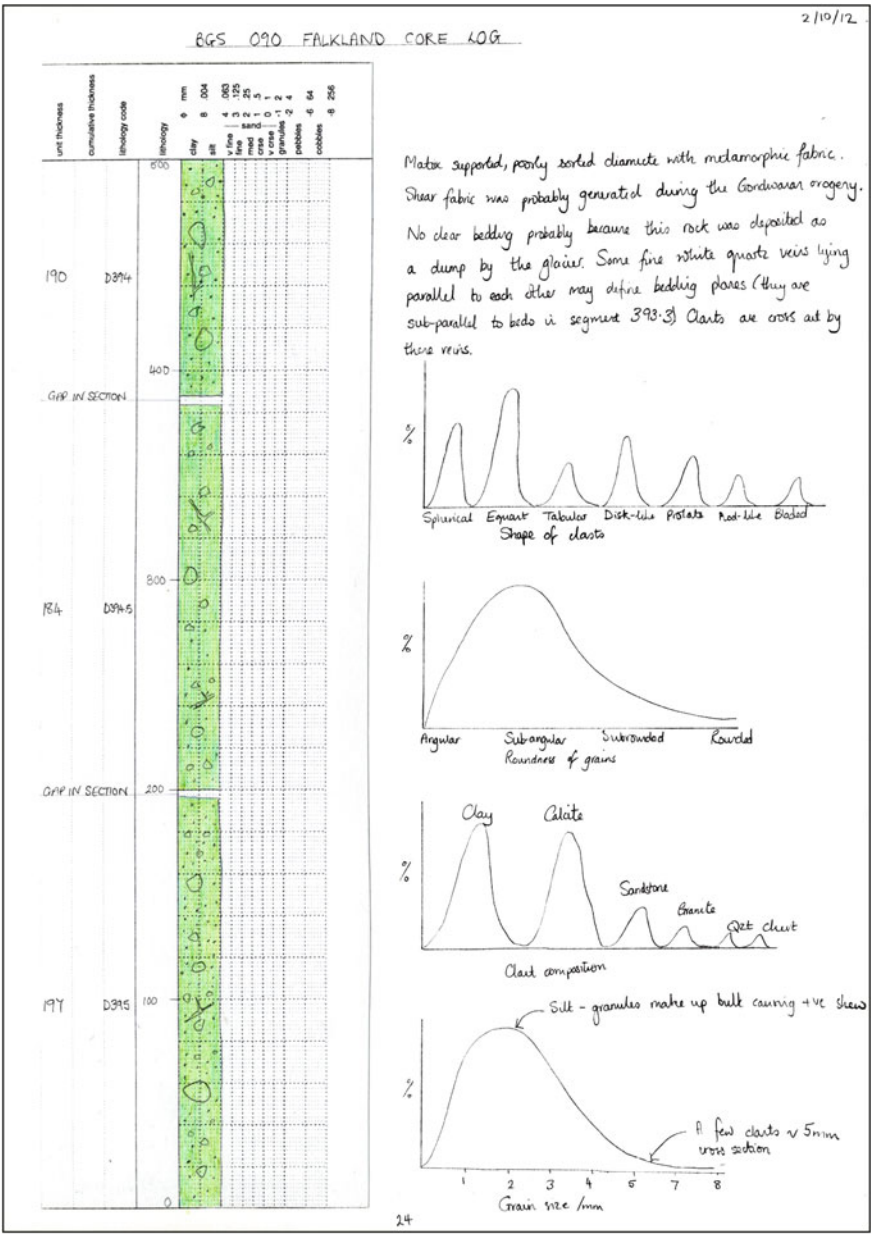
2/10/12
BGS 090 FALKLAND CORE LOG
unit thickness
cumulative thickness
lithology code
lithology
clay
silt
vf fine
f fine
med
crse
v crse
granules
pebbles
cobbles
sand
190
D394
GAP IN SECTION
184
D394.5
GAP IN SECTION
197
D395
600
400
800
200
100
0
Matrix supported, poorly sorted diamicte with metamorphic fabric. Shear fabric was probably generated during the Gondwanan orogeny. No clear bedding probably because this rock was deposited as a dump by the glacier. Some fine white quartz veins lying parallel to each other may define bedding planes (they are sub-parallel to beds in segment 393.3) Clasts are cross cut by these veins.
%
Spherical
Equant
Tabular
Disk-like
Prolate
Rod-like
Bladed
Shape of clasts
%
Angular
Sub-angular
Well-rounded
Rounded
Roundness of grains
%
Clay
Calcite
Sandstone
Granite
Qtz chert
Clast composition
%
Silt - granules make up bulk causing +ve skew
A few clasts > 5mm cross section
1
2
3
4
5
7
8
Grain size /mm
24

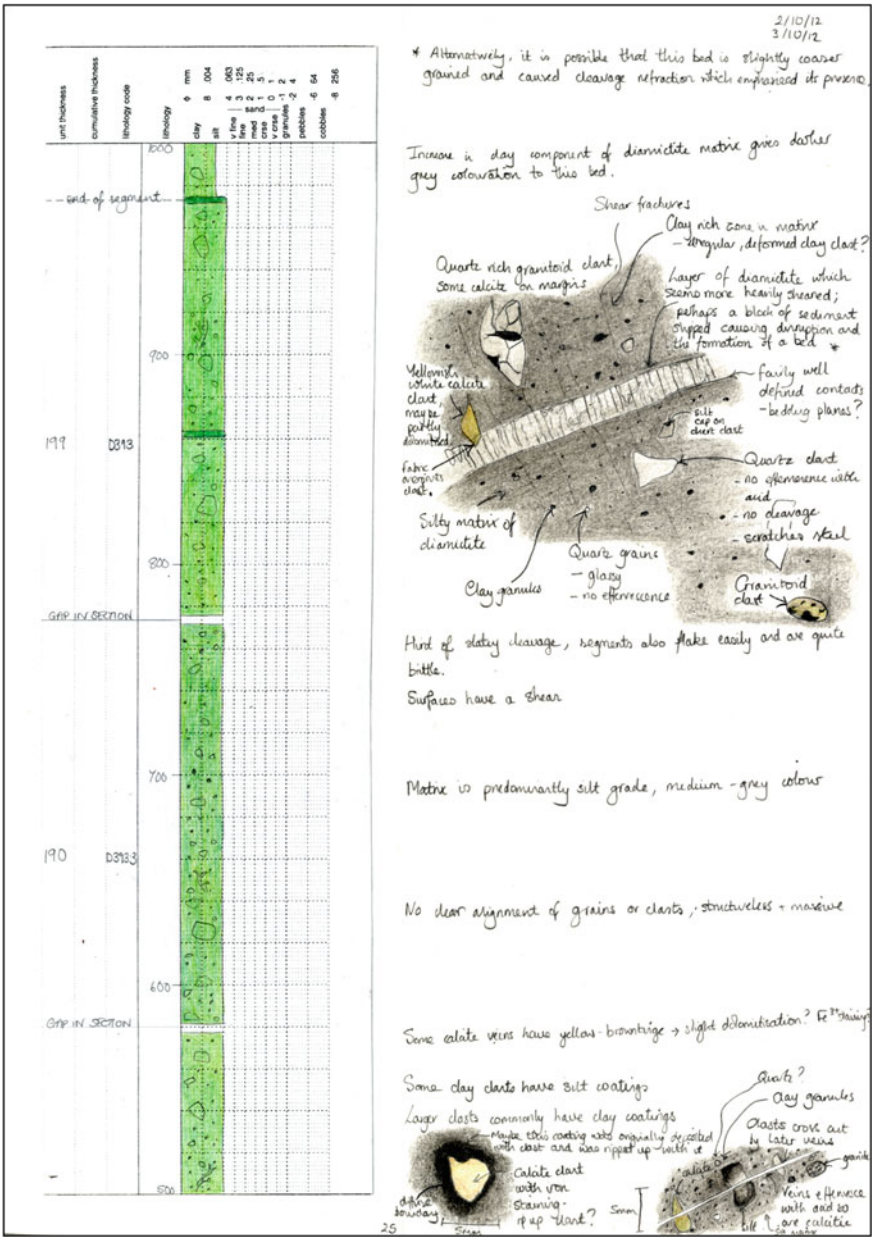
unit thickness
cumulative thickness
lithology code
lithology
φ mm
clay
silt
v fine
fine
med
crse
v crse
granules
pebbles
cobbles
sand
end of segment
199
D813
GAP IN SECTION
190
D3933
GAP IN SECTION
1000
900
800
700
600
500
2/10/12
3/10/12
* Alternatively, it is possible that this bed is slightly coarser grained and caused cleavage refraction which emphasised the process
Increase in clay component of diamictite matrix gives darker grey colouration to this bed.
Shear fractures
Clay rich zone in matrix - irregular, deformed clay clast?
Quartz rich granitoid clast, some calcite on margins
Layer of diamictite which seems more heavily sheared; perhaps a block of sediment slipped causing disruption and the formation of a bed *
Yellowish volute calcite clast, may be partly dissolved
Fairly well defined contacts - bedding planes?
silt cap on clast
Quartz clast
- no effervescence with acid
- no cleavage
- scratches steel
Fabric of clasts
Silty matrix of diamictite
Quartz grains
- glassy
- no effervescence
Clay granules
Granitoid clast
Hint of slaty cleavage, segments also flake easily and are quite brittle.
Surfaces have a sheen
Matrix is predominantly silt grade, medium - grey colour
No clear alignment of grains or clasts, structureless + massive
Some calcite veins have yellow-brown tinge → slight dolomitisation? Fe staining?
Some clay clasts have silt coatings
Larger clasts commonly have clay coatings
Maybe this coating was originally associated with clast and was ripped up with it
Calcite clast with iron staining - ripped up clast?
diffuse boundary
5mm
Quartz?
Clay granules
Clasts cross cut by later veins
calcite
Veins of fine/coarse calcite
25

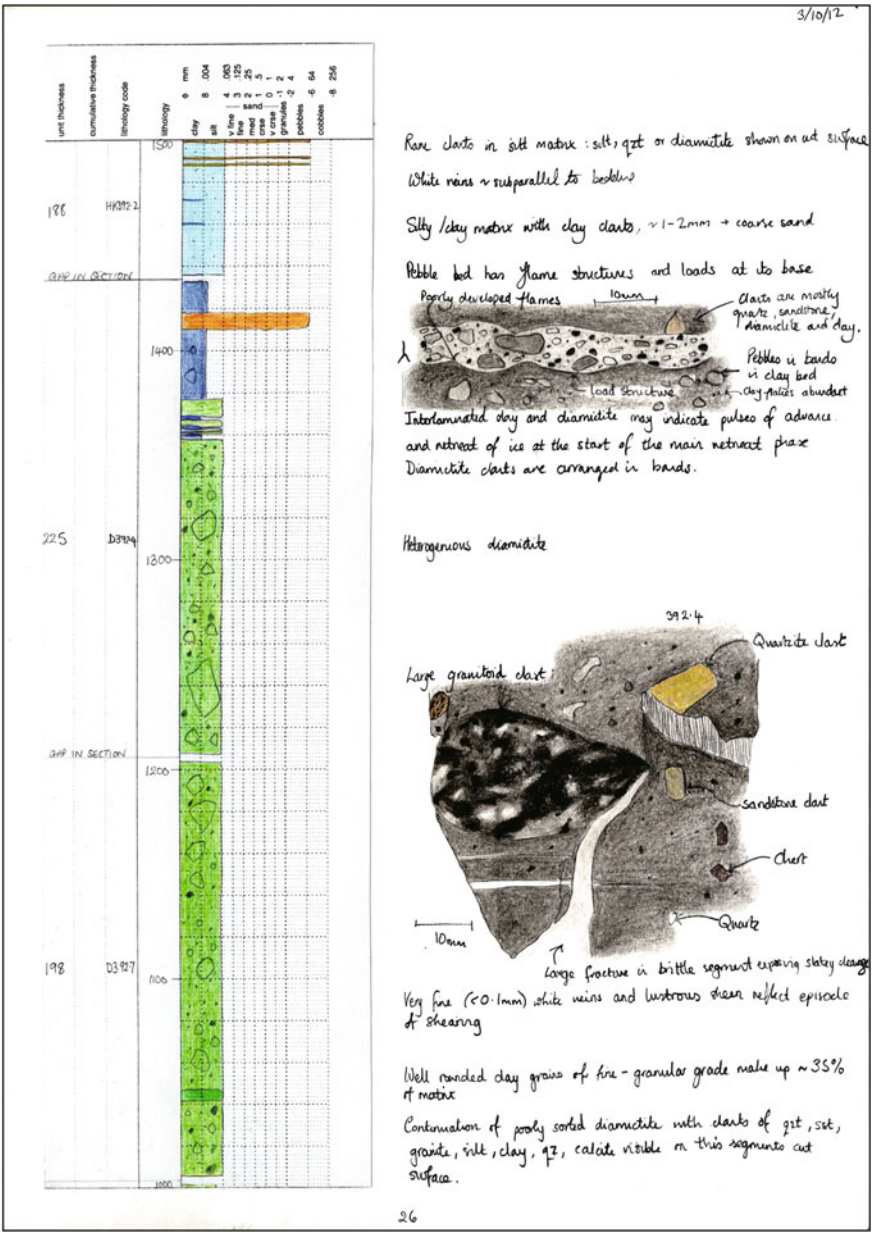
3/10/12
unit thickness
cumulative thickness
lithology code
lithology
mm
clay
silt
sand
pebbles
cobbles
1500
188
HK392.2
GAP IN SECTION
1400
225
D3924
1300
GAP IN SECTION
1200
198
D3927
1100
1000
Rare clasts in silt matrix : silt, qzt or diamictite shown on cut surface
White veins ~ subparallel to bedding
Silty / clay matrix with clay clasts, ~1-2mm + coarse sand
Pebble bed has flame structures and loads at its base
Poorly developed flames
10mm
Clasts are mostly quartz, sandstone, diamictite and clay.
Pebbles in bands in clay bed
Load structure
Clay flakes abundant
Interlaminated clay and diamictite may indicate pulses of advance and retreat of ice at the start of the main retreat phase
Diamictite clasts are arranged in bands.
Heterogeneous diamictite
392.4
Quartzite clast
Large granitoid clast
Sandstone clast
Chert
Quartz
10mm
Large fracture in brittle segment exposing slatey cleavage
Very fine (<0.1mm) white veins and lustrous shear reflect episodic shearing
Well rounded clay grains of fine - granular grade make up ~35% of matrix
Continuation of poorly sorted diamictite with clasts of grit, sst, granite, silt, clay, qz, calcite visible on this segments cut surface.
26

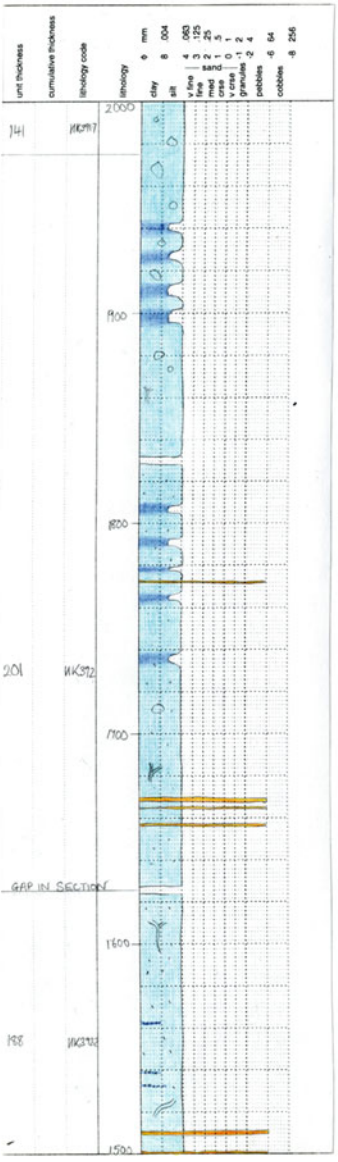

4/10/12

Note : It will be important to do a more thorough analysis of clast composition (with %) for both cores but maybe this should be performed on a broader scale since the current log has been summarised.

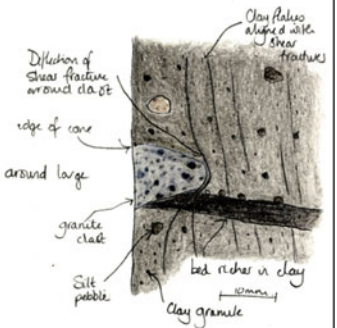

Pebble beds of this segment :

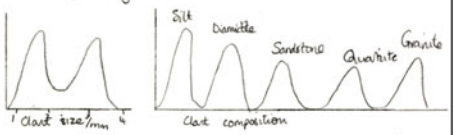

Some layers of increased clay content visible under DI water

Vein sub-parallel to bedding (calcite)

Clast analysis later identified a fourth coarse band at ~ 10mm up this segment

White veins up to 1.5mm thick effervesce with acid ; they are calcite

Fine, ~ 0.1 - 0.4mm, clay flakes are aligned in bands // bedding .

Thin pebble beds may reflect fall out from the base of the ice sheet . Flame structures indicate that the sediments were deposited in an aqueous environment ; perhaps the ice sheet had extended over the ocean .

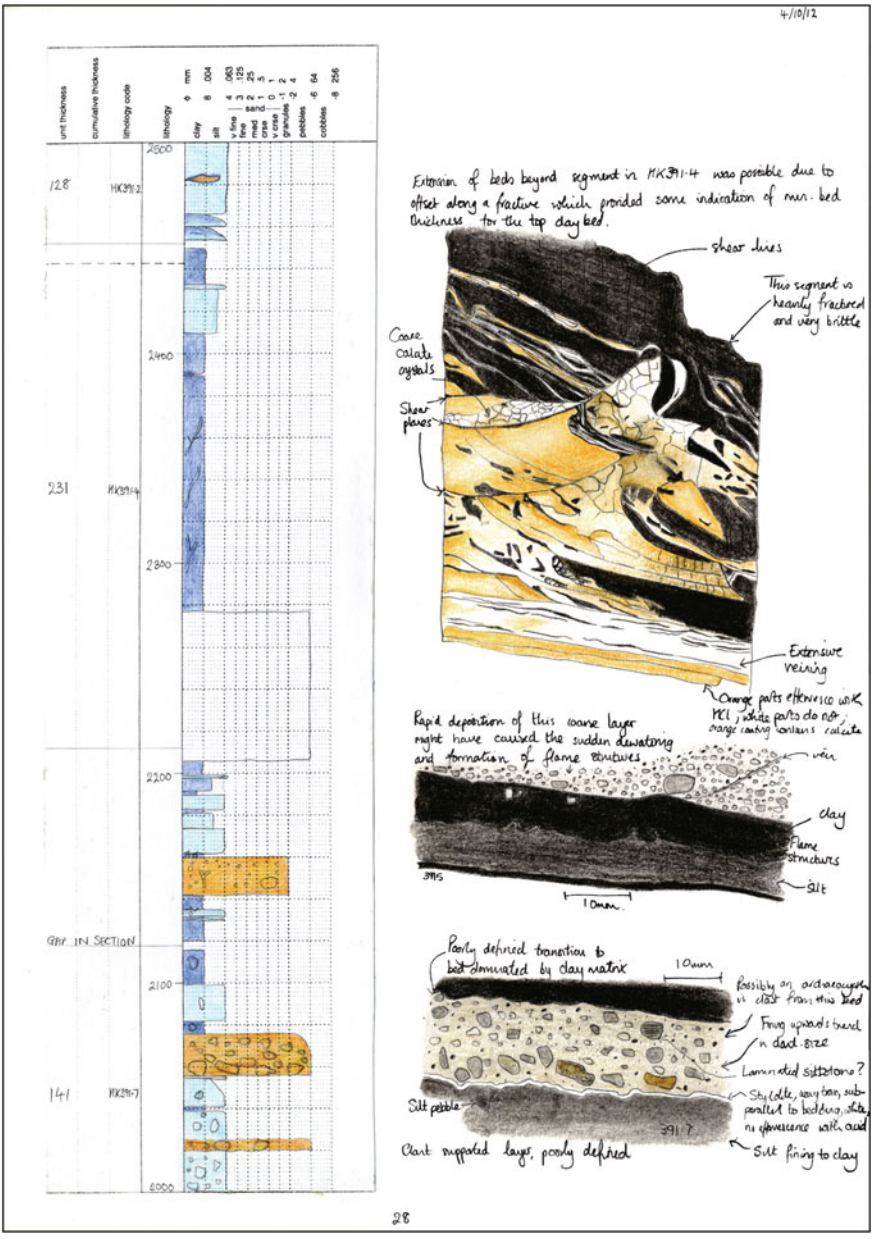
4/10/12
unit thickness
cumulative thickness
lithology code
lithology
clay
silt
sand
pebbles
cobbles
128
HK3912
231
HK3914
141
HK3917
2600
2400
2300
2200
2100
2000
GAP IN SECTION
Extension of beds beyond segment in HK3911-4 was possible due to offset along a fracture which provided some indication of min. bed thickness for the top clay bed.
shear lines
This segment is heavily fractured and very brittle
Coarse calcite crystals
Shear planes
Extensive veining
Orange parts of this core will HCl, white parts do not, orange coating contains calcite
Rapid deposition of this coarse layer might have caused the sudden dewatering and formation of flame structures.
vein
clay
Flame structures
silt
3915
10mm
Poorly defined transition to bed dominated by clay matrix
10mm
Possibly an orthoquartzite clast from this bed
Fining upwards trend in clast size
Laminated siltstone?
Silt pebble
Steeply dipping, wavy base, sub-parallel to bedding, slight effervescence with acid
3911.7
Clast supported layer, poorly defined
Silt fining to clay
28

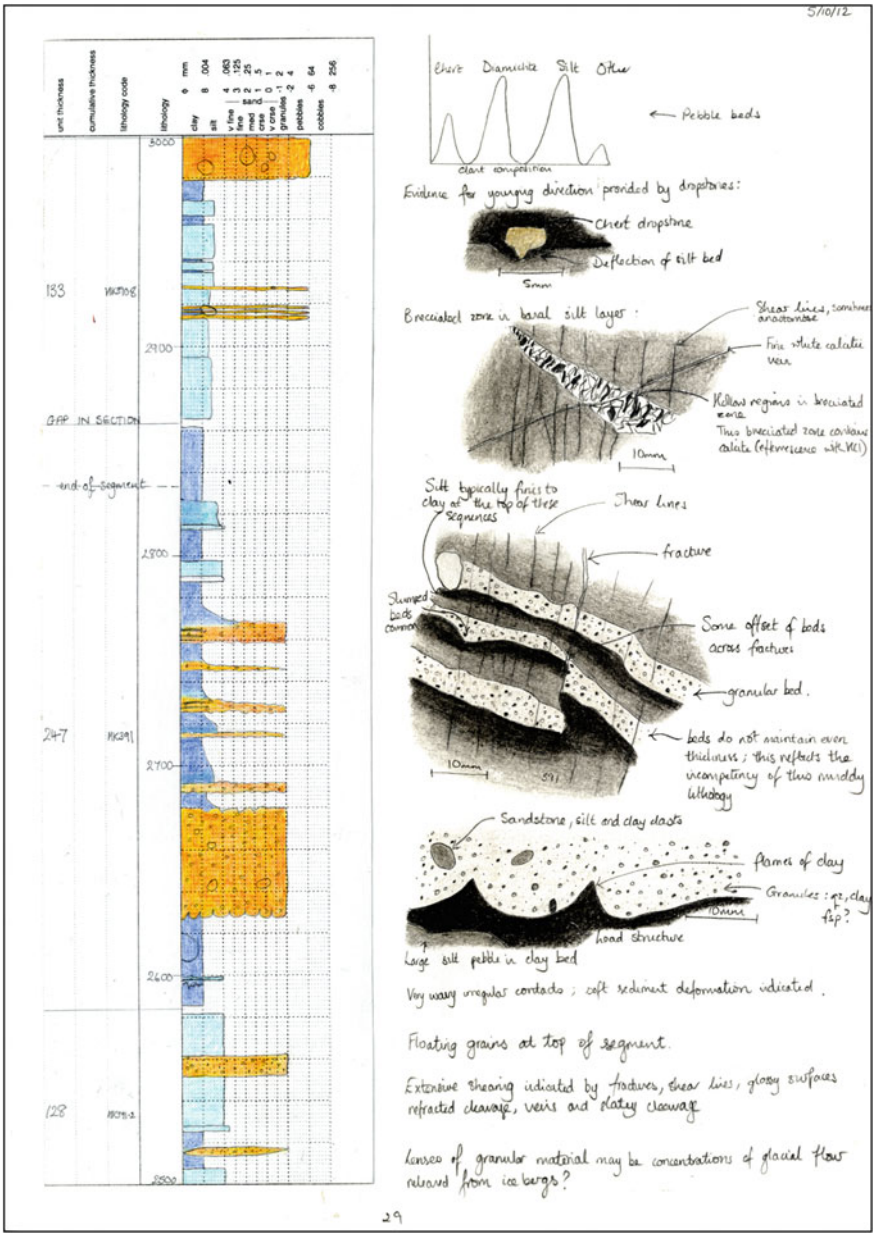
5/10/12
unit thickness
cumulative thickness
lithology code
lithology
clay
silt
v fine
fine
med
crse
v crse
granules
pebbles
cobbles
mm
sand
3000
2900
2800
2700
2600
2500
133
247
128
GAP IN SECTION
end-of-segment
Chert
Diamictite
Silt
Other
Pebble beds
clast composition
Evidence for younging direction provided by dropstones:
Chert dropstone
Deflection of silt bed
5mm
Brecciated zone in basal silt layer:
Shear lines, sometimes anastomose
Fine white calcite veins
Yellow regions in brecciated zone
This brecciated zone contains calcite (cf. presence with WC1)
10mm
Silt typically fines to clay at the top of these sequences
Shear lines
fracture
Slumped beds common
Some offset of beds across fractures
granular bed.
Beds do not maintain even thickness; this reflects the incompetency of this muddy lithology
10mm
Sandstone, silt and clay clasts
flames of clay
Granules: qz, clay ftp?
10mm
load structure
Large silt pebble in clay bed
Very wavy irregular contacts; soft sediment deformation indicated.
Floating grains at top of segment.
Extensive shearing indicated by fractures, shear lines, glossy surfaces refracted cleavage, veins and flaky cleavage
Lenses of granular material may be concentrations of glacial flour released from ice bergs?
29

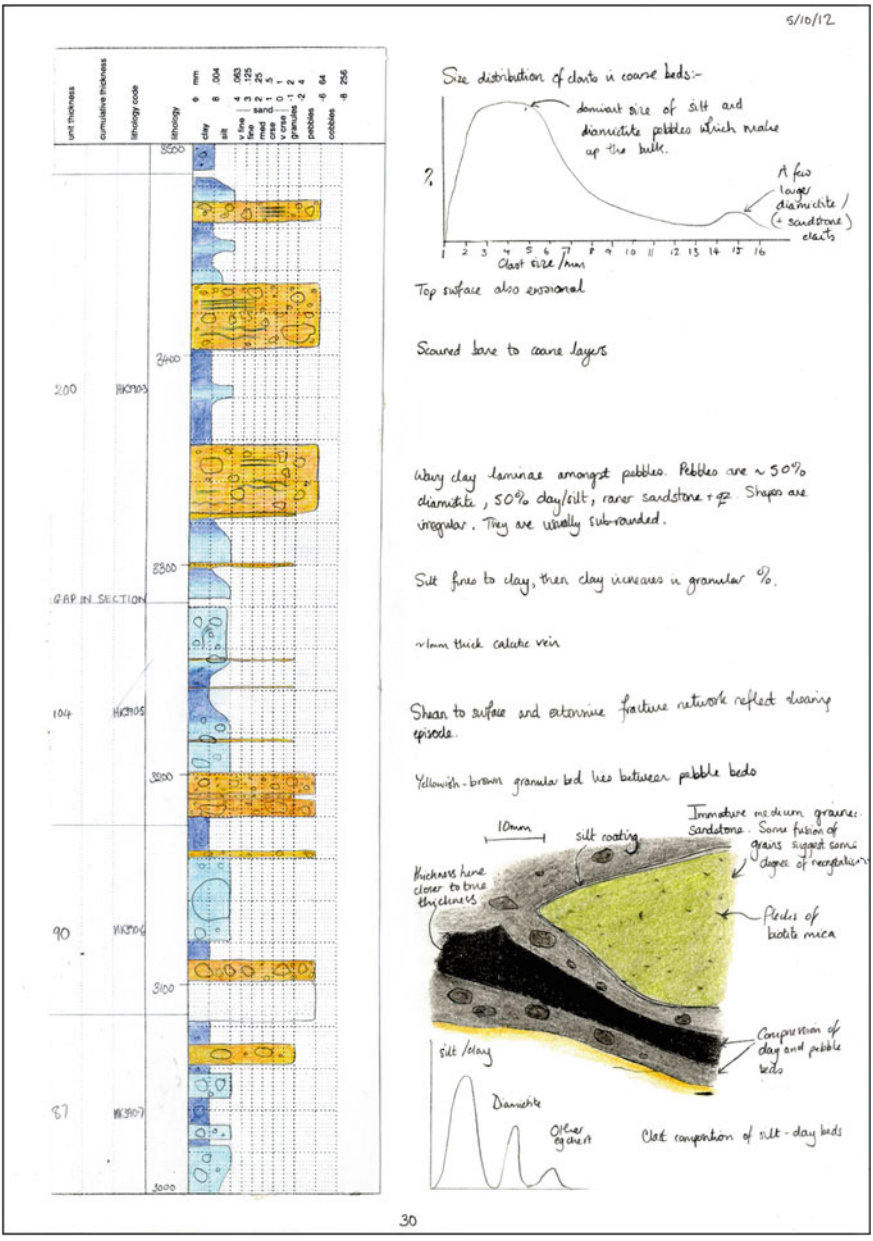
5/10/12
unit thickness
cumulative thickness
lithology code
lithology
clay
silt
sand
granules
pebbles
cobbles
3500
3400
3300
3200
3100
3000
GAP IN SECTION
Size distribution of clasts in coarse beds:-
dominant size of silt and diamictite pebbles which make up the bulk.
A few larger diamictite / (+ sandstone) clasts
%
Clast size /mm
Top surface also erosional
Scoured base to coarse layers
Silty clay laminae amongst pebbles. Pebbles are ~50% diamictite, 50% clay/silt, rarer sandstone + qz. Shapes are irregular. They are usually sub-rounded.
Silt fines to clay, then clay increases in granular %.
~1mm thick calcite vein
Shear to surface and extensive fracture network reflect shearing episode.
Yellowish-brown granular bed lies between pebble beds
10mm
silt coating
Immature medium grained Sandstone. Some fusion of grains suggest some degree of recrystallisation
thickness here closer to true thickness
Flecks of biotite mica
Compression of clay and pebble beds
silt/clay
Diamictite
Other eg chert
Clast composition of silt-clay beds

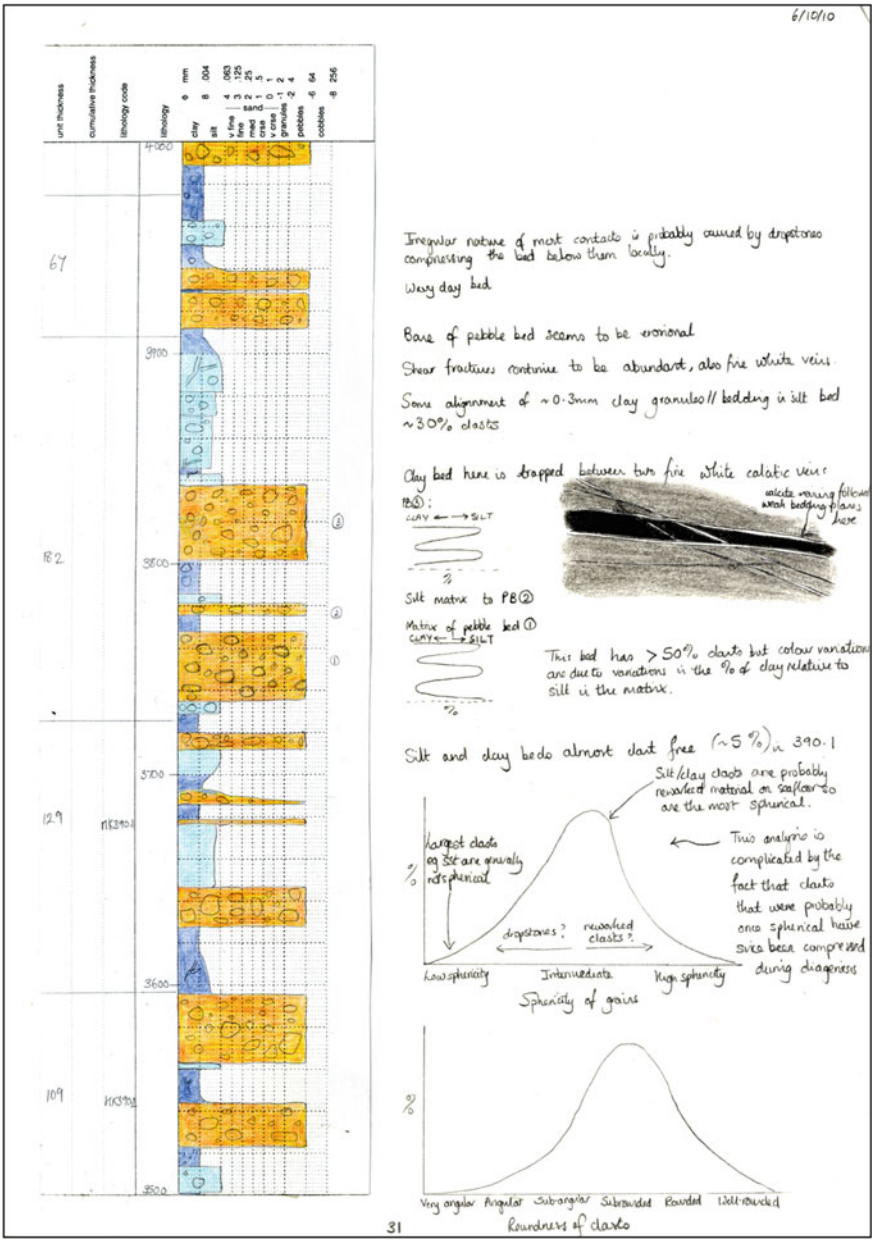
6/10/10
unit thickness
cumulative thickness
lithology code
lithology
clay
silt
sand
pebbles
cobbles
4000
3900
3800
3700
3600
3500
67
182
129
109
Irregular nature of most contacts is probably caused by dropstones compressing the bed below them locally.
Very clay bed
Base of pebble bed seams to be erosional
Shear fractures continue to be abundant, also fine white veins
Some alignment of ~0·3mm clay granules // bedding in silt bed
~30% clasts
Clay bed here is trapped between two fine white calcite veins
PB③:
CLAY ← → SILT
Silt matrix to PB②
Matrix of pebble bed ①
CLAY ← → SILT
%
calcite veins following weak bedding of silt here
This bed has >50% clasts but colour variations are due to variations in the % of clay relative to silt in the matrix.
Silt and clay beds almost clast free (~5%) in 390.1
Silt/clay clasts are probably reworked material on seafloor so are the most spherical.
Largest clasts eg SSt are usually not spherical
Thus analysis is complicated by the fact that clasts that were probably once spherical have since been compressed during diagenesis
%
dropstones?
reworked clasts?
low sphericity
Intermediate
high sphericity
Sphericity of grains
%
Very angular
Angular
Subangular
Subrounded
Rounded
Well rounded
Roundness of clasts
31

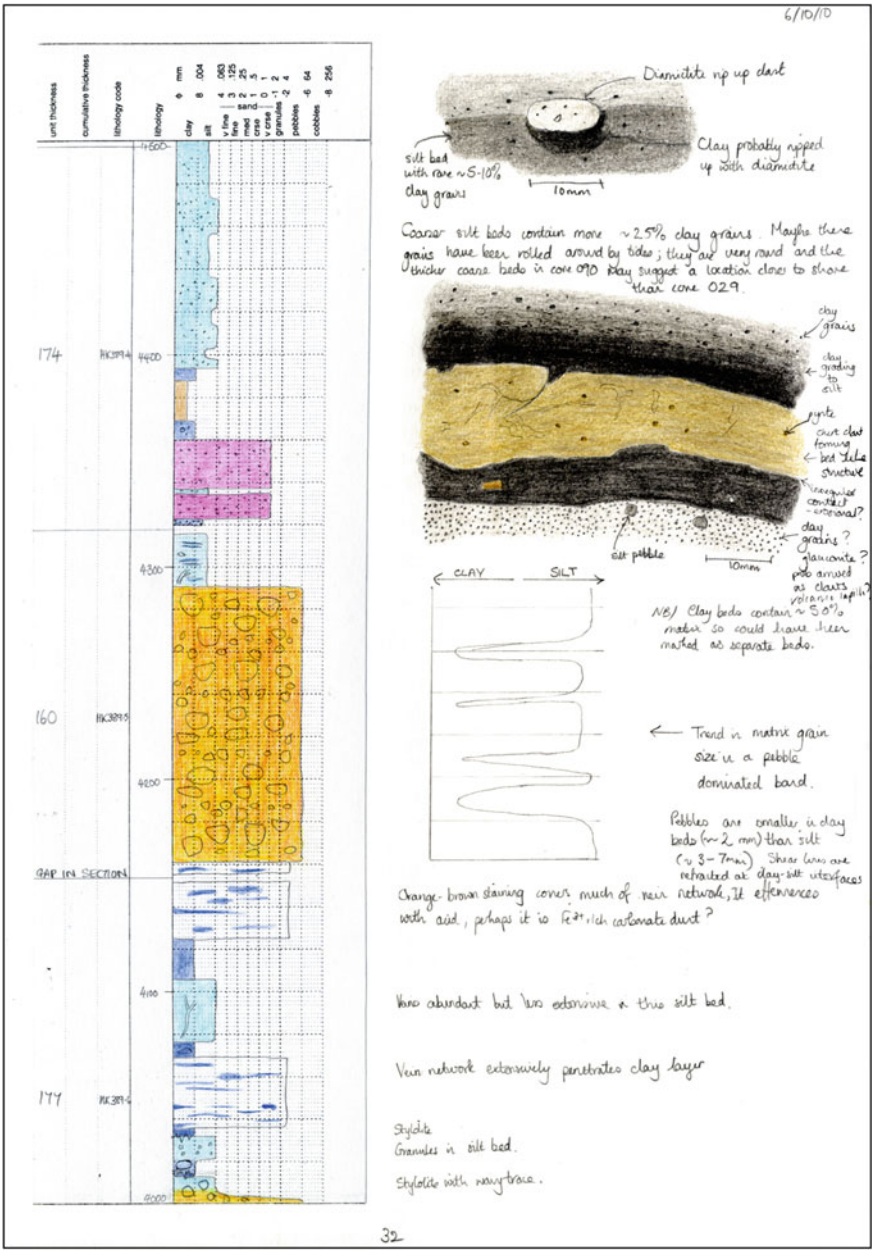
6/10/10
unit thickness
cumulative thickness
lithology code
lithology
mm
clay
silt
sand
v fine
fine
med
coarse
v coarse
granules
pebbles
cobbles
174
HK3914
4400
160
HK3915
4050
GAP IN SECTION
4100
177
HK3916
4000
Diamictite ripped up clast
Clay probably ripped up with diamictite
silt bed with rare ~5-10% clay grains
10mm
Coarser silt beds contain more ~2.5% clay grains. Maybe these grains have been rolled around by tides; they are very round and blue. Thicker coarse beds in core 090 may suggest a location closer to shore than core 029.
clay grains
clay grading to silt
pyrite
quartz clast forming bed load structure
irregular contact - erosional?
clay grains?
glauconite?
pods arrived as clasts volcanic tuff?
silt pebble
10mm
CLAY
SILT
NB/ Clay beds contain ~30% matrix so could have been mapped as separate beds.
Trend in matrix grain size in a pebble dominated bed.
Pebbles are smaller in clay beds (~2 mm) than silt (~3–7mm). Shear lines are retracted at clay-silt interfaces
Orange-brown staining covers much of vein network, it effervesces with acid, perhaps it is Fe²⁺ rich carbonate dust?
Vein abundant but less extensive in thin silt bed.
Vein network extensively penetrates clay layer
Stylolite
Granules in silt bed.
Stylolite with wavy trace.

7/10/10

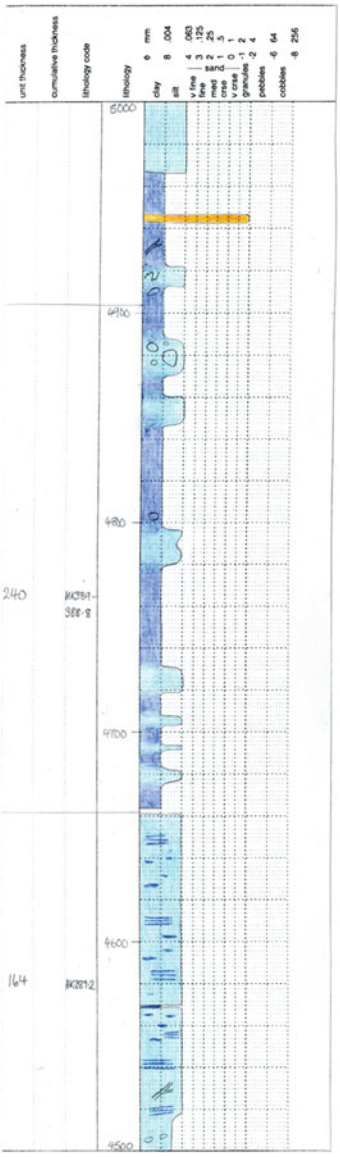

This silt bed and the overlying clay bed have variable thicknesses due to pressure dissolution

Granite, set + diamictite clast + silt clasts in this granular bed
Curved bedding planes typical.

1% calcite veins subparallel to bedding

~ 20% clasts in this silt bed: diamictite and silt

Sandstone clast ~ 4 x 3mm, medium grained
Interbedded clay and silt with gradational contacts.

Abundant shear lines ~ perpendicular to beds on cut surface.

Rise in silt after possible volcanic lapilli / clay granules may reflect more distal deposition to the glacier front

Some clay flakes and lenses

Fine (sub mm) lamination gives streaky appearance.

No dropstones

Vein is calcite.

A few ~ 20% well rounded silt pebbles in finer silt band.

33

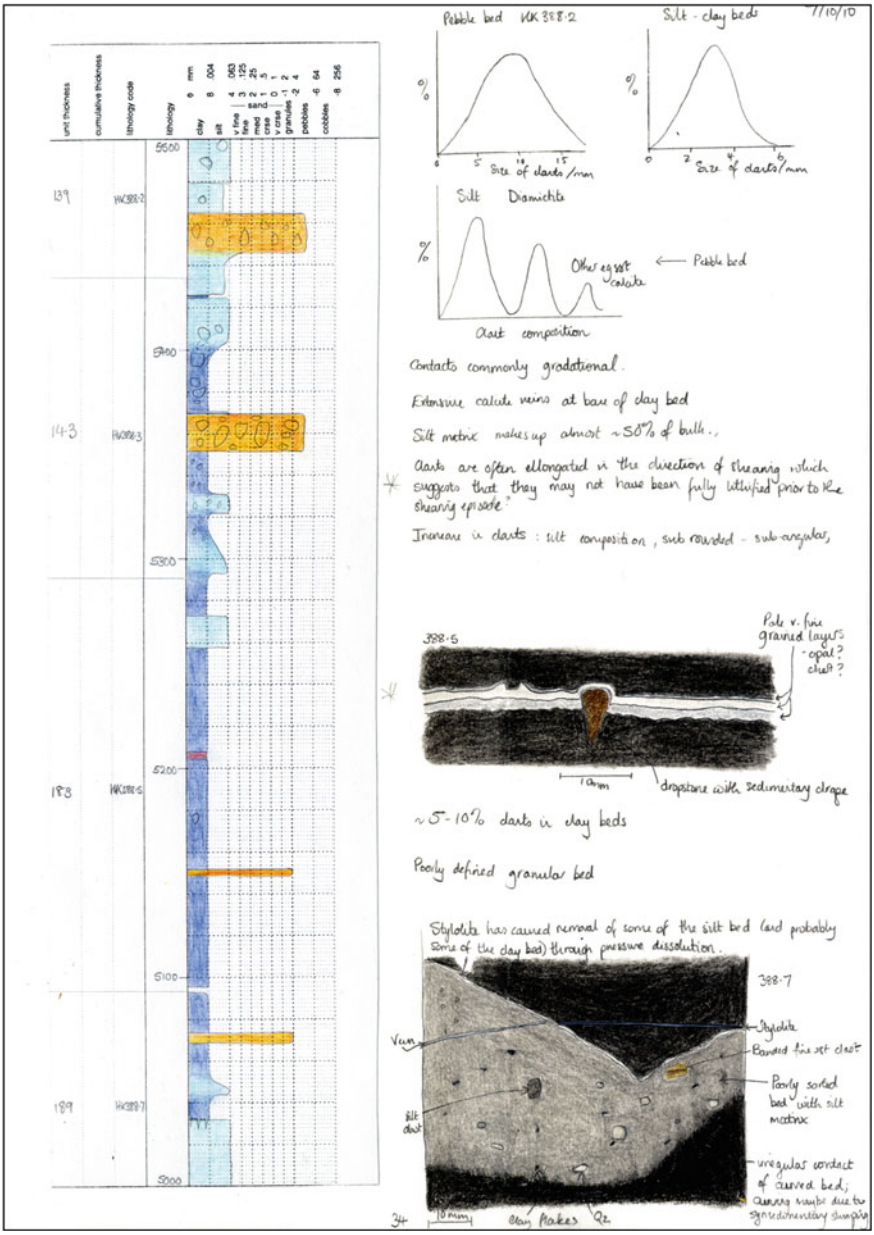
Pebble bed VK 388-2
Silt - clay bed
7/10/10
Size of clasts/mm
Silt
Diamictite
Other exotic calcite
Pebble bed
Clast composition
Contacts commonly gradational.
Extensive calcite veins at base of clay bed
Silt matrix makes up almost ~50% of bulk.
Clasts are often elongated in the direction of shearing which suggests that they may not have been fully lithified prior to the shearing episode.
Increase in clasts : silt composition, sub rounded - sub angular,
388-5
Pale v. fine grained layers - opal? chert?
dropstone with sedimentary drape
~5-10% clasts in clay beds
Poorly defined granular bed
Stylolite has caused removal of some of the silt bed (and probably some of the clay bed) through pressure dissolution.
388-7
Stylolite
Poorly sorted bed with silt matrix
irregular contact of curved bed; cannot rule out due to sedimentary slumping
clay flakes
Qz
139
143
183
199
5600
5400
5300
5200
5100
5000

8/10/10

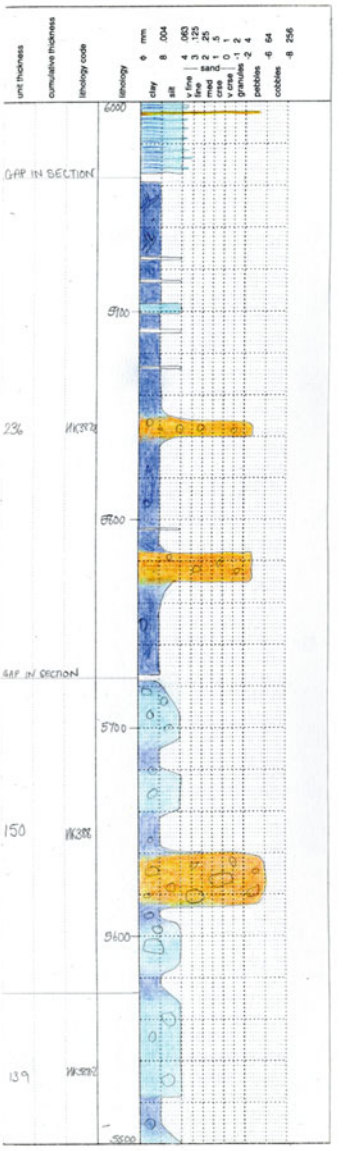

Sub-mm - parallel laminations of clay and silt - varves?

Eroval (~5%) silt pebbles average ~ 1-2 mm diameter

Calcite veining quite extensive, sometime // to bedding planes. No obvious pressure dissolution associated with them.

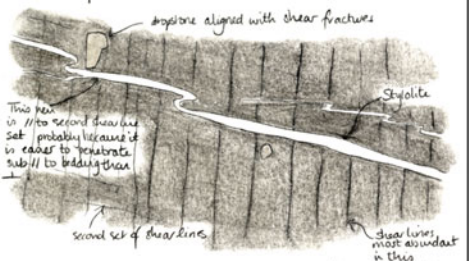

Granular beds are rich in ~ 1-2 mm silt clasts.

~ 5% clasts in clay bed

Some of the silt beds contain black granules similar to those in "389.4m": magnetite? clay?

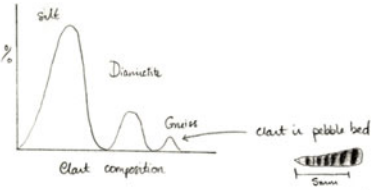

Pebble beds have more lithological variety generally (as would be expected).

Pebbles in silt and clay beds are generally silt with occasional diamictite (~25%) and rare other clasts eg granite (< 5%)

35

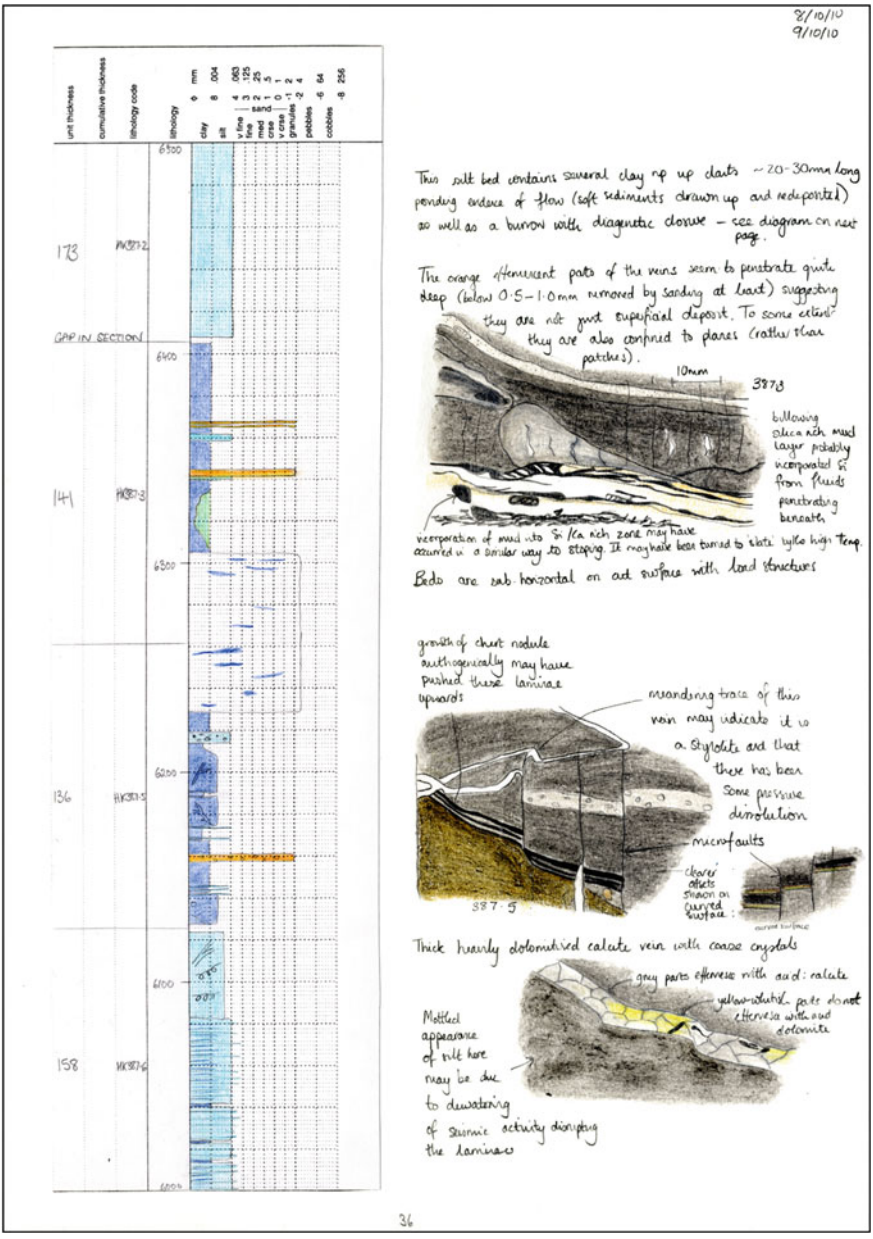
8/10/10
9/10/10
unit thickness
cumulative thickness
lithology code
lithology
clay
silt
sand
fine
med
coarse
granules
pebbles
cobbles
mm
173
141
136
158
GAP IN SECTION
6500
6400
6300
6200
6100
6000
This silt bed contains several clay rip up clasts ~20-30mm long pending evidence of flow (soft sediments drawn up and redeposited) as well as a burrow with diagenetic closure – see diagram on next page.
The orange ferruginous parts of the veins seem to penetrate quite deep (below 0.5–1.0mm removed by sanding at least) suggesting they are not just superficial deposit. To some extent they are also confined to planes (rather than patches).
10mm
3878
billowing silica rich mud layer probably incorporated Si from fluids penetrating beneath
incorporation of mud into Si rich zone may have occurred in a similar way to stoping. It may have been turned to slate by high temp.
Beds are sub horizontal on cut surface with load structures
growth of chert nodule authigenically may have pushed these laminae upwards
meandering trace of this vein may indicate it is a stylolite and that there has been some pressure dissolution
microfaults
clearer offsets shown on curved surface
3875
Thick heavily dolomitised calcite vein with coarse crystals
grey parts effervesce with acid: calcite
yellow-stained parts do not effervesce with acid: dolomite
Mottled appearance of silt here may be due to dewatering of seismic activity disrupting the laminae

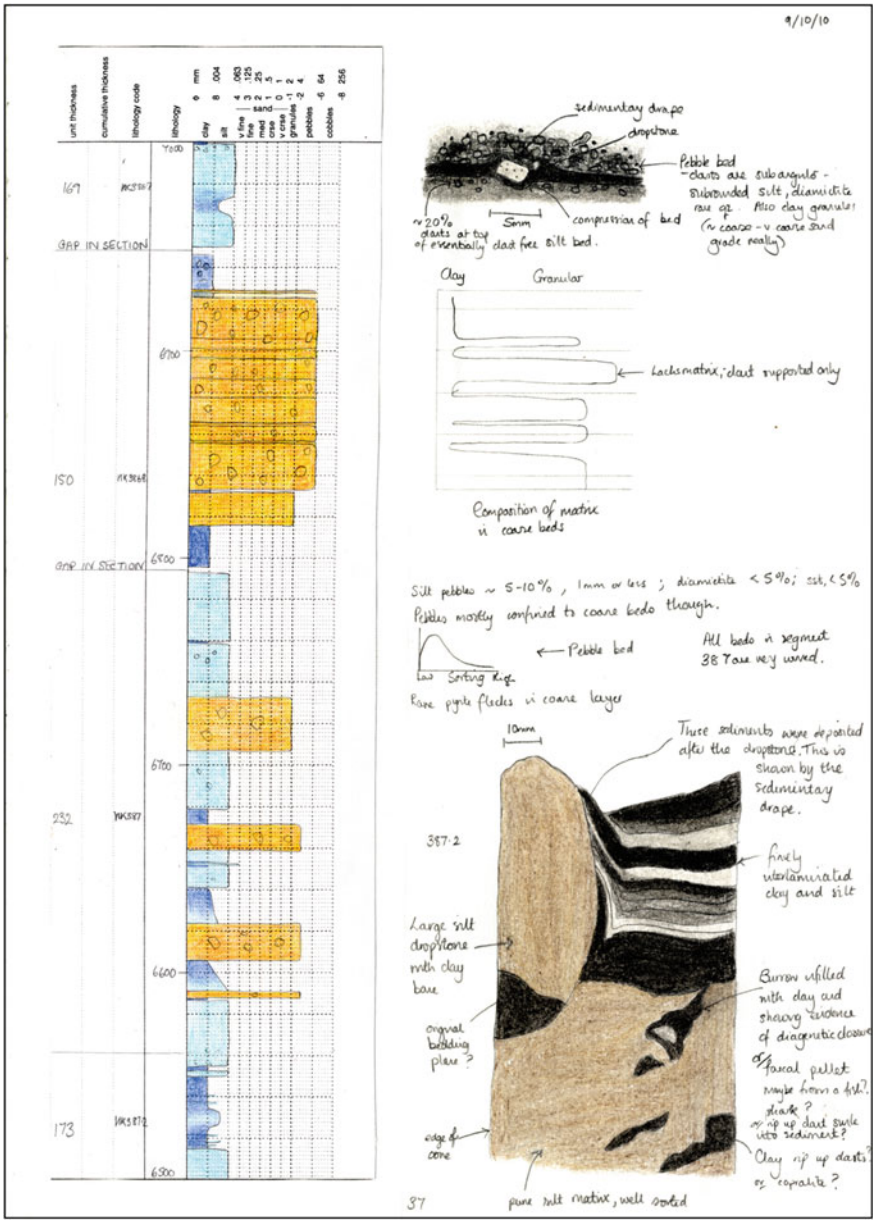
9/10/10
unit thickness
cumulative thickness
lithology code
lithology
mm
clay
silt
sand
granules
pebbles
cobbles
167
GAP IN SECTION
150
GAP IN SECTION
232
173
6700
6600
6500
sedimentary drape
dropstone
Pebble bed
clasts are subangular - subrounded silt, diamictite or qz. Also clay granules (v coarse - v coarse sand grade really)
5mm
compression of bed
~20% clasts at top of eventually clast free silt bed.
Clay
Granular
Lacks matrix; clast supported only
Composition of matrix in coarse beds
Silt pebbles ~ 5-10%, 1mm or less; diamictite < 5%; sst, < 5%
Pebbles mostly confined to coarse beds though.
Pebble bed
Low Sorting Rge
All beds in segment 38 are very curved.
Rare pyrite flecks in coarse layer
10mm
Three sediments were deposited after the dropstone. This is shown by the sedimentary drape.
387·2
finely interlaminated clay and silt
Large silt dropstone with clay base
Burrow infilled with clay and shows evidence of diagenetic closure
original bedding plane?
faecal pellet maybe from a bird?
shark?
or rip up clast sank into sediment?
edge of core
Clay rip up clasts? or coprolite?
37
pure silt matrix, well sorted

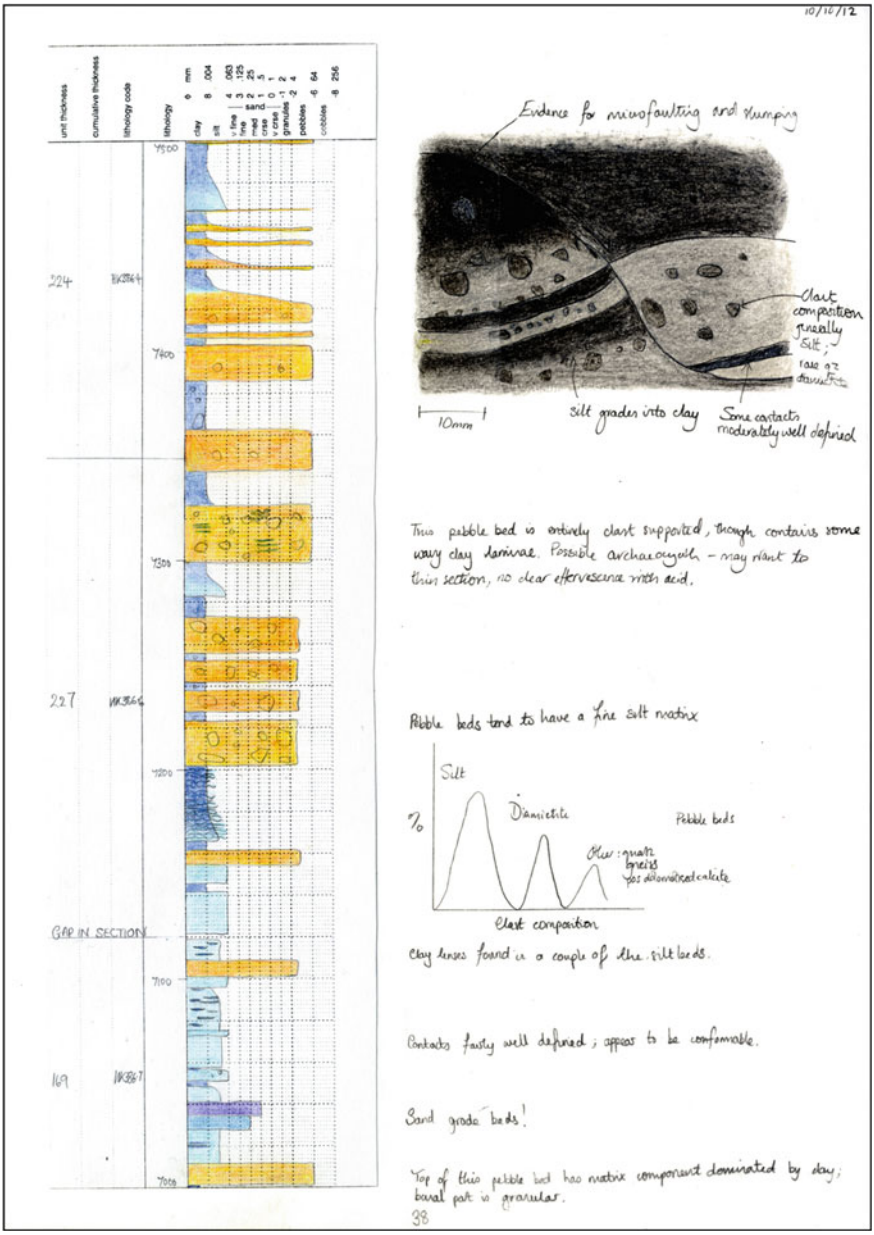
10/10/12
unit thickness
cumulative thickness
lithology code
lithology
Ø mm
clay
silt
sand
v fine
fine
med
crse
v crse
granules
pebbles
cobbles
224
227
169
GAP IN SECTION
Evidence for microfaulting and slumping
clast composition generally Silt; rare qz
10mm
silt grades into clay
Some contacts moderately well defined
This pebble bed is entirely clast supported, though contains some wavy clay laminae. Possible archaeocyath – may want to thin section, no clear effervescence with acid.
Pebble beds tend to have a fine silt matrix
Silt
%
Diamictite
Pebble beds
Qtz : quartz
Lmst : limestone
clast composition
Clay lenses found in a couple of the silt beds.
Contacts fairly well defined; appear to be conformable.
Sand grade beds!
Top of this pebble bed has matrix component dominated by clay; basal part is granular.
38

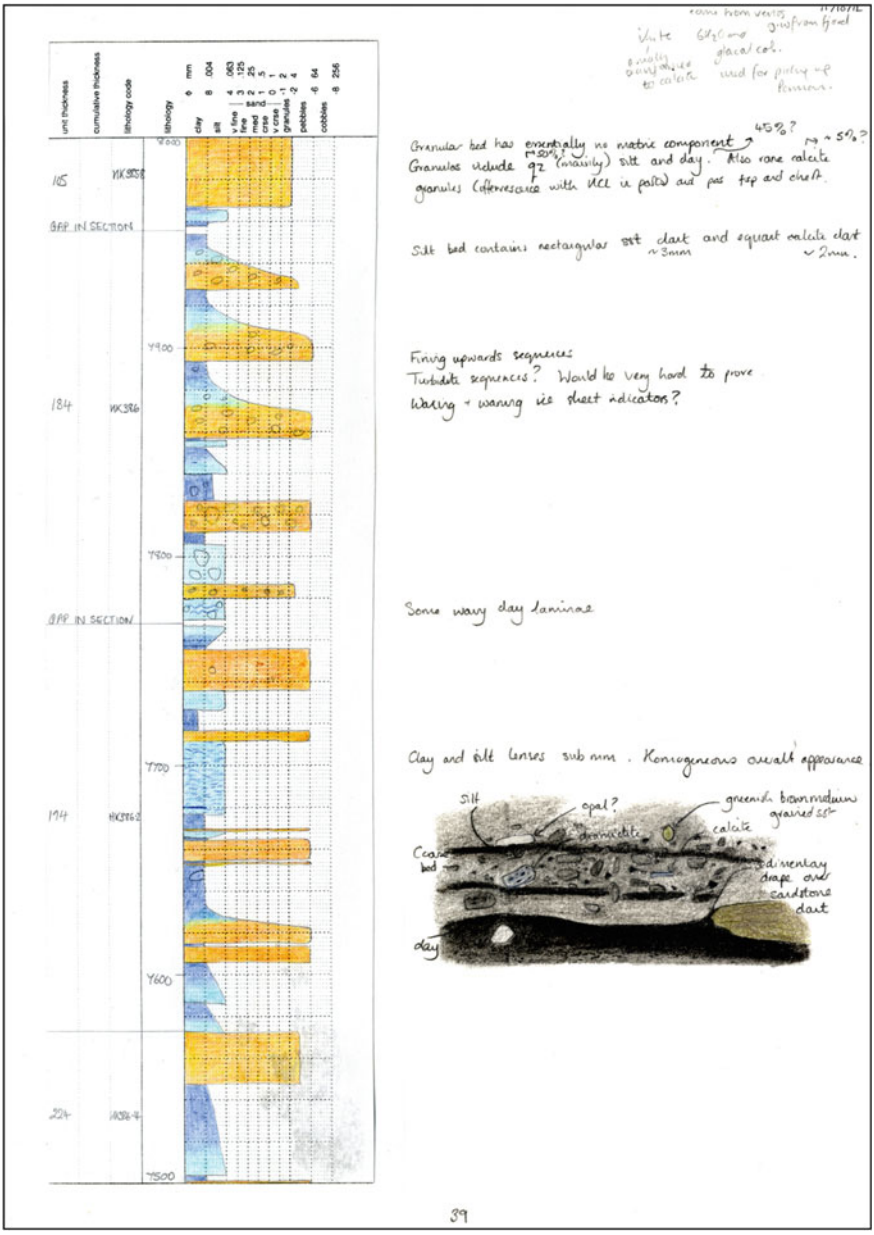
unit thickness
cumulative thickness
lithology code
lithology
Φ mm
clay
silt
v fine
fine
med
crse
v crse
sand
granules
pebbles
cobbles
Granular bed has essentially no matrix component
45%?
Granules include qz (mainly) silt and clay. Also rare calcite
granules (differences with HCL in paste) and pos fsp and chert.
Silt bed contains rectangular sst clast and equant calcite clast
~3mm
~2mm.
Fining upwards sequences
Turbidite sequences? Would be very hard to prove
Waxing + waning ice sheet indicators?
Some wavy clay laminae
Clay and silt lenses sub mm. Homogeneous overall appearance
Silt
opal?
greenish brown medium grained sst
calcite
Coarse bed
sedimentary drape over sandstone clast
clay
39

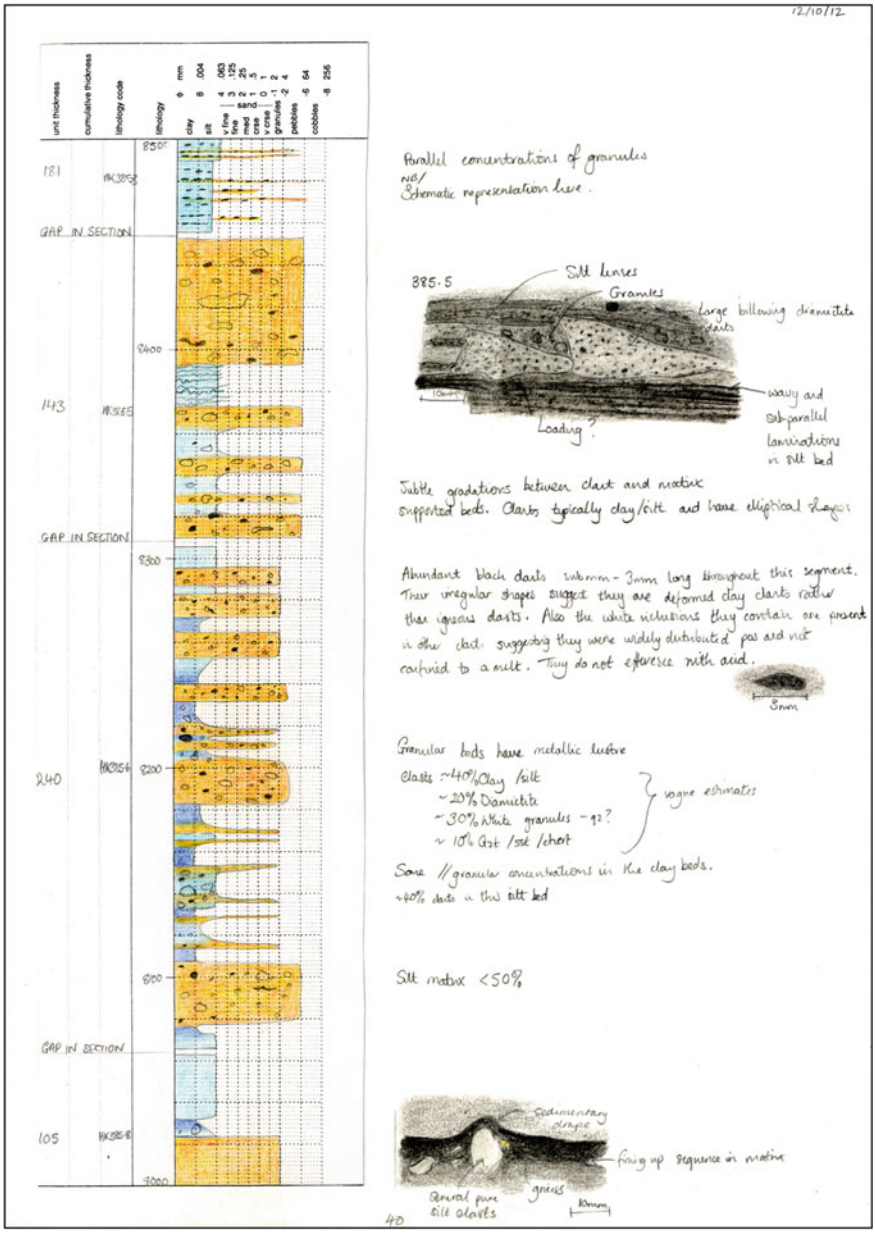
12/10/12
unit thickness
cumulative thickness
lithology code
lithology
φ mm
8 .004
4 .063
3 .125
2 .25
1 .5
0 1
−1 2
−2 4
−3 8
−6 64
−8 256
clay
silt
v fine
fine
med
coarse
v crse
granules
pebbles
cobbles
sand
181
HK(3B)3
GAP IN SECTION
143
HK(3E)5
GAP IN SECTION
240
HK(3)4
105
HK(3E)1
8500
8400
8300
8200
8100
8000
Parallel concentrations of granules
NB/
Schematic representation here.
385.5
Silt lenses
Granules
Large billowing diamictite
Loading?
wavy and sub-parallel laminations in silt bed
Subtle gradations between clast and matrix supported beds. Clasts typically clay/silt and have elliptical shapes
Abundant black clasts 1mm - 3mm long throughout this segment. Their irregular shapes suggest they are deformed clay clasts rather than igneous clasts. Also the white inclusions they contain are present in other clasts suggesting they were widely distributed pre and not confined to a melt. They do not effervesce with acid.
5mm
Granular beds have metallic lustre
Clasts ~40% Clay /silt
~20% Diamictite
~30% White granules - qz?
~10% Grit /sst /chert
vague estimates
Some // granular concentrations in the clay beds.
~40% clasts in this silt bed
Silt matrix <50%
Sedimentary clasts
fining up sequence in matrix
Reversed pure silt clasts
gneiss
10mm
40

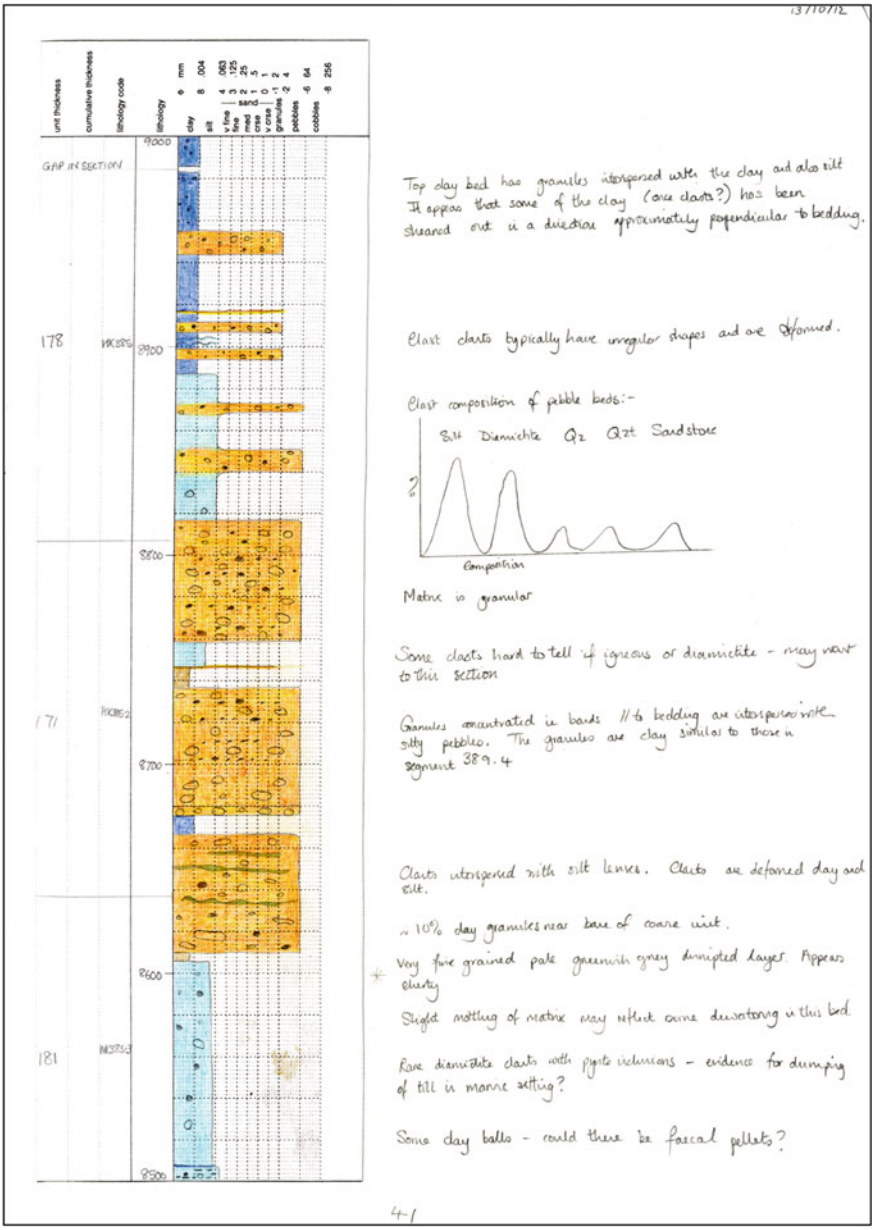
13/10/12
unit thickness
cumulative thickness
lithology code
lithology
clay
silt
v fine
fine
med
coarse
v coarse
granule
pebbles
cobbles
mm
GAP IN SECTION
178
171
181
9000
8900
8800
8700
8600
8500
Top clay bed has granules interspersed with the clay and also silt It appears that some of the clay (once clasts?) has been sheared out in a direction approximately perpendicular to bedding.
Clast clasts typically have irregular shapes and are deformed.
Clast composition of pebble beds:-
Silt
Diamictite
Qz
Qzt
Sandstone
%
Composition
Matrix is granular
Some clasts hard to tell if igneous or diamictite - may want to thin section
Granules concentrated in bands // to bedding are interspersed with silty pebbles. The granules are clay similar to those in segment 389.4
Clasts interspersed with silt lenses. Clasts are deformed clay and silt.
~ 10% clay granules near base of coarse unit.
Very fine grained pale greenish grey disrupted layer. Appears clayey
Slight mottling of matrix may reflect some dewatering in this bed
Rare diamictite clasts with pyrite inclusions - evidence for dumping of till in marine setting?
Some clay balls - could these be faecal pellets?
4-1

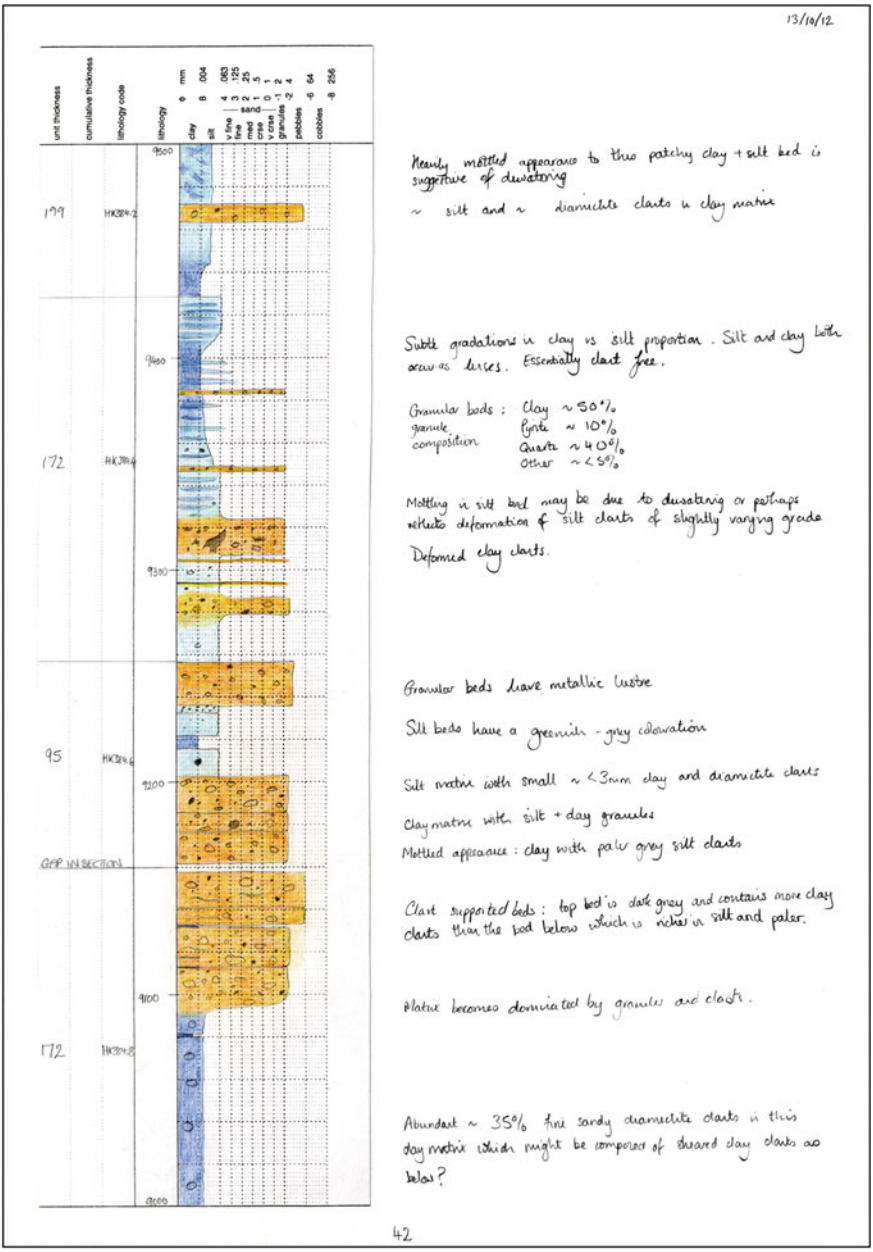
13/10/12
unit thickness
cumulative thickness
lithology code
lithology
clay
silt
sand
gravel
pebbles
cobbles
mm
199
HK3N2
172
HK3N4
95
HK3N6
GAP IN SECTION
172
HK3N8
9500
9400
9300
9200
9100
9000
Nearly mottled appearance to this patchy clay + silt bed is suggestive of dewatering
~ silt and ~ diamictite clasts in clay matrix
Subtle gradations in clay vs silt proportion. Silt and clay both occur as lenses. Essentially clast free.
Granular beds: granule composition
Clay ~ 50%
Pyrite ~ 10%
Quartz ~ 40%
Other ~ < 5%
Mottling in silt bed may be due to dewatering or perhaps reflects deformation of silt clasts of slightly varying grade
Deformed clay clasts.
Granular beds have metallic lustre
Silt beds have a greenish - grey colouration
Silt matrix with small ~ < 3mm clay and diamictite clasts
Clay matrix with silt + clay granules
Mottled appearance: clay with pale grey silt clasts
Clast supported beds: top bed is dark grey and contains more clay clasts than the bed below which is richer in silt and paler.
Matrix becomes dominated by granules and clasts.
Abundant ~ 35% fine sandy diamictite clasts in this clay matrix which might be composed of sheared clay clasts as below?
42

14/10/12

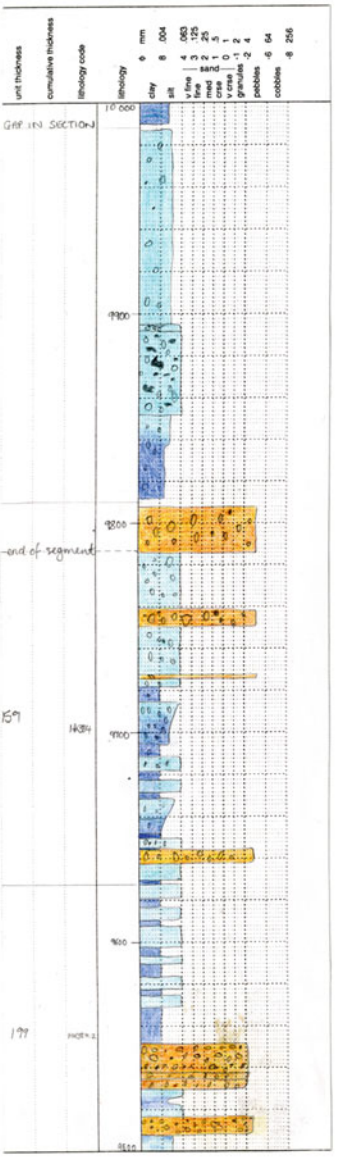

~30% clasts.

Thin silt bed with clasts has the highest % of deformed clay clasts relative to the other beds in this seqt (~65% vs 10%)

Silt clasts in silt matrix ~30%.

Most contacts are gradational.

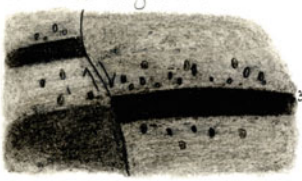

Micro-fault found in this segment.

Maximum offset ~14mm.

Clasts similar in silt and coarse beds.

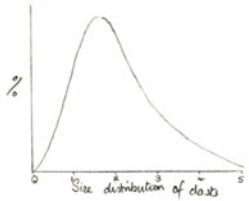

Clasts are almost entirely silt

Rare cherty clasts, sst, ?granite

<5% clasts in thin interbedded clay and silt unit

43

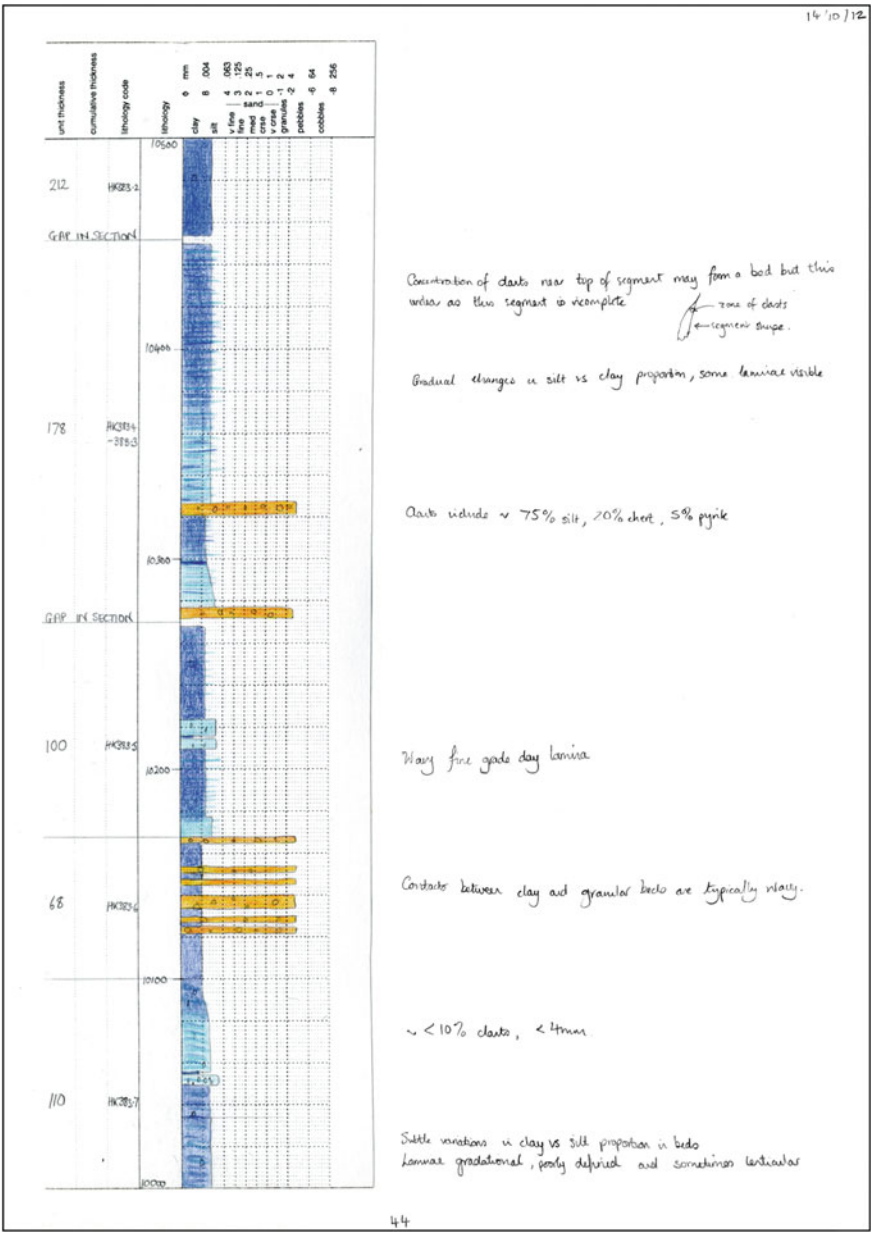
14/10/12
unit thickness
cumulative thickness
lithology code
lithology
clay
silt
sand
pebbles
cobbles
212
HK823.2
GAP IN SECTION
178
HK3134
-319.3
100
HK319.5
68
HK319.6
110
HK319.7
10500
10400
10300
10200
10100
10000
Concentration of clasts near top of segment may form a bed but this wears as this segment is incomplete
zone of clasts
segment shape.
Gradual changes in silt vs clay proportion, some laminae visible
Clasts include ~ 75% silt, >10% chert, 5% pyrite
GAP IN SECTION
Wavy fine grade clay lamina
Contacts between clay and granular beds are typically wavy.
~ <10% clasts, < 4mm
Subtle variations in clay vs silt proportion in beds
Laminae gradational, poorly defined and sometimes lenticular
44

14/10/12

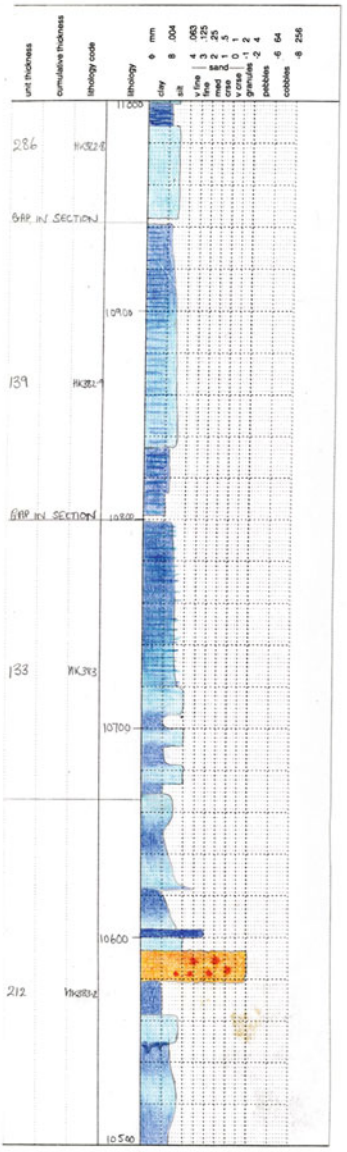

Ribbons of clay in fine silty - clay matrix.

Mudrock. Slightly varying grade.

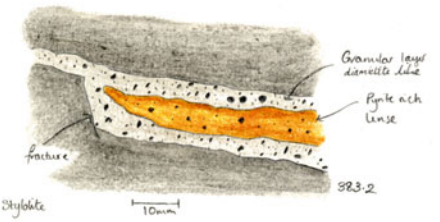

Hargely homogeneous mudrock with slight variations in clay vs silt %.

45

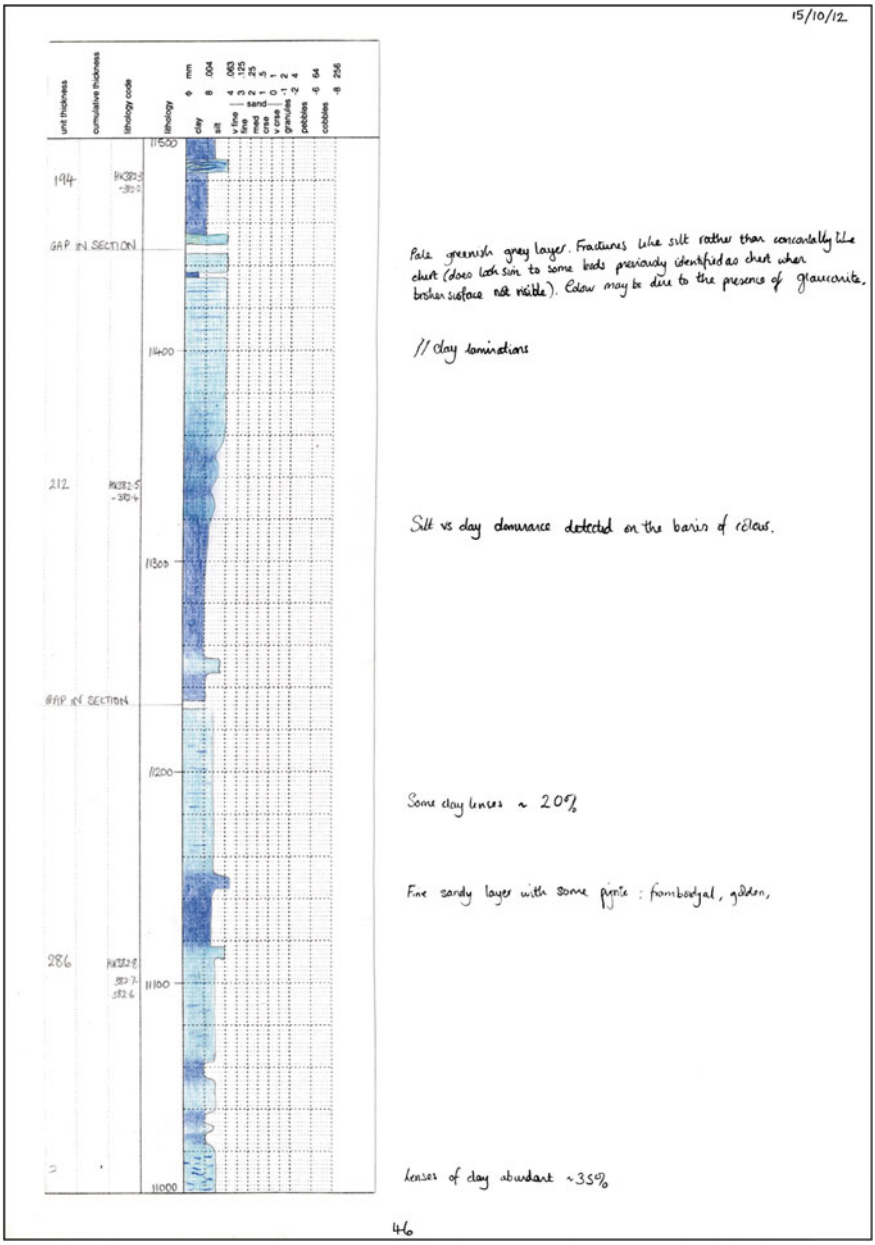
15/10/12
unit thickness
cumulative thickness
lithology code
lithology
clay
silt
v fine
fine
med
crse
v crse
granules
pebbles
cobbles
mm
11500
11400
11300
11200
11100
11000
194
GAP IN SECTION
212
GAP IN SECTION
286
Pale greenish grey layer. Fractures like silt rather than concavally like chert (does both similar to some beds previously identified as chert when broken surface not visible). Colour may be due to the presence of glauconite.
// clay laminations
Silt vs clay dominance detected on the basis of colour.
Some clay lenses ~ 20%
Fine sandy layer with some pyrite : Fornbodgal, golden,
lenses of clay abundant ~35%
46

15/10/12

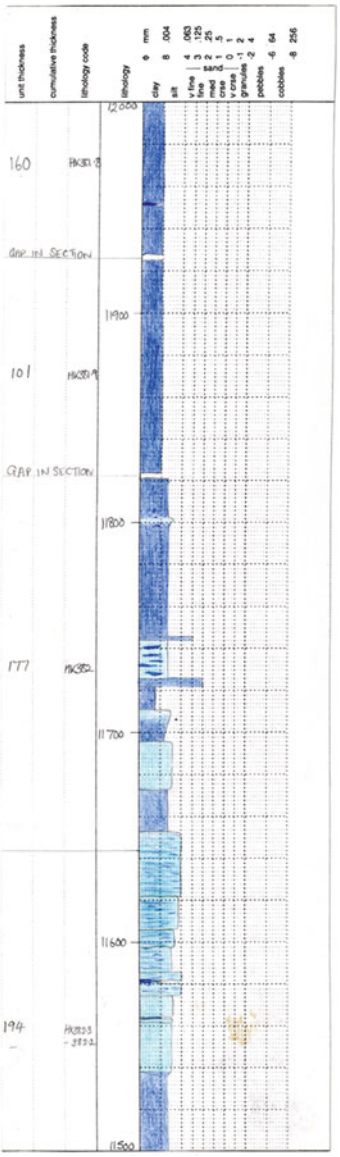

largely homogeneous mudrock. Possibly some minor fluctuations in grainsize but this is very subtle.

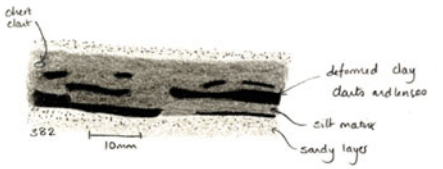

v. fine-medium sand grade layer

mm-submm clay and silt laminations and lenses. Silt matrix forms the bulk and is greenish grey + scim to bed at sequence base.

Could these silt beds / laminations reflect tidal cycles? They are unlikely to represent Milankovitch cycles as the sediment volume is too low for a kyr record.

47

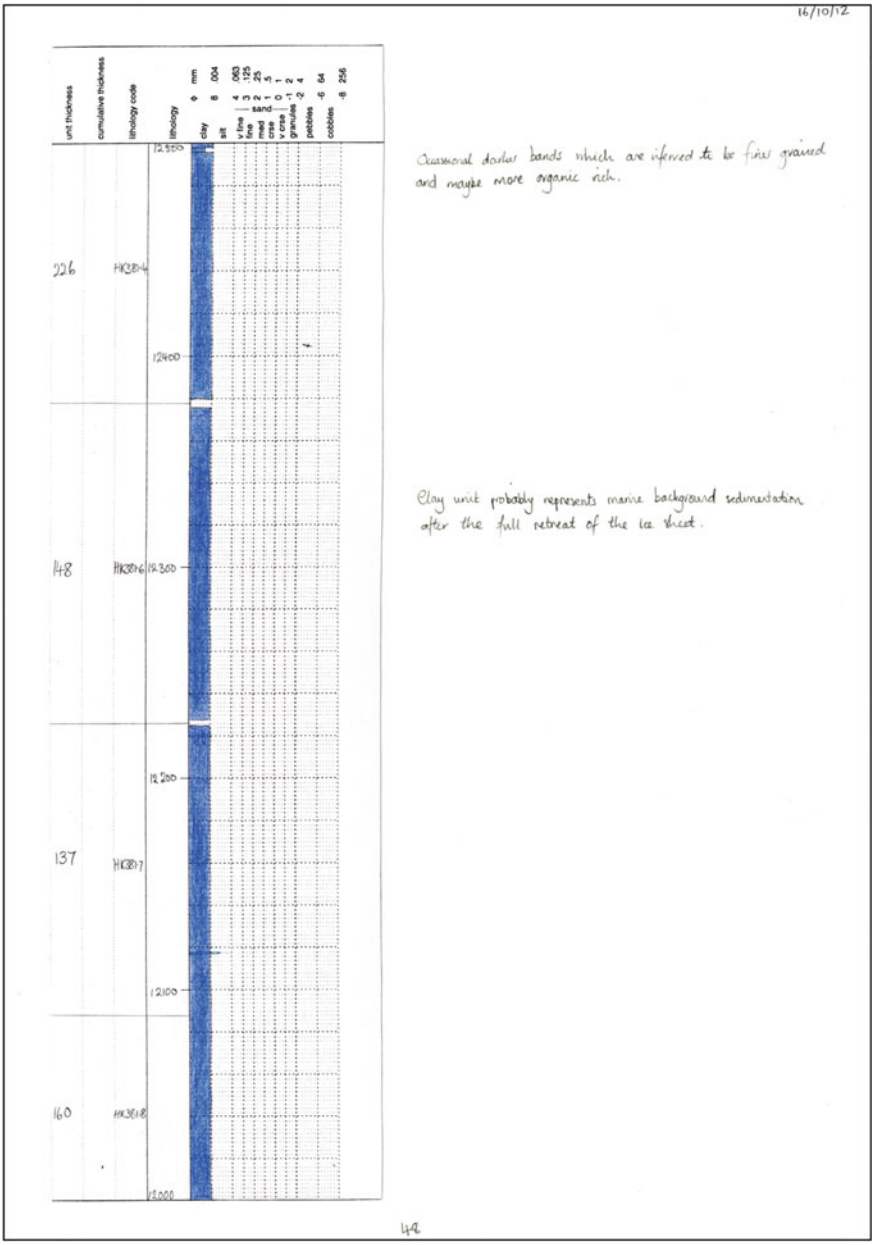
16/10/12
unit thickness
cumulative thickness
lithology code
lithology
φ mm
clay
silt
v fine
fine
med
coarse
v coarse
granules
pebbles
cobbles
sand
12,500
12400
12,300
12,200
12100
12,000
226
148
137
160
HK3014
HK3016
HK3017
HK3018
Occasional darker bands which are inferred to be finer grained and maybe more organic rich.
Clay unit probably represents marine background sedimentation after the full retreat of the ice sheet.
42

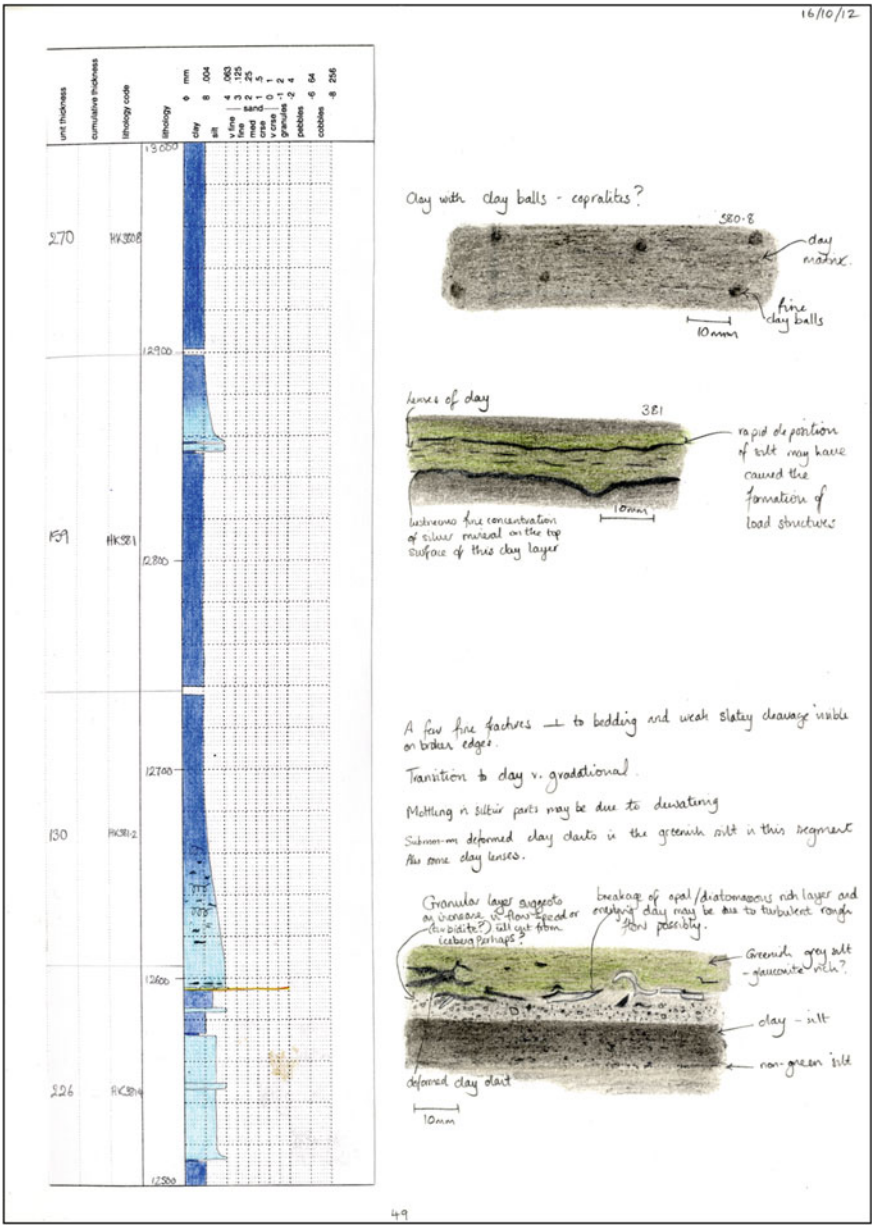
16/10/12
unit thickness
cumulative thickness
lithology code
lithology
clay
silt
v fine
fine
med
crse
v crse
granules
pebbles
cobbles
sand
270
159
130
226
HK3308
HK321
HK311.2
HK3114
13000
12900
12800
12700
12600
12500
Clay with clay balls - coprolites?
380·8
clay matrix
fine clay balls
10mm
Lenses of clay
381
rapid deposition of silt may have caused the formation of load structures
10mm
Increased fine concentration of silver mineral on the top surface of this clay layer
A few fine fractures ⊥ to bedding and weak slatey cleavage visible on broken edges.
Transition to clay v. gradational.
Mottling in silty parts may be due to dewatering
Sub-mm deformed clay clasts in the greenish silt in this segment Also some clay lenses.
Granular layer suggests an increase in flow speed or (turbidite?) silt out from iceberg perhaps?
breakup of opal/diatomaceous rich layer and overlying clay may be due to turbulent rough flow possibly.
Greenish grey silt - glauconite rich?
clay - silt
non-green silt
deformed clay clast
10mm
49

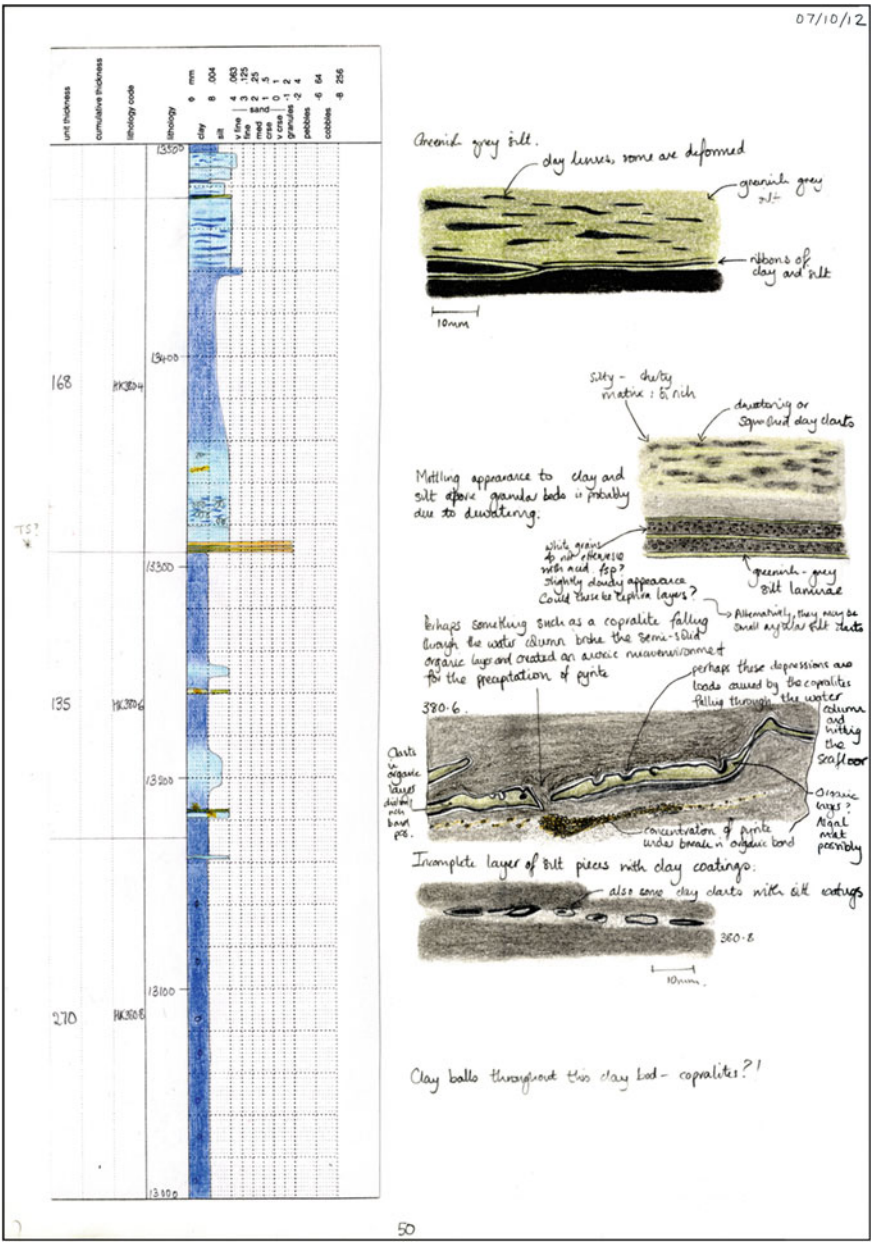
07/10/12
unit thickness
cumulative thickness
lithology code
lithology
mm
clay
silt
sand
v fine
fine
med
coarse
v coarse
granules
pebbles
cobbles
13300
13400
13500
13600
13700
13800
168
135
270
HK3804
HK3806
HK3808
Greenish grey silt.
clay lenses, some are deformed
greenish grey silt
ribbons of clay and silt
10mm
Silty - clayey matrix : S rich
dewatering or squeezed clay clasts
Mottling appearance to clay and silt above granular beds is probably due to dewatering.
white grains do not effervesce with acid. Fsp?
Slightly cloudy appearance
Could these be capilva layers?
greenish - grey silt laminae
Alternatively, they may be small argillac silt clasts
Perhaps something such as a copralite falling through the water column broke the semi-solid organic layer and created an anoxic microenvironment for the precipitation of pyrite
perhaps these depressions are loads caused by the copralites falling through the water column and hitting the seafloor
380·6
Clasts in organic layer? Probably pelagic bone pcs.
Organic layer?
Algal mat possibly
concentration of pyrite under broader organic bed
Incomplete layer of silt pieces with clay coatings.
also some clay clasts with silt coatings
380·8
10mm
Clay balls throughout this clay bed - copralites?!
50

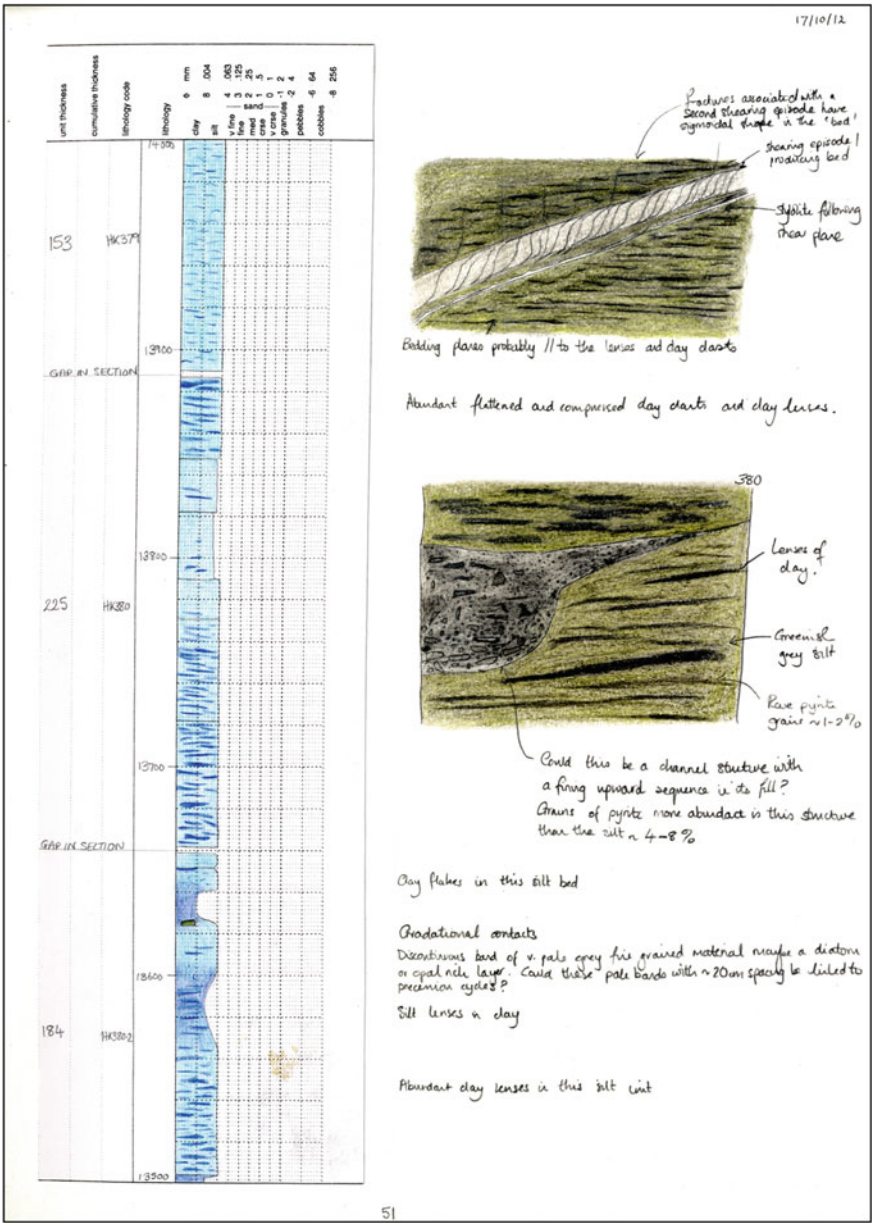
17/10/12
unit thickness
cumulative thickness
lithology code
lithology
clay
silt
v fine
fine
med
crse
v crse
granules
pebbles
cobbles
153
HK379
GAP IN SECTION
225
HK380
GAP IN SECTION
184
HK380?
13900
13800
13700
13600
13500
Fractures associated with a second shearing episode have sigmoidal shape in the 'bed'
Shearing episode / predating bed
Sylolite following shear plane
Bedding planes probably // to the lenses and clay clasts
Abundant flattened and compressed clay clasts and clay lenses.
380
Lenses of clay.
Greenish grey silt
Rare pyrite grains ~1-2%
Could this be a channel structure with a fining upward sequence in its fill?
Grains of pyrite more abundant in this structure than the silt ~ 4-8%
Clay flakes in this silt bed
Gradational contacts
Discontinuous band of v. pale grey fine grained material maybe a diatom or opal rich layer. Could these pale bands with ~20cm spacing be linked to precession cycles?
Silt lenses in clay
Abundant clay lenses in this silt unit
51

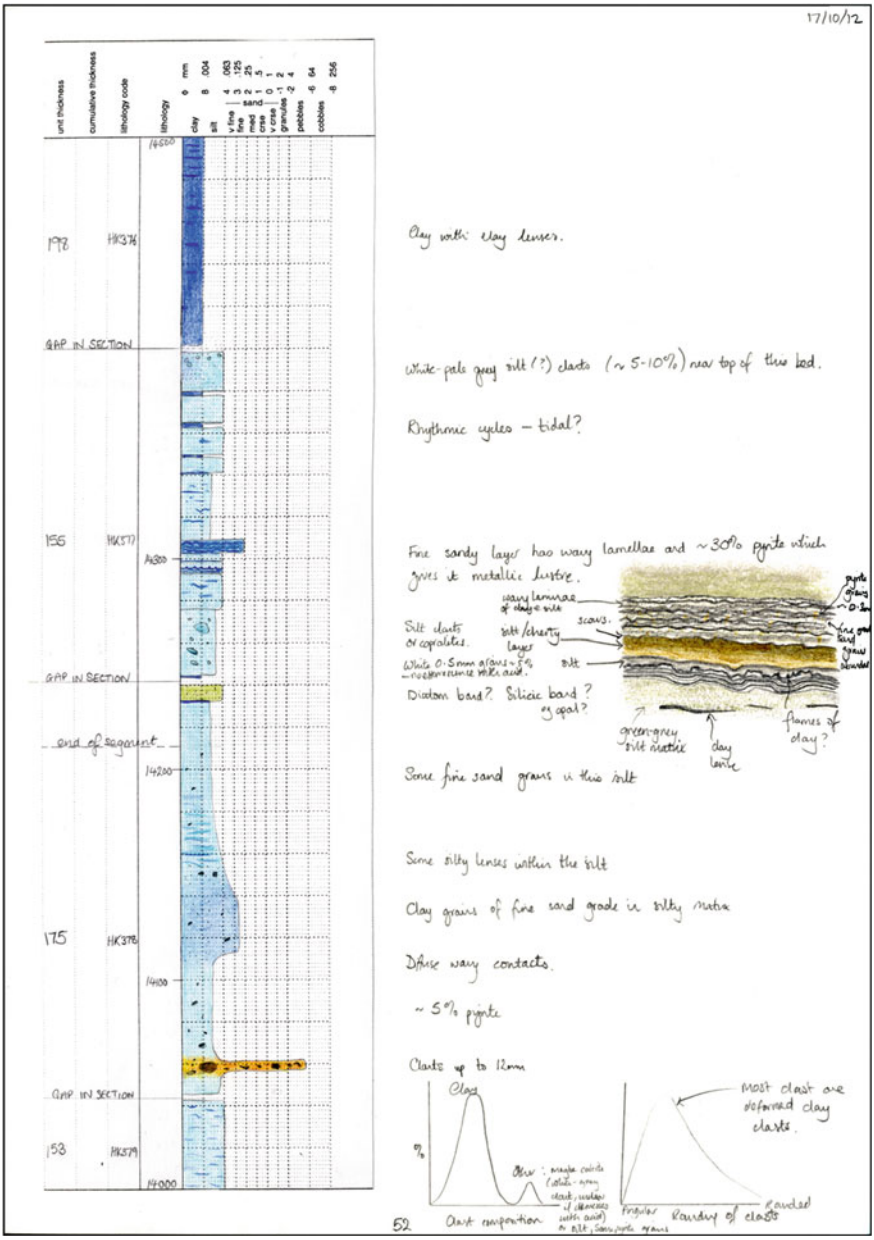
17/10/12
unit thickness
cumulative thickness
lithology code
lithology
clay
silt
sand
pebbles
cobbles
198
HK37A
GAP IN SECTION
156
HK37
GAP IN SECTION
end of segment
175
HK37B
GAP IN SECTION
53
HK37C
14500
14300
14200
14100
14000
Clay with clay lenses.
White-pale grey silt (?) clasts (~ 5-10%) near top of this bed.
Rhythmic cycles – tidal?
Fine sandy layer has wavy lamellae and ~30% pyrite which gives it metallic lustre.
wavy laminae of clay & silt
scours.
Silt clasts or cupolates.
silt/clayey layer
silt
White 0.5mm grains ~5% – recognisable white acid.
Diatom band? Silicic band? eg opal?
green-grey silt matrix
clay lenses
flames of clay?
Some fine sand grains in this silt
Some silty lenses within the silt
Clay grains of fine sand grade in silty matrix
Diffuse wavy contacts.
~ 5% pyrite
Clasts up to 12mm
Clay
%
Clast composition
Most clast are deformed clay clasts.
Roundy of clasts
Angular
Rounded
52

17/10/12
18/10/12

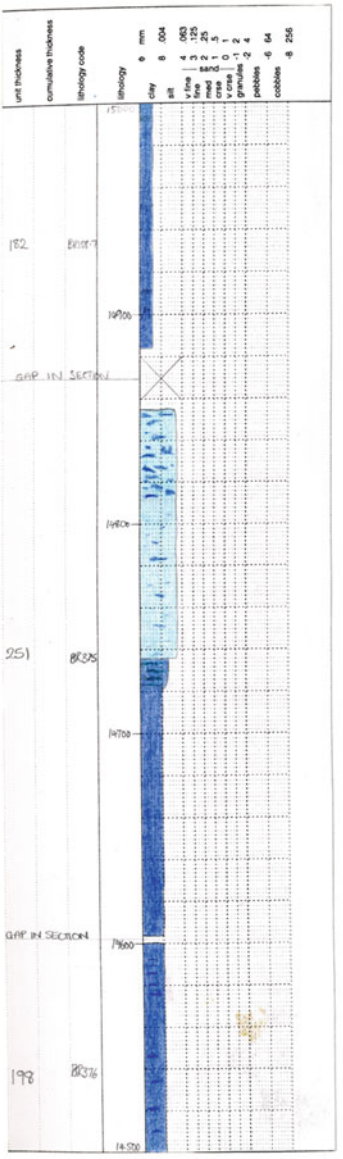

A few ~ 1% white needle like grains - actinolite?

When sanding this fine clay unit it seemed very oily and smelt of hydrocarbons.
It is very rich in organic matter.

Stylolite probably // to bedding visible on curved surface

Upper lithologies now expected to be mudstone from the Black Rock member. Two 1m cores were collected from BGS to confirm this.

Deformed clay clasts increase in abundance; ~ 40% at top of segment

lenses of clay and silt

Homogeneous clay.

53

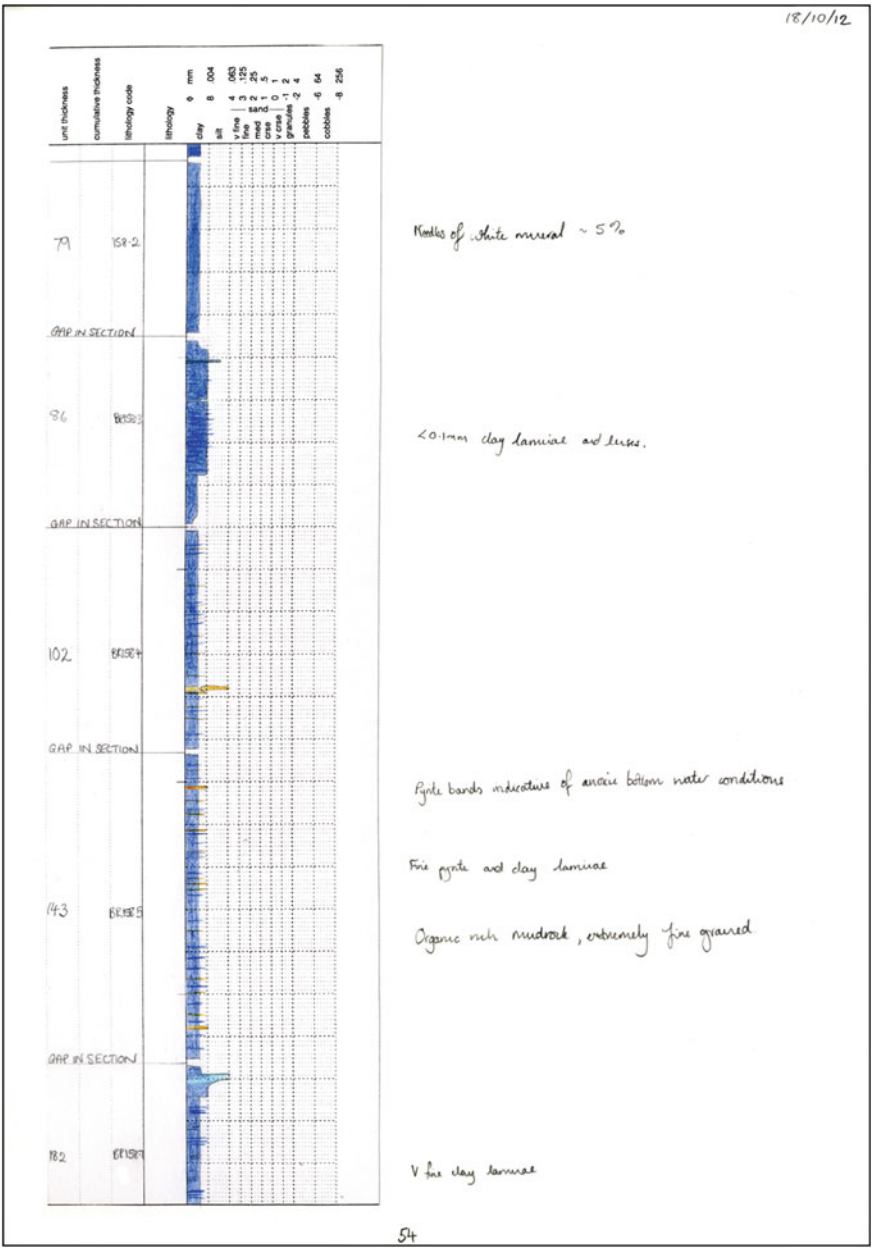
18/10/12
unit thickness
cumulative thickness
lithology code
lithology
Φ mm
clay 8 .004
silt 4 .063
v fine 3 .125
fine 2 .25
med 1 .5
coarse 0 1
v coarse -1 2
granules -2 4
pebbles -6 64
cobbles -8 256
sand
79
158·2
GAP IN SECTION
86
BRSB3
GAP IN SECTION
102
BRSB4
GAP IN SECTION
143
BRSB5
GAP IN SECTION
182
BRSB7
Nodules of white mineral ~ 5%
<0.1mm clay laminae and lenses.
Pyrite bands indicative of anoxic bottom water conditions
Fine pyrite and clay laminae
Organic rich mudrock, extremely fine grained
V fine clay laminae
54

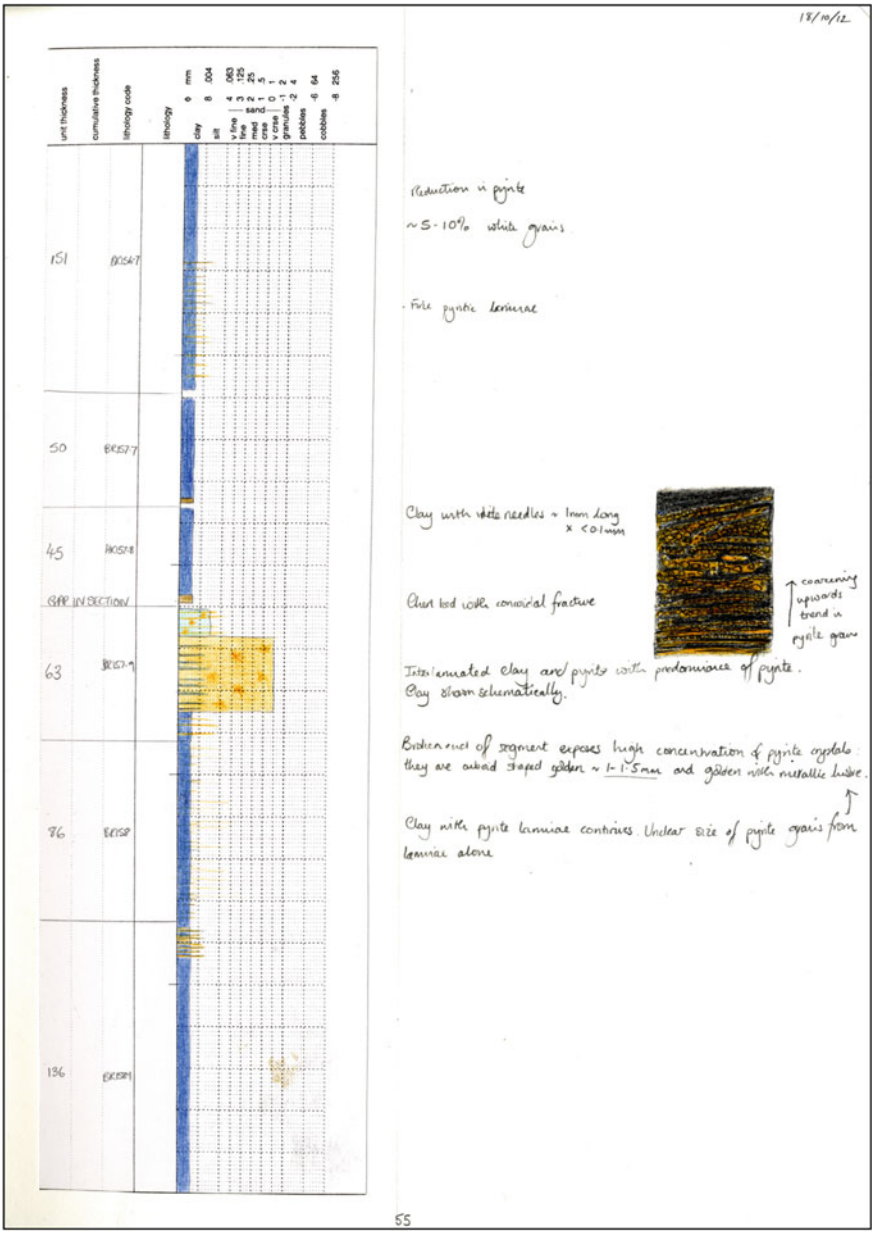
13/10/12
unit thickness
cumulative thickness
lithology code
lithology
φ mm
clay 8 .004
silt 4 .063
v fine 3 .125
fine 2 .25
med 1 .5
crse 0 1
v crse -1 2
granules -2 4
pebbles -6 64
cobbles -8 256
sand
151
BDS47
50
BRS77
45
BDS78
GAP IN SECTION
63
BRS79
86
BRS8
136
BRS81
Reduction in pyrite
~5-10% white grains
Pale pyritic laminae
Clay with white needles ~ 1mm long x <0.1mm
Chert bed with conchoidal fracture
coarsening upwards trend in pyrite grain
Interlaminated clay and pyrite with predominance of pyrite. Clay drawn schematically.
Broken end of segment exposes high concentration of pyrite crystals they are cuboid shaped golden ~ 1-1.5mm and golden with metallic lustre.
Clay with pyrite laminae contains. Unclear size of pyrite grains from laminae alone
55

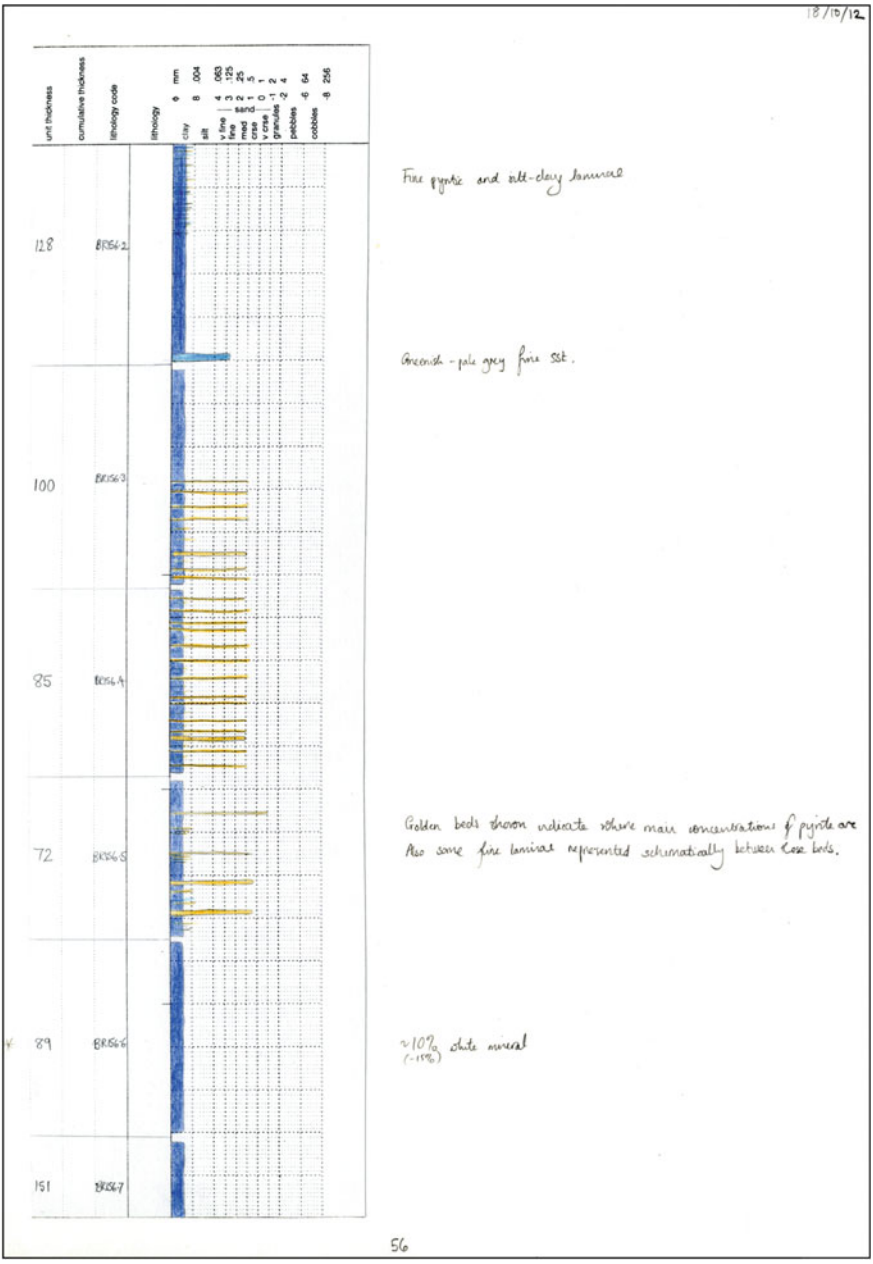
18/10/12
unit thickness
cumulative thickness
lithology code
lithology
Φ mm
clay 8 .004
silt 4 .063
v fine 3 .125
fine 2 .25
med 1 .5
coarse 0 1
v coarse -1 2
granules -2 4
pebbles -6 64
cobbles -8 256
sand
128
BR562
100
BR563
85
BR564
72
BR565
89
BR566
151
BR567
Fine pyrite and silt-clay laminae
Greenish - pale grey fine sst.
Golden beds shown indicate where main concentrations of pyrite are
Also some fine laminae represented schematically between these beds.
~10% (~15%) white mineral
56

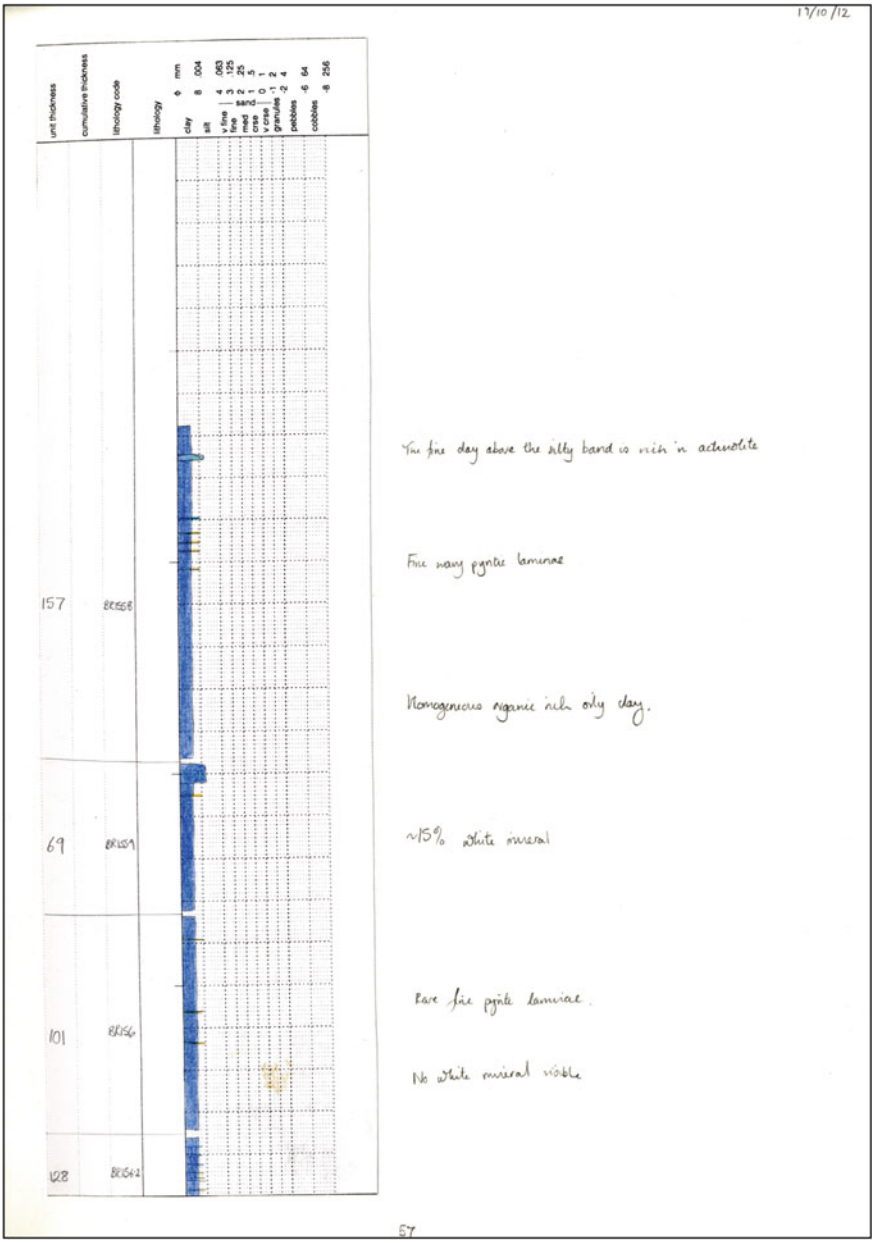
17/10/12
unit thickness
cumulative thickness
lithology code
lithology
Φ mm
clay 8 .004
silt 4 .063
v fine 3 .125
fine 2 .25
med 1 .5
coarse 0 1
v coar -1 2
granules -2 4
pebbles -6 64
cobbles -8 256
157
BK568
69
BK569
101
BK566
128
BK562
Fine fine clay above the silty band is rich in actinolite
Fine wavy pyrite laminae
Homogeneous organic rich oily clay.
~15% white mineral
Rare fine pyrite laminae.
No white mineral visible
57

6.2 Reflectance Scanning Data

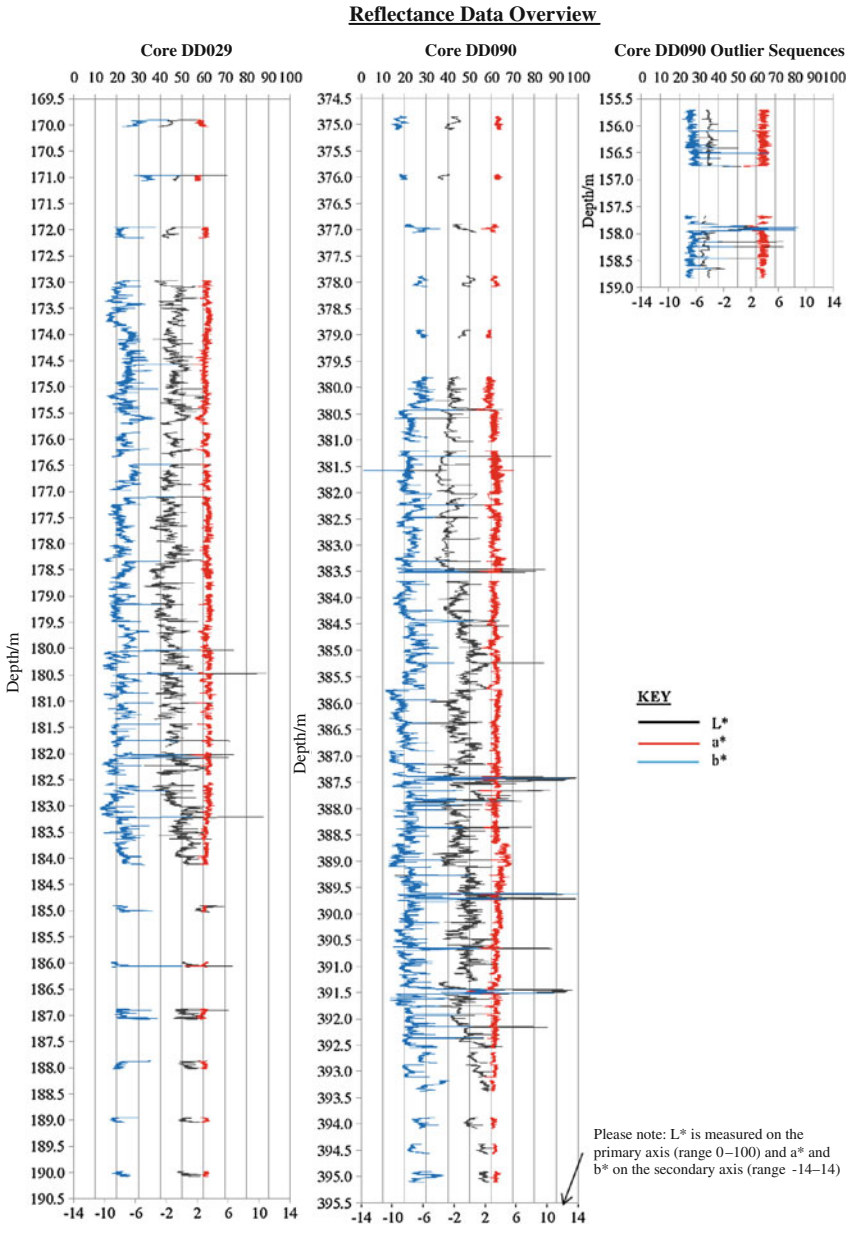

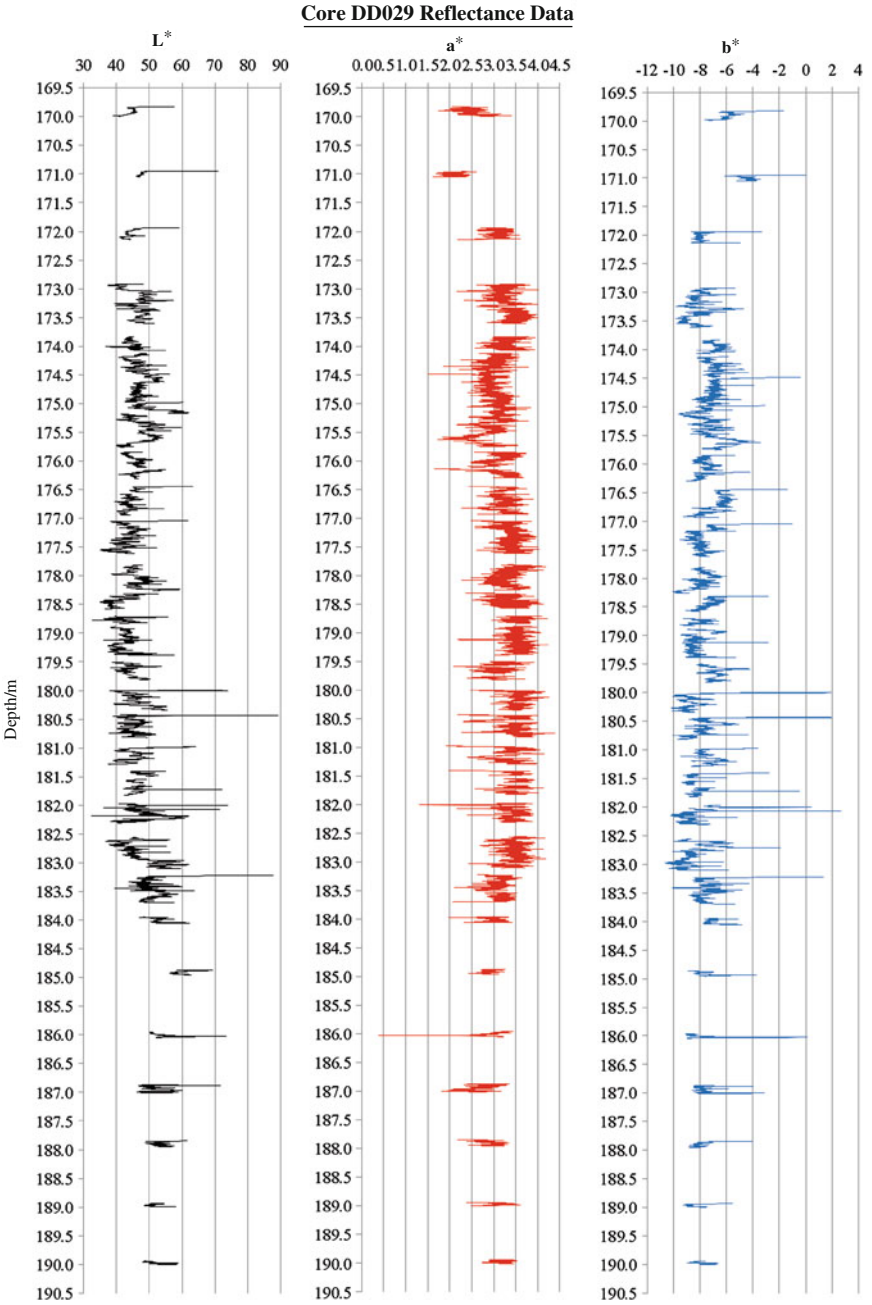
Core DD029 Reflectance Data
L*
a*
b*
Depth/m
30 40 50 60 70 80 90
0.0 0.5 1.0 1.5 2.0 2.5 3.0 3.5 4.0 4.5
-12 -10 -8 -6 -4 -2 0 2 4
169.5 170.0 170.5 171.0 171.5 172.0 172.5 173.0 173.5 174.0 174.5 175.0 175.5 176.0 176.5 177.0 177.5 178.0 178.5 179.0 179.5 180.0 180.5 181.0 181.5 182.0 182.5 183.0 183.5 184.0 184.5 185.0 185.5 186.0 186.5 187.0 187.5 188.0 188.5 189.0 189.5 190.0 190.5

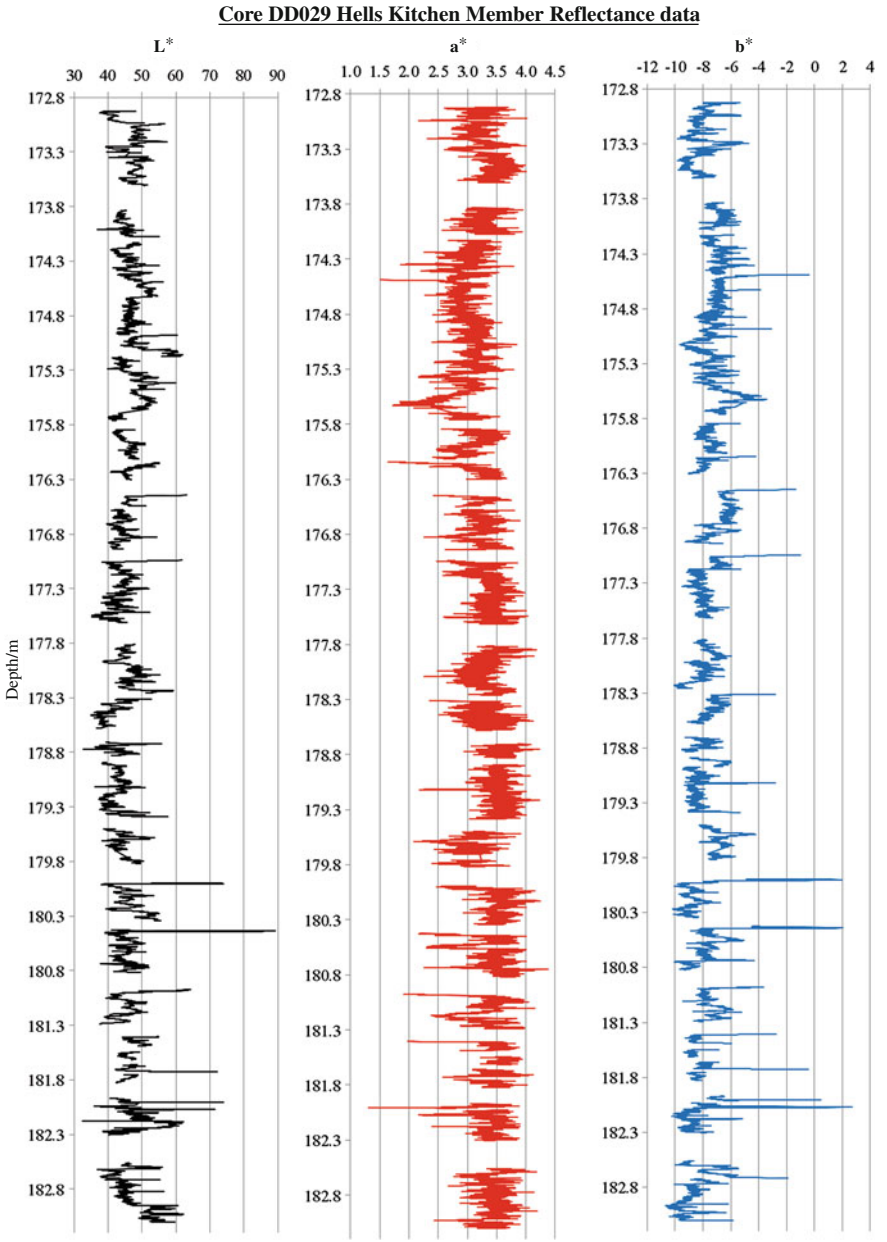
Core DD029 Hells Kitchen Member Reflectance data
L*
a*
b*
Depth/m
30 40 50 60 70 80 90
1.0 1.5 2.0 2.5 3.0 3.5 4.0 4.5
-12 -10 -8 -6 -4 -2 0 2 4
172.8
173.3
173.8
174.3
174.8
175.3
175.8
176.3
176.8
177.3
177.8
178.3
178.8
179.3
179.8
180.3
180.8
181.3
181.8
182.3
182.8

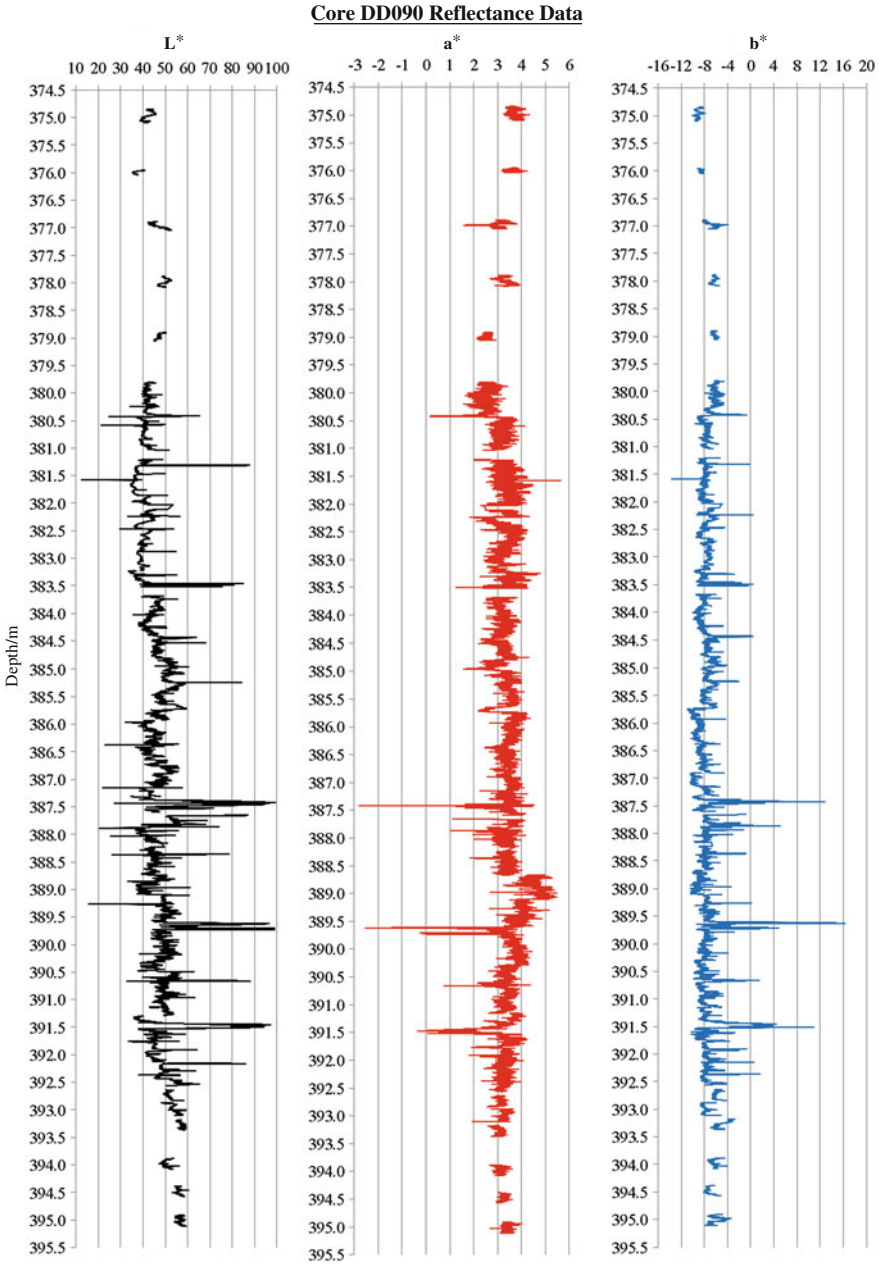
Core DD090 Reflectance Data
L*
10 20 30 40 50 60 70 80 90 100
a*
-3 -2 -1 0 1 2 3 4 5 6
b*
-16 -12 -8 -4 0 4 8 12 16 20
Depth/m
374.5 375.0 375.5 376.0 376.5 377.0 377.5 378.0 378.5 379.0 379.5 380.0 380.5 381.0 381.5 382.0 382.5 383.0 383.5 384.0 384.5 385.0 385.5 386.0 386.5 387.0 387.5 388.0 388.5 389.0 389.5 390.0 390.5 391.0 391.5 392.0 392.5 393.0 393.5 394.0 394.5 395.0 395.5

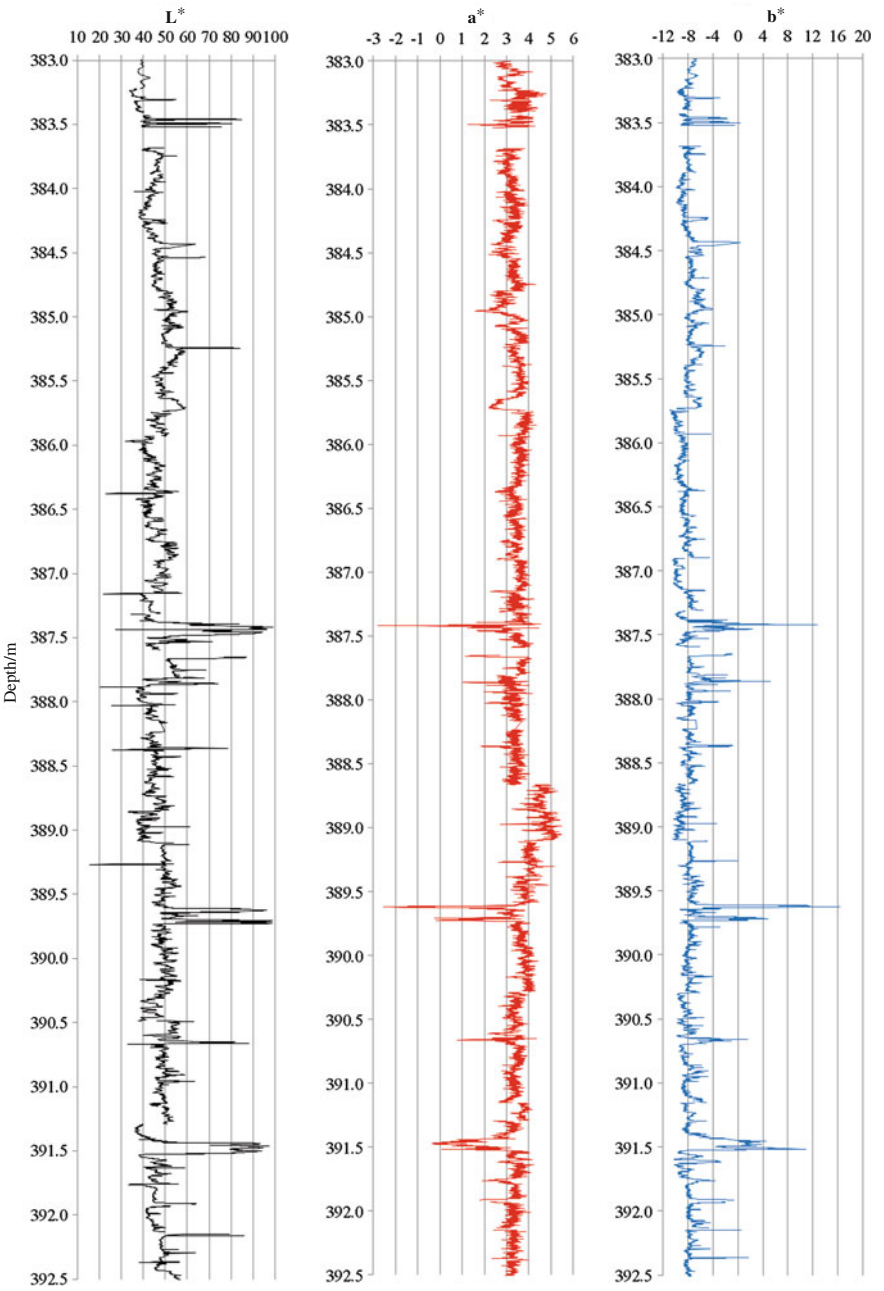
Core DD090 Hells Kitchen Member Reflectance Data
L*
10 20 30 40 50 60 70 80 90100
a*
-3 -2 -1 0 1 2 3 4 5 6
b*
-12 -8 -4 0 4 8 12 16 20
Depth/m
383.0
383.5
384.0
384.5
385.0
385.5
386.0
386.5
387.0
387.5
388.0
388.5
389.0
389.5
390.0
390.5
391.0
391.5
392.0
392.5

6.3 XRF Data

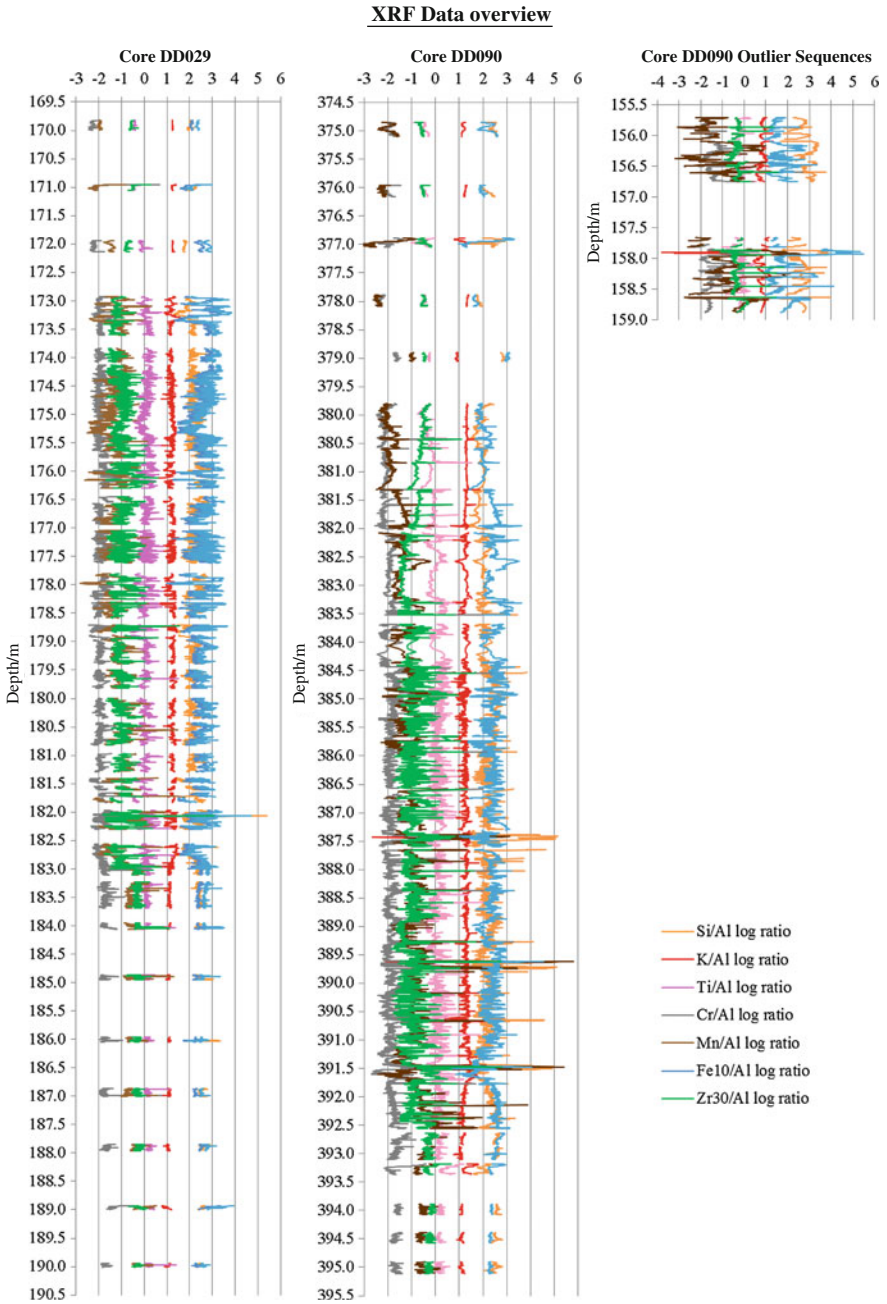
XRF Data overview
Core DD029
Core DD090
Core DD090 Outlier Sequences
Depth/m
Si/Al log ratio
K/Al log ratio
Ti/Al log ratio
Cr/Al log ratio
Mn/Al log ratio
Fe10/Al log ratio
Zr30/Al log ratio

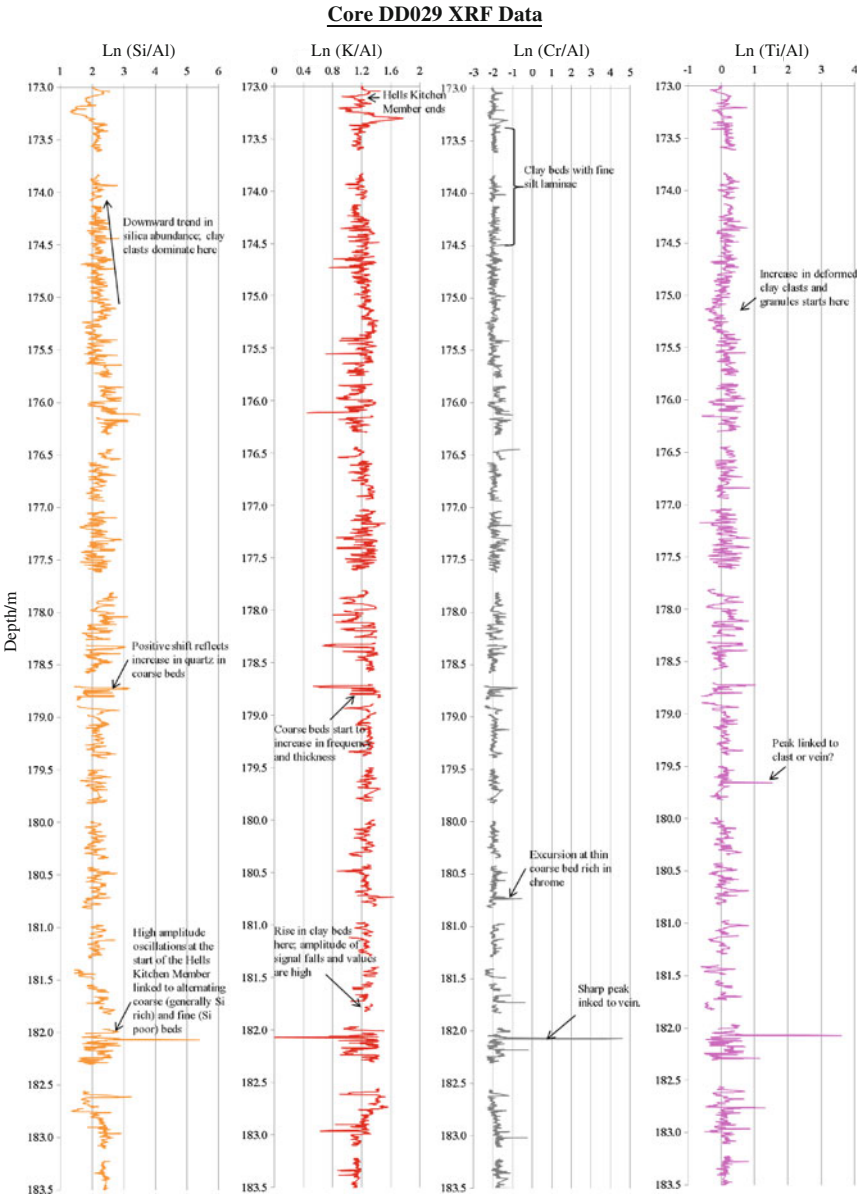
Core DD029 XRF Data
Ln (Si/Al)
Ln (K/Al)
Ln (Cr/Al)
Ln (Ti/Al)
Depth/m
Hells Kitchen Member ends
Clay beds with fine silt laminae
Increase in deformed clay clasts and granules starts here
Downward trend in silica abundance; clay clasts dominate here
Positive shift reflects increase in quartz in coarse beds
Coarse beds start to increase in frequency and thickness
Peak linked to clast or vein?
Excursion at thin coarse bed rich in chrome
High amplitude oscillations at the start of the Hells Kitchen Member linked to alternating coarse (generally Si rich) and fine (Si poor) beds
Rise in clay beds here; amplitude of signal falls and values are high
Sharp peak inked to vein

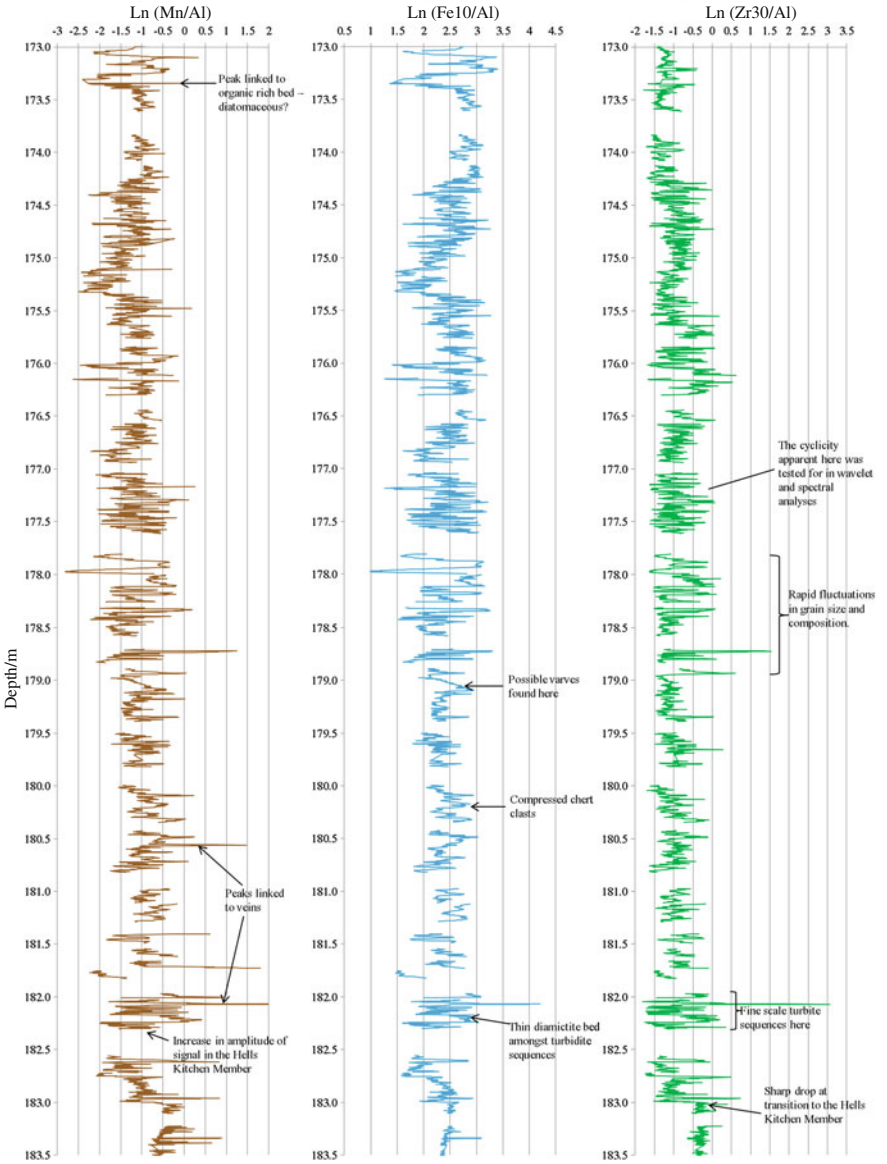
Ln (Mn/Al)
Ln (Fe10/Al)
Ln (Zr30/Al)
Depth/m
Peak linked to organic rich bed – diatomaceous?
Peaks linked to veins
Increase in amplitude of signal in the Hells Kitchen Member
Possible varves found here
Compressed chert clasts
Thin diamictite bed amongst turbidite sequences
The cyclicity apparent here was tested for in wavelet and spectral analysis
Rapid fluctuations in grain size and composition
Fine scale turbite sequences here
Sharp drop at transition to the Hells Kitchen Member

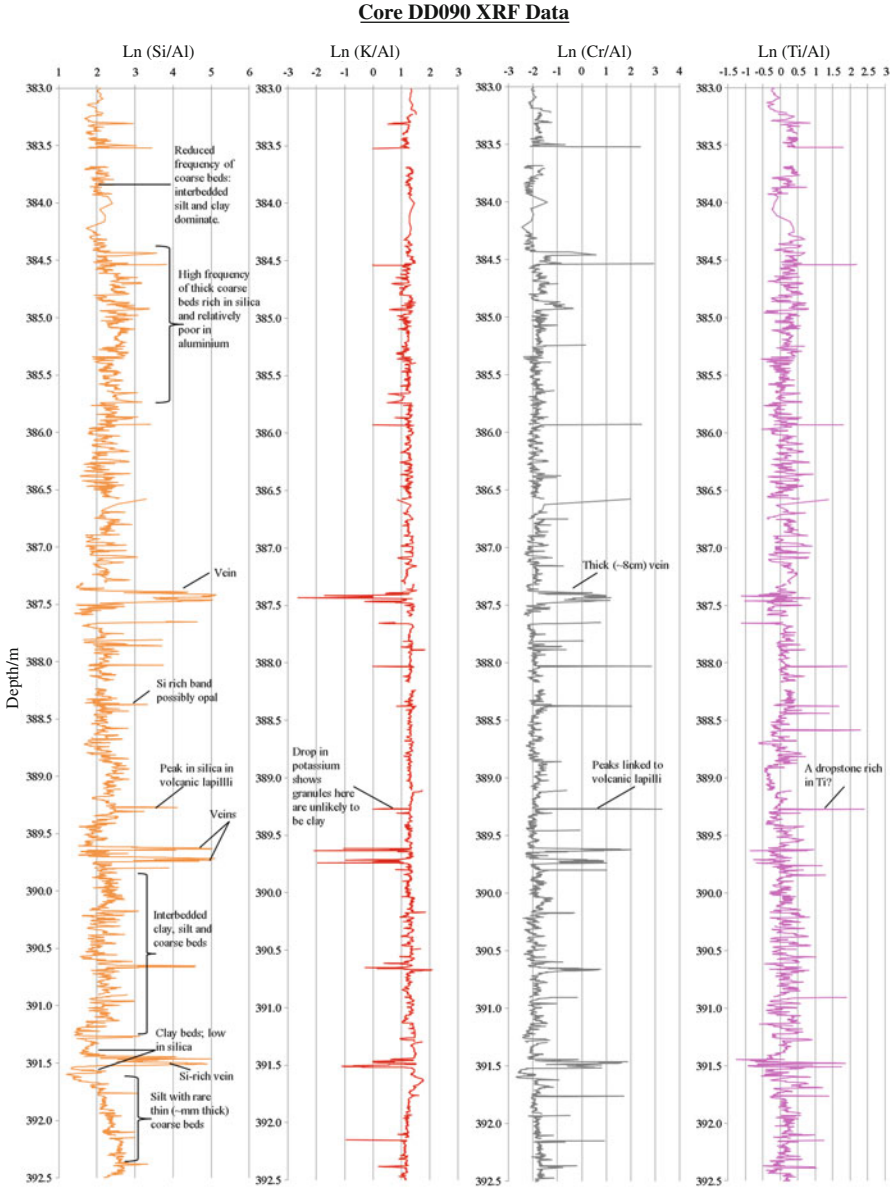
Core DD090 XRF Data
Ln (Si/Al)
Ln (K/Al)
Ln (Cr/Al)
Ln (Ti/Al)
Depth/m
Reduced frequency of coarse beds: interbedded silt and clay dominate.
High frequency of thick coarse beds rich in silica and relatively poor in aluminium
Vein
Si rich band possibly opal
Peak in silica in volcanic lapilli
Veins
Interbedded clay, silt and coarse beds
Clay beds; low in silica
Si-rich vein
Silt with rare thin (~mm thick) coarse beds
Drop in potassium shows granules here are unlikely to be clay
Thick (~8cm) vein
Peaks linked to volcanic lapilli
A dropstone rich in Ti?

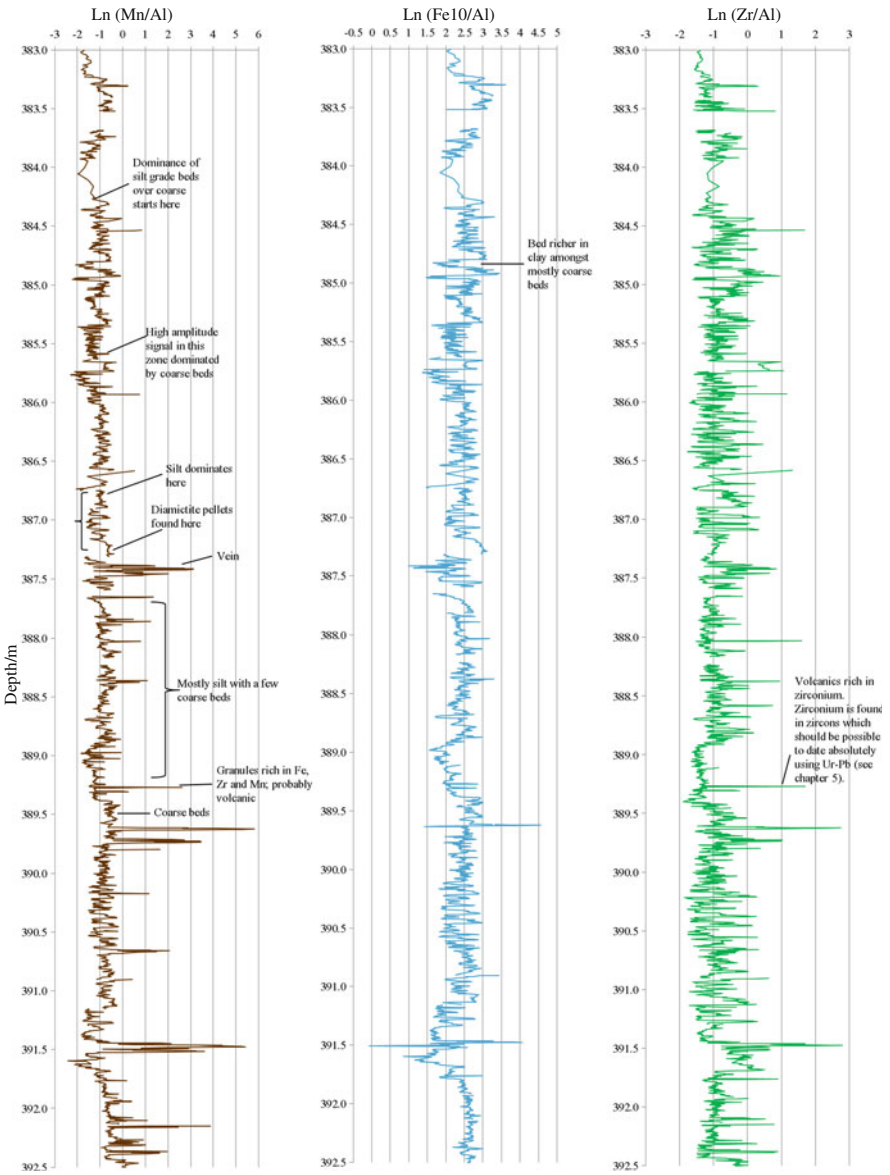
Ln (Mn/Al)
Ln (Fe10/Al)
Ln (Zr/Al)
Depth/m
Dominance of silt grade beds over coarse starts here
High amplitude signal in this zone dominated by coarse beds
Silt dominates here
Diamictite pellets found here
Vein
Mostly silt with a few coarse beds
Granules rich in Fe, Zr and Mn; probably volcanic
Coarse beds
Bed richer in clay amongst mostly coarse beds
Volcanics rich in zirconium. Zirconium is found in zircons which should be possible to date absolutely using Ur-Pb (see chapter 5).

6.4 Clast Data

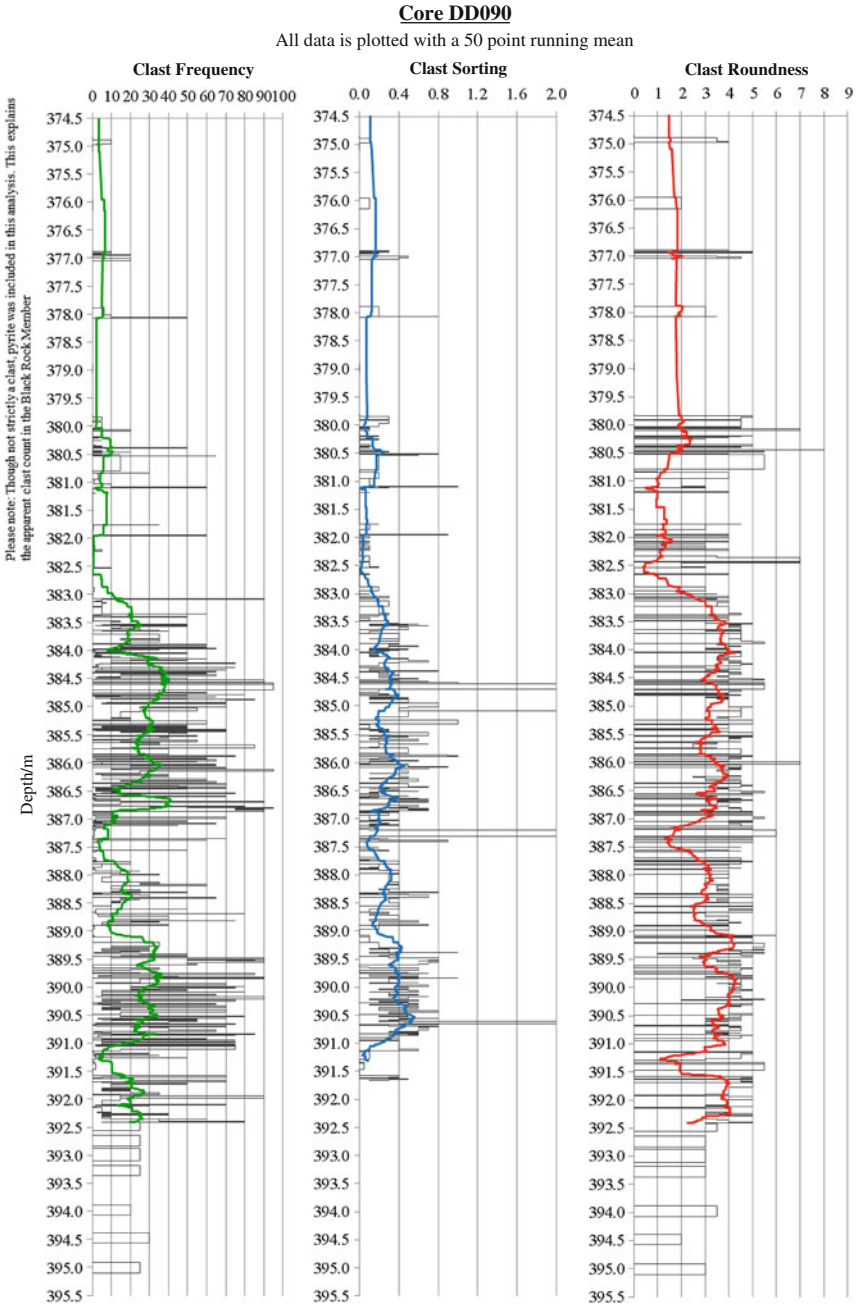

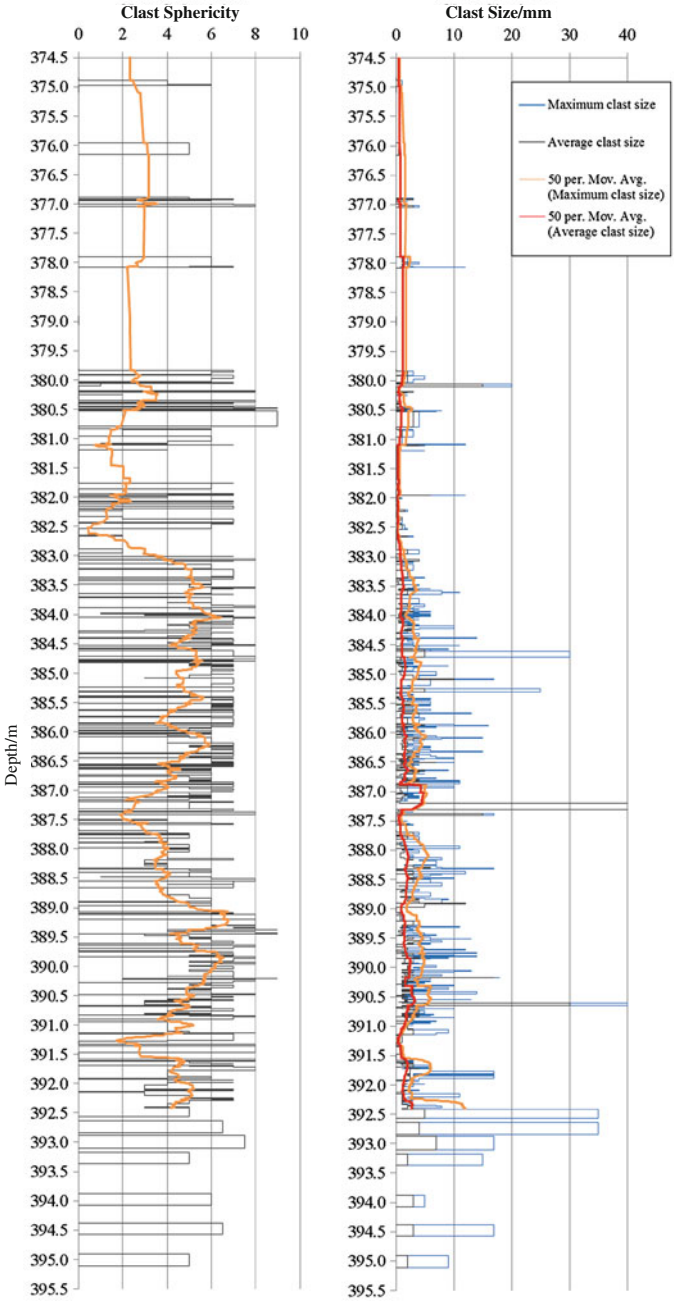
Clast Sphericity
0
2
4
6
8
10
Clast Size/mm
0
10
20
30
40
Depth/m
374.5
375.0
375.5
376.0
376.5
377.0
377.5
378.0
378.5
379.0
379.5
380.0
380.5
381.0
381.5
382.0
382.5
383.0
383.5
384.0
384.5
385.0
385.5
386.0
386.5
387.0
387.5
388.0
388.5
389.0
389.5
390.0
390.5
391.0
391.5
392.0
392.5
393.0
393.5
394.0
394.5
395.0
395.5
Maximum clast size
Average clast size
50 per. Mov. Avg. (Maximum clast size)
50 per. Mov. Avg. (Average clast size)

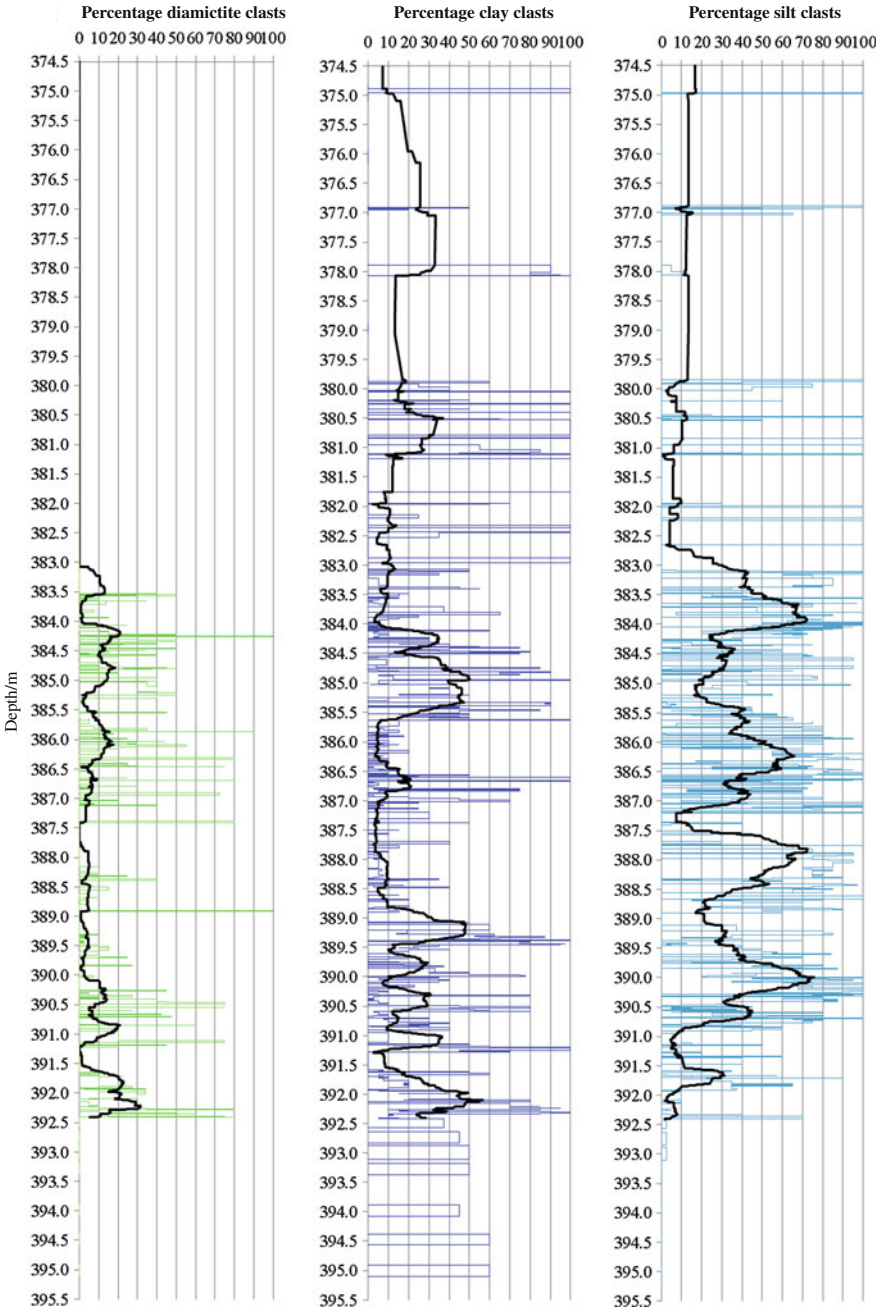
Percentage diamictite clasts
Percentage clay clasts
Percentage silt clasts
0 10 20 30 40 50 60 70 80 90 100
Depth/m
374.5
375.0
375.5
376.0
376.5
377.0
377.5
378.0
378.5
379.0
379.5
380.0
380.5
381.0
381.5
382.0
382.5
383.0
383.5
384.0
384.5
385.0
385.5
386.0
386.5
387.0
387.5
388.0
388.5
389.0
389.5
390.0
390.5
391.0
391.5
392.0
392.5
393.0
393.5
394.0
394.5
395.0
395.5

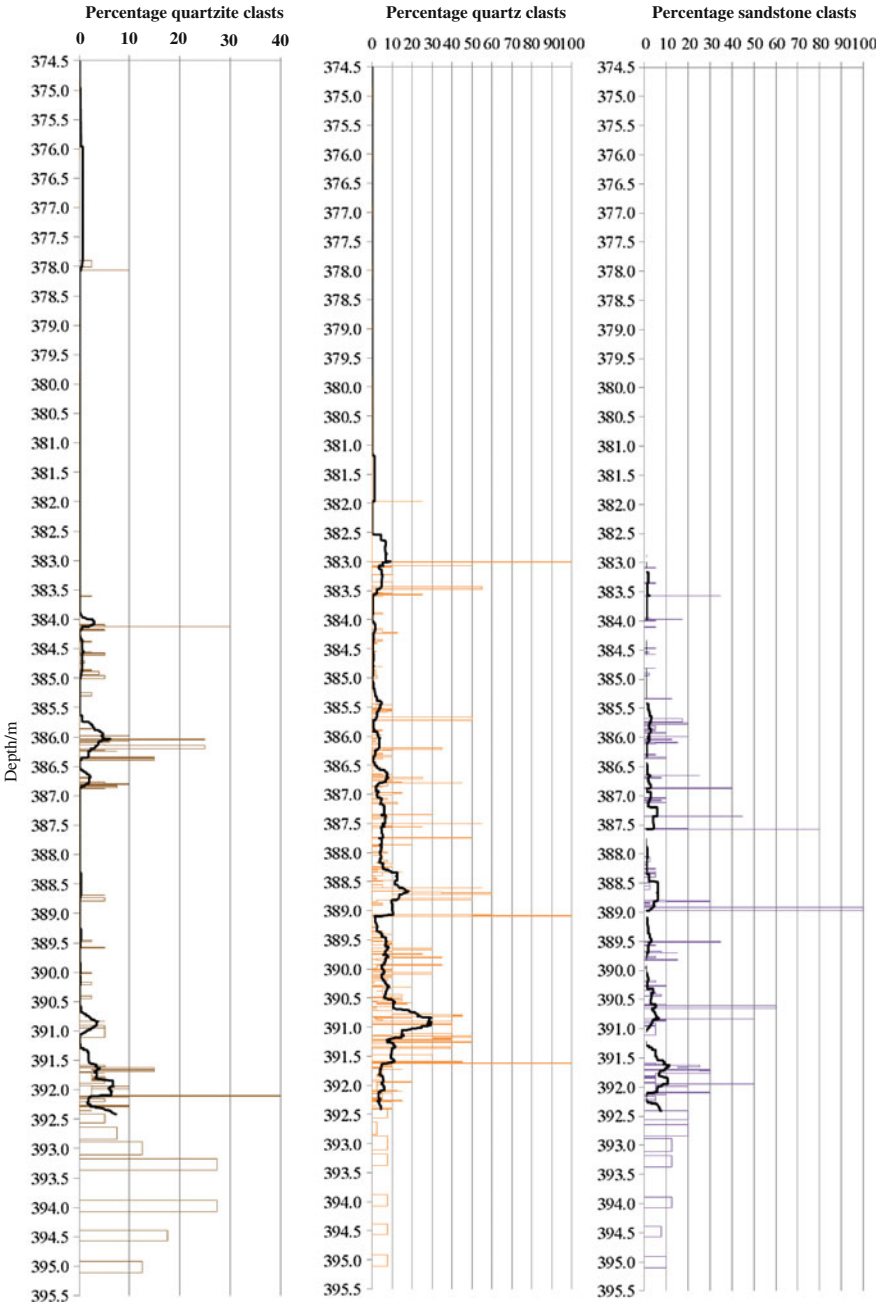
Percentage quartzite clasts
0 10 20 30 40
Percentage quartz clasts
0 10 20 30 40 50 60 70 80 90 100
Percentage sandstone clasts
0 10 20 30 40 50 60 70 80 90 100
Depth/m
374.5
375.0
375.5
376.0
376.5
377.0
377.5
378.0
378.5
379.0
379.5
380.0
380.5
381.0
381.5
382.0
382.5
383.0
383.5
384.0
384.5
385.0
385.5
386.0
386.5
387.0
387.5
388.0
388.5
389.0
389.5
390.0
390.5
391.0
391.5
392.0
392.5
393.0
393.5
394.0
394.5
395.0
395.5

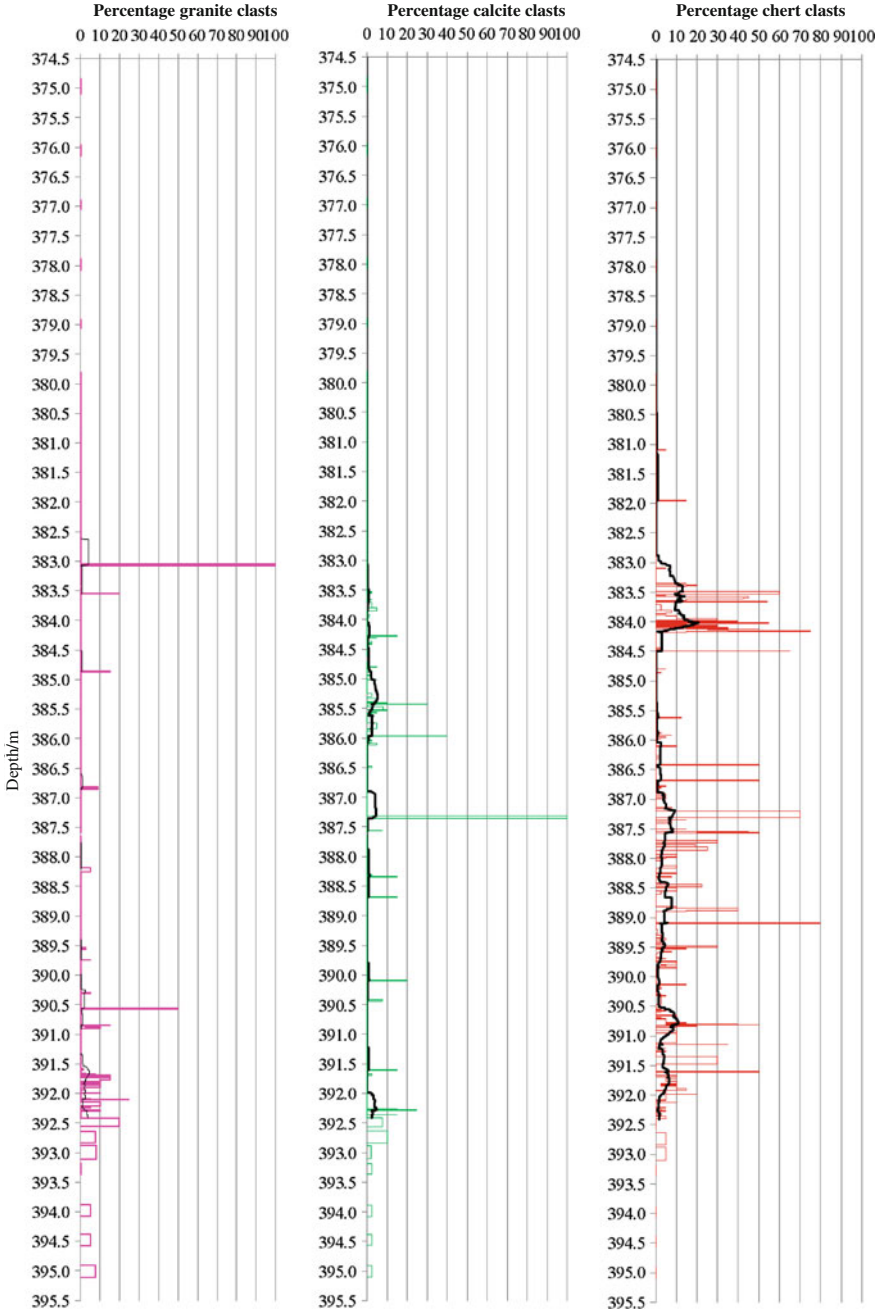
Percentage granite clasts
Percentage calcite clasts
Percentage chert clasts
0 10 20 30 40 50 60 70 80 90 100
Depth/m
374.5
375.0
375.5
376.0
376.5
377.0
377.5
378.0
378.5
379.0
379.5
380.0
380.5
381.0
381.5
382.0
382.5
383.0
383.5
384.0
384.5
385.0
385.5
386.0
386.5
387.0
387.5
388.0
388.5
389.0
389.5
390.0
390.5
391.0
391.5
392.0
392.5
393.0
393.5
394.0
394.5
395.0
395.5

6.5 Total Organic Carbon Data

Tables 6.1 and 6.2.

Table 6.1 Preparation details for total organic carbon procedure

Sample: segment label	Lithology	Mass prior to drying/g (includes sample bag)	Mass after drying/g for 4 h (includes sample bag)	Mass after drying for 8 h/g (includes sample bag)	Mass before adding to HCl/g (excludes sample bag)	Mass after adding to HCl/g (excludes sample bag)
395	Diamictite	1.743	1.738	1.738	1.185	1.037
391.7	Coarse bed	2.435	2.430	2.430	1.879	1.674
391.4	Clay	9.425	9.410	9.408	8.864	8.473
391	Diamictite and clay	1.277	1.272	1.271	0.726	0.633
387.3	Clay	2.768	2.760	2.759	2.210	1.959
385.5	Silt and silt clasts	2.424	2.418	2.419	1.870	1.697
382.2	Green silt	0.988	0.983	0.984	0.441	0.410
382.0	Interlaminated silt and clay	3.785	3.772	3.772	3.231	2.953
155.9	Fine clay	8.039	8.018	8.018	7.468	7.333

Table 6.2 Total inorganic and organic carbon content and $\delta^{13}C/^{12}C$ for samples

Sample: segment label	Total inorganic carbon content (%)	Total organic carbon content (%)	$\delta^{13}C/^{12}C$
395	12.5	0.18	−23.82
391.7	10.9	0.20	−23.65
391.4	4.4	0.12	−23.48
391	12.8	0.15	−23.08
387.3	11.4	0.34	−23.59
385.5	9.3	0.15	−23.38
382.2	7.0	0.10	−25.54
382.0	8.6	0.07	−23.83
155.9	1.8	3.00	−20.93

Appendix

A.1 Generation of Depth Scale

1. Measure offset to the top of each segment from the labels marked approximately on segments.
2. Calculate the position of the base of the segments: = segment label + (segment top – offset to top). Make sure to divide the difference in brackets which is in millimetres by 1,000 to convert to metres.
3. Calculate the position of the beds (= position of base – bed height).
4. For segments that are continuous, there should be no overlap or spacing implied by the labelling. However, because the labels were approximate this is not the case. The offset to top should therefore be recorded for the youngest segment in a sequence. The offset for the segment above it (which should but will not be continuous) is then calculated: = offset for youngest segment + (position of this segment top – position of segment below's base). Again, make sure to multiply the part in brackets by 1,000 to put it in mm.
5. Calculate the position of segment top: = segment label – offset to top recorded in youngest segment.
6. There should now be no overlap within groups of segments that join together. However, sometimes gaps which are clearly present appear to overlap due again to errors in the original labelling. Adjust the 'offset to top' measurement by as little as possible to make the numbers work (continuous sequence). Make sure the position of segment top is a formula (e.g., in excel) when doing this adjustment so the adjustments propagate through groups of segments.

Further stages for plotting clast data

1. Copy all data including the y-axis into a second spreadsheet and duplicate it using the sort function in excel.
2. Copy the position of the segment base, position of beds and y-axis variable (e.g., clast frequency) into a third spreadsheet. Where there are gaps, insert a row so that there are three empty rows in any gap. Then move the segment base numbers to the position of beds column. There should now be only one row in any gap.

K. Horan, *Falkland Islands (Islas Malvinas) in the Permo-Carboniferous*,
Springer Earth System Sciences, DOI 10.1007/978-3-319-08708-5

3. Shift the y-axis variable data up one row and insert a '0' at the top and bottom of each segment/segment group so that the line plotted returns to the axis before a gap.

Further stage for plotting XRF/reflectance data

1. The extent of overlap is greater in the XRF and reflectance data than in the clast/log data because the measurements were not taken perpendicular to bedding. Although the log/clast data and the XRF/reflectance data can be linked through the photographs, it is difficult to compare them directly. To improve the correlation between them, depth control points were inserted into the depth scales for reflectance and XRF data at the beginning and end of every segment in both cores, and the depths between calculated by linear interpolation. Care must be taken when more gaps are present in the XRF/reflectance data than in the log. Using linear interpolation has the disadvantage that the XRF data was not always measured from the start to the end of each segment where broken edges necessitated starting and stopping the detector within a segment. In such cases, the XRF/reflectance data is stretched slightly over the segment interval defined by the log/clast scale depths.

The following core images show the measurements used to improve the depth scale for cores DD029 and DD090, respectively.

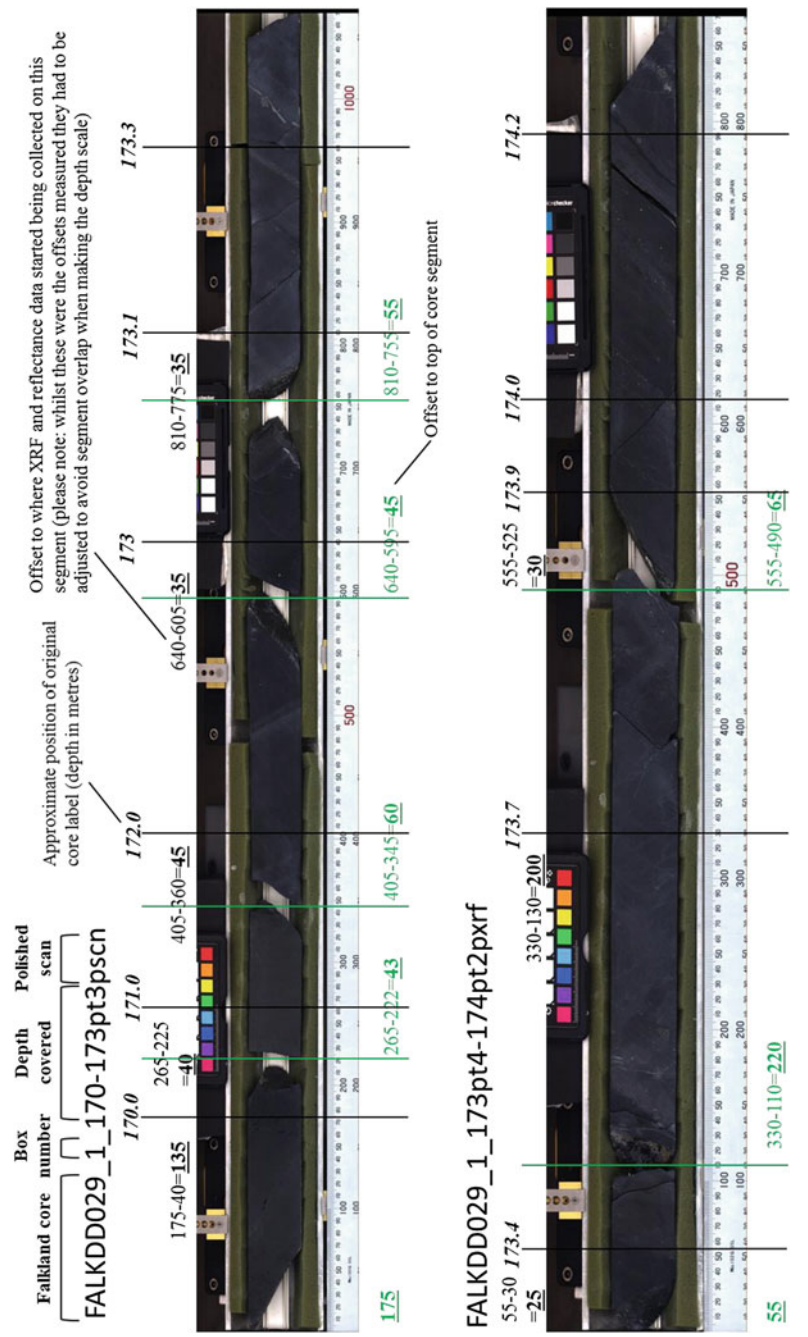
Falkland core
Box number
Depth covered
Polished scan
FALKDD029_1_170-173pt3pscn
175-40=135
265-225 =40
405-360=45
640-605=35
810-775=35
170.0
171.0
172.0
173
173.1
173.3
Approximate position of original core label (depth in metres)
Offset to where XRF and reflectance data started being collected on this segment (please note: whilst these were the offsets measured they had to be adjusted to avoid segment overlap when making the depth scale)
175
265-222=43
405-345=60
640-595=45
810-755=55
Offset to top of core segment
FALKDD029_1_173pt4-174pt2pxrf
55-30 =25
330-130=200
555-525 =30
173.4
173.7
173.9
174.0
174.2
55
330-110=220
555-490=65

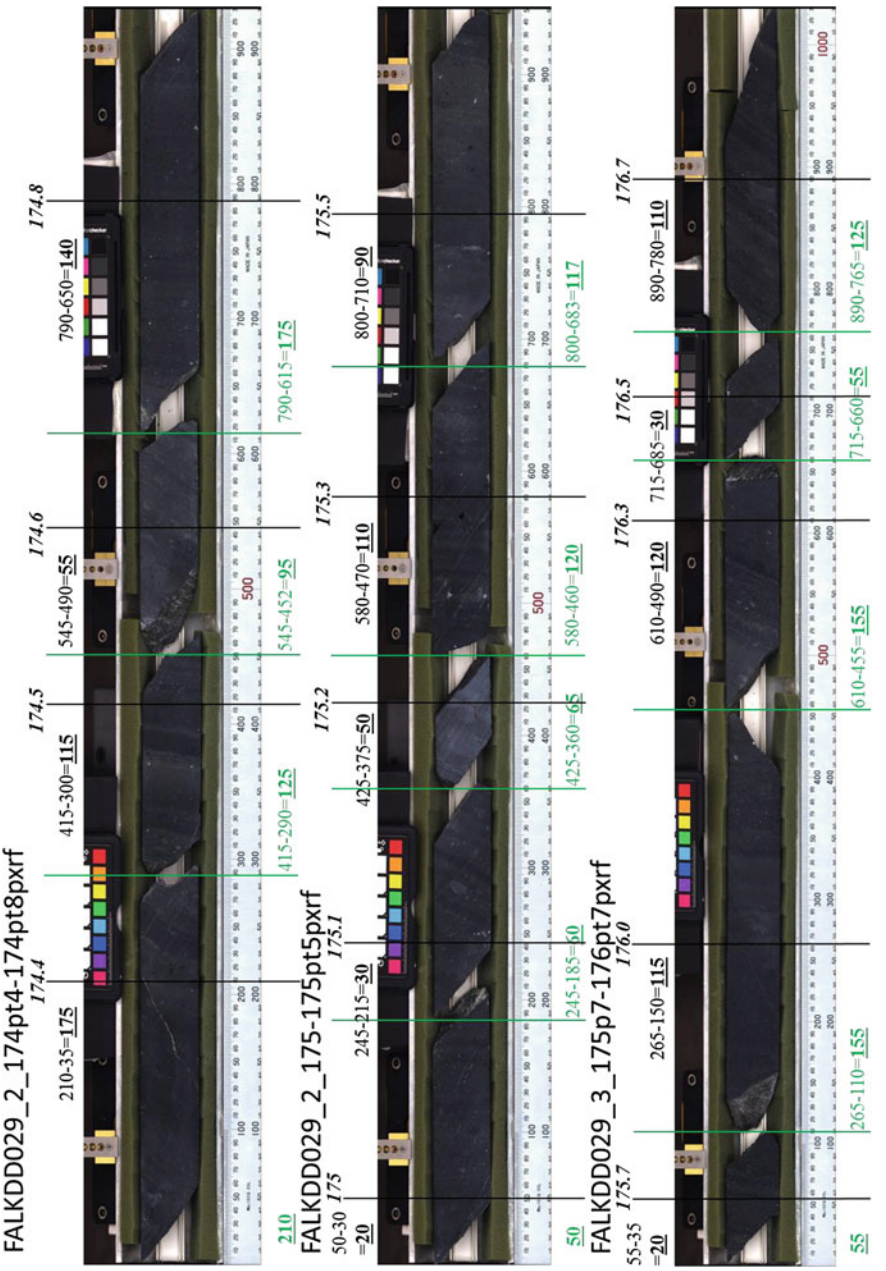
FALKDD029_2_174pt4-174pt8pxrf
210-35=175
415-300=115
545-490=55
790-650=140
210
415-290=125
545-452=95
790-615=175
FALKDD029_2_175-175pt5pxrf
50-30=20
245-215=30
425-375=50
580-470=110
800-710=90
50
245-185=60
425-360=65
580-460=120
800-683=117
FALKDD029_3_175p7-176pt7pxrf
55-35=20
265-150=115
610-490=120
715-685=30
890-780=110
55
265-110=155
610-455=155
715-660=55
890-765=125

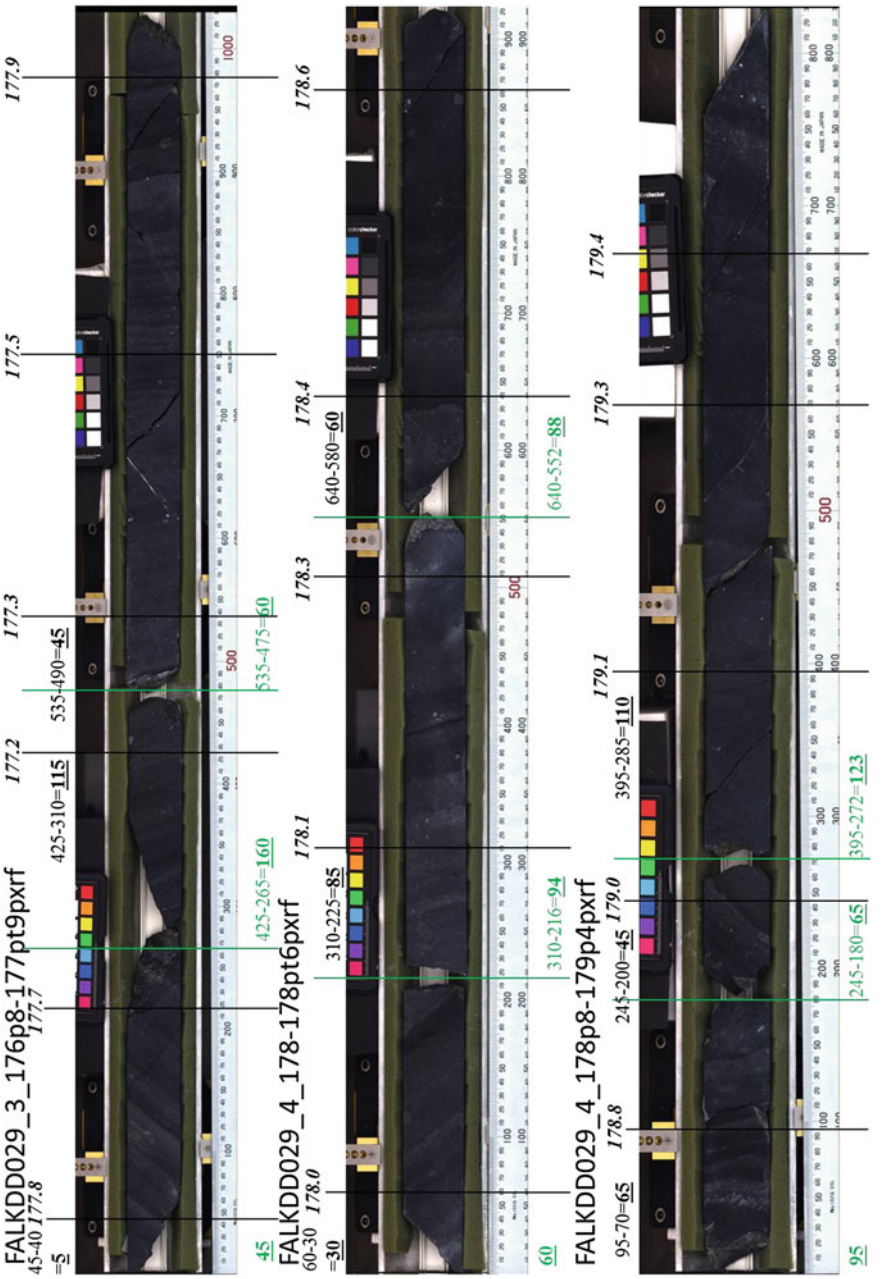
FALKDD029_3_176p8-177pt9pxrf
45-40 177.8 177.7 177.2 177.3 177.5 177.9
=5
425-310=115
535-490=45
425-265=160
535-475=60
45
FALKDD029_4_178-178pt6pxrf
60-30 178.0 178.1 178.3 178.4 178.6
=30
310-225=85
640-580=60
310-216=94
640-552=88
60
FALKDD029_4_178p8-179p4pxrf
95-70=65 178.8 179.0 179.1 179.3 179.4
245-200=45
395-285=110
245-180=65
395-272=123
95

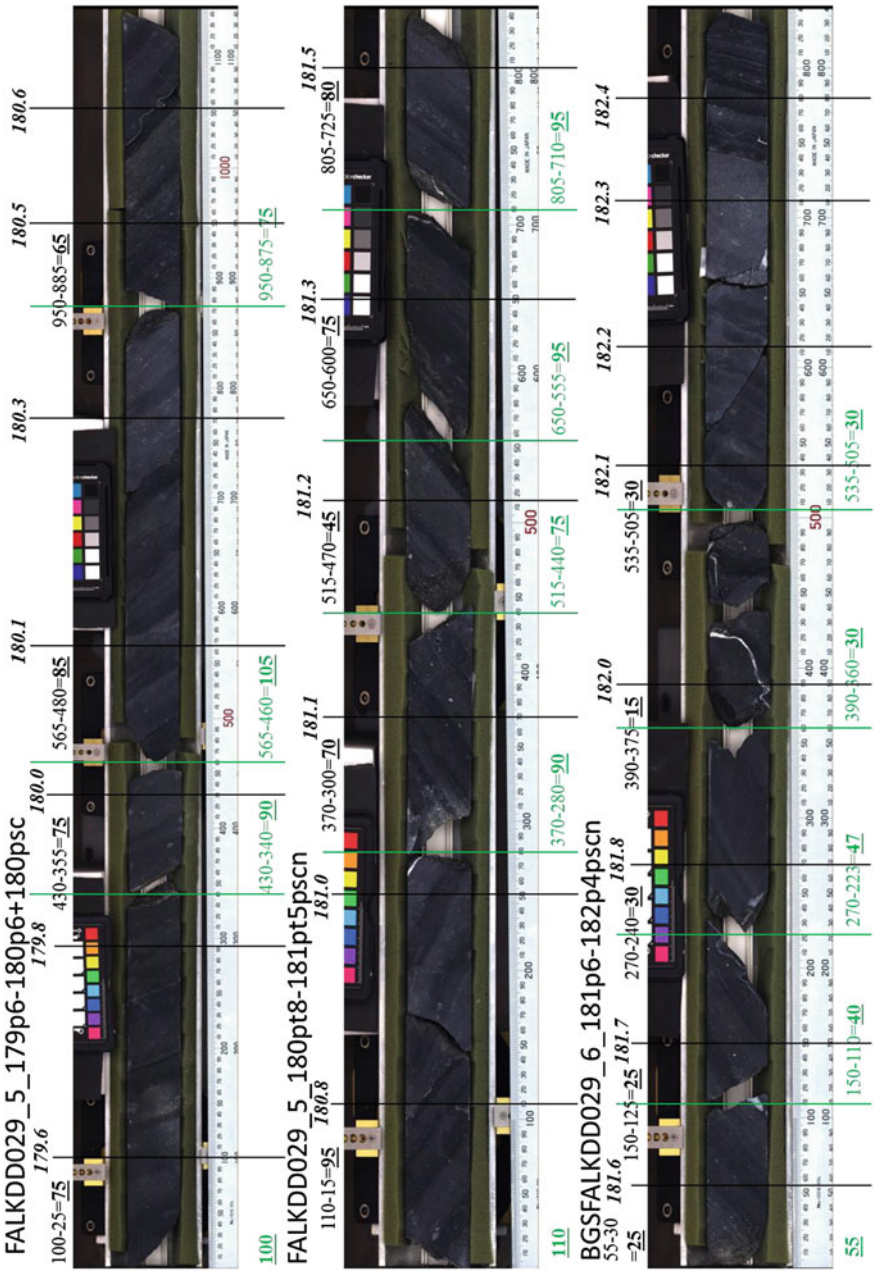
FALKDD029_5_179p6-180p6+180psc
179.6
179.8
180.0
180.1
180.3
180.5
180.6
100-25=75
430-355=75
565-480=85
950-885=65
100
430-340=90
565-460=105
950-875=75
FALKDD029_5_180pt8-181pt5pscn
180.8
181.0
181.1
181.2
181.3
181.5
110-15=95
370-300=70
515-470=45
650-600=75
805-725=80
110
370-280=90
515-440=75
650-555=95
805-710=95
BGSFALKDD029_6_181p6-182p4pscn
181.6
181.7
181.8
182.0
182.1
182.2
182.3
182.4
55-30=25
150-125=25
270-240=30
390-375=15
535-505=30
55
150-110=40
270-223=47
390-360=30
535-505=30

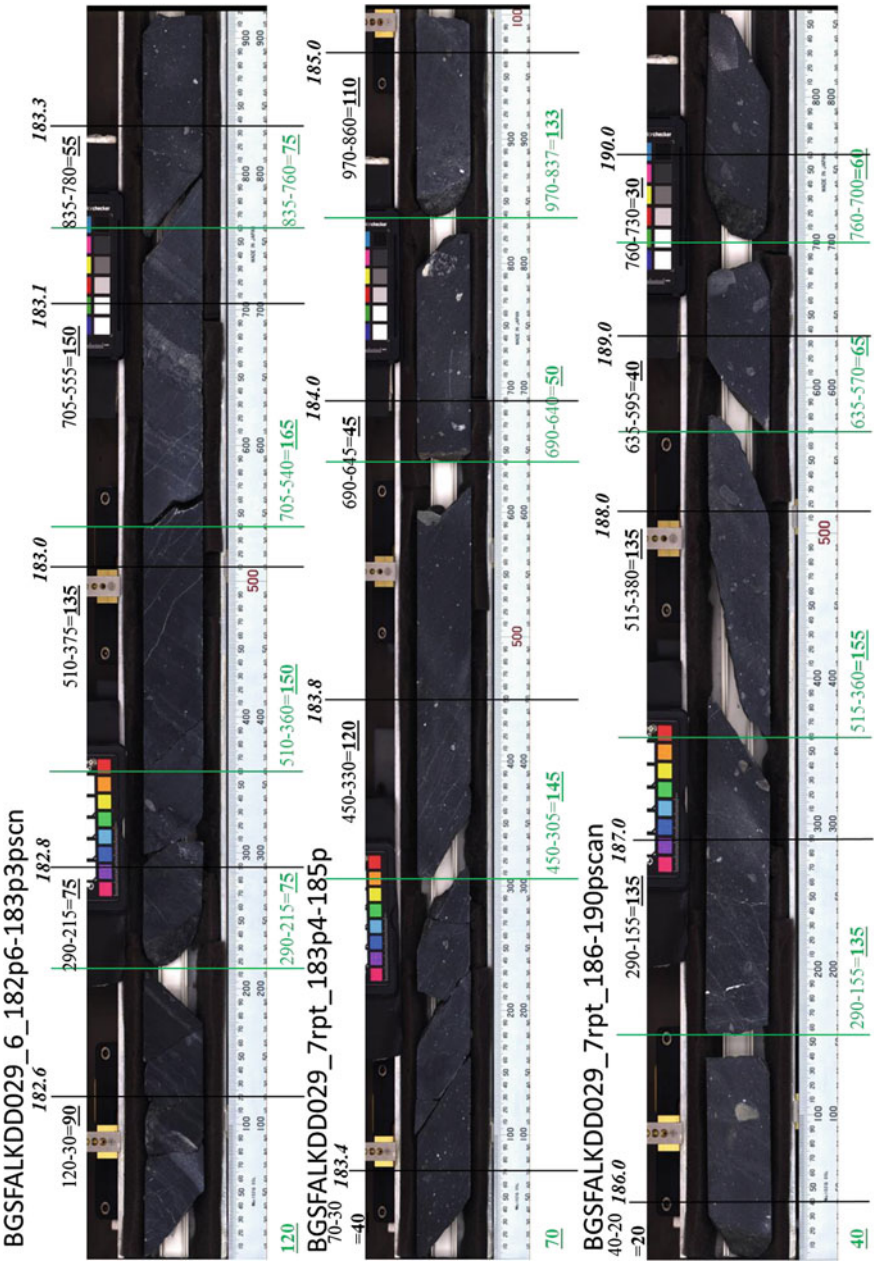
BGSFALKDD029_6_182p6-183p3pscn
182.6
120-30=90
182.8
290-215=75
183.0
510-375=135
183.1
705-555=150
183.3
835-780=55
120
290-215=75
510-360=150
705-540=165
835-760=75
BGSFALKDD029_7rpt_183p4-185p
70-30=40
183.4
183.8
450-330=120
184.0
690-645=45
185.0
970-860=110
70
450-305=145
690-640=50
970-837=133
BGSFALKDD029_7rpt_186-190pscan
40-20=20
186.0
187.0
290-155=135
188.0
515-380=135
189.0
635-595=40
190.0
760-730=30
40
290-155=135
515-360=155
635-570=65
760-700=60

FALKDD090_3_155p8-156p7pxrf
155.8
80-10
=70
155.9
200-175
=25
156.0
290-260
=30
156.2
470-395
=75
156.3
590-525
=65
156.4
710-
650=60
156.5
795-755
=40
156.6
885-845
=40
156.7
1050-960
=90
80
200-170
=30
290-257
=33
470-375=95
590-518=72
710-640=70
795-753
=42
885-842
=43
1050-952=98
FALKDD090_5_157p7-158p7pxrf
157.7
30-10
=20
157.8
90-70
=20
157.9
165-145
=20
158.0
295-
230=65
158.1
158.2
510-460
=50
158.3
625-565
=60
158.4
740-680
=60
158.6
860-815
=45
158.7
1020-965=55
30
90-62
=28
165-124
=41
295-228=67
510-460
=50
625-562=63
740-675=65
860-815=45
1020-960=60

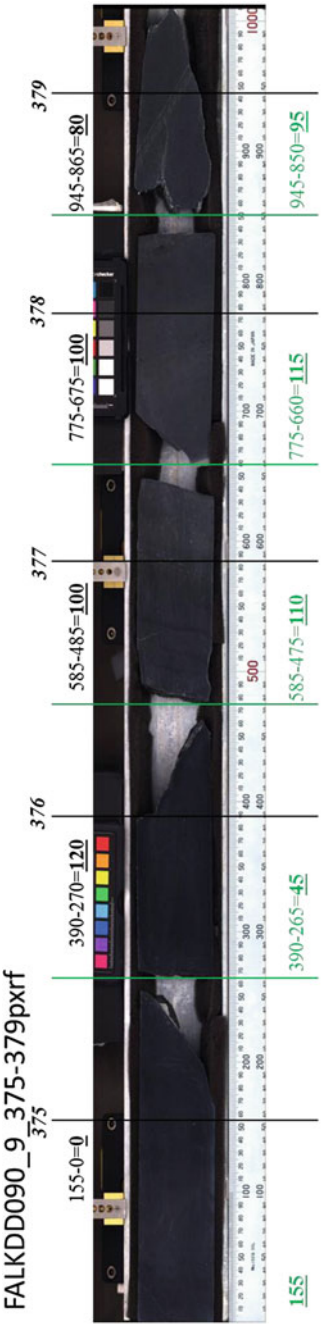
FALKDD090_9_375-379pxrf
375
376
377
378
379
155-0=0
390-270=120
585-485=100
775-675=100
945-865=80
155
390-265=45
585-475=110
775-660=115
945-850=95


FALKDD090_10_380-380p8pxrf
380
380.2
380.4
380.6
380.8
100-30=70
290-230=60
100

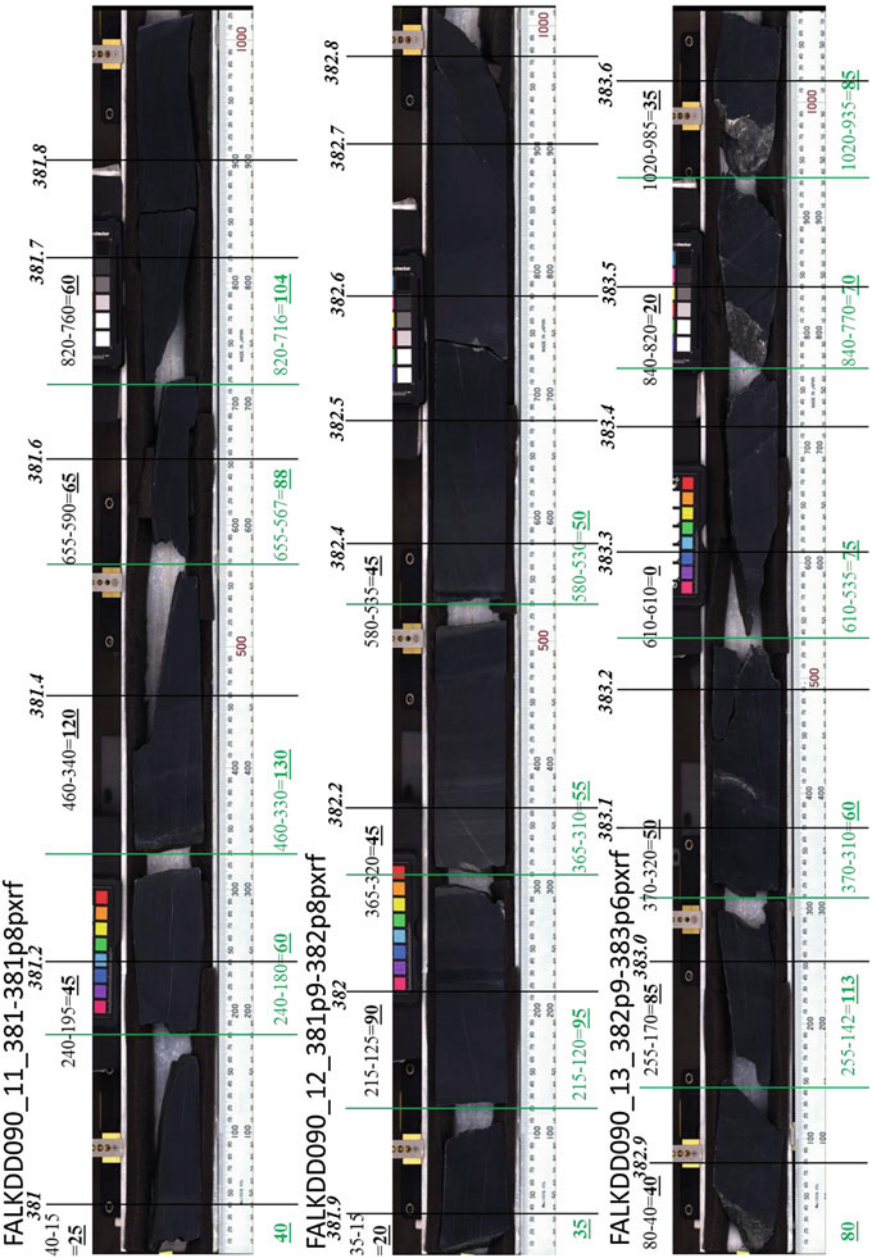
FALKDD090_11_381-381p8pxrf
381
381.2
381.4
381.6
381.7
381.8
40-15
=25
240-195=45
460-340=120
655-590=65
820-760=60
40
240-180=60
460-330=130
655-567=88
820-716=104
FALKDD090_12_381p9-382p8pxrf
381.9
382
382.2
382.4
382.5
382.6
382.7
382.8
35-15
=20
215-125=90
365-320=45
580-535=45
35
215-120=95
365-310=55
580-530=50
FALKDD090_13_382p9-383p6pxrf
382.9
383.0
383.1
383.2
383.3
383.4
383.5
383.6
80-40=40
255-170=85
370-320=50
610-610=0
840-820=20
1020-985=35
80
255-142=113
370-310=60
610-535=75
840-770=70
1020-935=85

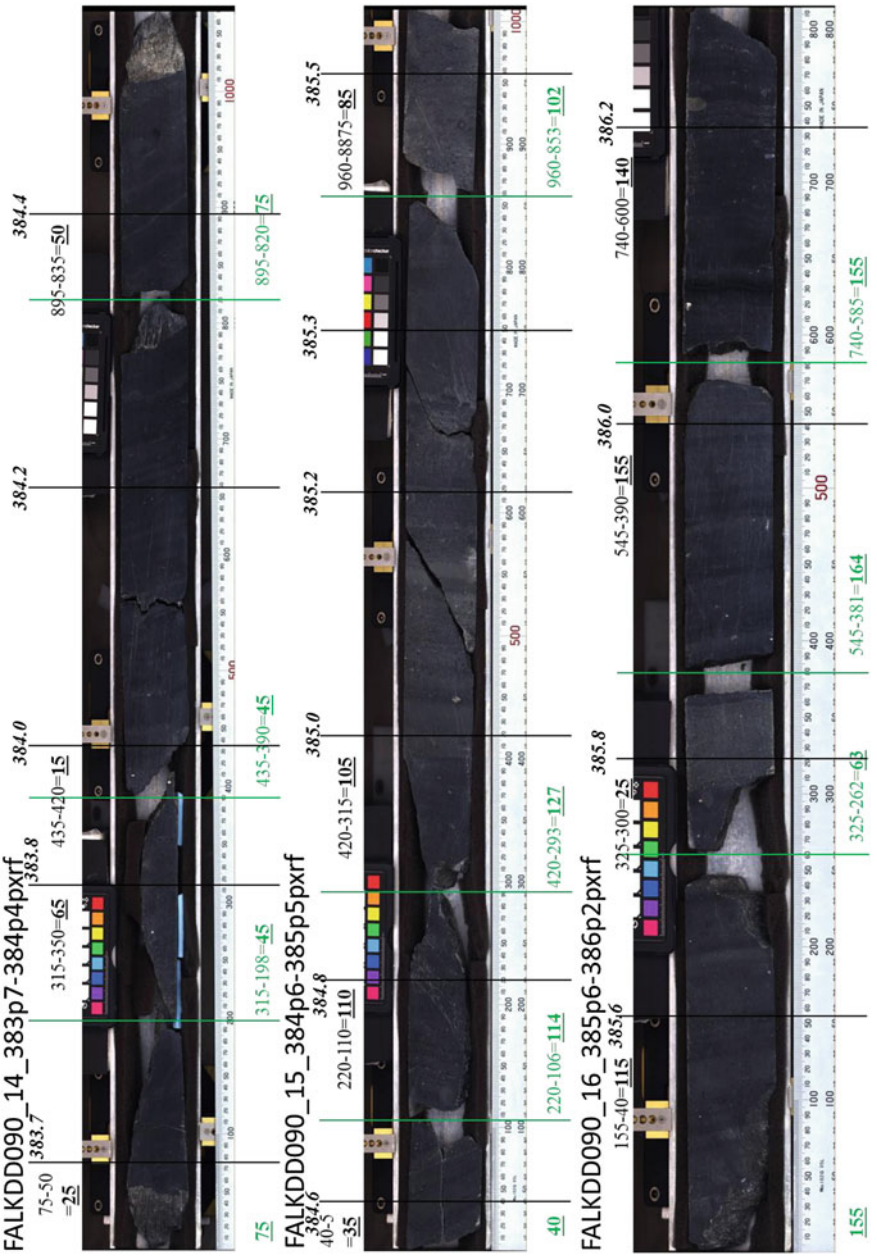
FALKDD090_14_383p7-384p4pxrf
383.7
75-50
=25
383.8
315-350=65
384.0
435-420=15
384.2
384.4
895-835=50
75
315-198=45
435-390=45
895-820=75
FALKDD090_15_384p6-385p5pxrf
384.6
40-5
=35
384.8
220-110=110
385.0
420-315=105
385.2
385.3
385.5
960-8875=85
40
220-106=114
420-293=127
960-853=102
FALKDD090_16_385p6-386p2pxrf
385.6
155-40=115
385.8
325-300=25
386.0
545-390=155
386.2
740-600=140
155
325-262=63
545-381=164
740-585=155

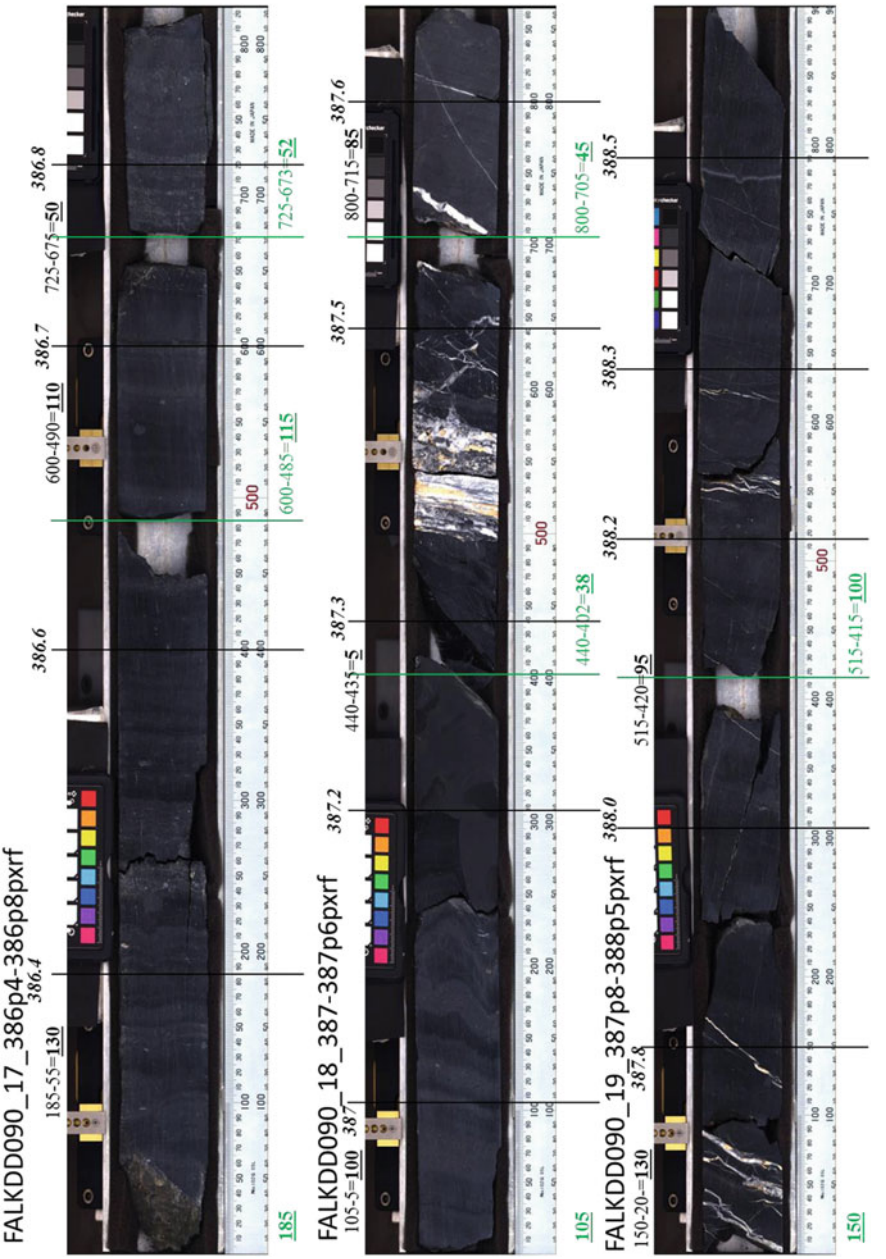
FALKDD090_17_386p4-386p8pxrf
386.4
185-55=130
386.6
600-490=110
386.7
725-675=50
386.8
500
600-485=115
725-673=52
185
FALKDD090_18_387-387p6pxrf
387.2
105-5=100
387
387.3
440-435=5
387.5
800-715=85
387.6
500
440-402=38
800-705=45
105
FALKDD090_19_387p8-388p5pxrf
387.8
150-20=130
388.0
515-420=95
388.2
388.3
388.5
500
515-415=100
150

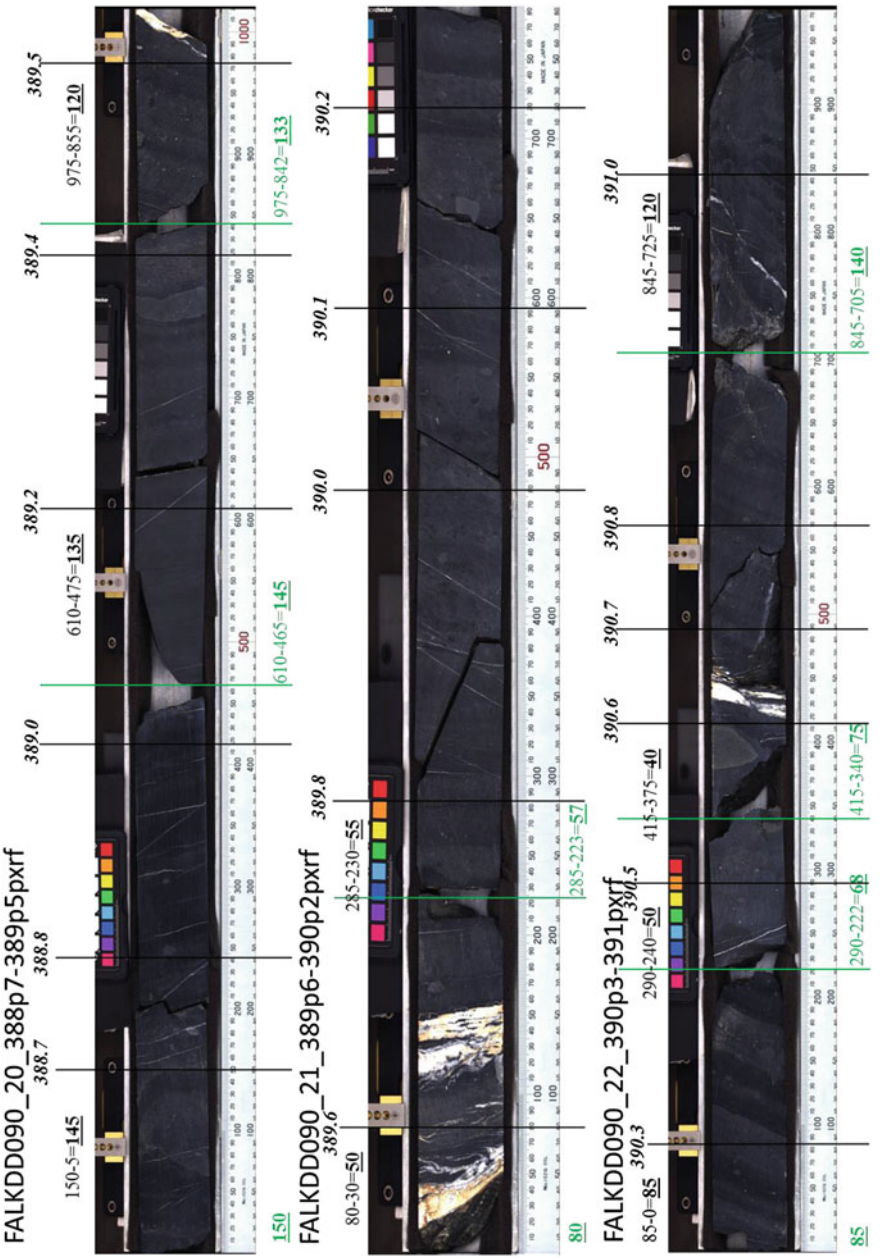
FALKDD090_20_388p7-389p5pxrf
388.7
388.8
389.0
389.2
389.4
389.5
150-5=145
610-475=135
975-855=120
150
610-465=145
975-842=133
FALKDD090_21_389p6-390p2pxrf
389.6
389.8
390.0
390.1
390.2
80-30=50
285-230=55
80
285-223=57
FALKDD090_22_390p3-391pxrf
390.3
390.5
390.6
390.7
390.8
391.0
85-0=85
290-240=50
415-375=40
845-725=120
85
290-222=68
415-340=75
845-705=140

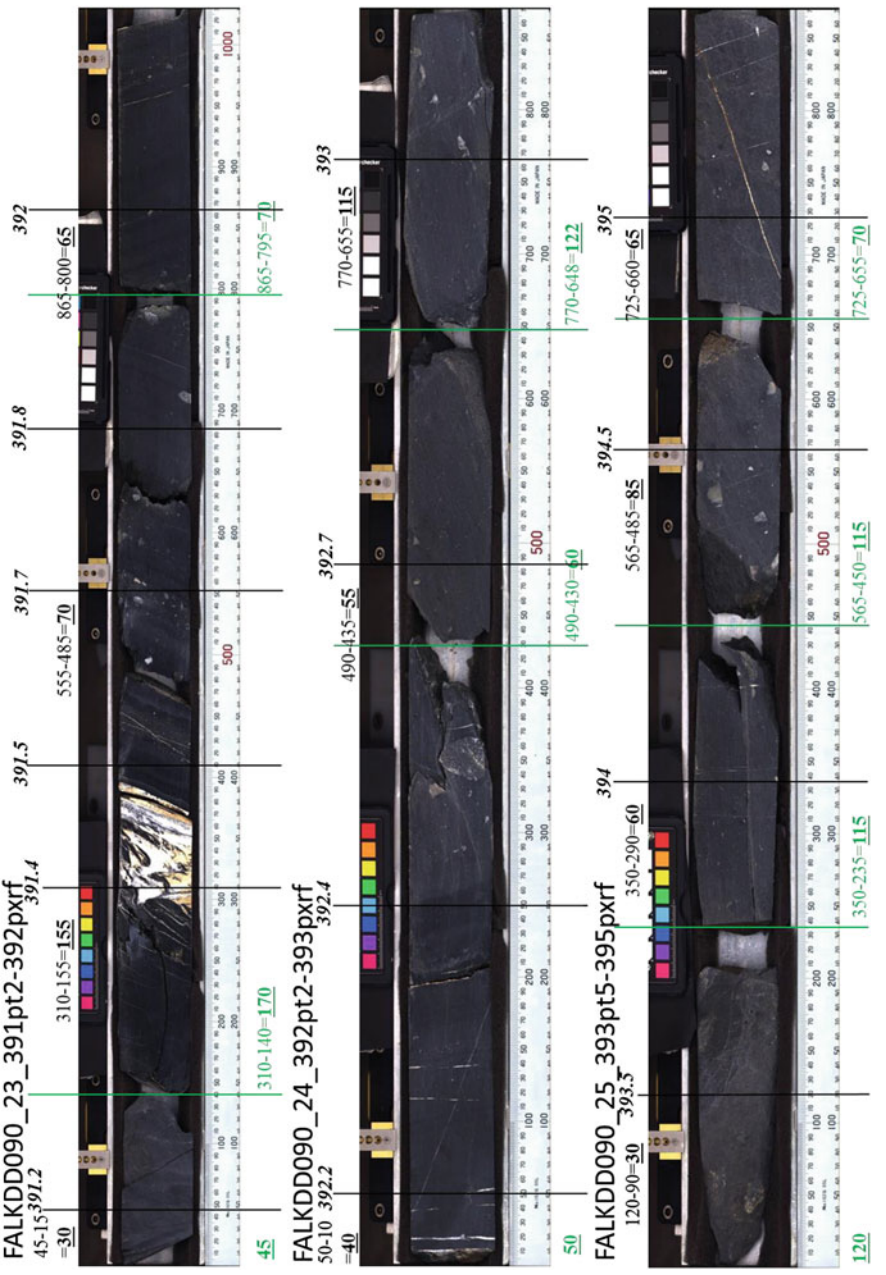
FALKDD090_23_391pt2-392pxrf
391.2
391.4
391.5
391.7
391.8
392
45-15=30
310-155=155
555-485=70
863-800=65
865-795=70
310-140=170
45
FALKDD090_24_392pt2-393pxrf
392.2
392.4
392.7
393
50-10=40
490-435=55
770-655=115
770-648=122
490-430=60
50
FALKDD090_25_393pt5-395pxrf
393.5
394
394.5
395
120-90=30
350-290=60
565-485=85
725-660=65
350-235=115
565-450=115
725-655=70
120

A.2 Preliminary Spectral Analyses and Age Modelling

Prior to the depth scale adjustment, the XRF and reflectance data were used in preliminary spectral analyses, wavelet analyses and age modelling and an auto-correlation was run between the cores. Although the outcome was suggestive of cyclical forcing, this was tentative due partly to the overlaps on the depth scale and could not be used alone to draw reliable conclusions. In these preliminary tests, the a* reflectance parameter showed the best-defined power peaks and these had frequency ratios suggestive of Milankovitch astronomical forcing of the depositional process. Use of this parameter was, therefore, pursued further (see Chap. 4).

Spectral analysis identifies periodicities (where present) and calculates their temporal ratio. It was used first in this study to look for Milankovitch cyclicity over the Hells Kitchen Member where cyclical changes in sedimentation were observed during logging. Spectral analyses were run using Analyseries software on data from both cores independently and compared. Both data sets suggested the possibility of strong power at frequencies corresponding to eccentricity and obliquity. Precession, if present in the cores, may have been lost in the background noise at the high frequency end of the spectrum. Some results are presented in Figs. A.1, A.2 and A.3.

The prominent periodicities identified in the spectral analysis were used to develop a relative age model (Fig. A.4). Based on the presence of high power at frequencies plausibly representing Milankovitch cycles, a time frame ~1.3 Ma was placed on the length of the Hells Kitchen Member. This initial age model appears to have 400 kyr cyclicity which would have been used to refine the age model if the data was non-overlapping. Such adjustments would be valid since the assumption that sedimentation rates were constant throughout the Hells Kitchen Member is poor.

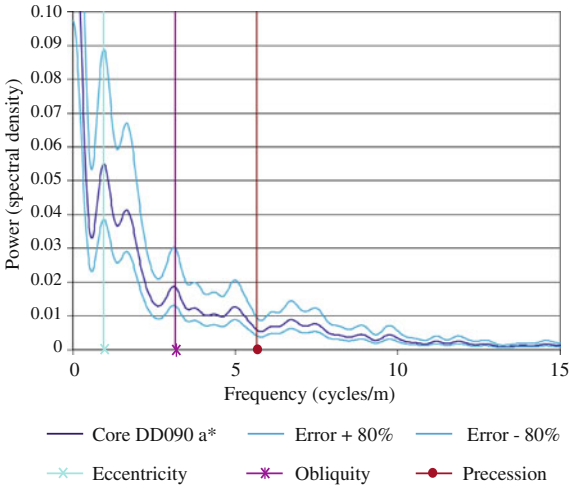

Fig. A.1 Spectral analysis in the depth domain on the a* parameter of core DD090 when the data still had overlaps. The *vertical lines* represent the recurrence ratio of cycles if the eccentricity were to be fixed in the position shown. The calculated periods correspond approximately to those of the anticipated orbital parameters

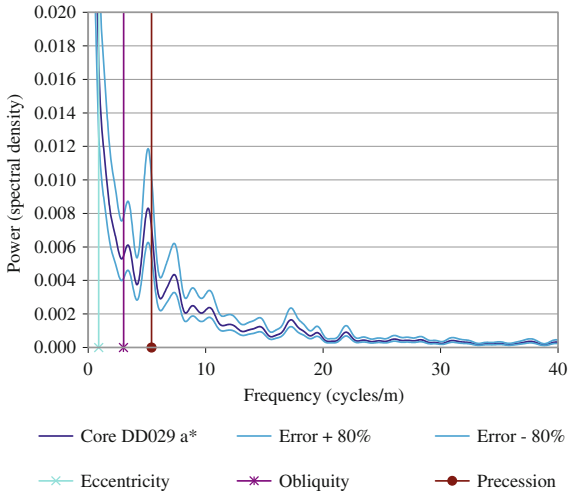

Fig. A.2 Spectral analysis on the a* parameter of core DD029 in the depth domain when the data still had overlaps. The *vertical lines* represent the recurrence ratio of cycles if the eccentricity were to be fixed in the position shown. Note, however, the absence of power at the 'precessional' depth periodicity. A sedimentation rate of 0.9 m/100 kyr (9 m/Ma) is implied

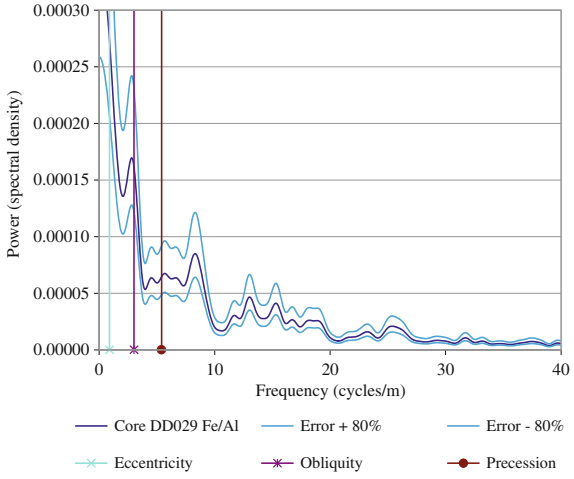

Fig. A.3 An example of a spectral analysis on the elemental data Ln(Fe/Al), for core DD029, which showed one of the most promising set of peaks

Sudden inputs of meltwater or turbidites for example introduce rates higher than the average when tuning to eccentricity periods. Such abrupt changes would usually be swamped by longer term changes, such as river runoff or productivity, but repeated turbidites or meltwater events might have an effect on the long-term rates.

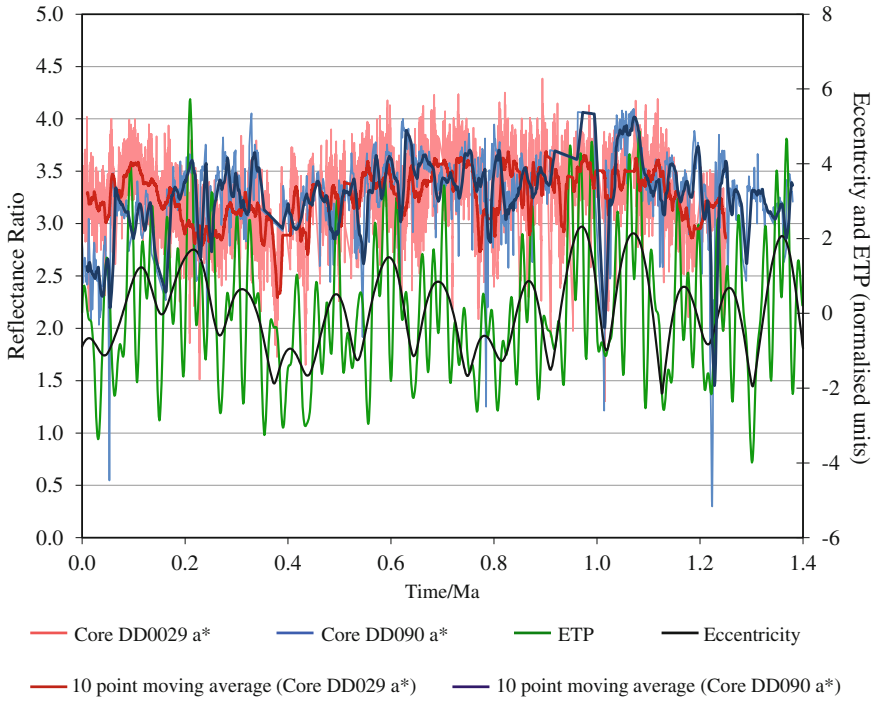

Fig. A.4 Preliminary age modelling showing some clustering of cycle periods around Milankovitch Periods represented by the ETP (eccentricity, obliquity and precession forcing). Power units are reflectance ratios. The eccentricity units are normalised eccentricity

There is some suggestion of similarity between the wavelet spectra of the orbital variations and palæoclimatic cycles even in these preliminary experiments (Fig. A.5). A preliminary autocorrelation was carried out with the hope of finding an adjustment in time on a simple age model which would be required for the cores to have the closest correspondence (Fig. A.6). This autocorrelation suggested that there is very low correlation between the two cores over the Hells Kitchen Member with a correlation coefficient maximum of ~ 0.08. However, it is possible that a higher correlation between the cores has been obscured by the high frequency nature of the data since the spectral and wavelet analyses showed prominent periodicities that could reflect Milankovitch forcing in both. The datasets therefore benefitted from smoothing before the autocorrelation was run (see Sect. 4.1.2).

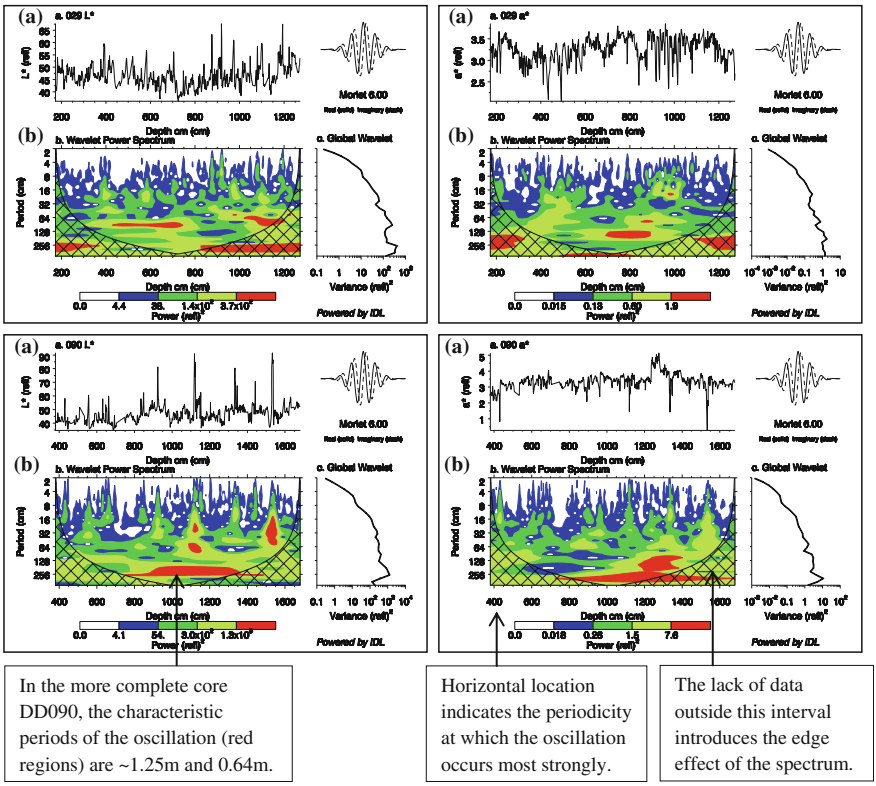

Fig. A.5 Wavelet analysis showing the prominent periodicities in the depth domain through the cores

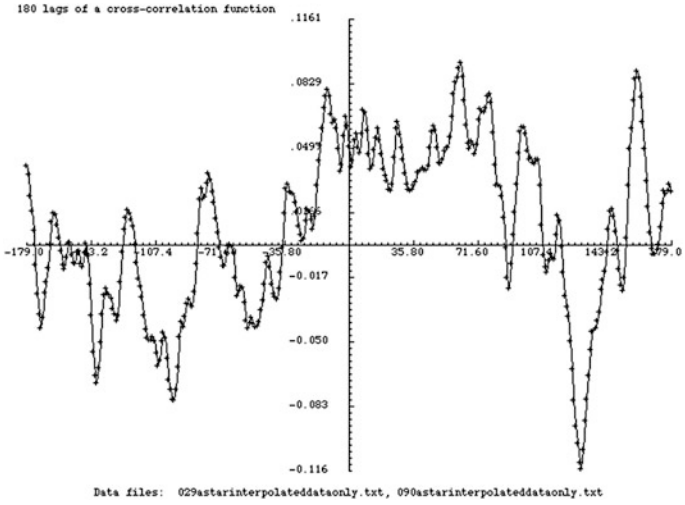

Fig. A.6 Preliminary autocorrelation between cores calculated using the a* reflectance data when the cores had an overlapping depth scale

A.3 Principal Component Analysis Output

Core DD029 (Tables A.1 and A.2).
Core DD090 (Tables A.3 and A.4).

Table A.1 Results from a Principal Component Analysis on core DD029 XRF data

Total variance explained					
Component	Initial eigenvalues			Extraction sums of squared loadings	
	Total	% of Variance	Cumulative %	Total	% of Variance
1	9.253	48.700	48.700	9.253	48.700
2	2.457	12.931	61.632	2.457	12.931
3	1.327	6.982	68.614	1.327	6.982
4	1.043	5.490	74.104	1.043	5.490
5	0.784	4.124	78.228	0.784	4.124
6	0.685	3.603	81.832		
7	0.591	3.112	84.944		
8	0.451	2.372	87.316		
9	0.415	2.183	89.498		
10	0.402	2.118	91.617		
11	0.341	1.795	93.411		
12	0.312	1.645	95.056		
13	0.270	1.423	96.479		
14	0.186	0.977	97.456		
15	0.159	0.836	98.292		
16	0.133	0.699	98.992		
17	0.098	0.514	99.506		
18	0.066	0.348	99.853		
19	0.028	0.147	100.00		

Component matrix[a]					
	Component				
	1	2	3	4	5
Si/A log ratio	0.782	0.292	−0.070	−0.205	0.197
S/Al log ratio	0.466	0.429	0.405	0.289	−0.293
Cl/Al log ratio	0.865	0.216	−0.006	−0.178	0.064
K/Al log ratio	−0.816	0.326	0.182	0.125	−0.19
Ca/Al log ratio	0.756	0.151	−0.480	0.156	0.007

(continued)

Table A.1 (continued)

Ti/Al log ratio	0.736	−0.56	−0.007	0.163	0.095
Cr/Al log ratio	0.868	0.252	0.114	−0.113	0.001
Mn/Al log ratio	0.847	−0.229	−0.255	0.096	−0.085
Fe/Al log ratio	0.663	−0.663	0.101	0.029	0.035
Cu/Al log ratio	0.502	0.239	0.282	0.553	0.359
Zn/Al log ratio	0.626	−0.287	0.238	0.387	0.238
Br/Al log ratio	0.784	0.041	0.216	−0.224	−0.112
Rb/Al log ratio	−0.931	0.274	−0.039	0.093	0.045
Sr/Al log ratio	0.173	0.544	−0.681	0.266	−0.44
Zr/Al log ratio	0.770	0.115	−0.227	−0.35	−0.004
Pb/Al log ratio	0.603	0.174	0.194	0.147	−0.597
Ni/Al log ratio	0.739	0.373	0.101	−0.198	0.006
Br/Al log ratio	0.495	0.194	0.180	−0.384	0.216
Ba/Al log ratio	−0.292	0.811	0.162	−0.042	0.181

Extraction Method: Principal Component Analysis[a]

[a] 5 components extracted

Table A.2 Correlation matrix for core DD029

BGS Core DD029 Correlation Matrix		Si/Al log ratio	S/Al log ratio	Cl/Al log ratio	K/Al log ratio	Ca/Al log ratio	Ti/Al log ratio	Cr/Al log ratio	Mn/Al log ratio	Fe/Al log ratio	Cu/Al log ratio	Zn/Al log ratio	Br/Al log ratio	Rb/Al log ratio	Sr/Al log ratio	Zr/Al log ratio	Pb/Al log ratio	Ni/Al log ratio	Br/Al log ratio	Ba/Al log ratio
Correlation	Si/Al log ratio	1.000	0.367	0.828	−0.668	0.582	0.465	0.729	0.507	0.303	0.393	0.367	0.578	−0.640	0.246	0.666	0.392	0.687	0.413	0.022
	S/Al log ratio	0.367	1.000	0.431	−0.201	0.244	0.220	0.476	0.252	0.064	0.449	0.281	0.404	−0.327	0.155	0.338	0.483	0.434	0.264	0.143
	Cl/Al log ratio	0.828	0.431	1.000	−0.674	0.653	0.535	0.815	0.634	0.420	0.404	0.426	0.700	−0.767	0.201	0.658	0.486	0.711	0.448	−0.062
	K/Al log ratio	−0.688	−0.201	−0.674	1.000	−0.569	−0.589	−0.554	−0.735	−0.704	−0.253	−0.501	−0.581	0.870	−0.057	−0.677	−0.356	−0.455	−0.311	−0.547
	Ca/Al log ratio	0.582	0.244	0.653	−0.569	1.000	0.524	0.638	0.807	0.357	0.372	0.371	0.477	−0.618	0.515	0.621	0.415	0.526	0.316	−0.160
	Ti/Al log ratio	0.465	0.220	0.535	−0.589	0.524	1.000	0.585	0.648	0.686	0.366	0.539	0.493	−0.701	0.045	0.519	0.394	0.424	0.280	−0.388
	Cr/Al log ratio	0.729	0.476	0.815	−0.554	0.638	0.585	1.000	0.660	0.432	0.448	0.445	0.741	−0.772	0.174	0.617	0.554	0.778	0.479	0.002
	Mn/Al log ratio	0.507	0.252	0.634	−0.735	0.807	0.648	0.660	1.000	0.713	0.313	0.532	0.592	−0.832	0.192	0.623	0.458	0.508	0.332	−0.452
	Fe/Al log ratio	0.303	0.064	0.420	−0.704	0.357	0.686	0.432	0.713	1.000	0.208	0.624	0.496	−0.808	−0.272	0.350	0.283	0.261	0.212	−0.637
	Cu/Al log ratio	0.393	0.449	0.404	−0.253	0.372	0.366	0.448	0.323	0.208	1.000	0.460	0.328	−0.360	0.126	0.342	0.303	0.375	0.224	0.056
	Zn/Al log ratio	0.367	0.281	0.426	−0.501	0.371	0.539	0.445	0.532	0.624	0.460	1.000	0.420	−0.605	−0.072	0.394	0.323	0.320	0.219	−0.313
	Br/Al log ratio	0.578	0.404	0.700	−0.581	0.477	0.493	0.741	0.592	0.496	0.328	0.420	1.000	−0.752	0.009	0.527	0.490	0.621	0.433	−0.161
	Rb/Al log ratio	−0.640	−0.327	−0.767	0.870	−0.618	−0.701	−0.772	−0.832	−0.808	−0.360	−0.605	−0.752	1.000	0.025	−0.663	−0.512	−0.611	−0.412	0.484
	Sr/Al log ratio	0.246	0.155	0.201	−0.057	0.515	0.045	0.174	0.192	−0.272	0.126	−0.072	0.009	0.025	1.000	0.275	0.120	0.191	0.056	0.234
	Zr/Al log ratio	0.666	0.338	0.658	−0.677	0.621	0.519	0.617	0.623	0.350	0.342	0.394	0.527	−0.663	0.275	1.000	0.432	0.579	0.349	−0.189
	Pb/Al log ratio	0.392	0.483	0.486	−0.356	0.415	0.394	0.554	0.458	0.283	0.303	0.323	0.490	−0.512	0.120	0.432	1.000	0.477	0.265	−0.086
	Ni/Al log ratio	0.687	0.434	0.711	−0.455	0.526	0.424	0.778	0.508	0.261	0.375	0.320	0.621	−0.611	0.191	0.579	0.477	1.000	0.419	0.103
	Br/Al log ratio	0.413	0.264	0.448	−0.311	0.316	0.280	0.479	0.332	0.212	0.224	0.219	0.433	−0.412	0.056	0.349	0.265	0.419	1.000	0.008
	Ba/Al log ratio	0.022	0.143	−0.062	0.547	−0.160	−0.338	0.002	−0.452	−0.637	0.056	−0.313	−0.161	0.484	0.234	−0.189	−0.086	0.103	0.008	1.000
Sig. (1-tailed)	Si/Al log ratio	–	0.000	0.000	0.000	0.000	0.000	0.000	0.000	0.000	0.000	0.000	0.000	0.000	0.000	0.000	0.000	0.000	0.000	0.062
	S/Al log ratio	0.000	–	0.000	0.000	0.000	0.000	0.000	0.000	0.000	0.000	0.000	0.000	0.000	0.000	0.000	0.000	0.000	0.000	0.000
	Cl/Al log ratio	0.000	0.000	–	0.000	0.000	0.000	0.000	0.000	0.000	0.000	0.000	0.000	0.000	0.000	0.000	0.000	0.000	0.000	0.000
	K/Al log ratio	0.000	0.000	0.000	–	0.000	0.000	0.000	0.000	0.000	0.000	0.000	0.000	0.000	0.000	0.000	0.000	0.000	0.000	0.000
	Ca/Al log ratio	0.000	0.000	0.000	0.000	–	0.000	0.000	0.000	0.000	0.000	0.000	0.000	0.000	0.000	0.000	0.000	0.000	0.000	0.000
	Ti/Al log ratio	0.000	0.000	0.000	0.000	0.000	–	0.000	0.000	0.000	0.000	0.000	0.000	0.000	0.001	0.000	0.000	0.000	0.000	0.000
	Cr/Al log ratio	0.000	0.000	0.000	0.000	0.000	0.000	–	0.000	0.000	0.000	0.000	0.000	0.000	0.000	0.000	0.000	0.000	0.000	0.454
	Mn/Al log ratio	0.000	0.000	0.000	0.000	0.000	0.000	0.000	–	0.000	0.000	0.000	0.000	0.000	0.000	0.000	0.000	0.000	0.000	0.000
	Fe/Al log ratio	0.000	0.000	0.000	0.000	0.000	0.000	0.000	0.000	–	0.000	0.000	0.000	0.000	0.000	0.000	0.000	0.000	0.000	0.000
	Cu/Al log ratio	0.000	0.000	0.000	0.000	0.000	0.000	0.000	0.000	0.000	–	0.000	0.000	0.000	0.000	0.000	0.000	0.000	0.000	0.000

(continued)

Table A.2 (continued)

BGS Core DD029 Correlation Matrix		Si/Al log ratio	S/Al log ratio	Cl/Al log ratio	K/Al log ratio	Ca/Al log ratio	Ti/Al log ratio	Cr/Al log ratio	Mn/Al log ratio	Fe/Al log ratio	Cu/Al log ratio	Zn/Al log ratio	Br/Al log ratio	Rb/Al log ratio	Sr/Al log ratio	Zr/Al log ratio	Pb/Al log ratio	Ni/Al log ratio	Br/Al log ratio	Ba/Al log ratio
	Zn/Al log ratio	0.000	0.000	0.000	0.000	0.000	0.000	0.000	0.000	0.000	0.000	–	0.000	0.000	0.000	0.000	0.000	0.000	0.000	0.000
	Br/Al log ratio	0.000	0.000	0.000	0.000	0.000	0.000	0.000	0.000	0.000	0.000	0.000	–	0.000	0.279	0.000	0.000	0.000	0.000	0.000
	Rb/Al log ratio	0.000	0.000	0.000	0.000	0.000	0.000	0.000	0.000	0.000	0.000	0.000	0.000	–	0.041	0.000	0.000	0.000	0.000	0.000
	Sr/Al log ratio	0.000	0.000	0.000	0.000	0.000	0.001	0.000	0.000	0.000	0.000	0.000	0.279	0.041	–	0.000	0.000	0.000	0.000	0.000
	Zr/Al log ratio	0.000	0.000	0.000	0.000	0.000	0.000	0.000	0.000	0.000	0.000	0.000	0.000	0.000	0.000	–	0.000	0.000	0.000	0.000
	Pb/Al log ratio	0.000	0.000	0.000	0.000	0.000	0.000	0.000	0.000	0.000	0.000	0.000	0.000	0.000	0.000	0.000	–	0.000	0.000	0.000
	Ni/Al log ratio	0.000	0.000	0.000	0.000	0.000	0.000	0.000	0.000	0.000	0.000	0.000	0.000	0.000	0.000	0.000	0.000	–	0.000	0.000
	Br/Al log ratio	0.000	0.000	0.000	0.000	0.000	0.000	0.000	0.000	0.000	0.000	0.000	0.000	0.000	0.000	0.000	0.000	0.000	–	0.303
	Ba/Al log ratio	0.062	0.000	0.000	0.000	0.000	0.000	0.454	0.000	0.000	0.000	0.000	0.000	0.000	0.000	0.000	0.000	0.000	0.303	–

Table A.3 Results from a Principal Component Analysis on core DD090 XRF data

Total variance explained					
Component	Initial eigenvalues			Extraction sums of squared loadings	
	Total	% of Variance	Cumulative	Total	% of Variance
1	9.595	50.501	50.501	9.595	50.501
2	2.556	13.454	63.955	2.556	13.454
3	1.388	7.306	71.260	1.388	7.306
4	0.943	4.962	76.223	0.943	4.962
5	0.818	4.307	80.530	0.818	4.307
6	0.741	3.897	84.427		
7	0.563	2.961	87.388		
8	0.439	2.309	89.697		
9	0.374	1.969	91.666		
10	0.295	1.555	93.221		
11	0.282	1.484	94.705		
12	0.213	1.119	95.824		
13	0.198	1.041	96.865		
14	0.153	0.807	97.671		
15	0.137	0.722	98.394		
16	0.104	0.550	98.944		
17	0.084	0.444	99.387		
18	0.065	0.345	99.732		
19	0.051	0.268	100.000		

Component matrix[a]					
	Component				
	1	2	3	4	5
Si/AI log ratio	0.852	−0.155	−0.037	−0.207	0.012
S/AI log ratio	0.773	−0.249	−0.097	0.083	−0.166
CI/AI log ratio	0.936	−0.154	−0.022	−0.104	0.111
K/AI log ratio	−0.693	0.005	0.151	0.461	0.410
Ca/AI log ratio	0.782	0.081	0.516	−0.019	−0.090
Ti/AI log ratio	0.244	0.714	0.054	0.437	0.155
Cr/AI log ratio	0.917	0.018	−0.013	−0.008	0.267
Mn/AI log ratio	0.683	0.523	0.416	−0.057	−0.008
Fe/AI log ratio	0.147	0.900	−0.098	−0.073	0.108
Cu/AI log ratio	0.737	−0.154	−0.159	0.325	−0.284
Zn/AI log ratio	0.575	0.384	−0.248	0.314	−0.339

(continued)

Table A.3 (continued)

Br/AI log ratio	0.889	−0.028	−0.127	−0.099	0.183
Rb/AI log ratio	−0.879	−0.190	0.190	0.254	0.011
Sr/AI log ratio	0.416	−0.151	0.834	0.059	−0.185
Zr/AI log ratio	0.569	−0.074	−0.231	0.210	−0.192
Pb/AI log ratio	0.748	0.045	−0.095	0.177	0.014
Ni/AI log ratio	0.895	−0.139	−0.034	0.020	0.233
Br/AI log ratio	0.714	−0.095	−0.045	−0.030	0.347
Ba/AI log ratio	0.336	−0.762	−0.047	0.331	0.143

Extraction Method: Principal Component Analysis[a]

[a] 5 components extracted

Table A.4 Correlation matrix for core DD090

BGS Core DD090 Correlation Matrix		Si/Al log ratio	S/Al log ratio	Cl/Al log ratio	K/Al log ratio	Ca/Al log ratio	Ti/Al log ratio	Cr/Al log ratio	Mn/Al log ratio	Fe/Al log ratio	Cu/Al log ratio	Zn/Al log ratio	Br/Al log ratio	Rb/Al log ratio	Sr/Al log ratio	Zr/Al log ratio	Pb/Al log ratio	Ni/Al log ratio	Br/Al log ratio	Ba/Al log ratio
Correlation	Si/Al log ratio	1.000	0.597	0.880	−0.679	0.633	0.063	0.773	0.468	−0.014	0.582	0.403	0.740	−0.724	0.326	0.456	0.572	0.797	0.596	0.332
	S/Al log ratio	0.597	1.000	0.690	−0.563	0.506	−0.011	0.668	0.381	−0.071	0.662	0.402	0.671	−0.615	0.315	0.419	0.683	0.669	0.513	0.428
	Cl/Al log ratio	0.880	0.690	1.000	−0.632	0.711	0.099	0.891	0.545	0.014	0.647	0.423	0.857	−0.828	0.360	0.535	0.648	0.881	0.672	0.413
	K/Al log ratio	−0.679	−0.563	−0.632	1.000	−0.502	0.000	−0.522	−0.418	−0.070	−0.477	−0.397	−0.586	0.737	−0.211	−0.408	−0.441	−0.523	−0.416	−0.059
	Ca/Al log ratio	0.633	0.506	0.711	−0.502	1.000	0.262	0.668	0.783	0.113	0.501	0.382	0.612	−0.632	0.696	0.361	0.487	0.636	0.498	0.228
	Ti/Al log ratio	0.063	−0.011	0.099	0.000	0.262	1.000	0.257	0.476	0.552	0.113	0.395	−0.164	−0.229	0.031	0.209	0.242	0.172	0.123	−0.306
	Cr/Al log ratio	0.773	0.668	0.891	−0.522	0.668	0.257	1.000	0.626	0.181	0.607	0.454	0.862	−0.810	0.325	0.441	0.687	0.887	0.678	0.323
	Mn/Al log ratio	0.468	0.381	0.545	−0.418	0.783	0.476	0.626	1.000	0.562	0.359	0.474	0.546	−0.630	0.518	0.244	0.471	0.517	0.414	−0.134
	Fe/Al log ratio	−0.014	−0.071	0.014	−0.070	0.113	0.552	0.181	0.562	1.000	−0.039	0.398	0.143	−0.327	−0.173	−0.035	0.157	0.014	0.047	−0.571
	Cu/Al log ratio	0.582	0.662	0.647	−0.477	0.501	0.113	0.607	0.359	−0.039	1.000	0.575	0.602	−0.563	0.251	0.452	0.561	0.626	0.479	0.393
	Zn/Al log ratio	0.403	0.402	0.423	−0.397	0.382	0.395	0.454	0.474	0.398	0.575	1.000	0.450	−0.539	0.062	0.319	0.441	0.402	0.324	0.003
	Br/Al log ratio	0.740	0.671	0.857	−0.586	0.612	0.164	0.862	0.546	−0.143	0.602	0.450	1.000	−0.839	0.241	0.465	0.634	0.825	0.647	0.318
	Rb/Al log ratio	−0.724	−0.615	−0.828	0.737	−0.632	−0.229	−0.810	−0.630	−0.327	−0.563	−0.539	−0.839	1.000	−0.166	−0.509	−0.606	−0.749	−0.592	−0.079
	Sr/Al log ratio	0.326	0.315	0.360	−0.211	0.696	0.031	0.325	0.518	−0.173	0.251	0.062	0.241	−0.166	1.000	0.134	0.257	0.326	0.238	0.253
	Zr/Al log ratio	0.456	0.419	0.535	−0.408	0.361	0.209	0.441	0.244	−0.035	0.452	0.319	0.465	−0.509	0.134	1.000	0.388	0.484	0.368	0.222
	Pb/Al log ratio	0.572	0.683	0.648	−0.441	0.487	0.242	0.687	0.471	0.157	0.561	0.441	0.634	−0.606	0.257	0.388	1.000	0.660	0.467	0.208
	Ni/Al log ratio	0.797	0.669	0.881	−0.523	0.636	0.172	0.887	0.517	0.014	0.628	0.402	0.825	−0.749	0.326	0.484	0.660	1.000	0.658	0.420
	Br/Al log ratio	0.596	0.513	0.672	−0.416	0.498	0.123	0.678	0.414	0.047	0.479	0.324	0.647	−0.592	0.238	0.368	0.467	0.658	1.000	0.306
	Ba/Al log ratio	0.332	0.428	0.413	−0.059	0.228	−0.306	0.323	−0.134	−0.571	0.393	0.003	0.318	−0.079	0.253	0.222	0.208	0.420	0.308	1.000
Sig. (1-tailed)	Si/Al log ratio	−	0.000	0.000	0.000	0.000	0.000	0.000	171.128	0.000	0.000	0.000	0.000	0.000	0.000	0.000	0.000	0.000	0.000	0.000
	S/Al log ratio	0.000	−	0.000	0.000	0.189	0.000	0.000	0.000	0.000	0.000	0.000	0.000	0.000	0.000	0.000	0.000	0.000	0.000	0.000
	Cl/Al log ratio	0.000	0.000	−	0.000	0.000	0.000	0.000	0.000	0.140	0.000	0.000	0.000	0.000	0.000	0.000	0.000	0.000	0.000	0.000
	K/Al log ratio	0.000	0.000	0.000	−	0.000	0.489	0.000	0.000	0.000	0.000	0.000	0.000	0.000	0.000	0.000	0.000	0.000	0.000	0.000
	Ca/Al log ratio	0.000	0.000	0.000	0.000	−	0.000	0.000	0.000	0.000	0.000	0.000	0.000	0.000	0.000	0.000	0.000	0.000	0.000	0.000
	Ti/Al log ratio	0.000	0.189	0.000	0.489	0.000	−	0.000	0.000	0.000	0.000	0.000	0.000	0.000	0.007	0.000	0.000	0.000	0.000	0.000
	Cr/Al log ratio	0.000	0.000	0.000	0.000	0.000	0.000	−	0.000	0.000	0.000	0.000	0.000	0.000	0.000	0.000	0.000	0.000	0.000	0.000
	Mn/Al log ratio	0.000	0.000	0.000	0.000	0.000	0.000	0.000	−	0.000	0.000	0.000	0.000	0.000	0.000	0.000	0.000	0.000	0.000	0.000

(continued)

Table A.4 (continued)

BGS Core DD090 Correlation Matrix		Si/Al log ratio	S/Al log ratio	Cl/Al log ratio	K/Al log ratio	Ca/Al log ratio	Ti/Al log ratio	Cr/Al log ratio	Mn/Al log ratio	Fe/Al log ratio	Cu/Al log ratio	Zn/Al log ratio	Br/Al log ratio	Rb/Al log ratio	Sr/Al log ratio	Zr/Al log ratio	Pb/Al log ratio	Ni/Al log ratio	Br/Al log ratio	Ba/Al log ratio
	Fe/Al log ratio	0.128	0.000	0.140	0.000	0.000	0.000	0.000	0.000	–	0.001	0.000	0.000	0.000	0.000	0.002	0.000	0.139	0.000	0.000
	Cu/Al log ratio	0.000	0.000	0.000	0.000	0.000	0.000	0.000	0.000	0.001	–	0.000	0.000	0.000	0.000	0.000	0.000	0.000	0.000	0.000
	Zn/Al log ratio	0.000	0.000	0.000	0.000	0.000	0.000	0.000	0.000	0.000	0.000	–	0.000	0.000	0.000	0.000	0.000	0.000	0.000	0.417
	Br/Al log ratio	0.000	0.000	0.000	0.000	0.000	0.000	0.000	0.000	0.000	0.000	0.000	–	0.000	0.000	0.000	0.000	0.000	0.000	0.000
	Rb/Al log ratio	0.000	0.000	0.000	0.000	0.000	0.000	0.000	0.000	0.000	0.000	0.000	0.000	–	0.000	0.000	0.000	0.000	0.000	0.000
	Sr/Al log ratio	0.000	0.000	0.000	0.000	0.000	0.007	0.000	0.000	0.000	0.000	0.000	0.000	0.000	–	0.000	0.000	0.000	0.000	0.000
	Zr/Al log ratio	0.000	0.000	0.000	0.000	0.000	0.000	0.000	0.000	0.002	0.000	0.000	0.000	0.000	0.000	–	0.000	0.000	0.000	0.000
	Pb/Al log ratio	0.000	0.000	0.000	0.000	0.000	0.000	0.000	0.000	0.000	0.000	0.000	0.000	0.000	0.000	0.000	–	0.000	0.000	0.000
	Ni/Al log ratio	0.000	0.000	0.000	0.000	0.000	0.000	0.000	0.000	0.139	0.000	0.000	0.000	0.000	0.000	0.000	0.000	–	0.000	0.000
	Br/Al log ratio	0.000	0.000	0.000	0.000	0.000	0.000	0.000	0.000	0.000	0.000	0.000	0.000	0.000	0.000	0.000	0.000	0.000	–	0.000
	Ba/Al log ratio	0.000	0.000	0.000	0.000	0.000	0.000	0.000	0.000	0.000	0.000	0.417	0.000	0.000	0.000	0.000	0.000	0.000	0.000	–

Index

K. Horan, *Falkland Islands (Islas Malvinas) in the Permo-Carboniferous*,
Springer Earth System Sciences, DOI 10.1007/978-3-319-08708-5